MAX Phase Ternary Carbides: Synthesis, Nanocomposites and Exfoliated 2D MAXene/MXene Nanostructures for Multifunctional Applications

Thesis submitted to the

UNIVERSITY OF KERALA

For the Award of the Degree of

DOCTOR OF PHILOSOPHY IN CHEMISTRY

Under the faculty of Science

By

MAHESH K. V.

Functional Materials Section
Materials Science and Technology Division
CSIR- National Institute for Interdisciplinary Science and Technology
(CSIR-NIIST), Thiruvananthapuram, India

September 2016

DECLARATION

I, Mahesh K. V., hereby declare that the work presented in the Ph. D. thesis entitled *"**MAX Phase Ternary Carbides: Synthesis, Nanocomposites and Exfoliated 2D MAXene/MXene Nanostructures for Multifunctional Applications**"* is an independent research work carried out by me for the award of degree of Doctor of Philosophy in Chemistry of the University of Kerala, under the guidance of Dr. S. Ananthakumar, Senior Principal Scientist, Functional Materials Section, Materials Science and Technology Division, CSIR-National Institute for Interdisciplinary Science and Technology (CSIR-NIIST), Trivandrum. I further declare that this thesis or any part of it has not been submitted anywhere else for any other degree, diploma or other similar title.

(MAHESH K. V.)

Place: Trivandrum
Date: 08-09-2016

COUNCIL OF SCIENTIFIC & INDUSTRIAL RESEARCH
NATIONAL INSTITUTE FOR INTERDISCIPLINARY SCIENCE AND TECHNOLOGY (CSIR-NIIST)
Industrial Estate P.O., Pappanamcode,
Trivandrum - 695 019, Kerala, INDIA
www.niist.res.in

Dr. S. Ananthakumar
Senior Principal Scientist
Functional Materials Section
Materials Science and Technology Division

Off: 0471-2515289
Mob: 09497271547
Fax: +91-471-249171
E-mail: ananthakumar70@gmail.com

CERTIFICATE

Certified that the work embodied in the thesis entitled, *"MAX Phase Ternary Carbides: Synthesis, Nanocomposites and Exfoliated 2D MAXene/MXene Nanostructures for Multifunctional Applications"* is an authentic record of the research work carried out by Mr. Mahesh K. V., Functional Materials Section, Materials Science and Technology Division, CSIR-National Institute for Interdisciplinary Science and Technology (CSIR-NIIST), Trivandrum, under my supervision in partial fulfillment of the requirement for the degree of Doctor of Philosophy of the University of Kerala. It is further certified that no part of this thesis has been presented previously anywhere else for the award of any other degree.

Dr. S. Ananthakumar

(Research Guide)

Place: Trivandrum
Date: 08-09-2016

Dedicated to

My Family..........

Acknowledgements

CONTENTS

CHAPTER 1: MAX Phase Ternary Carbides: Evolution, Properties and Applications

CHAPTER 2: MAX Phase- Polymer Composites

Polyaryletherketone (PAEK) Polymer Engineered with Nanolaminated Ti$_3$SiC$_2$ Ceramic Fillers

LIST OF FIGURES

LIST OF TABLES

LIST OF ABBREVIATIONS

2D	Two dimensional
3D	Three dimensional
ASTM	American Society for Testing and Materials
CLSI	Clinical and Laboratory Standards Institute
CLSM	Confocal Laser Scanning Microscopy
CVD	Chemical Vapor Deposition
DMF	N,N Dimethyl Formamide
DMSO	Dimethyl sulfoxide
EDX	Energy Dispersive X-ray spectroscopy
HBSS	Hanks balanced salt solution
HIP	Hot Isostatic Pressing
HP	Hot Pressing
ICDD	International Centre for Diffraction Data
in vitro	Test tube experiments
MIC	Minimum Inhibitory Concentration
MS	Magnetron Sputtering
MTCC	Microbial Type Culture Collection
MTT	Methyl thiazolyl tetrazolium
NMP	N-Methyl pyrolidinone
PAEK	Polyaryletherketone
PBS	Phosphate buffered saline/solution
PDS	Pulsed discharge sintering
PI	Propidium iodide
PLD	Pulsed laser deposition
ROS	Reactive Oxygen Species
SEM	Scanning Electron Microscopy
SHS	Self-propagating high temperature synthesis
SPS	Spark plasma sintering
TEM	Transmission Electron Microscopy
TGA	Thermogravimetric Analysis
UV-Vis	Ultra-violet visible
XPS	X-ray Photoelectron Spectroscopy
XRD	X-ray Diffraction

LIST OF SYMBOLS

%	Percent
˚C	Degrees Celsius
μL	Microliter
μm	Micrometer
2θ	Diffraction angle in degrees
K	Kelvin
Å	Angstrom
ca.	Circa (around)
g	Gram
η	Viscosity
μ	Coefficient of friction
h	Hour
min	Minute
mL	Milliliter
mol	Mole
V%	% volume per volume
ρ	Density
GPa	Giga Pascal
MPa	Mega Pascal
S	Siemens
W	Watts
J	Joules
K_{IC}	Fracture toughness
σ	Flexural strength
λ	Wavelength
Ω	Ohm
GHz	Giga Hertz

Preface

Growing technological requirements demand more reliable and multifunctional materials in the fields of energy, environment, and electronics fields. Discovery of *'graphene'* is one such innovative functional material which had created a great sensation in the last decade. Unusual physico/chemical properties of graphene generated renowned interest to look forward for other potential layered nanostructures. Recent years documented the processing of layered MoS_2, BN and WS_2 nanosheets and their beneficial properties to design the next generation miniature devices, energy storage batteries and electronic gadgets.

Interestingly, there is another group of layered materials that has received great attention after a long hibernation period since its discovery. This family is named as '*MAX phase'* by the re-inventor Prof. M.W. Barsoum, gained significant attraction due to its 'intermetallic-ceramic' properties. MAX phase materials are found to offer many essential engineering properties suitable for structural, electronics, and energy related applications. More recently, the MAX phase research is turned towards the synthesis of 2D layered nanostructures, titled as *MAXenes* and *MXenes.*

In this work, a challenging research problem is identified and executed in a systematic way in order to unveil the potential and beneficial properties of the selected MAX phase nanostructures. Aspects such as design of polymer matrix nano composites with MAX phase reinforcements, MAX phase synthesis via microwave heating, new and faster technique to exfoliate bulk MAX phase into 2D MAXene layers, processing of MAXene thermal fluids as 'nanocoolant', and finally the synthesis and antimicrobial properties of MXene nanostructures are investigated and presented. All these aspects are in fact 'first-of-its-kind' and these research findings are successfully published in reputed journals having high impact factor which is considered as one of the productive outcome of this research work.

The thesis has been divided into five chapters. **Chapter 1** covers general introduction on the layered materials with the thrust over MAX phase inter-metallic

layered material. The material history, crystal structure, synthesis, properties and applications of MAX phase are briefly discussed. Furthermore, the evolution of new nanostructures namely, MXenes, a 2D derivative of MAX phase was also discussed. The scope of the research problem and objectives of the present thesis are also described.

In **Chapter 2**, the potential beneficial properties of MAX phase dispersoids in polymer matrix was systematically investigated. Ti_3SiC_2 MAX phase nanolaminate was employed as reinforcement in PAEK matrix for the first time to obtain thermally stable, low friction, low wear PAEK (Polyaryletherketone) polymer composite without compromising the inhererent machinability. The advantages realised with nano laminate Ti_3SiC_2 include decreased thermal decomposition and recrystallisation temperature, at least 50% enhancement in the mechanical hardness, flexural and compressive strengths and ~40% reduction in the thermal expansion values. The PAEK-Ti_3SiC_2 composites showed progressive wear resistance and low coefficient of friction suitable for developing thermo-mechanically stable engineeirng components.

Chapter 3 devoted to the exfoliation or delaminantion of laminated MAX phase into 2D nanostructures. This work was carried out in two parts. In the first part, a new micromechanical cleavage strategy was successfully demonstrated to produce 2D MAX phase by retaining the 'A' layer atoms. We have named this exotic newly derived 2D MAX phase as '*MAXenes*' in order to emphasize it's 2D characteristics analogues to graphene. The effect of exfoliation in different solvents with time was studied. Subsequently, the stability 2D Ti_3SiC_2 MAXene dispersion has been studied. The electrical conductivity of MXene nanosheets is also ascertained and found to be six times higher than the bulk Ti_3SiC_2 counterpart. In this part of the work, synthesis of nanostructured 2D carbides via a simple and innovative method is achieved.

In the second part of **Chapter 3**, 2D MAXene nanosheets were studied for the thermal fluid application. *In situ* milling of Ti_3SiC_2 MAXene nanosheets in propylene glycol medium induced micromechanical shear that resulted in highly stable surfactant-free thermal nanofluid. This new nanofluid qualifies all the necessary requirements for a heat-transport thermal management fluid. The rheology and the thermal property were studied and the results are discussed. Stable MAXene nanostructures increased

the fluid thermal conductivity to a large extent. Interestingly, the MAXene-propylene glycol nanofluids also showed excellent lubrication property.

The works covered in **Chapter 4** is also contains two parts. In **Part I,** synthesis of Ti_3AlC_2 MAX phase materials by microwave hybrid heating is discussed. The role of microwave energy on the phase formation of MAX phase is reported. The role of nano SiC as *in situ* susceptor is examined. Application of microwave energy for producing Ti_3AlC_2 MAX phase is a new idea attempted in this research. The reaction conditions to form Ti_3AlC_2 were successfully optimized. The **Part II** of this chapter brings light into the antimicrobial, antibiofilm and cytotoxicity properties of $Ti_3C_2T_x$ MXenes produced by selective removal of 'Al' atoms from the bulk Ti_3AlC_2 MAX phase. We have successfully shown that $Ti_3C_2T_x$ MXenes possess excellent resistance against range of bacteria and fungi. It also acts as an excellent antibiofilm agent. The preliminary cytotoxicity studies suggest that $Ti_3C_2T_x$ MXenes is not toxic to mammalian cells. The summary and conclusions as well as future directions regarding this research are given in **Chapter 5**.

CHAPTER 1

MAX Phase Ternary Carbides: Evolution, Properties and Applications
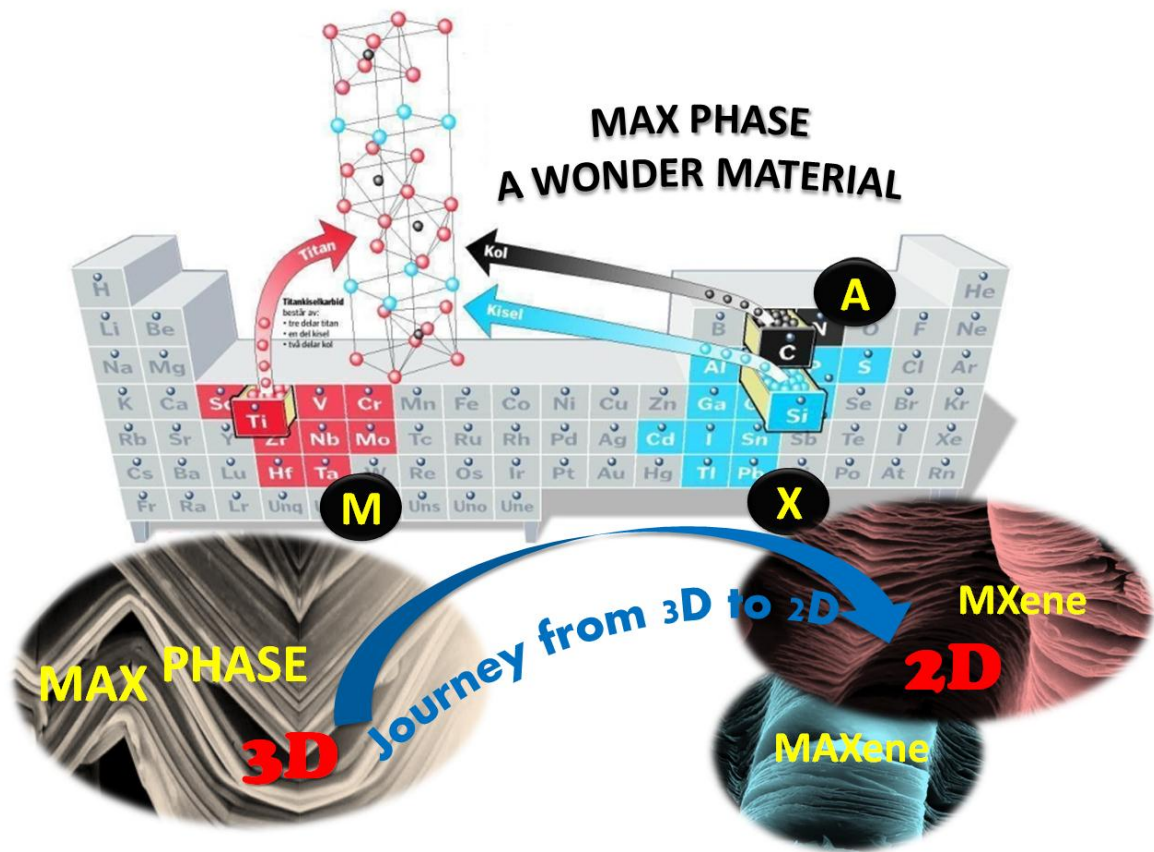
MAX Phase Ternary Carbides:
Evolution, Properties and Applications

Materials science is an interdisciplinary field, where the focus is on the cutting edge studies on the design and discovery of new materials, and their properties and applications. Researchers engaged in basic science and engineering fields are constantly working for developing new and advanced materials to meet the never-ending demand from the industrial and strategic sectors. New materials with exotic functional properties are very much needed to meet the growing technological requirements in automobile, aerospace, defense, and nuclear fields. It requires tremendous efforts on finding economically viable advanced processing techniques, analysis of structure, properties, performance, and reliability of the new tailor-made materials.

The discovery or identification of exotic new materials always created unimaginable breakthrough in the history of materials science. The discovery of fullerenes in 1985 [H. W. Kroto *et al.* 1985] and carbon nanotubes (CNTs) in 1991 [Iijima 1991] were such scientific breakthroughs that happened in the last century. It stimulated scientific curiosity among the researchers to design several other inorganic nanostructured materials, for example, WS_2, MoS_2, and BN nano tubes. In materials research, no other material created history in the last decade, as 'graphene', the two dimensional network of sp^2-hybridized carbon atoms derived from the bulk layers of graphite. The potential functional properties of graphene nanosheets generated research interest in various other layered structured materials such as dichalcogenides [Tenne *et al.*1992], BN, natural clay platelets etc. As the work in this thesis is mainly focused on MAX phase bulk and nanostructured layered materials and their functional properties, we have briefly discussed the state-of-art on some of the well-known layered materials.

1.1 Layered Materials

Materials having one of the three principal dimensions significantly smaller than the other two, are named as layered materials. They are found in various sizes,

from macroscopic to the nanoscopic levels. Layered materials represent an attractive class of materials with their structure consisting of nanosheets stacked one on another. These materials received much attention from the ancient days onwards due to their versatile surface properties.

Natural clays are the oldest layered materials identified by us. Mostly, clay minerals are aluminosilicates and they have layered structures consisting of polymeric sheets of SiO_4 tetrahedra linked to sheets of octahedral (Al, Mg, Fe)$(O,OH)_6$. In short, the primary structure of clay is lamellar with parallel layers of tetrahedral silicate and octahedral aluminate sheets. These are formed on the earth by the chemical weathering of other silicate materials [Ismadji *et al.* 2015]. The research interest on clays is actually owing to its plentiful opportunities to modify the surface functional properties via intercalation chemistry. The properties such as ion exchange capacity, sorptive, and swelling, etc. made it suitable for adsorption, catalysis, water purification, paper coatings, skin care products and enzyme immobilization applications [Gil *et al.* 2010; Sanjay and Sugunan 2005].

1.1.1 Layered Graphite

Graphite is another naturally occurring layered material with weak interlayer bonding and has been known for more than 500 years. It is one of the allotropes of carbon. Structure of graphite consists of hexagonally arranged carbon atoms in a planar condensed ring system, and these layers are stacked parallel to each other. The atoms within the same layers are held together by covalent bonds, whereas each layer is bonded to the adjacent layer through van der Waals forces. These weak Van der Waals bonding between individual layers allows the layers to slide over one another. This unique property makes graphite an ideal solid lubricant. It is widely used in industries for making crucibles, ladles, and moulds for metals melting. They are also recognized for refractory applications because of their moderate high temperature stability and chemical inertness. The low neutron absorption capacity and high thermal conductivity properties of graphite find application in nuclear reactors as moderators. Due to its excellent electrical conductivity and low friction they are also utilized in the form of carbon brushes for electrical motors. The high mechanical stiffness of graphite was explored in carbon

fiber composites. All these industrial uses made graphite a hot material and there is a worldwide demand of more than one million tons annually.

1.1.2 Graphene nanostructures

The discovery of fullerenes and carbon nanotubes motivated and triggered research on carbon based nanostructures. Many scientists realized the possibility of obtaining a single sheet of graphite, referred to as graphene. The efforts to get layered graphite started by the end of the last century. In 1999, graphite slabs having thickness ~ 200 nm were successfully produced by Ruoff and co-workers by peeling off layers using an atomic force microscope (AFM) tip [Xuekun *et al.* 1999]. However, it could be only demonstrated with approximately 600 layers. Later, Kim and co-workers modified this technique to obtain graphite slabs as thin as ~10 nm. Here, they could obtain the graphite sheets with 30 layers [Zhang *et al.* 2005]. But the real landmark victory was made by Andre Geim and Kostya Novoselov in 2004. The historical isolation of single-atom-thick crystallites of graphene from the bulk graphite was successfully shown by Andre Geim and Kostya Novoselov via the scotch tape method that created great sensation in materials science and related areas [Novoselov *et al.* 2004]. This two dimensional honeycomb network was considered as the basic building unit for other exciting carbon forms. The stacking of graphene layers forms 3D graphite, and their rolling creates 1D nanotubes and wrapping would form 0D fullerenes. Even though a bright future is envisaged in graphene layered materials, the advanced level graphene research faced a technological barrier due to the difficulty in producing good quality single layers by the mechanical exfoliation technique. Enormous amount of efforts have been made by researchers to discover alternate routes to produce high quality single layer graphene.

It was Rouff's group, which first introduced a chemical technique to produce single layered graphene [Stankovich *et al.* 2006; Stankovich *et al.* 2007]. They employed Hummers' oxidation method to convert graphite to graphite oxide which upon mechanical exfoliation produced layers of graphene oxide. The graphitic network is substantially restored either through thermal annealing or through chemical reduction. The advantage of this method is its cost effectiveness and scalability to produce gram level or more graphene layers. Over the past few years,

several other methods such as thermal decomposition of SiC, epitaxial growth on transition metal substrates via chemical vapor deposition of alcohols and hydrocarbons etc. were also identified for producing high quality graphene layers in industrial scale. [de Heer *et al.* 2007; Li *et al.* 2009; Kwon *et al.* 2009].

Graphene oxide (GO) and graphene nanomaterials are recommended for many applications. Ruoff's group demonstrated the fabrication of free-standing GO films with high tensile strength up to ~42 GPa [Dikin *et al.* 2007]. The chemically derived GO and graphene dispersions allow uniform and reproducible deposition on various substrates which is in fact critical in fabrication of many devices [Wu *et al.* 2008a; Cote *et al.* 2009]. Today graphene is considered as one of the promising materials for energy, electronics, and sensor fields. Due to the modification in local carrier concentration of graphene layers, it shows variation in resistance when gas molecules are adsorbed. This property was used to detect gases like NH_3, CO, NO_2, and H_2O [Schedin *et al.* 2007]. Another potential application with graphene is in the Field Effect Transistors (FET) [Novoselov *et al.* 2004]. In optoelectronics, graphene plays the role of transparent conducting electrodes [Kim *et al.* 2009; Wu *et al.* 2008b]. The superior electrical conductivity, high surface area and chemical tolerance made graphene a candidate material for anode in Li-ion batteries. Decoration with metal oxides was employed to further enhance the performance, for e.g. the graphene decorated with SnO_2 exhibits a reversible capacity of 810 mAh/g and enhanced cycling performance [Paek *et al.* 2009].

1.1.3 Layered Inorganic Materials Other than Graphite and Graphene

The unusual and unique properties of carbon based layered nanomaterials have stimulated enormous interest in other layered materials. Researchers in recent years looked into the possibility of making many inorganic layered materials. Development of single as well as a few-layered thick chalcogenides has been demonstrated out of MoS_2, WS_2, WSe_2, $MoSe_2$, GaSe, and BN. Boron nitride (BN) is isoelectronic with graphene. In addition to these layered materials, there are also layered oxides such as iron and titania nano sheets. Boehmite, a monohydroxy aluminiumoxide, also possesses layered structure. Enormous amount of work has been dedicated to the research on layered double hydroxide (LDH). As anticipated, these 2D materials exhibit fascinating properties, and some have potential

multifunctional applications. For example, the layered transition-metal dichalcogenides has the capability to intercalate Li ions in its layered structure, and also exhibit fast ion conductivity, rendering them good host materials for rechargeable batteries. Haering *et al.* demonstrated for the first time the use of MoS_2 as the electrode material for Li-ion battery, [Haering *et al.* 1980]. Over the years, 2D as well as few layered MoS_2 has been explored for different applications including electronics, energy storage, catalysis, thermoelectrics, gas sensing, etc. [Deepesh *et al.* 2014]. In fact, WS_2 and WSe_2 were recently identified as good dielectric interface material for FETs [Sik Hwang *et al.* 2012]. Excellent thermal conductivity, mechanical stability, very low electrical conductivity, and chemical inertness of 2D BN nanosheets made it active fillers for electrically insulating high thermal conducting composites. BN nanostructures were also explored and recommended for thermal fluids [Jaime *et al.* 2012].

There is another group of layered materials that gained lots of attention in the recent years after a long hibernation period since it's discovery. This family is named as 'MAX phase' by the re-inventor M.W. Barsoum. MAX phase material has versatile properties suitable for structural, electronics, engineering, energy, and environmental applications. The following sections describe the history, evolution, structure, properties, and applications of MAX phase materials reported till date.

1.2 Layered MAX Phase Ternary Carbides- a Wonder Material

1.2.1 What are MAX Phases?

MAX phases are an important class of layered ternary carbides and nitrides of early transition metals. The name "MAX phases" was first coined in the late 1990s. They are so called because of their chemical composition represented by the general formula: $M_{n+1}AX_n$ where, M is an early transition metal, A is an A-group element (specifically, the subset of elements 13–16), X is carbon and/or nitrogen, and n = 1, 2, or 3 [Barsoum *et al.* 2000a]. As shown in Figure 1.1, the 'M' group elements mainly include Sc, Ti, V, Cr, Zr, Nb, Mo, Hf, and Ta. The 'A' elements may be Al, Si, P, S, Ga, Ge, As, Cd, In, Sn, Tl, and Pb. The 'X' elements are either C and/or N. Based on the different stoichiometries (M_2AX, M_3AX_2, etc.), they are often referred as 211, 312 and 413 MAX phases. The existence of higher order MAX phases such as 514, 615,

and 716 [Palmquist *et al.* 2004; Lane *et al.* 2012] are also predicted either experimentally or theoretically. The layered structure and metal type bonding in MAX phases are responsible for their unique properties. In many aspects they behave like ceramics by possessing high stiffness, corrosion, oxidation and creep resistance properties. On the other hand they also have properties of metals such as good electrical and thermal conductivity, machinability, low hardness, thermal shock resistance etc. Thus they bridge the gap between properties of both metals and ceramics. The remarkable blend of metallic and ceramic characteristics of the MAX phases made it an interesting candidate for designing advanced functional materials, and composites.
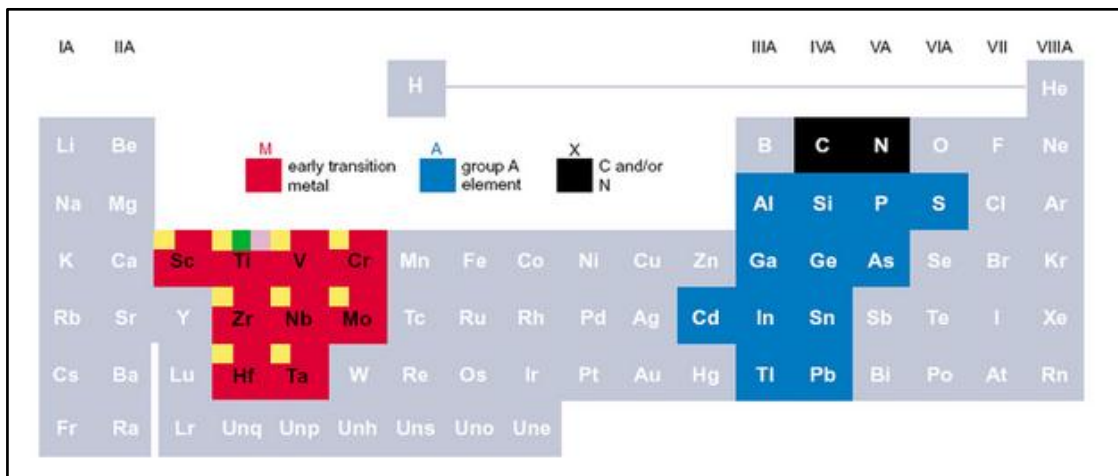
Figure 1.1: The periodic table showing the constituent elements that form the MAX phase materials

1.2.2 History of MAX Phases

"Like many other materials, the identification of MAX phase was purely by luck" says M.W. Barsoum, the man behind this material [Barsoum 2013]. The historical discovery of MAX phases happened in the beginning of the 1960's when Nowotny and Benesovsky started their research on early transition metals based ternary systems. In the following years, they synthesized many new ternary systems. The team identified around 40 new complex-carbides within the ternary compounds and characterized them by X-ray and neutron diffraction techniques. They called these compounds with the general term *H-phase* or *Hagg phase* and also called by the name M_2BX phase [Nowotony 1971]. It is worth to note that the term 'H' in H-phase is not an abbreviation of the term *'Hagg'*. Carbides, nitrides, borides,

and hydrides with metal atoms forming close-packed or hexagonal arrays with C, N, B, or H occupied in the interstitial octahedral or trigonal sites are known as *Hagg* phases. The "H phases" do not satisfy these conditions; the C or N atoms do occupy an interstitial octahedral site, but the metal substructure is not close-packed or nearly close-packed. In short, MAX phase can fall in both categories, but all 'H phases' are not 'Hagg phases' [Eklund *et al.* 2010].

It is also interesting to know the story behind the name 'MAX phases'. As mentioned earlier, they were initially named as H-phase or M_2BX phases. Later, Barsoum *et al.* noticed the fact that the IUPAC scrambled the periodic table in 1980s by interchanging the A and B elements i.e. A elements became B and B elements became A. That is how they coined the name 'MAX phase'. The periodic table was modified yet again. The letters were eschewed and number was given to the column. The A- group elements of MAX phase now belong to group13-16. However, the existence of one MAX phase, Ti_2CdC suggest that the label "A" in "MAX phases" is not strictly accurate since in this material "A" element is from group 12. Ever since this new naming, the notation 'MAX' is ubiquitous and other notation are not in use today.

The initial contributions on MAX phase materials were mainly by Russians. Dense Ti_2AlC and Ti_2AlN [Ivchenko and Kosolapova 1975; Ivchenko *et al.* 1976 a, b], Ti_3SiC_2, [Jeitschko and Nowotony 1967] and Ti_3GeC_2 [Wolfsgruber *et al.* 1967] are a few of the MAX phases successfully synthesized in 211 and 312 groups. Unfortunately these materials received less attention due to the lack of knowledge on their structural, thermal, and chemical properties. Within a few years, they disappeared into oblivion. It took more than 30 years to realize the potential of MAX phases. Approximately 30 years later, a report on the phase pure bulk synthesis of Ti_3SiC_2 was published by M.W. Barsoum and El-Raghy from Drexel University, USA. Their report on the unusual combination of ceramic and metal properties in a single material accelerated the renewed attention on MAX phases. From then onwards these compounds were named as $M_{n+1}AX_n$ (MAX) phases. In the last decade, several M_4AX_3 phases with n = 3 were added to the list and the family is still growing, with new members like are Ti_4AlN_3, Ta_4AlC_3, Nb_4AlC_3 and V_4AlC_3. Currently there are

more than 60 ternary carbides and nitrides in MAX phase family. List of MAX phases known to date are summarized in Table 1.1 [Barsoum M.W. 2013].

Table 1.1 List of MAX phases known to date. The theoretical density (g m⁻³) is given in bold. The *a* and *c* lattice parameters in angstrom are given in parentheses

Group 12	13	14	15	16
	Al	**Si**	**P**	**S**
	Ti_2AlC, **4.11** (3.04, 13.60)	Ti_3SiC_2 **4.52** (3.07, 17.67)	V_2PC **5.38** (3.08,10.91)	Ti_2SC, **4.62** (3.21,11.22)
	V_2AlC, **4.87** (2.91, 13.10)			
	Cr_2AlC, **5.24** (2.86, 12.8)		Nb_2PC **7.09** (3.28, 11.5)	Zr_2SC, **6.20** (3.40,12.13)
	Nb_2AlC, **6.50** (3.10, 13.8)			
	Ta_2AlC, **11.82** (3.07, 13.8)			
	Ti_2AlN, **4.31** (2.99, 13.61)			$Nb_2SC_{0.4}$, (3.27, 11.4)
	Ti_3AlC_2, **4.50** (3.07, 18.58)			
	Ta_3AlC_2 , **12.20** (3.09, 19.16)			Hf_2SC, (3.36,11.99)
	Ti_4AlN_3, **4.76** (2.99, 23.37)			
	α-Ta_4AlC_3, **12.92** (3.11, 24.10)			
	β-Ta_4AlC_3, **13.36** (3.09, 23.71)			
	Nb_4AlC_3, **7.06** (3.13, 24.12)			
	$V_4AlC_{2.7}$, **5.16** (2.93, 22.74)			
	Ga	**Ge**	**As**	
	Ti_2GaC, **5.53** (3.07, 13.52)	Ti_2GeC, **5.68** (3.07, 12.93)	V_2AsC **6.63** (3.11, 11.3)	
	V_2GaC, **6.39** (2.93, 12.84)			
	Cr_2GaC, **6.81** (2.88, 12.61)	V_2GeC, **6.49** (3.00, 12.25)		
	Nb_2GaC, **7.73** (3.13, 13.56)			
	Mo_2GaC, **8.97** (3.01, 13.18)			
	Ta_2GaC, **13.05** (3.10, 13.57)	Cr_2GeC,**6.88** (2.95, 12.08)	Nb_2AsC **8.025** (3.31, 11.9)	
	Ti_2GaN, **5.75** (3.00, 13.3)			
	Cr_2GaN, **6.82** (2.87, 12.70)	Ti_3GeC_2, **5.55** (3.07, 17.76)		
	V_2GaN, **5.94** (3.00, 13.3)			
	Ta_4GaC_3, **13.99** (3.07, 23.44)			

Table1.1   (Continued)….

Group 12	13	14	15	16
Cd	**In**	**Sn**		
Ti$_2$CdC **9.71** (3.1, 14.41)	Sc$_2$InC Ti$_2$InC, **6.2** (3.13, 14.06)	Ti$_2$SnC, **6.36** (3.163,13.679)		
	Zr$_2$InC, **7.1** (3.34, 14.91) Nb$_2$InC, **8.3** (3.17, 14.37)	Zr$_2$SnC, **7.16** (3.3576,14.57)		
	Hf$_2$InC, **11.57** (3.30, 14.73) Ti$_2$InN, **6.54** (3.07, 13.97) Zr$_2$InN, **7.53** (3.27, 14.83)	Nb$_2$SnC, **8.4** (3.24, 13.80) Hf$_2$SnC, **11.8** (3.32, 14.39) Hf$_2$SnN, **7.72** (3.31, 14.3) Ti$_3$SnC$_2$, **5.95** (3.14, 18.65)		
	Tl Ti$_2$TlC, **8.63** (3.15, 13.98) Zr$_2$TlC, **9.17** (3.36, 14.78) Hf$_2$TlC **13.65** (3.32, 14.62) Zr$_2$TlN, **9.60** (3.3, 14.71)	**Pb** Ti$_2$PbC, **8.55** (3.20, 13.81) Zr$_2$PbC, **9.2** 3.38, 14.66 Hf$_2$PbC, **12.13** (3.55, 14.46)		

1.2.3 MAX Phase Materials: - Crystal Structure and Atomic Bonding

The MAX phases have hexagonal layered crystal structure and belong to the space group D$^4_{6h}$-P6$_3$/mmc. Each unit cell consists of two formula units. Figure 1.2 illustrates the crystal structure of MAX phases with 'n' equals 1 to 3. The unit cell of MAX phases consist of M$_6$X octahedra that are linked together by edges which are identical to those seen in rock salt structure of MX binaries. The X- atoms reside the octahedral sites between the M-atoms. A-atoms reside at the centers of trigonal prism that are large enough to accommodate larger A-atoms. The octahedra are alternate with layers of pure A-elements. The main structural difference between 211, 312, and 413 MAX phases is the number of MX layers between the two adjacent A-layers. When n=1, there are two M-layers separate the A- layers. When n=2, A-layers are separated by three M-layers. When n=3, the separation is by four M-

layers. When the number of X-atoms increase stacking sequence become more complex such as in M_5AX_4, M_6AX_5 and M_7AX_6.
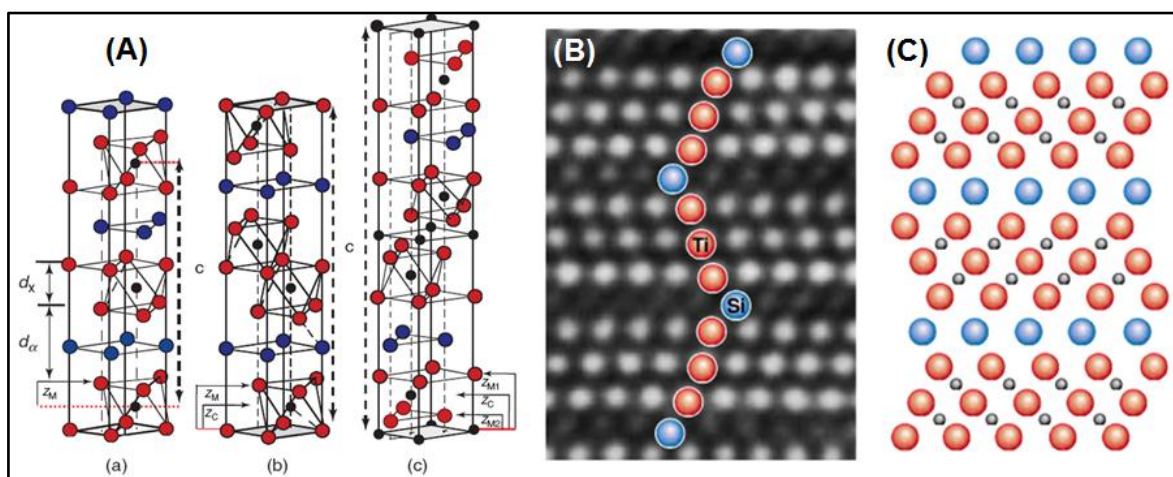
Figure 1.2: (A) Unit cells of (a) 211, (b) 312, and (c) 413 phases. Vertical dashed lines depicts the *c* parameters; d_X denotes the thickness – from atom center to atom center– of the $M_{n+1}X_n$ layers; d_α that of the A layers. (B) a high-resolution TEM showing the cross section of the structure of Ti_3SiC_2 (the small carbon atoms are not visible in the micrograph); and (C) a diagrammatic representation of the layered structure of MAX phases [Barsoum and Radovic 2011]

In MAX phase, the labeling is important and is described by the positions of the M and X atoms in the atomic stacking sequence. This is particularly difficult in higher order MAX phases like 312 and 413 phases. In these cases two locations are possible for the M and X atoms. When the M atom is bonded to A atom, in the crystal structure it is labelled as M_I and those only bonded to X atom as M_{II} [Etzkorn *e. al.* 2009]. The same protocol is followed for labeling X atoms. Those bonded to M_I as X_I, and that are only bonded to M_{II} as X_{II}.

In-depth analysis of the electronic structure and chemical bonding of MAX phase were reported using DFT calculations. It revealed that MAX phases have a combination of covalent, ionic, and metallic bonds [Radovic *et al.* 1999; Radovic *et al.* 2013]. In general;

➢ M-X layers are composed of the M and X atoms bonded through strong directional covalent bonds. The M d-X 2p interactions between the M and X atoms are relatively strong [Medvedeva *et al.* 1998].

- ➢ M–d–M–d metallic bonding dominates the electronic density of states at the Fermi level, $N(E_F)$

- ➢ In most MAX phases, the interaction between d electron of M atoms and p electrons of A atoms are very weak with states -1eV relative to E_F, i.e. the M–A bonds are relatively weaker than the M–X bonds.

- ➢ There are no A-A or X-X bonds.

Depending on the structure, MAX phases show polymorphism; the ability to exist in more than one crystal structure. Polymorphic phase transformations in MAX phase were first reported by Barsoum and coworkers [Farber *et al.* 1999; Barsoum *et al.* 1999]. The polymorphic phase transformations of 211, 312 and 413 phases are schematically depicted in Figure1.3. 211 type MAX phases have only one polymorph. However, in 312 type MAX phases, α and β phases were reported. This type of polymorphism is formed due to the shearing of A layers. As depicted in Figure 1.3 (b, c) only the shearing of the A-group layers transform α-M_3AX_2 to the β form. Here, the M-X slab remains unaffected. Since there is no breaking of M–X bonds, the polymorphic transformation is relatively a low activation energy process [He *et al.* 2011]. The effect of this transformation on crystal structure is distinguishable from their XRD patterns as shown in Figure 1.4. The second kind of polymorphism is reported for Ta_4AlC_3, and not for the other 413 phases known today. In this case, there are three polymorphs viz. α, β and γ as shown in Figure 1.3(e-f). The polymorphism in this type is not due to the difference in the A-element layers. It is primarily due to the positions of Ta and C atoms. The α and β Ta_4AlC_3 differ in the positions of the Ta(2) and C(2) atoms. Recent DFT studies confirm that at room temperature and pressure, the α-phase is more stable than the β form [Wang *et al*. 2008; Du *et al*. 2008a]. Even though other 413 MAX phases such as Nb_4AlC_3 and V_4AlC_3 were reported in due course of research, no polymorphism was observed in these materials. A convincing explanation given by Wang *et al.* is that the absence of polymorphism is due to the differences in the Gibb's free energy [ΔG] of the α and β forms calculated for Ta_4AlC_3, Nb_4AlC_3, V_4AlC_3, and Ti_4AlN_3 MAX phases [Wang *et al.* 2008]. Among them, a phase stability reversal was predicted in the case of Ta_4AlC_3 1875 K, i.e. β - form is more stable than α-form. For the others, α polymorph is the more stable up to 3000 K.
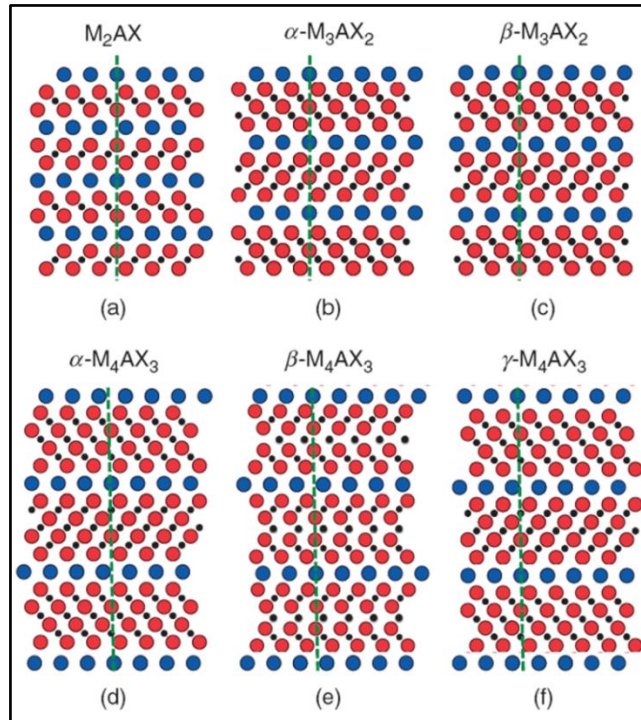
Figure 1.3: Schematics of 1120 planes in (a) M₂AX, (b) α-M₃AX₂, (c) β-M₃AX₂, (d) α-M₄AX₃, (e) β-M₄AX₃, and (f) γ-M₄AX₃. The dashed vertical lines are guides to the eyes. [Barsoum M.W. 2013]
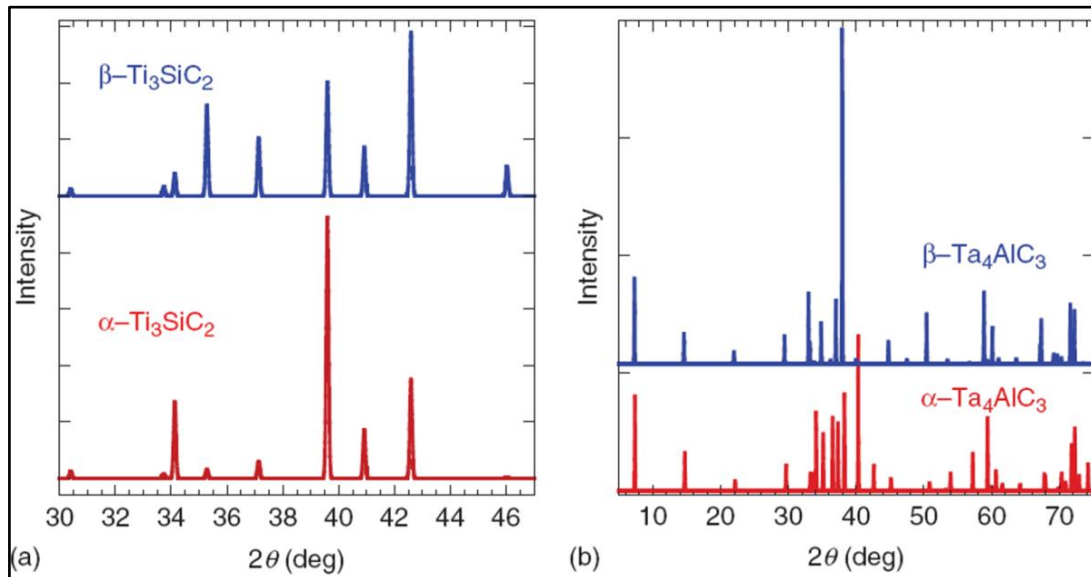
Figure 1.4: Simulated XRD patterns for Cu Kα radiation of (a) α- and β-Ti₃SiC₂ [Farber *et al.* 1999] and (b) α-Ta₄AlC₃ and β-Ta₄AlC₃ [Wang *et al.* 2004]

1.2.4 Synthesis of MAX Phases

Over the years, many methods have been employed for the synthesis of MAX phase materials. Ti_3SiC_2 is the most studied MAX phase material so far. Some of the

techniques adopted so far for the synthesis of Ti_3SiC_2 is summarised in Table 1.2 [Zhang et al. 2009].

Table 1.2: Some of the methods reported so far for the synthesis of Ti_3SiC_2

Methods	Synthesis conditions	Products	Ref.
CVD	Precursors: $TiCl_4$, $SiCl_4$, CCl_4, H_2; substrate: graphite and Ta; temperature: 1273 to 1573 K; pressure: 10^5 Pa	Single crystal Ti_3SiC_2 (containing a little $TiSi_2$)	[Nickl *et al.* 1972]
Reactive Sintering	Precursors: Ti/Si/C (0.42/0.29/0.29); 1100 °C for 10h	Ti_3SiC_2 powder (95 wt% purity)	[Racault *et al.* 1994]
HIP-SHS	Precursors: Ti, Si and C; Ti_3SiC_2 SHS followed by hot isostatic pressing at 1400°C	Bulk Ti_3SiC_2 (82 vol% purity) +TiC	[Lis *et al.* 1997]
Arc-melting and post annealing	Precursors: Ti/Si/C Arc melting followed by post annealing treatment at 1200 °C for 100 h	Bulk Ti_3SiC_2 +2 vol% TiC	[Arunajatesan *et al.* 1995]
In-situ hot pressing/ solid-liquid fluid reaction synthesis	Precursors: Ti/Si/C (0.42/0.23/0.35) temperature:1450 to 1600 °C for 1 h pressure : 38 MPa	Bulk Ti_3SiC_2 (purity 93 wt%)	[Zhou *et al.* 1998]
HIP	Precursors: Ti/C/SiC powders temperature:1600 °C for 4 h pressure : 40 MPa	Bulk Ti_3SiC_2 + (2 vol% TiC and SiC)	[Barsoum and El-Raghy 1996]
Hot pressing	Precursors: Ti/Si/C (3/1.2/2) temperature:1500-1700 °C / 2 h pressure :25 MPa	Bulk Ti_3SiC_2 (purity 99 wt%)	[Yongming *et al.* 2002]
SPS/ PDS	Precursors: 4Ti/2SiC/TiC temperature:1250 to 1450 °C pressure :50 MPa	Bulk Ti_3SiC_2 (purity 92 vol%)	[Zhang *et al.* 2001]
Pressure less sintering	Precursors: 3Ti/Si/2C ,cold pressed at 200 MPa; sintering at 1100 to 1500 °C for 1 h in Argon	Bulk Ti_3SiC_2 (purity of 80 wt%)	[Li *et al.* 2003]
Magnetron sputtering	Precursors: Ti, Si and C substrates : MgO and Al_2O_3 pressure :10^{-9} Torr,	Ti_3SiC_2+(Ti_4SiC_3, Ti_5SiC_3 and $Ti_7Si_2C_6$)	[Palmquist *et al.* 2004]
Mechanical alloying	Precursors: Ti, Si, and C.	Ti_3SiC_2 powder (30 % TiC)	[Li *et al.* 2005a]

In general, controlling the impurity phases during synthesis is the main hurdle in most of the MAX phases. Processing of single-phase Ti_3SiC_2 is truly difficult. The initial reaction mixtures used for the synthesis of Ti_3SiC_2 includes

Ti/SiC/C [Barsoum *et al.* 1996; Goesmann *et al.* 1998], Ti/Si/C [Racault *et al.* 1994; Zhang *et al.* 2002a], Ti/Si/C/SiC [Klemm *et al.* 1993], Ti/Si/TiC [Radhakrishnan *et al.* 1996; Zhang *et al.* 2002b] and Ti/SiC/TiC [Zhang *et al.* 2001]. The major impurity phases associated with Ti_3SiC_2 synthesis are TiC, SiC, $TiSi_2$, and Ti_5Si_3. Out of these, TiC is the main impurity and the complete removal of this phase is succeeded only to a certain extent even though varieties of preparation methods and precursors have been tried. Even in the best methods suggested for the synthesis of high purity Ti_3SiC_2 MAX phase, there exist a detectable amount TiC impurity [Barsoum and El-Raghy 1996; Arunajatesan *et al.* 1995; Radhakrishnan *et al.* 1996; Zhang *et al.* 2002b]. The structural relationship between TiC and Ti_3SiC_2 was believed to be the reason for the same. The in-depth investigation of crystallographic relations between Ti_3SiC_2 and TiC by Zhou *et al*. demonstrated that the crystal structure of Ti_3SiC_2 is formed by intercalation of a layer of Si atoms into the {111} twin boundary of TiC [Zhou *et al.* 2000]. The de-intercalation of Si from Ti_3SiC_2 resulted in the decomposition of Ti_3SiC_2 into TiC. This structure relationship illustrates why TiC is always present as a main impurity phase in Ti_3SiC_2 synthesis.

The synthesis techniques employed till date for MAX phase materials include chemical vapor deposition (CVD), pulsed laser deposition (PLD), magnetron sputtering (MS), hot isostatic pressing (HIP), hot pressing (HP), self-propagating high-temperature synthesis (SHS) or self-propagating high temperature synthesis-hot isostatic pressing (SHS-HIP), spark plasma sintering (SPS) and pulse discharge sintering (PDS), arc-melting and post annealing, reactive sintering, solid-liquid reaction synthesis and simultaneous densification, pressureless sintering, mechanical alloying (MA), *etc*. [Zhang *et al.* 2009].

In early stages of development, the material was synthesized from the gaseous reactants at temperatures as high as 2273 K, or by CVD technique. The very first study on CVD synthesis of Ti_3SiC_2 was carried out by Nickl *et al.* in 1972. They used the $TiCl_4$-$SiCl_4$-CCl_4-H_2 system at the temperature of 1473 K and pressure of 10^5 Pa, and studied the effective deposition of ternary diagram [Nickl *et al.* 1972]. They observed that the reaction conditions favorable to obtain the deposition of pure Ti_3SiC_2 were very narrow, and final product very often produced mixture of Ti_3SiC_2 with TiC, Ti_5Si_3, $TiSi_2$, SiC, or two of these binary compounds. Later, Goto and

Hirai also confirmed the existence of these mixed phases [Goto and Hirai 1987]. A new route for the deposition of Ti_3SiC_2 coating on carbon substrates was also attempted by combining both low pressure-pulsed chemical vapor deposition (CVD) and reactive CVD [Jacques *et al.* 2005]. Here, in this reaction, mixture of $SiCl_4$, $TiCl_4$ and H_2 reactants deposited on pyrocarbon film convert the C into SiC and TiC_x followed by transformation into Ti_3SiC_2. The CVD techniques mostly produced MAX phase ternary carbide films.

Lin and co-workers extensively attempted on the bulk synthesis of Ti_3SiC_2 [Pampuch *et al.* 1989; Lis *et al.* 1993; Morgiel *et al.* 1996]. They followed the combustion synthesis, both alone and coupled with hot isostatic pressing (HIP). But in their attempts only 80–90 vol% Ti_3SiC_2 could be realized. Arc melting and post annealing were also done for obtaining MAX phase materials [Arunajatesan *et al.* 1995].

Recault *et al.* put forward the reactive sintering technique for Ti_3SiC_2 synthesis. The pellet made out of the reactant mixture in desired stoichiometry was placed in an evacuated silica tube and heated at 1100 °C for 10 h. The resultant product containing Ti_3SiC_2, $TiSi_2$ and TiC was treated further with aqueous HF to remove $TiSi_2$ phase. The resulted two phase mixture after neutralizing with ammonia, and subsequent washing and drying produced 85 % pure Ti_3SiC_2. In the third stage, the 15 % TiC impurity was removed by controlled oxidation at 450 °C/ 10 h in air. TiC has comparatively higher oxidation kinetics than Ti_3SiC_2. It was converted to TiO_2 and then removed from the product by dissolving in $(NH_4)SO_4$ and aqueous H_2SO_4 at about 100 °C. Further neutralization with NH_3 followed by washing and drying finally resulted in high-purity Ti_3SiC_2 powders [Recault *et al.* 1994].

Nearly single phase Ti_3SiC_2 was synthesized by Barsoum *et al.* using HP or HIP [Barsoum and El-Raghy 1997; Barsoum *et al.* 1996]. These synthetic techniques received wide attention and were quickly applied to make other MAX phase systems like Ti_3GeC_2, Ti_2AlC, Ti_2AlN, Ti_2GeC, V_2AlC, Ta_2AlC and Nb_2AlC [Barsoum *et al.* 1997b]. A method reported by Zhou et al, namely *in situ* HP solid–liquid synthesis, could yield Ti_3SiC_2 product with 92 wt% phase purity [Zhou *et al.* 1998]. Yongming *et al.* employed HP technique and succeeded to obtain bulk Ti_3SiC_2. Here they could

obtain the materials with > 99 % phase purity. In this method, the initial mixtures of Ti, Si and active carbon powders were cold pressed first at a pressure of 100 MPa to obtain the green compacts which were subsequently hot pressed at a pressure of 25 MPa, and temperature of 1500 to 1700 ℃ in inert gas atmosphere and finally produced 99 % pure Ti_3SiC_2 [Yongming *et al.* 2002].

Self-propagating high-temperature synthesis (SHS) that works based on the exothermic heat of formation to stimulate a self-sustaining reaction was also utilized for the synthesis of MAX phases [Lis *et al.* 1997; Riley *et al.* 2002]. In SHS technique, the reactants consisting of 3Ti / Si / 2C were ignited for SHS reaction to take place that would generate heating rates of 500 ℃/min, finally resulting in MAX phase material. Unfortunately, here also the product purity seemed to vary from 10 to 90 wt%. The causation for this was attributed to evaporative loss of reactants due to high combustion temperature associated with rapid heating rate. Riley *et al.* showed that the high temperature mechanical alloying could possibly depress the SHS reaction temperature, and improve the purity of Ti_3SiC_2 [Riley *et al.* 2002].

Synthesis of phase pure MAX phase was also attempted via pulse discharge sintering (PDS) or as spark plasma sintering (SPS) [Sun *et al.* 2002; Zhang *et al.* 2002; 2004;]. The PDS technique was initially tried to obtain single phase Ti_3SiC_2 in bulk. Later, the technique was extended to Ti_3AlC_2 [Zhuo *et al.* 2003], and Cr_2AlC [Tian *et al.* 2008a] MAX phases. Gao *et al.* demonstrated formation of Ti_3SiC_2 phase with 2 wt% TiC impurity from mixtures of Ti/Si/2TiC by SPS technique in the temperature range of 1250 to 1300 ℃.

The reactive sintering processes such as HP, HIP or PDS discussed above are not commercially viable and cannot easily be applied to the bulk production of MAX phases. In this context, pressureless sintering, an easy and scalable process, was recommended. A highly dense Ti_3SiC_2 compact was fabricated from the mechanically alloyed Ti, Si and C powder mixture through pressureless sintering at around 1500 ℃ [Li *et al.* 2003]. Sun *et al.* also reported the successful synthesis of dense and phase pure Ti_3SiC_2 through reactive pressureless sintering [Sun *et al.* 2004]. It was also reported that the addition of Al into the reaction mixture enhanced the phase formation and densification of Ti_3SiC_2 [Sun *et al.* 2006; 2007; Zou *et al.* 2008].

Another method reported for the synthesis of Ti_3SiC_2 was the *in situ* pyrolysis of polycarbosilane and titanium [Yongming *et al.* 2008].

Many researchers employed Magnetron sputtering method for the synthesis of epitaxial films of Ti-Si-C, Ti-Al-C, Ti-Ge-C, and Ti-Al-N systems [Emmerlich *et al.* 2004; Palmquist *et al.* 2004].They successfully prepared films of Ti_3SiC_2, Ti_3GeC_2, Ti_3AlC_3, Ti_2GeC, Ti_2AlC, Ti_2AlN, Ti_4SiC_3, and Ti_4GeC_3 at 900 to 1000 ℃ on substrates such as Al_2O_3 (0001) and MgO (111) planes. In addition to these, several other techniques such as pulsed cathodic arc [Rosen *et al.* 2007], mechanical alloying [Li *et al.* 2005], high velocity oxy fuel spraying [Frodelius *et al.* 2008] and plasma sprayed coatings [Pasumarthi *et al.* 2009] etc., were also reported for the synthesis of MAX phases.

1.2.5 Reaction Mechanism to Form MAX Phases

Different reaction mechanisms/pathways are suggested for the synthesis of Ti_3SiC_2 MAX phase depending upon the synthetic method and the type of reactants used. El-Raghy *and* Barsoum claims that the Ti_3SiC_2 is formed through the reactive intermediate phases $Ti_5Si_3C_x$ and TiC_x when the Ti/SiC/C reactant mixture is employed [El-Raghy and Barsoum 1999]. Later, Wu *et al.* confirmed this prediction using the *in-situ* neutron powder diffraction. The study confirms that the following reaction pathways are possible in the formation of Ti3SiC2 MAX phase;

$$3Ti + SiC + C \rightarrow \tfrac{4}{3}\, TiC_x + \tfrac{1}{3}\, Ti_5Si_3C_y + \tfrac{6-4x-y}{3}\, C \qquad (1.1)$$

$$\tfrac{4}{3}\, TiC_x + \tfrac{1}{3}\, Ti_5Si_3C_y + \tfrac{6-4x-y}{3}\, C \rightarrow Ti_3SiC_2 \qquad (1.2)$$
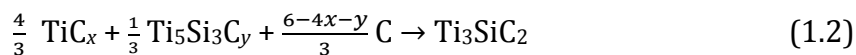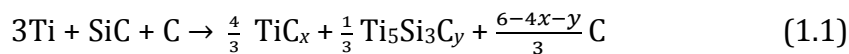
Riley *et al.* monitored the formation mechanism of Ti_3SiC_2 from Ti/SiC/C powders during self-propagating high temperature synthesis (SHS) using *in-situ* neutron powder diffraction studies [Riley *et al.* 2002]. Their observations are consistent with the earlier reports and it is suggested that the intermediate phase to be a solid solution of Si in TiC with an overall stoichiometry of 3Ti:1Si:2C.

With a change in the initial reactants, the reaction proceeds through different intermediates. The synthesis reported by Yang *et al* specified that Ti_5Si_3 was the only intermediate phase formed when Ti/Si/TiC powders was used as reactants [Yang *et al.* 2004]. They found the reaction steps as;

$$5Ti + 3Si \rightarrow Ti_5Si_3 \qquad\qquad (1.3)$$

$$Ti_5Si_3 + 10TiC + 2Si \rightarrow 5Ti_3SiC_2 \qquad\qquad (1.4)$$
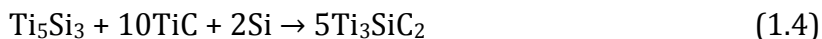
When Ti_3SiC_2 was obtained from the elemental Ti/Si/C powders, the formation sequence was again different. Sato *et al* investigated the formation of Ti_3SiC_2 from Ti/Si/C powders, and proposed that initially the Ti and C reacted together to form TiC; later the eutectic liquid of Ti-Si formed near the eutectic temperature (1603 K) and finally the Ti_3SiC_2 crystals grew up between this eutectic liquid phase and the TiC particles [Sato *et al.* 2000].

1.2.6 Properties of MAX Phases

1.2.6.1 Phase Stability

The stability of MAX phases depends upon their constituent elements, atmosphere and vapor pressure of elements. The oxidation resistance of MAX phase with temperature was studied for both bulk and powder forms [Barsoum *et al.* 1997 c; Yang *et al.* 2003; Lee *et al.* 2007]. It was found that the oxidation rate of MAX phase bulk material was lower than that of MX counterpart. The initial studies predicted that the Ti_3SiC_2 phase was unstable in the temperature range 1273 to 1673 K [Oo *et al.* 2006; Eklund *et al.* 2006; Emmerlich *et al.* 2007]. But later El-Raghy and Barsoum proved the Ti_3SiC_2 phase is thermodynamically stable at least up to 1873 K in vacuum for 24 h [El-Raghy and Barsoum 1999]. Unfortunately, the Ti_3SiC_2 exhibits an unexpected and serious degradation in nitrogen atmosphere and this phenomenon was termed as 'Ti_3SiC_2 pest'. The volume change associated with the formation of mixtures of TiC_x, $Ti(C,N)_x$ and TiN was the causation for this phenomenon. This 'Ti_3SiC_2 pest' can be prevented by increasing the partial pressure oxygen in the nitrogen atmosphere.

Wang and Zhou reported the stability of Ti_3AlC_2. Here also the authors claim that the material is stable up to 1744 K in Ar with low oxygen content [Wang and Zhou 2003]. The surface reactivity possibly oxidizes the Al atom which in turn resulted in the transformation of Ti_3AlC_2 into substoichiometric TiC_x and Al_2O_3. The passive oxide layer formed on the surface retards further decomposition. Not surprisingly, Ti_3AlC_2 possess much better oxidation resistance than Ti_3SiC_2 due to

the formation of an adherent, inert, continuous inner Al_2O_3 layer below the outer TiO_2 layer.

The oxidation of Cr_2AlC MAX phase is somewhat different. Here, the formation of carbide layers (Cr_7C_3 and Cr_3C_2) on the outermost oxide layer prevents the oxidation [Tian *et al.* 2008b]. The oxidation resistance of Cr_2AlC is comparable or even better than Ti_3AlC_3 and better than Ti_3SiC_2. Some bulk 211 phases are reported to have good stability over a wide range of temperatures. Ti_2AlN, Ti_2SC, and Ta_2AlC etc. were found to exhibit stability up to 1723, 1873, and 1873 K, respectively [Amini et al. 2007; Hu et al. 2008]. Compared to bulk counterpart, thin films of MAX phases show decreased stability owing to their difference in diffusion length [Beckers *et al.* 2006].

1.2.6.2 Physical Properties

MAX phases are excellent electrical conductors, with reported room temperature resistivity in the range 0.2–0.7 μΩ m [Barsoum M.W. 2006; 2013]. They have shown decreased conductivity with increasing temperatures, like many metallic conductors. It is worthwhile to notice that most of the MAX phases have higher electrical conductivity than Ti metal. Many of the MAX phases are reported as compensated conductors. Materials in which equal number of electrons and holes present, and contribute approximately equally to the electrical conductivity are termed as compensated conductors. In Ti_3AlC_2 and Ti_4AlN_3, the electrical conductivity is mainly due to the presence of holes [Barsoum M. W. 2006]. In materials like Ti_2SC the conductivity is governed by electrons [Scabarozi *et al.* 2008].

The higher electrical conduction of MAX phases compared to their binary counterparts can be explained by taking Ti-A-C system as example. The binary transition-metal carbides, TiC are ceramics with predominant covalent bonding. Since the conduction of electrons concentration is too low in TiC, their resistivity is relatively high (~200 μΩ cm). If 'A' layers are inserted between the Ti-C layers to form the MAX phase structure, the electrical conductivity is increased by an order of magnitude. The presence of 'A' atoms, weakens the $Ti_{(1)}$-C bonds and thereby enhances the relative strength of the metallic $Ti_{(1)}$-$Ti_{(1)}$ bonds within the basal planes. This provides the material with a stronger metallic character, with higher

conductivity. It is anticipated that the insertion of more A layers into the MAX structure obviously improve the electrical conductivity. Therefore, a system with low M to A molar ratio is expected to show high electrical conductivity. 211 Ti_2GeC possess better conductivity than 312 Ti_3SiC_2 and Ti_3GeC_2, which in turn are better conductors than 413 Ti_4SiC_3. But there are some anomalies to this predictions and reasoning. Ti_3AlC_2 and Ti_2AlC have nearly equal conductivities [Eklund *et al*. 2010].

MAX phases exhibit thermal properties much in common with their MX counterparts. They are good conductors of heat. At room temperatures thermal conductivity of MAX phases fall in the range 12–60 W m^{-1} K^{-1} [Barsoum M.W. 2006; 2013]. MAX phases exhibit relatively low thermal expansion. The coefficients of thermal expansion (CTE) of most of the MAX phases fall in the range of 5–10 μK^{-1}. There are some exceptions; like Cr - containing phases have CTEs in the range 12–14 x 10^{-6} $°C^{-1}$ [Radovic and Barsoum 2013]. Barsoum *et al.* studied the thermal properties of Ti_3SiC_2 using the normal dilatometry technique as well as the Rietveld refinement of high temperature neutron diffraction data, in the temperature range 25–1000 °C. Both techniques were found to have good agreement in the CTEs. The bulk CTE measured by dilatometry was 9.1 (± 0.2) x 10^{-6} $°C^{-1}$, and the CTE inferred from the neutron diffraction results showed the value as 8.9 (±0. 1) x 10^{-6} $°C^{-1}$. The thermal conductivity measured at room temperature was 37 W m^{-1} K^{-1} which was decreased linearly to 32 W m^{-1} K^{-1}, at 1200 °C [Barsoum *et al.* 1999a].

MAX phases display quite high stiffness and have high elastic constants. Young's modulus E, for MAX phases measured till date falls in the range 178 to 340 GPa range [El-Raghy *et al.* 2000a; Finkel *et al.* 2004] and bulk modulus, B was in the range of 138 to 261 GPa [Hettinger *et al.* 2005; Manoun *et al.* 2006]. Some MAX phases possess high specific stiffness values due to relatively low densities (4–5 g cm^{-3}). The specific stiffness value of Ti_3SiC_2 is roughly three times that of titanium metal and is also comparable to Si_3N_4. The highest stiffness value experimentally reported to date for 211 phases is for Ti_2SC (E= 316 GPa) and the value is nearly equal to that of 413 phase [Amini *et al.* 2007]. The causation for this high stiffness is attributed to the smallest c/a ratio and the exceptionally strong M–A bonds in Ti_2SC [Du *et al.* 2008b]. The same was accounted for its high thermal conductivity also. The typical properties of Ti_3SiC_2 are showcased in table 1.3 [Zhang *et al.* 2009].

Table 1.3: Typical Properties of Ti$_3$SiC$_2$

Properties	Values	Temperatures	Ref.
Density (g cm^{-3})	4.5	25 ^{o}C	[Barsoum *et al.* 1996]
Young's modulus (GPa)	322-333	25 ^{o}C	[Barsoum *et al.* 1996]
Shear modulus (GPa)	185-206	25 ^{o}C	[Finkel *et al.* 2000]
Bulk modulus (GPa)	185-206	25 ^{o}C	[Finkel *et al.* 2000]
Poisson's ratio	0.2	25 ^{o}C	[Finkel *et al.* 2000]
Vickers hardness (GPa)	4.0	25 ^{o}C	[Finkel *et al.* 2000]
Three-point bending strength (MPa)	450	25 ^{o}C	[Zhou *et al.* 1998]
Fracture toughness (MPa m$^{1/2}$)	7.0	25 ^{o}C	[Zhou *et al.* 1998]
Compressive strength (MPa)	900	25 ^{o}C	[Zhou *et al.* 2001]
	600	1000 ^{o}C	[El-Rahgy *et al.* 1999]
	500	1150 ^{o}C	[Zhou *et al.* 2001]
	300	1300 ^{o}C	[El-Rahgy *et al.* 1999]
Tensile strength (MPa)	200	25 ^{o}C	[Zhou *et al.* 2001]
	123	1100 ^{o}C	[Radovic *et al.* 2000]
	60	1200 ^{o}C	Radovic *et al.* 2000
	12	1300 ^{o}C	[Radovic *et al.* 2000]
Shear strength (MPa)	226	25 ^{o}C	[Bao *et al.* 2004]
	40	25 ^{o}C	[Bao *et al.* 2003]
Brittle-to-ductile transition temperature (^{o}C)	1050		[Zhou *et al.* 2001]
Electrical conductivity (S m^{-1})	9.6 x 10^6	25 ^{o}C	[Zhou *et al.* 2001]
Heat capacity (J mol^{-1} K^{-1})	110	25 ^{o}C	[Barsoum *et al.* 1999a]
Debye temperature (K)	670		[Barsoum *et al.* 1999a]
Thermal conductivity (W m^{-1} K^{-1})	37	25 ^{o}C	[Barsoum *et al.* 1999a]
Thermal expansion coefficient (K^{-1})	9.2 x 10^{-6}	25 ^{o}C	[Zhou *et al.* 2001]

1.2.6.3 Mechanical Properties

Even though physical properties of the MX and MAX phases are very close, they show intriguing difference in their mechanical properties. Most of the MX phases belong to the hardest solids family. They are brittle, damage intolerant, nonmachinable, and possess very weak thermal shock resistance. In exact contradistinction, the MAX phases are exceptionally damage tolerant and thermal shock resistant. They also show remarkable machinability. The presence of mobile dislocations in MAX phases is the primary driving force that enables them to exhibit different mechanical properties when compared to binary counterparts.

It is fairly proven that basal plane dislocations (BPD) are abundant in the MAX phases. These BPDs are mobile, and able to multiply at ambient temperatures. These dislocations are constrained to the basal planes [Farber *et al.* 1999]. Therefore, the number of slip systems in MAX phases is fewer than the five required for polycrystalline ductility. This enable the MAX phases to occupy an exciting middle class between metals and ceramics with remarkable mechanical properties. They show pseudoductility at high temperatures, or under confined deformations; but at the same time they are brittle at room temperature, particularly in tension and thin form.

Research reports clearly indicate that the MAX phases deform through the formation of kink bands within individual grains. The different steps involved in this deformation process are depicted schematically in Figure 1.5. The BPDs themselves are arranged either in walls (shown in Figure 1.5 a), in arrays or dislocation pileups parallel to the basal planes. MAX phases under the action of mechanical stress show kink band (KB) formation, an important micromechanism that is quite ubiquitous in the MAX phases regardless of lengths scales. The kink band (KB) formation seen in MAX phase is a direct result of dislocations confinement to the basal planes (Figure 1.5). There are two types of grains, 'soft grains' (blue grains in Figure 1.7c) and 'hard grains' (red grains in Figure 1.5c) present in the bulk MAX phases [Barsoum *et al.* 2003b; Barsoum and M. Radovic 2004]. When a load is applied, the soft grains –the grains with basal planes favorably oriented for easy slip started to deform which in turn force the hard grains to develop incipient kink bands (IKB). IKBs are coaxial dislocation loops, and are spontaneously and fully reversible as long as their ends

are not split apart. That is, IKBs would annihilate as the load was removed since this was a reversible process [Barsoum *et al.* 2005]. However, with further increase in applied load, IKBs lead to the formation of mobile dislocation walls (MDW) and ultimately resulted in permanent kink band (KB). Since the grain boundaries are soft at high temperature, the IKBs easily transformed into MDWs and KBs, and delamination occurs. Formation of MDWs and delamination is an irreversible process. It was reported by Barsoum *et al* that at room temperature, the polycrystalline Ti$_3$SiC$_2$ could be compressed to stress of 1 GPa and original shape can be fully recovered after the withdrawal of the load [Barsoum *et al.* 2003b]. The stress-strain curves show non-linear, strain rate independent, fully reversible closed loops. This kind of mechanical deformation behavior has not been reported for any other crystalline ceramics.
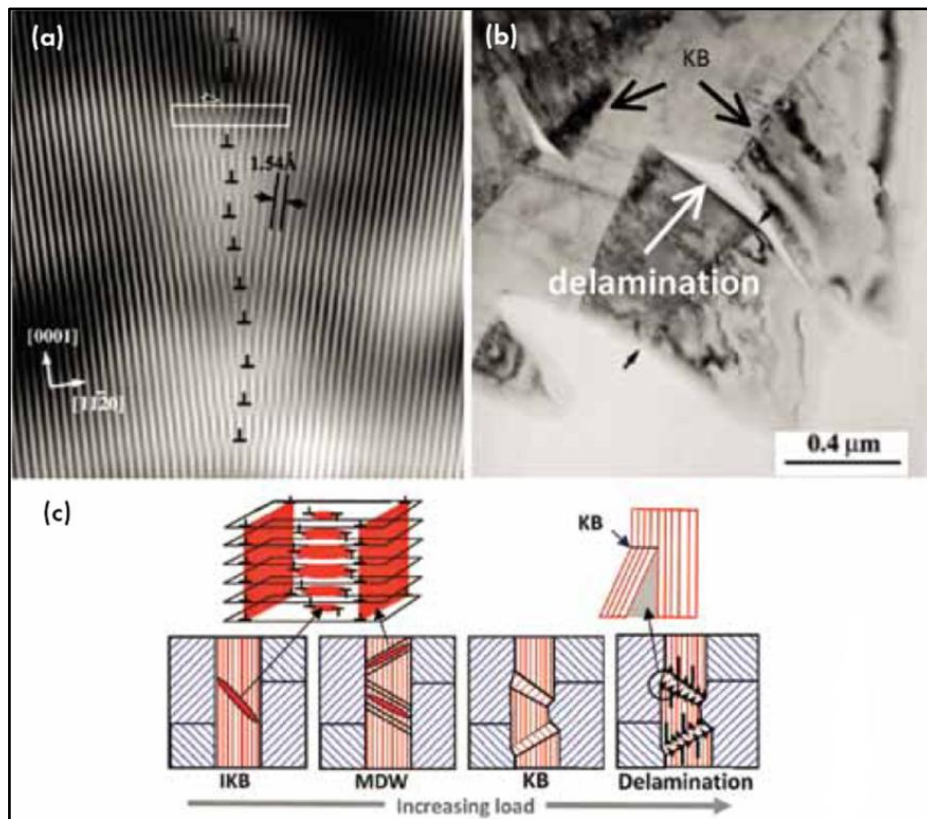
Figure 1.5: TEM images showing the (a) dislocation wall consisting of basal plane dislocations, and (b) area containing kink band in Ti$_3$SiC$_2$ after compression ;(c) Schematic of the formation of incipient kink band, mobile dislocation walls kink bands, and delaminations. Red grains are "hard" grains, and blue grains are "soft" grains [Barsoum and El-Raghy 1999; Barsoum *et al.* 2003b]

1.2.6.3.1 Compressive, Tensile and Shear Strength

The compressive strengths of polycrystalline MAX phases strongly depend on composition and grain size, and at room temperature, it is ranging from 300 MPa to 2 GPa. At room temperature, their flexural and tensile strengths are lower than their compressive strength, like many other conventional ceramics [Barsoum M.W. 2013; Radovic and Barsoum 2013; Sun Z.M. 2011]. Since Ti_3SiC_2 is the well-known and well-studied member of MAX phase family, obviously most of the data available on the mechanical properties belong to Ti_3SiC_2 MAX phase. For dense Ti_3SiC_2 with 5 μm grains have compressive and tensile strengths 1,050 MPa and 300 MPa, respectively. They fail in a brittle manner at room temperature- fail along planes inclined 30°–40° with respect to the compression axis, and they do not shatter, i.e. fail gracefully. The compressive behavior of Ti_3SiC_2 at room temperature was studied by Zhou *et al.* and they confirmed the graceful deformation under compressive loading. Figure 1.6 (a) shows a scanning electron micrograph adopted from their report which clearly describes the shear- fracture behavior Ti_3SiC_2 wherein a crack is oriented ~45° to the direction of compression loading [Zhou *et al.* 1998]. It is clear that although the sample cracks, it is still not completely broken into small pieces. The presence of voids and cavities bridged by laminated Ti_3SiC_2 grains can also be identified in the high magnification image.
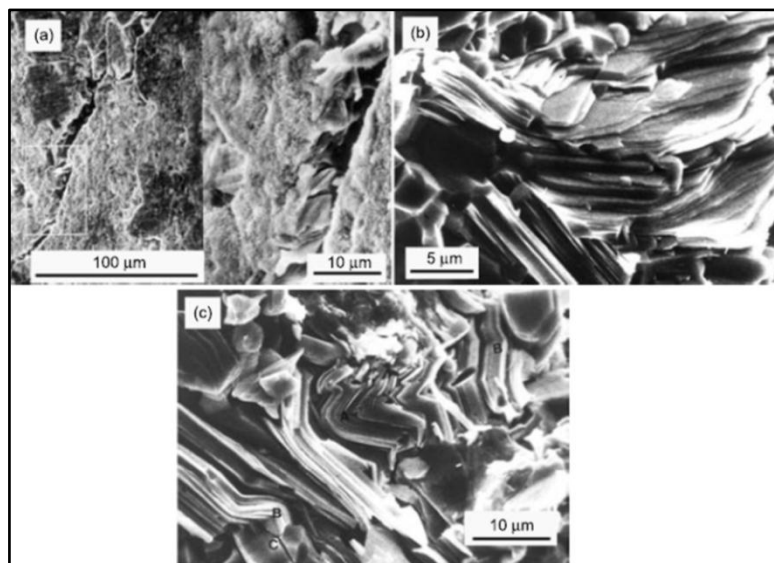
Figure 1.6: Typical fracture surfaces of Ti_3SiC_2 after compressive loading at room temperature [Zhou *et al.* 1998]

The representative microstructure of the Ti_3SiC_2 fractured surface depicted in Figure 1.6 (b) shows the laminar deformation of Ti_3SiC_2. Third image in Figure 1.6 shows the kinking and delamination of individual grains that leads to the deformation of polycrystalline Ti_3SiC_2 under compression [Zhou *et al.* 1998]. Under compressive load below 900 ℃, polycrystalline Ti_3SiC_2 display a quasi-brittle behaviour but it shows some plastic deformation between 800 to 1000 ℃ and this brittle to ductile transformation is more probable beyond 1050 ℃ [Sun *et al.* 2000].

Ti_3SiC_2 exhibits temperature and strain rates dependent tensile properties. Under tensile stress, no necking occurs and main cause for failure is the damage accumulation in the form of cavitations, microcracks, pores, etc. [El-Raghy *et al.* 1999b; Radovic *et al.* 2003]. At low temperatures and high stain rates, it fails in brittle manner. On the other hand, failure is much more sensitive to strain rate at higher temperature and low strain rates. Radovic *et al.* performed a series of experiments by varying the conditions and obtained the coefficients of strain rate sensitivity of ~ 0.5 for both fine and coarse grained Ti_3SiC_2 [Radovic *et al.* 2002].

In real time applications, a material may undergo complex stresses and in such situations, the material failure is determined by weakest strength. Therefore, due attention must be paid to determine the weakest strength of a material which is very important for ensuring the safety and reliability. In MAX phases, shear induced facture is a route to failure. Since Ti_3SiC_2 has relatively high fracture toughness/bending strength (K_{IC}/σ_b, ~0.018) ratio, and low Vickers hardness/elastic modulus (HV/E, ~0.013) ratio; they possess high impact resistance and energy absorbing capacity. These results proposed a fracture behavior reminiscent to cast iron or graphite in which shear induced fracture accounted for the main failure mechanism. The ratio of shear strength to bending strength is less than 1 for Ti_3SiC_2 and is above 1 for brittle ceramics. The delamination of layered grains, and easy inter-grain slipping are responsible for low shear strength of Ti_3SiC_2. Many researchers adopted various methods to determine the shear strength of Ti_3SiC_2. Barsoum and El-Raghy determined shear strength of Ti_3SiC_2 indirectly from the compressive strength and reported a value of 36 MPa [Barsoum and El-Raghy 1999]. However, they point out that this value may not represent the true value due to the influence of compressive stress normal to the shear plane.

1.2.6.3.2 Hardness, Damage Tolerance, Machinability and Thermal Shock Resistance

Unlike binary counterparts, MAX phases are relatively soft and have very low hardness. The Vickers hardness of MAX phases fall in the range of 2–8 GPa [Barsoum M.W. 2013; Barsoum and Radovic 2004]. This suggests that they are softer than conventional ceramics but harder than metals. Ti_3SiC_2 show low hardness of 4GPa and the low hardness is preserved even at temperatures as low as 77 K [Kuroda *et al.* 2001]. In the case of brittle solids, the Vickers indentation mark creates a sharp crack that originate from the corners of the indents, and extend toward outside. However, such crack formation and propagation is difficult in Ti_3SiC_2 confirming its extraordinary damage tolerance [Finkel *et al.* 2000; Pampuch *et al.* 1989]. Instead of forming cracks and propagation of cracks, in Ti_3SiC_2 delamination of layers, grain push outs and pullouts, or kinking of individual grains were seen near the indented zone as shown in Figure 1.7 [Low *et al.* 1998; Low I M. 1998]. The capability of Ti_3SiC_2 to contain and confine the extent of damage in a small area around the indentations reflects its excellent damage tolerance. It is worthwhile to note that the flexural strength of Ti_3SiC_2 was not decreased abruptly when measured after giving an indentation on the surfaces. This also supports its damage tolerance capacity. Weibull modulus is a key parameter for understanding the reliability of strength and damage tolerance. Since conventional ceramics are brittle and are very sensitive to defects, they show low Weibull modulus, and are in the range from 5 to 20. Bao *et al.,* using the three-point bending tests showed that Weibull modulus of Ti_3SiC_2 was 29.1, the highest value for any monolithic ceramics [Bao *et al.* 2007].
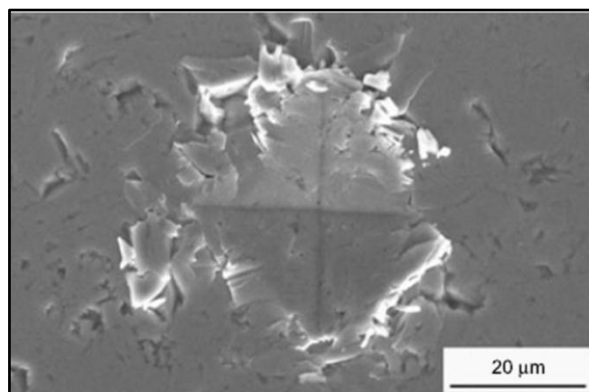
Figure 1.7: SEM morphology of the indentation of a Ti_3SiC_2 sample tested at 10 N [Zhang *et al.* 2009]

MAX phases also show superior fracture toughness (K_{Ic}) when compared with other ceramics. KIC values of MAX phases strongly depend on microstructures. Benefited from the deflection and delamination of cracks by single grains, coarse grained microstructures exhibit higher K_{Ic} values. For Ti_3SiC_2, it ranges from 4.5 to 16 MPa m$^{1/2}$ [Zhou *et al.* 1998; Li *et al.* 2001] and for Ti_3AlC_2 the value varies from 4.6 to 9.1 MPa m$^{1/2}$[Wang *et al.* 2002; Zhou *et al.* 2003]. MAX phases are also known for its *R*-curve behavior, i.e., increase of K_{Ic} with increase in crack length. For e.g., with an increase in crack size, the coarse grained Ti_3SiC_2 showed an increase in K_{Ic} from 8.5 to 11 MPa m$^{1/2}$ [Gilbert *et al.* 1999]. These exciting properties result from the formation of plastic bridging ligaments and presence of kink bands. The profusion of such crack bridging ligaments in the crack wake is shown in Figure 1.8 (a). The very high fracture toughness, damage tolerance and the microplasticity make MAX phases very reminiscent to metals. The evidence of one such property is shown Figure 1. 8b, where the surfaces of an 8 inch Ti_2AlC block (the commercially available in the trade name Maxthal plate) was hit repeatedly with a heavy steel hammer. It did not shatter nor showed any sign of cracks; only surface dents were formed just like metals.
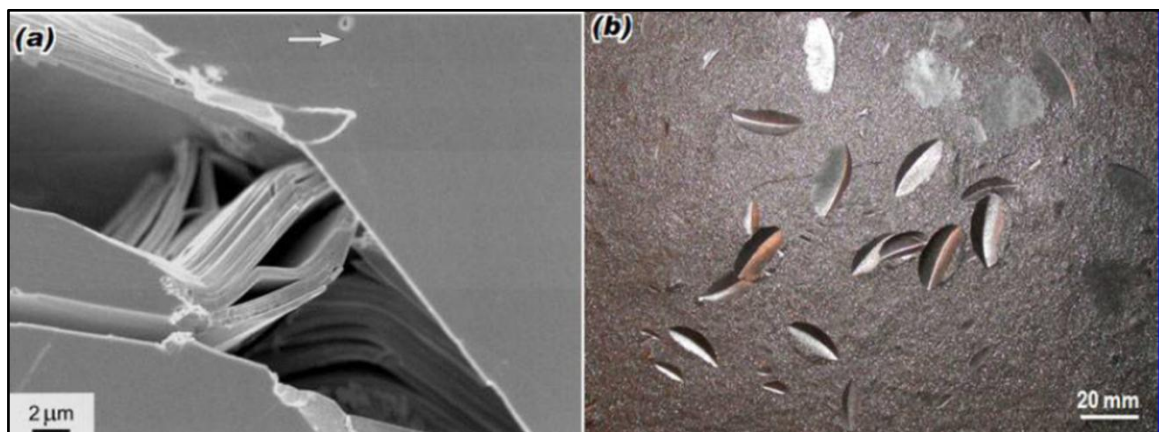
Figure 1.8: a) lamellae bridge observed in crack wake of coarse grained Ti_3SiC_2 in R curve measurement [Gilbert *et al.* 1999] and b) an 8 inch Ti_2AlC block indented by steel hammer (courtesy of 3-ONE-2, LLC)

In addition to these exciting mechanical properties, the MAX phase exhibited excellent machinability which is considered as its signature property. The low hardness and damage tolerance together with their nanolayered nature enable MAX phases to show high level machinability. The MAX phases can be easily machined

with regular high-speed cutting tools or even manually with a hacksaw. Figure 1.9 shows Ti$_3$SiC$_2$ samples perfectly machined to various shapes using conventional machining tools.
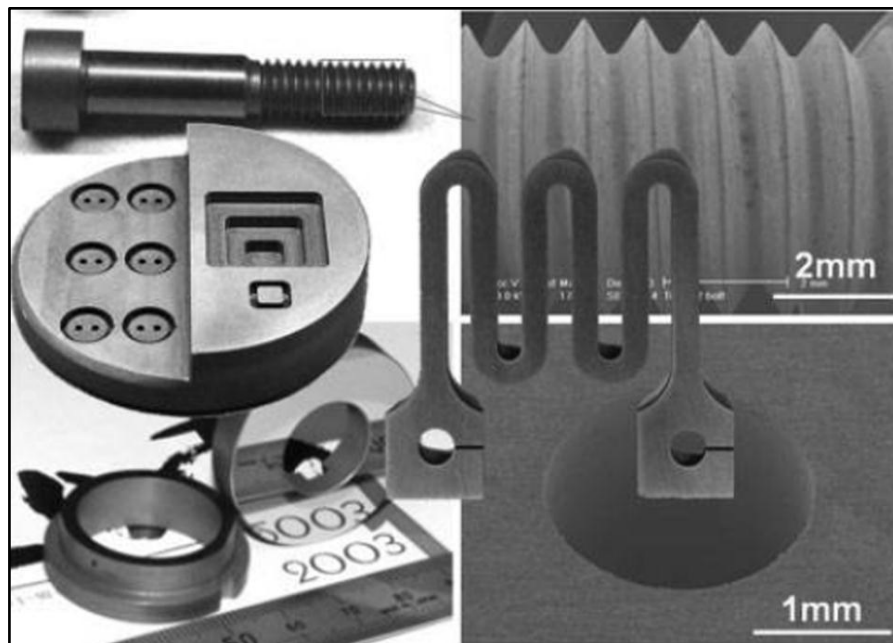
Figure 1.9: Ti$_3$SiC$_2$ fabricated with reactive PDS process and machined to different geometries [Sun et al. 2010]

In general, very high melting point, thermal stability, and excellent high temperature mechanical properties make most of the structural ceramic materials ideal for high temperature applications. However, their brittle nature renders them vulnerable to thermal shock damage and failure. Most of the ceramics show catastrophic drops in mechanical properties once subjected to thermal shock [Koh *et al.* 2004]. Fortunately MAX phase ceramics have exceptionally better thermal shock resistance. It was experimentally observed that with increase in the quench temperatures above a critical temperature, the strengths of the water quenched samples were increased. Such quenching behavior is unique for MAX phases, and has never been observed for any other structural ceramics to date. Several mechanisms were proposed to account for this amazing phenomenon. The measurement of retained strength *vs* numbers of quenching indicated that thermal shock alone could not improve the strength of the substrates. Therefore, the quench strengthening behavior exhibited by MAX phases was not due to the water quenching. The formation of oxide layer on the surface was regarded as one reason

for this behavior [Bao *et al.* 2005]. The oxide layers were very thin at low quench temperatures and therefore they cause negligible effect on transient tensile stresses. As a result, the residual strength decreased with quench temperatures. On the other hand, thick oxide layer is formed at high quench temperatures. Consequently, oxide layers played a more vital role than quench temperatures in deciding the transient tensile stresses. Therefore, degree of damage of the substrate decreased, which in turn resulted in the quench strengthening [Zhang *et al.* 2006].

Some researchers studied the role of surface treatment on the thermal shock resistance. They also confirmed that the thermal shock resistance can be improved by the formation of a surface oxide layer or a chemically leached porous surface. Above all, following three major facts are believed to contribute to this exceptional thermal shock resistance: (1) Since MAX phases are damage tolerant and significantly resistant to crack propagation, they show excellent thermal shock resistance [Zhou *et al.* 1998; 1999]; (2) High thermal conductivity is a desirable factor for high thermal shock resistance and MAX phases exhibit higher thermal conductivity compared to brittle ceramics; (3) The existence of high temperature ductility in MAX phases would inhibit thermal failure [Zhou *et al.* 2001].

1.2.6.4 Tribological Properties

A good tribological performance is envisaged for MAX phases inspired from their nanolayered nature. Tribological performance of a material strongly depends on the experimental conditions. It usually shows varying frictional properties with respect to the counter surface employed. To date, tribological behavior of MAX phases were studied mostly on Ti_3SiC_2. The earlier observations on structure and mechanical properties suggested a possible ultra-low friction for this material. In an initial study, a friction coefficient of $\sim$0.025 was measured on cleaved basal planes of individual grains [Crossley *et al.* 1999]. The kinetic friction coefficient of the basal planes of Ti_3SiC_2 measured using a lateral force microscopy reported a value as low as 2 to 5 x10^{-3} [Myhra *et al.* 1999]. Even the exposure to air for several months did not deteriorate the low friction property. When measured against a lightly peened stainless steel, polycrystalline Ti_3SiC_2 showed a friction coefficient of 0.12, under a load of 0.15 to 0.9 N.

El-Raghy *et al*. reported a two stage friction and wear behavior in Ti_3SiC_2. They found that when tested against steel, both coarse and fine grained Ti_3SiC_2 experienced an initial transition stage in which the friction coefficient (μ) value showed a linear increase from 0.15 to 0.45 followed by a steady state with the μ value of about 0.83 [El-Raghy *et al.* 2000b]. This transition from the lower μ value to higher μ value was attributed to accumulation of debris on the wear track. The study also demonstrated that the coarse grained structure show high wear resistance than that of fine grain structure. Sun *et al.* reported the tribological properties of Ti_3SiC_2 using pin-on-disc method. Their experiment showed the µ value was 0.4 - 0.5 under normal load range of 7.7 N to 14.7 N [Sun *et al.* 2002b]. The debris on the Ti_3SiC_2 disc mainly contained Ti_3SiC_2 and steel pin materials, whereas the debris on the steel sliders consisted of the pin material. The wear mechanism was concluded as the fracture and delamination of Ti_3SiC_2 materials and subsequent adhesive wear of steel sliders.

Zhang *et al.* determined the friction coefficient of Ti_3SiC_2 by taking two types of counter materials [Zhang *et al.* 2002c]. The first combination was Ti_3SiC_2 against Ti_3SiC_2, and the second was Ti_3SiC_2 against diamond. The first pair showed a very high friction coefficient, whereas the second pair exerted extremely low frictional force and the friction coefficient was as low as 0.1. The formation of a tribofilm on the Ti_3SiC_2 surface, a behavior similar to that of graphite was believed to be the driving force for this intriguing tribological performance in Ti_3SiC_2/diamond pairs. Two successive friction regimes were identified for friction behavior of coarse and fine grained Ti_3SiC_2 against steel and Si_3N_4 balls [Souchet *et al.* 2005]. In the type I regime, a relatively low friction coefficient (0.1 to 0.15) and little wear was observed followed by type II regime with increased friction coefficients (0.4 to 0.5) and considerable wear. Sarkar *et al* reported the coefficient of friction value in the range 0.5 to 0.6 for Ti_3SiC_2/steel tribocouple [Sarkar *et al.* 2005]. All these reports suggest that, the tribological performance of MAX phases strongly depends on the experimental conditions, and prediction of a general behavior is difficult. In many cases, Ti_3SiC_2 offered a friction coefficient below 0.5 which was lower than the conventional ceramics.

1.2.7 MAX phase Composites

Ceramic-Ceramic matrix MAX phase composites: Composites are materials formed by the combination of two or more constituent materials having different physical and chemical properties. The composite thus formed show properties that differ from their constituent materials even though the individual constituents remain as separate phases in the final product. The constituent with larger volume percent is generally called as matrix phase, and constituents present in low volume percent is termed as fillers. The unusual combinations of mechanical properties make MAX phase a unique structural material. It has been used to develop several engineering composites, sometimes as the matrix, and sometimes as the filler.

The early MAX based composites reported were Ti_3SiC_2–SiC and Ti_3SiC_2–TiC. Tong *et al.* found increased flexural strength and decreased fracture toughness in Ti_3SiC_2–20SiC–8TiC (vol%) composite than its monolithic Ti_3SiC_2 counterpart at high temperatures [Tong *et al.* 1995]. The incorporation of SiC in Ti_3SiC_2 was thought to be an ideal method to increase the oxidation resistance and hardness of Ti_3SiC_2. Li *et al.* fabricated SiC reinforced Ti_3SiC_2 composites by *in situ* hot pressing technique [Li *et al.* 2004]. This was done through displacement reaction of Si and TiC powders at 1350 °C for 2 h, followed by densification at 1500 °C for 1 h, and the final composites consisted of Ti_3SiC_2, SiC and TiC. They claimed that the SiC or TiC particles inhibited the grain-boundary migration of Ti_3SiC_2 and resulted in a fine grained Ti_3SiC_2 matrix. In reverse combination, Ti_3SiC_2 was used as fillers to improve the toughness of SiC [Mogilevsky *et al.* 2006]. Benko *et al* employed cubic boron nitride (cBN) to increase the hardness of Ti_3SiC_2 in Ti_3SiC_2/cBN composites [Benko *al.* 2004].

MAX-Oxide composites were also reported in literature. Luo *et al.* synthesized and studied the properties Al_2O_3/Ti_3SiC_2 composites with full range of volume fractions (i.e., Ti_3SiC_2 volume fractions vary from 0 to 1; x= 0-1) by spark plasma sintering (SPS) [Luo *et al.* 2004a]. Above a loading of 30 wt % Ti_3SiC_2, the composites showed good machinability. Vickers hardness of these composites showed a positive trend with increased Al_2O_3 content owing to the high hardness of Al_2O_3 (4.0 GPa for Ti_3SiC_2 to 19.9 GPa for Al_2O_3). The bending strength at room temperature was improved with Ti_3SiC_2 content; from 428 MPa (*x*=0) to 673 MPa

(x=1). Luo *et al.* in a separate study showed a toughness of 8.78±0.12 MPa m$^{1/2}$ and strength of 500±10.2 MPa when addition of 50 wt% Ti$_3$SiC$_2$ in Al$_2$O$_3$ matrix is reinforced [Luo *et al.* 2003]. Hu *et al.* utilized hard Al$_2$O$_3$ to improve the wear resistance property of Ti$_3$SiC$_2$ [Hu *et al.* 2006]. Shi *et al.* studied the dielectric behavior Ti$_3$SiC$_2$/3Y-TZP (3 % yttria stabilized zirconia) composites. A percolation in dielectric constant is observed with increase in the Ti$_3$SiC$_2$ concentration. This was attributed to the polarization effects between the clusters inside the composites near percolation threshold [Shi *et al.* 2005].

The bioinertness of Ti$_3$SiC$_2$ make it suitable bio-applications and the same was explored for improving the mechanical properties of hydroxyapatite; the well-known bioceramic used for osteo-implantation. The as fabricated composite showed improved flexural strengths and fracture toughness with Ti$_3$SiC$_2$ addition. On the other hand, a decrease in Vickers hardness was observed with Ti$_3$SiC$_2$ content, which is a favorable condition for bio-applications. Also the composite is highly machinable above Ti$_3$SiC$_2$ content of 20 vol.%.

Metal matrix- MAX phase composites: The relatively high modulus and electrical conductivity enable Ti$_3$SiC$_2$ to act as promising reinforcement for metal matrix composites. Zhang and Zhou fabricated copper matrix composite with Ti$_3$SiC$_2$ dispersions, and found that the addition of Ti$_3$SiC$_2$ improved the tensile yield strength and microhardness of copper [Zhang and Zhou 2000]. To improve the wettability of Ti$_3$SiC$_2$ with Cu matrix, Zhou *et al.* employed an electroless coating method, and coated a layer of copper over Ti$_3$SiC$_2$ particulates prior to the composite preparation. Compared to uncoated Ti$_3$SiC$_2$ reinforced composite, the copper coated Ti$_3$SiC$_2$ reinforced composites showed more homogeneous distribution of Ti$_3$SiC$_2$ within the copper matrix [Zhou *et al.* 2004]. Ti$_3$AlC$_2$ and Ti$_2$SnC were also used as active reinforcements in Cu matrix. The results demonstrated that the incorporation of Ti$_2$SnC noticeably decreased the grain size of Cu, and significantly strengthened the composite. Addition of 1 vol% Ti$_2$SnC resulted four times increase in the yield strength than that of pure copper [Wu *et al.* 2005]. The addition of Ti$_3$AlC$_2$ produced a composite with much superior flexural strength than the pure copper without significant loss in the fracture toughness [Peng *et al.* 2007].

Li *et al.* prepared Ni or Co based transition metal-Ti$_3$SiC$_2$ composites by powder metallurgy route [Li *et al.* 2005b]. Interestingly, in this study the poor wettability of Ti$_3$SiC$_2$ with Ni/Co resulted in composites with layered microstructures. The outer layer was composed of Ti$_3$SiC$_2$ and TiC phases. The inner core layers were formed with loose Ti$_3$SiC$_2$ and TiC particles. These two layers were separated with the porous transition layers of continuous metal nets and ceramic particles.

Al/Ti$_3$SiC$_2$ was fabricated by Ai *et al.* through pressureless sintering of Al and Ti$_3$SiC$_2$ powder mixtures [Ai *et al.* 2005]. In this case, reaction of Al with Ti$_3$SiC$_2$ in the temperature range of 700 to 800℃ was observed which was driven by the dissolution of Si in the molten Al metal. In this case, the hardness was found to be lower than that of single phase polycrystalline Ti$_3$SiC$_2$.

It is evident from the literature that MAX phase reinforcement and its beneficial properties are not explored in polymer matrix composites until our first report on Polyaryletherketone (PAEK) polymer reinforced with Ti$_3$SiC$_2$ was reported in the year 2014. In fact, we identified this research gap and started the work on the effect of MAX phase reinforcements in polymer matrix composites. In this thesis, the effect of Ti$_3$SiC$_2$ in PAEK polymer matrix is discussed in Chapter 2.

1.2.8 Applications of MAX Phases

The unique and unusual properties of MAX phase attracted enormous technical interest in design of various industrial products. The potential applications projected so far includes but not limited to kiln furniture, machinable ceramics, wear and corrosion protection. MAX phase is recommended for the rotating mechanical parts, heat exchangers, and low friction applications. Prof. M.W. Barsoum, the father of MAX phases together with El-Raghy founded the company 3-ONE-2, LLC, in 2001 as a joint venture with Kanthal AB (Sandvik Materials Technology). The company started manufacturing Ti$_3$SiC$_2$ and Ti$_2$Al$_C$ powders and dense structural parts under the trade name Maxthal 312 (Ti$_3$SiC$_2$) and Maxthal 211 (Ti$_2$AlC). These products are shown in Figure 1.10. The company is also marketing heating elements made of Maxthal 211 (Figure 1.11a), and was using in high temperature reactors (Figure 1.11b).
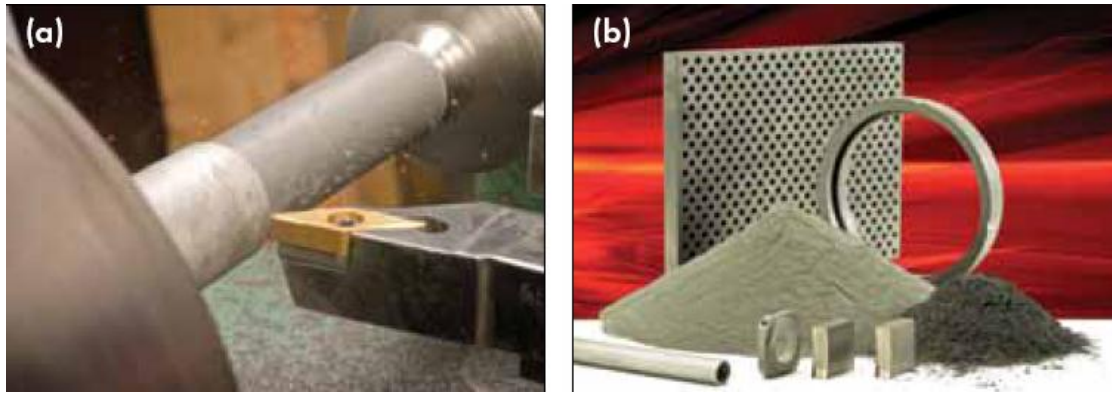
Figure 1.10: (a) A MAX phase billet machined by a lathe; (b) Ti$_2$AlC and Ti$_3$SiC$_2$ powders and parts fabricated by Sandvik Heating Technology, Sweden, and commercially available under the trade name MAXthal 211 and MAXthal 312.
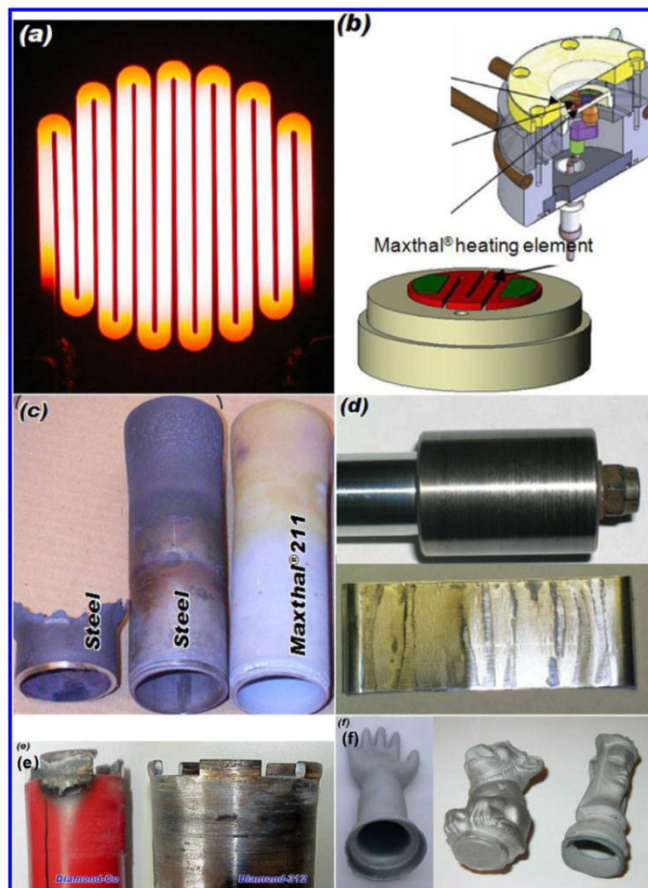
Figure 1.11: (a) Maxthal 211 heater glowing at 1723 K; (b) Maxthal 211 heating elements in reactor cell for three-way catalyst (c) gas burner nozzles made of Maxthal 211 and 353MA steels after one year in furnace at 1773 K; (d) foil bearing: Ta$_2$AlC/Ag shaft and superalloy foil after testing for 10000 cycles in a rig; (e) comparison of concrete dry drills made of diamond-Co and dimond-312; (f) slip casting of MAX phases to three-dimensional shapes followed by sintering (courtesy 3-ONE-2, LLC)

Superior mechanical and oxidation resistance properties of Ti_2AlC (Maxthal 211) over steel was utilized for making gas burner nozzles, in sulphur containing natural gas corrosive burning environments. The formation of α-Al_3O_2 scales on the surface of Ti_2AlC protected the material so that the material can be used until the temperature of 1673 K. Excellent machinability enabled easy threading of nozzles. A performance comparison of nozzles made of Maxthal 211 and 353MA steel after one year use in a furnace at 1473 K is shown Figure 1.11c.

MAX based materials are also employed for making foil bearings, with low friction and wear. The photograph of Ta_2AlC/Ag shaft and a superalloy foil after testing for 10000 cycles in a rig is shown in Figure 1.11(d). A drilling tool for dry concrete, consisting of diamonds in MAX 312 was developed by 3-ONE-2 and Hilti. As shown Figure 1.11(e), MAX phase segments showed superior performance than that of currently used diamond/Co segments. MAX phases can be easily slip casted into various shapes and this has extended to three-dimensional shaping, and sintering to fully dense and hollow objects that is difficult to fabricate by other methods (Figure 1.11f).

1.3 Two dimensional MAX Phases

Initially, the study and application of MAX phases was restricted only to three-dimensional (3D) bulk material. However, the discovery of graphene and its inorganic 2D analogues generated great interest and curiosity on 2D derivatives of MAX phases. However, the relatively strong interlayer bonding made the conventional exfoliation techniques inadequate to produce 2D MAX phases. If we consider the MAX phase structure, we can understand that two types of 2D MAX phases can be possibly obtained. One is by retaining all the atoms, and the other is by the removal of A layer atoms and subsequent layer separation.

Very recently, Naguib *et al.* succeeded in producing 2D MAX phase by successive removal of aluminium (Al) atoms from Ti_3AlC_2 using hydrofluoric acid [Naguib *et al.* 2011]. The process involved immersing Ti_3AlC_2 powders in 50 % hydrofluoric acid for 2 h at room temperature. In the product, Al layers were selectively removed and replaced by hydroxyl (OH), and fluorine (F) surface groups. The further exfoliation of these layers resulted in 2D MAX phase. This invention was

a breakthrough in MAX phase research, and the new 2D material was named as 'MXenes' to highlight their 2D nature and emphasize its similarity with graphene. Figure 1.12 illustrates the different steps involved in the synthesis of MXenes.
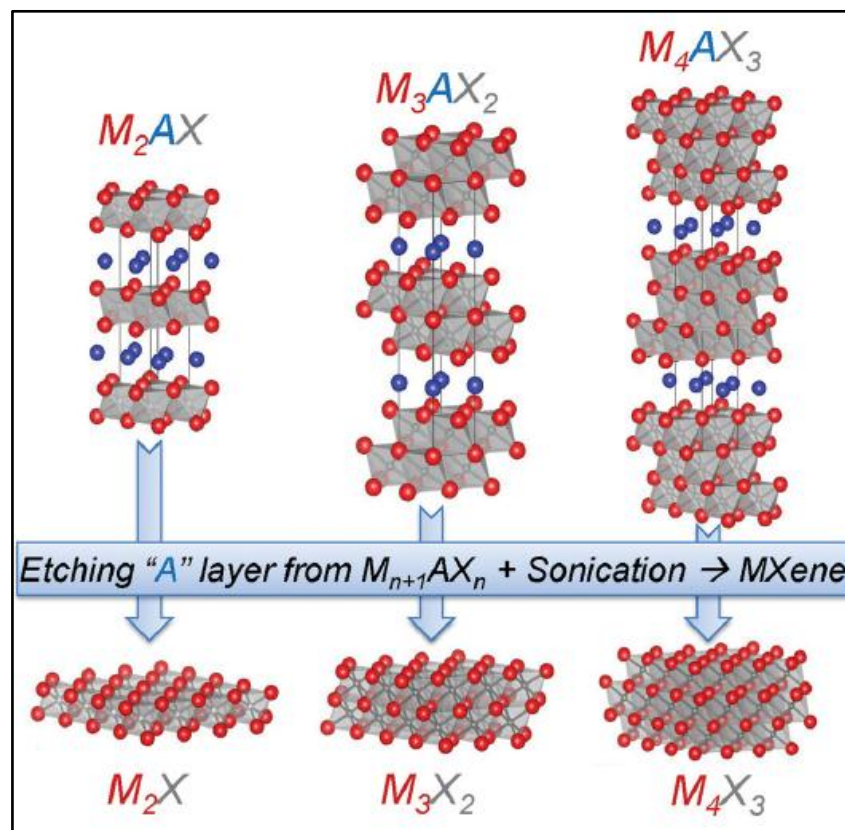
Figure 1.12: Structure of MAX phases and the corresponding MXenes [Naguib *et al.* 2014]

The same synthesis method was extended to other Al containing MAX phases and the constellation of MXenes now includes Ti_3C_2, Ti_2C, Ti_3CN, Nb_2C, V_2C, $(Ti_{0.5},Nb_{0.5})_2C$, $(V_{0.5},Cr_{0.5})_3C_2$, and Ta_4C_3. The reactions occur in the synthesis of MXene from bulk MAX phase are presumed to be as follows;

$$M_{n+1}AlX_n + 3HF \rightarrow AlF_3 + M_{n+1}X_n + 1.5H_2 \qquad (1.5)$$

$$M_{n+1}X_n + 2H_2O \rightarrow M_{n+1}X_n(OH)_2 + H_2 \qquad (1.6)$$

$$M_{n+1}X_n + 2HF \rightarrow M_{n+1}X_nF_2 + H_2 \qquad (1.7)$$
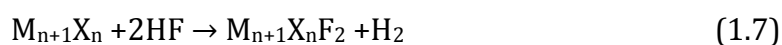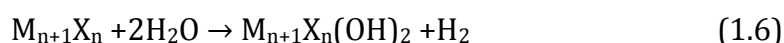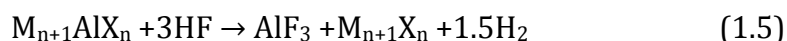
It was reported that the newly derived multilayered MX phase can be easily converted to single layers by intercalation with various molecules followed by exfoliation. While looking into the structure of MXenes, the initial DFT studies describe MXenes as stacked hydroxylated MX layers. However, in real situation the

MXene has highly complex nature. The presence of OH, O and F is confirmed experimentally using XPS. Therefore, MXenes are generally represented as $M_{n+1}X_nT_x$ (T represents the surface groups, F, OH, and/or O and x is the number of terminal groups). A schematic representation of Ti_3C_2 MXene is shown in Figure 1.13.
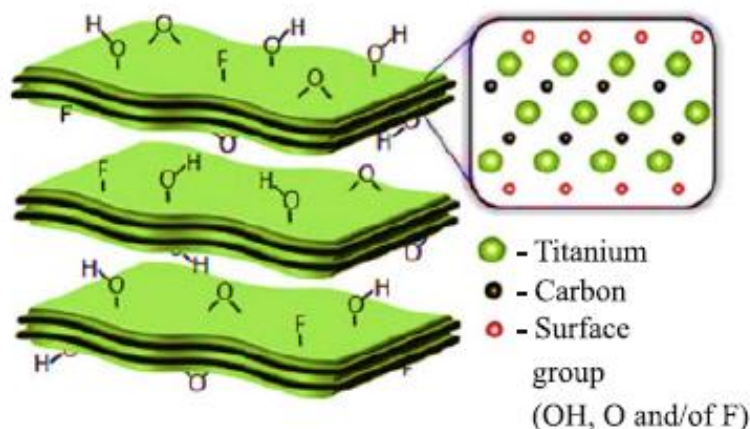
Figure 1.13: Schematic representation of $Ti_3C_2T_x$ MXene with terminal functional groups.

The growing interest on MXenes is owed to their exceptional properties. MXenes show electrical conductivity comparable to that of multilayered graphene. Computational studies showed that MXene is quite stiff and its in-plane elastic constant is more than 500 GPa. These exotic properties of MXenes opened up a new area of research, and now MXenes are widely accepted for energy and environmental applications. They have reported as promising material in electrochemical energy storage systems [Naguib *et al.* 2012; Mashtalir *et al.* 2013; Naguib *et al.* 2013].

Etching of A layer atoms using HF is a method followed in general for the preparation of 2D MAX phase. Unfortunately, this method can be applied to Al containing MAX phases only. Researchers are trying to explore new synthetic methods to produce 2D MAX phases by retaining A layer atoms. One such method was reported by Zang *et al.* for the preparation of ultrathin nanosheets of MAX phases. They used a substitutional solid solution based exfoliation process for the production of ultrathin nanosheets of A-layer-activated MAX phases. A series of doped phases, such as, $Ti_3Si_{0.75}Al_{0.25}C_2$ (TSAC) and $Ti_3Al_{0.9}Si_{0.1}C_2$ (TASC) were fabricated using a modified high-temperature self-propagation synthesis, and the

exfoliation process in various solvents to synthesise 2D MAX phase were studied. Free standing nanosheets with dimensions in the range of 100-200nm was successfully obtained. They also reported that the as-synthesized nanosheets are effective fillers for polymeric composites [Zang *et al.* 2013]. The synthesis steps adopted by the authors are schematically represented in Figure 1.14. However, this method did not get much attention. So in this thesis, we aimed to develop a new scalable method for the synthesis of 2D MAX phases by retaining the A layer atoms, and studied their functional properties.
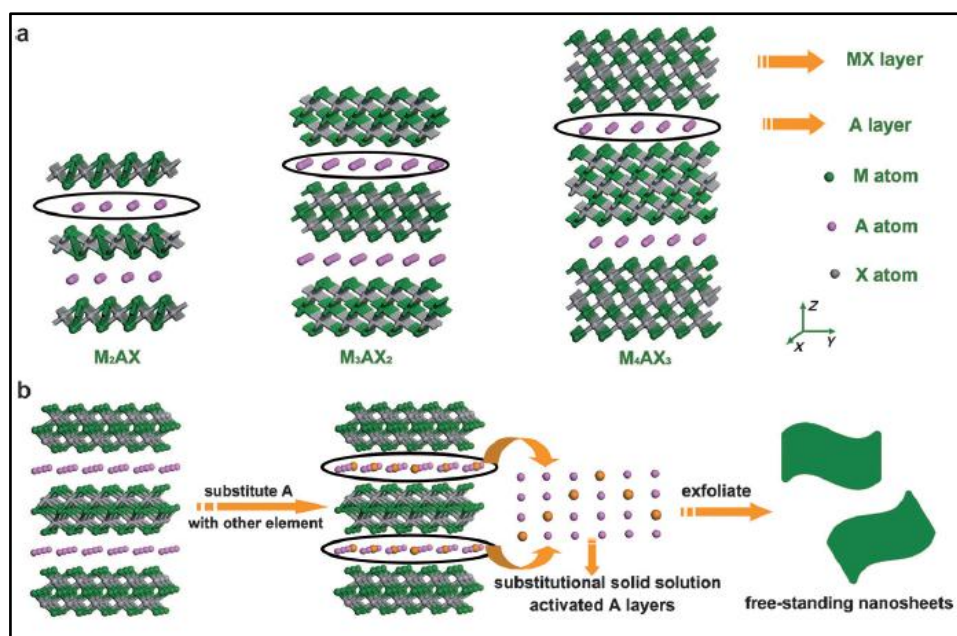
Figure 1.14: (a) Crystal structure of 211, 312, and 413 MAX phases; (b) Illustration of the substitutional solid solution based exfoliation process for the formation of free-standing nanosheets of MAX phases by activating the A layers

1.4 Scope of the thesis

In this introductory chapter, the research work carried out on the various aspects of MAX phase materials is accounted. The accidental discovery of MAX phase, different techniques employed so far for synthesizing many MAX phase materials, understanding of MAX phase crystal structures, literature evidences for the phase stability, the unique and beneficial thermal, electrical, and mechanical properties of MAX phases, and more predominantly the recent innovation made with MAX phases i.e., the discovery of 2D MAXene and MXene layered materials are highlighted.

When literature survey was conducted for exploring the facts behind history, evolution, and properties of the MAX phase materials in the past two decades, it was clearly understood that MAX phase is an excellent reinforcement phase that can greatly offer many functional properties. The reported literature mainly dealt with the advantages on the mechanical performance of MAX phase reinforcements in ceramic and metal matrix systems. In this thesis, we investigated the effect of Ti_3SiC_2 reinforcement in polymer matrix, for the first time. In fact, till date a very few research reports are published in polymer matrix. Earlier works had claimed that still better technique is required to synthesis MAX phase powders in easy and simple manner. Exactly this was the motivation for us to explore new processing techniques, and in this thesis we have employed microwave assisted synthesis for obtaining Ti_3AlC_2 MAX phase materials. Microwaves interact readily with materials having high dielectric constants. It was exciting to investigate the role of various MAX phase reactants in microwave heating to bring out the fastest reaction path way for producing the MAX phases.

Another challenge noted from the literature was processing of MAXene layers without disturbing the A layer atoms from the parent material. While most of the researchers successfully produced MXenes through the con. HF aided removal of A layers, conversion of layered MAX phase into MAXene by retaining the A layers is not attempted. In this work, a careful attempt on the new concept, namely, 'shear induced micromechanical exfoliation' was attempted for the first time to synthesise 2D MAXene nanosheets from the bulk MAX phase. Apart from the synthesis and composite fabrication, the unique novelty of this thesis is the successful demonstration of a range of functional materials with MAX phases which includes MAX phase thermal fluid, distinctly unique rheology of MAX phase nanofluid, thermally intact low wear MAX-phase polymer composite, and antimicrobial/antibiofilm property of $Ti_3C_2T_x$, the MX phase derived from Ti_3AlC_2 MAX phase nanomaterials. These are the new attempts that are never ever reported in the literature.

In total, the thesis has three working chapters apart from the introduction and summary chapters. In the first working chapter, the beneficial properties of Ti_3SiC_2 MAX phase reinforcement in PAEK polymer matrix composites are

investigated. The effect of Ti_3SiC_2 over the thermal stability, thermal conductivity, thermal expansion coefficient, wear and friction properties, mechanical strength and also machinability were studied systematically. In the second working chapter, exfoliation of MAX phases to obtain MAXene layers is described. The role of various polar solvents, MAXene morphology, phase stability, dispersion stability and electrical conductivity etc., have been studied and reported. The design of MAXene thermal fluid is carefully investigated. In the first part of the third working chapter, we investigated the efficiency of microwave energy for making Ti_3AlC_2 MAX phases. The literature evidences indicated that the MAX phases, are bio-inert and few works were devoted for the development of bioceramic composites. This motivated us for studying the bio-functionality of $Ti_3C_2T_x$ MXene nanostructures derived from Ti_3AlC_2 MAX phases. Hence, the second part of third working chapter is devoted for the synthesis of $Ti_3C_2T_x$ MXene and investigation on its antimicrobial, antibiofilm and cytotoxicity properties. In short, all the working chapters have created a spark of new scientific knowledge in the field of MAX phase research. In fact major research works on MAX phase materials are reported from the group headed by Prof. Barsoum, Drexel University, USA. Hence, we have carefully selected the research problem and sincere efforts are made to fill the gap that currently exist in the MAX phase research.

1.5 Research Statement

Briefly, the research problem can be defined as, 'Experimental exploration of the beneficial properties of MAX-phase reinforcements in polymer matrix composites, design and development of 2D MAX phase nanostructures through exfoliation/delamination techniques, and employment of the microwave assisted rapid synthesis route for obtaining MAX phase materials,' and finally reporting the unusual and unique properties for potential multifunctional applications. Accordingly the following research objectives are planned.

1.6 Objectives

1. Development of Polyaryletherketone (PAEK)-Ti_3SiC_2 polymer nanocomposite and evaluation of thermal, mechanical, and tribological properties.

2. Synthesis of 2D Ti_3SiC_2 MAX phase nanostructures through shear induced micromechanical cleavage technique.

3. Design of Ti_3SiC_2 MAXene nanofluids, and study the beneficial properties with respect to thermal conductivity, rheology and lubrication for thermal management applications.

4. Synthesis of Ti_3AlC_2 MAX phases via microwave hybrid heating

5. Conversion of Ti_3AlC_2 MAX phase in to $Ti_3C_2T_x$ MXene via hydrofluoric acid etching.

6. Investigation of antimicrobial, antibiofilm, and cytotoxicity properties of $Ti_3C_2T_x$ MXenes.

CHAPTER 2

MAX Phase- Polymer Composites
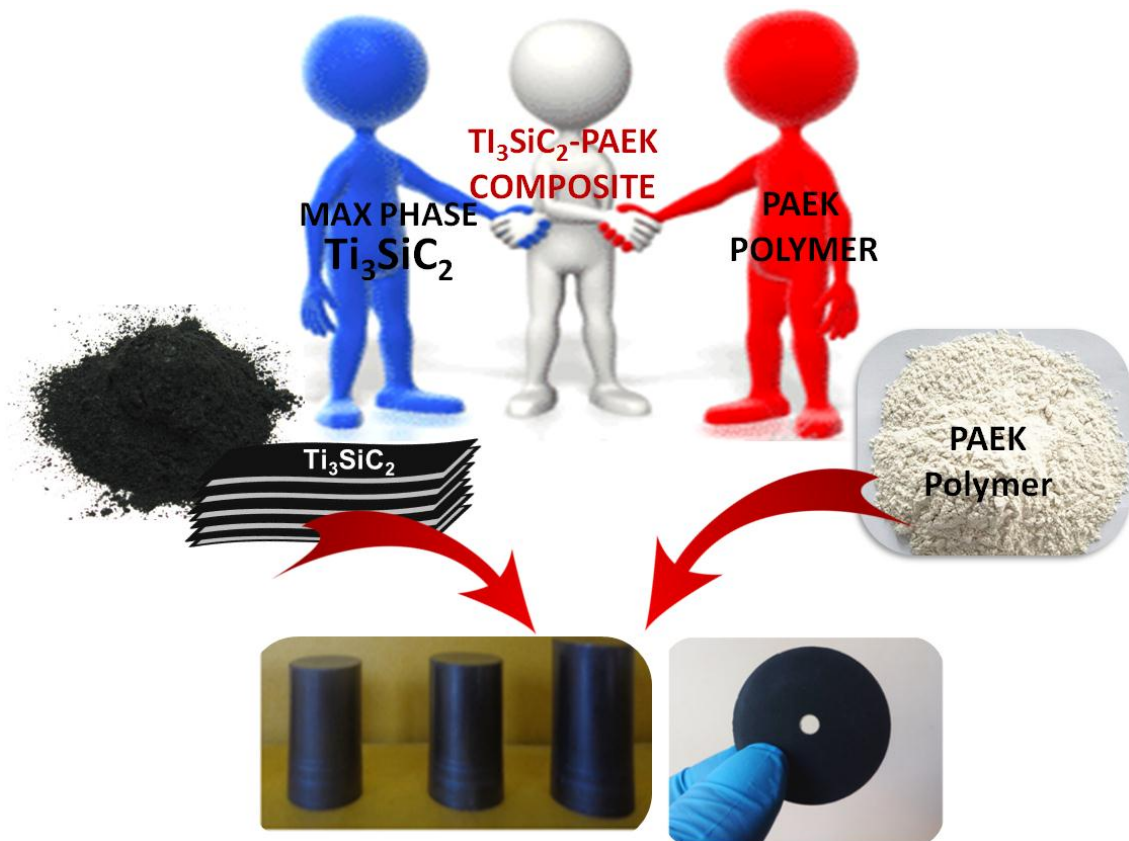
Polyaryletherketone (PAEK) Polymer Engineered with Nanolaminated Ti$_3$SiC$_2$ Ceramic Fillers

2.1 Abstract

A new polymer-ceramic nanocomposite in which polyaryletherketone (PAEK) polymer reinforced with titanium silicon carbide (Ti$_3$SiC$_2$), was developed for the first time. PAEK-Ti$_3$SiC$_2$ nanocomposites with varying volume fractions of Ti$_3$SiC$_2$ were processed by hot pressing. The effect of Ti$_3$SiC$_2$ on thermal, mechanical and tribological properties was systematically analyzed and the results are discussed. The study confirms that the Ti$_3$SiC$_2$ controlled the high thermal expansion property of PAEK polymer. In addition to that, it enhanced the wear resistance and mechanical strength of PAEK without affecting its inherent machinability and low-friction characteristics. The study brought out a new polymer composite which can be utilized for several engineering and structural applications.

2.2 Introduction

Design and development of state-of-art, futuristic engines and engine components is in need of energy efficient, advanced structural composites. Materials having high thermal stability, strength, toughness, damage tolerance, stress dissipation, wear and oxidation resistances, low friction, dry or green machining and lightweight are receiving much attention for meeting stringent requirements in aerospace and automotive sectors. Ceramically modified polymer composites are ideal candidate for developing high performance materials. Polymer composites have the benefit that they can be processed by easier and low cost methods. The advent of new high performing ceramic materials enabled the researchers to develop wide varieties of composites by the use of such materials as a reinforcing phase in polymer matrix. The structural materials used in different engine components will be subjected to various hostile operating conditions. So it is very much important that the new material should be superior to its counterpart in thermal and mechanical stability. The high load carrying capacity and good

tribological properties are also very much relevant for engineering materials like bearing.

Usually polymers are known for its low coefficient of friction but they suffer serious wear lose during operation. The incorporation of hard ceramic fillers often leads to high wear resistance of polymer composites. Among the various polymers, Polyarylether ketone (PAEK) having good thermal stability, toughness, mechanical strength, chemical inertness and biocompatibility received more attention as engineering material. Polyaryletherketone (PAEK) is a semi crystalline thermoplastic and it has glass transition (T_g) and melting temperatures of 157 °C and 370 °C, respectively. There are different kinds of PAEKs such as polyetheretherketone (PEEK), polyetherketone (PEK), polyetherketoneketone (PEKK) etc. with different ketone content. PAEK polymers inherently possess ultra-low coefficient of friction and green machining which makes them more attractive for designing complex engineering shapes and parts. Currently they are used as sub-sea connectors, heat exchanger parts and bio implants. Unfortunately the low wear resistance (2.87 x 10^{-6} mm^3 N^{-1} m^{-1}) and excessive thermal expansion (CTE= 127 x 10^{-6}/°C) properties of these materials have caused a setback from being a potential engineering material. Therefore, due attention is paid by the researchers to overcome these limitations. The effects of SiO_2 [Wang *et al.* 1997a], Al_2O_3 [Kuo *et al.* 2005; Goyal *et al.* 2006], ZrO_2, [Wang *et al.* 1996a; Wang *et al*. 1998], SiC [Wang *et al.* 1997b; Xue *et al.* 1997] and Si_3N_4 [Wang *et al.* 1996b] ceramic reinforcements on wear and friction properties of PEEK polymers were extensively studied by many researchers. They found that up to 10 wt % addition of nano particulate ceramic reinforcement increased the wear resistance without decreasing the coefficient of friction. However, in most of the reports, the effect of these fillers on the thermal and mechanical properties was not addressed. Goyal *et al.* showed an improvement in the thermal stability by the addition of Al_2O_3 ceramic filler [Goyal *et al.* 2006]. Interestingly, an isolated piece of work also exists on PEEK-hydroxyapatite nanocomposites as bioceramic hybrid composites [Li *et al.* 2012a]. It is clear from the reported works that the polymers achieve improvement in mechanical strength and wear resistance on reinforcing mechanically hard ceramic fillers such as Al_2O_3, SiC, AlN, Si_3N_4 and ZrO_2. On the other hand, the parent polymer matrix could not

retain the inherent quality of mechanical softness and turn out to be brittle. Kuo et al. demonstrated 20–50 % enhancement in the hardness, elastic modulus and tensile strength of PEEK when it was prepared with 5-7.5 wt% SiO_2 or Al_2O_3 nanoparticles. However in this case, PEEK lost the tensile ductility [Kuo *et al.* 2005]. Similarly, decrease in ductility and increase in coefficient of friction was also noticed when ZrO_2 was reinforced in PEEK [Mishra *et al.* 2012]. These studies confirm that it is important to identify new ceramic nano-fillers which can offer better thermal and mechanical properties without affecting the machinability and tribology.

In this context, we have investigated the effects of titanium silicon carbide (Ti_3SiC_2), which is characterized as a nanolaminate and a potentially soft-ceramic on the engineering properties in PAEK polymers without compromising the machinability and tribology. As we discussed in chapter 1, Ti_3SiC_2 belongs to the family of MAX phase ternary carbides and is categorized as a new classical ductile ceramic [Barsoum 2000; Nowotony *et al.* 1982; Barsoum and El-Raghy 2001]. Like metals, they are relatively soft and possess good thermal and electrical conductivity. At the same time, they are elastically stiff and exhibit high temperature mechanical properties, resembling ceramics. They also possess super-plasticity and low coefficient of friction. Above all, they are unusually damage tolerant and can be machined using a simple lathe even without a lubricant.

Ti_3SiC_2 is the first well studied engineering material in MAX phase family. The Ti_3SiC_2 nanolaminates can easily shear over other and offer a sort of self-lubricating character [Gupta *et al.* 2008; Barsoum and El-Raghy 1996]. The wear and friction property of dense Ti_3SiC_2 ceramics have been well explored and a steady state friction coefficient (μ) value of 0.4–0.5 has been reported for Ti_3SiC_2 against steel and Al_2O_3 [Sun *et al.* 2002; Gupta *et al.* 2008]. It is reported that the layered Ti_3SiC_2 in Al_2O_3 matrix can produce composites possessing high toughness (8.78 ± 0.12 MPa $m^{1/2}$) and low Vickers hardness (~5 GPa) without any reduction in the bulk mechanical strength [Yong Ming *et al.* 2003; Luo *et al.* 2003b; Yuang-Liang *et al.* 2011]. Ti_3SiC_2 as an active reinforcement in improving the mechanical and tribological properties of c-BN [Rampai *et al.* 2013), TiB_2 [Liya *et al.* 2012], Ni_3Al [Xiaoliang *et al.* 2013a], Cu [Ngai *et al.* 2013], WC (Xiaoliang *et al.* 2013b) and NiAl [Xiaoliang *et al.* 2013c] was earlier reported. To our surprise, the utilization of this

mechanically versatile material remains unattempted for developing high performance polymer composites.

In this work, we reported for the first time the thermal, mechanical and tribological properties of Ti_3SiC_2 ceramic reinforced PAEK polymer nanocomposites. Effect of different volume fractions (V_f) of Ti_3SiC_2 has been studied on thermal stability, thermal expansion, mechanical hardness, and the wear and friction properties of PAEK polymers and the results are discussed. The incorporation of such nanolaminated metallic-ceramic is a new concept for the polymers and our primary objective in this work is to verify whether the PAEK composite attains damage tolerance, high toughness, low friction and high wear resistance properties.

2.3 Experimental Details

2.3.1 Materials

The matrix polymer, polyaryletherketone (PAEK) in powder form was supplied as a gift by Gharda Chemicals Ltd. Mumbai, India under the trade name Polyetherketone (G-PAEK™). The reinforcement ceramic phase Ti_3SiC_2 powder was supplied by 3-ONE-2 LLC, USA. Distilled ethanol was used as solvent for ball milling.

2.3.2 Preparation of PAEK/Ti_3SiC_2 Nanocomposites

PAEK matrix composites containing Ti_3SiC_2 volume fractions (V_f) as 0.05, 0.10, 0.20, and 0.30 were prepared. The details of the composites and their sample codes with respect to the V_f of Ti_3SiC_2 are given in table 2.1. The procedures involved in the preparation of PAEK-Ti_3SiC_2 composites are schematically shown in Figure 2.1. The as received Ti_3SiC_2 and PAEK powders were vacuum dried at 100 °C for 6 h in order to make them moisture free. The required amount of Ti_3SiC_2 and PAEK powders were transferred to a polypropylene bottle and subjected to ball milling with zirconia balls in ethanol medium for 24 h. Highly dispersed, homogenous composite slurry was first obtained. The excess ethanol was vacuum distilled and the composite powder was dried at 70 °C in vacuum oven for 8 h to ensure the complete removal of alcohol and moisture. The dried composite powders were then hot pressed at a pressure of 100 MPa and a temperature of 350 °C with an average heating rate of 5 °C min^{-1}. At peak temperature, the composites were kept for 2 h and then allowed to cool naturally. All the samples were then systematically

polished using coarse to fine grades of SiC emery papers to obtain mirror like surface finishing.

Table 2.1: Formulation of the different composites and corresponding sample codes

Sample name	Volume fraction of PAEK	Volume fraction of Ti_3SiC_2
PT00	1.00	0.00
PT05	0.95	0.05
PT10	0.90	0.10
PT20	0.80	0.20
PT30	0.70	0.30
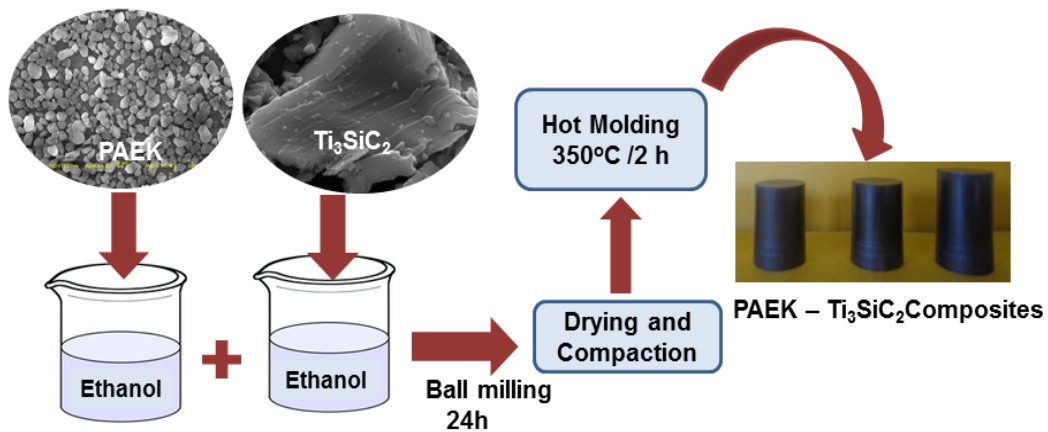
Figure 2.1: Fabrication procedure for dense PAEK/Ti_3SiC_2 composites

2.3.3 Characterization

Theoretical density (ρ_{th}) of the composite was calculated by rule of mixture (ROM) using the expression:

$$\rho_{th} = \rho_m\, V_m + \rho_f V_f \tag{2.1.1}$$

where ρ_m and ρ_f are the theoretical densities of PAEK and Ti_3SiC_2 which were taken as 1.30 and 4.50 g cm^{-3}, respectively. V_m and V_f are the respective volume fractions. The experimental density (ρ_{ex}) of the PAEK composites was measured by Archimedes principle using the relation :

$$\rho_{ex} = W_{air}/(W_{air} - W_{water}) \tag{2.1.2}$$

where W_{air} and W_{water} is the weight of the sample in air and in water medium, respectively. The morphologies of the as received Ti_3SiC_2 and PAEK as well as the distribution of the Ti_3SiC_2 in PAEK/Ti_3SiC_2 composites were observed under Scanning electron microscope (SEM, Zeiss EVO 18). For taking the SEM images of composites, the samples were polished with SIC paper to get a mirror finish followed by ultrasonication cleaning with distilled water and finally dried well to remove any moisture. The samples were then sputter coated with Au-Pd and the SEM images were recorded. The thermal stability study of pure PAEK and PAEK/Ti_3SiC_2 composites was carried out using Thermo gravimetric analyses (TGA, Shimadzu TGA 50 Thermal Analyzer). The samples were heated from room temperature to 1000 °C at the heating rate of 10 °C min^{-1} in N_2 atmosphere with flow rate of 50 mL min^{-1}. The cyclic heating and cooling characteristics of composites were determined using Differential scanning calorimetry (DSC, Perkin Elmer Pyris 6). Initially samples were heated from 30 °C to 400 °C at a rate of 5 °C min^{-1} and kept isothermally at 400 °C for 5 min, for completing the polymer melting. The samples were then cooled to 30 °C at a rate of 5 °C min^{-1}. All samples were subjected to single heating and cooling cycle with nitrogen flow rate of 20 mL min^{-1}. Thermal conductivity of the composite was measured in the temperature range 30-75 °C by laser flash technique using thermal properties analyzer (Flashline™ 2000 Anter Corporation, Pittsburgh, USA). Graphite coated samples having diameter 12.57 mm and thickness ~1.5 mm were used for the measurements. The thermal expansion characteristics of the polymer composites were studied by Thermomechanical analyzer (TMA, SS7300 SII Nanotechnology Inco.). The composite samples having 10 mm diameter and 15 mm height were heated at a rate of 10 °C min^{-1} up to 300 °C and the change in length with temperature was recorded. From the linear expansion with temperature plots, the coefficient of linear thermal expansion (CTE) was calculated for each 10 °C interval and the average was taken. The microhardness of the composites was determined by Vickers microhardness tester (Clemex) with a Vickers diamond pyramidal indenter. The finely polished and cleaned specimens were subjected to a load of 19.6 N for a time duration of 15 s. Five replicate tests were carried out and the average was taken. The flexural and compression strengths of the samples were determined by Universal testing machine (INSTRON-5500R) having a capacity of 10 ton with accuracy of 1 g. The effect of Ti_3SiC_2 on the flexural

strength was determined by 3-point bending method. The experiments were conducted on bar shaped samples of rectangular cross section according to ASTM: D790-10 standard. The rectangular bar was supported on a beam and the load was applied at the center of the specimen with cross head speed of 2 mm min^{-1}. The cross-section was bent until fracture. The flexural strength (σ) was calculated using the standard equation:

$$\sigma = 3FL/2bd^2 \qquad\qquad (2.1.3)$$

where F is the load (force) at the fracture point (N), L is the length of the support span (mm), b is width (mm) and d is thickness (mm). For determining the compressive strength, the experiments were performed as per ASTM: D695-10 standard. Cylindrical specimens having a diameter to height ratio of 1:2 was subjected to vertical load until it breaks. The compressive stress at which the fracture occurred was recorded as compressive strength of the composites.

The tribological performance of the PAEK/Ti$_3$SiC$_2$ composites was evaluated by pin-on-disc wear and friction technique (TR-201LE DUCOM, India). The cylindrical specimens having 10 mm diameter and 30 mm length were used as pin. EN 31 steel hardened to 62 HRc having diameter 100 mm and 8 mm thickness was used as the counter face material. A constant track diameter of 60 mm was given for all specimens. The wear tests were carried out with normal load of 49 N and time of 1 h. For all the tests, the sliding speed and sliding distance were maintained at 1m s^{-1} and 3600 m, respectively. The tests were carried out in the environmental chamber at ambient temperature without any lubrication. The weight of the test specimens before and after wear test was noted to determine the weight loss and was converted to volumetric loss by the equation:

$$\text{Volume loss} = (\text{Mass loss}/\text{Density}) \times 1000. \qquad\qquad (2.1.4)$$

The wear rate (ϖ) was determined using the relation:

$$\varpi = V/XL \ (\text{mm}^3 \ \text{N}^{-1} \ \text{m}^{-1}) \qquad\qquad (2.1.5)$$

where V is the volume loss (mm^3), X is the sliding distance (m) and L is the applied load (N). Five replicate tests were conducted and the average value was reported. The morphological features of the wear track after testing were observed using SEM. The surface profile of the wear scar was measured using Dektak XT Profilometer. The composition of the wear debris was analyzed using Powder X-ray diffraction

(X'Pert Pro, Philips X-ray diffractometer) with a monochromator on the diffraction beam side (Cu Kα radiation, λ=0.154 nm).

2.4 Results and Discussion

The theoretical and experimental densities of the PAEK/Ti$_3$SiC$_2$ composites hot presssed at 350 °C are plotted in Figure 2.2. It was observed that all the composites attained more than 99 % theoretical density at the given hot pressing conditions. This indicates the good matrix-filler interaction during hot pressing.
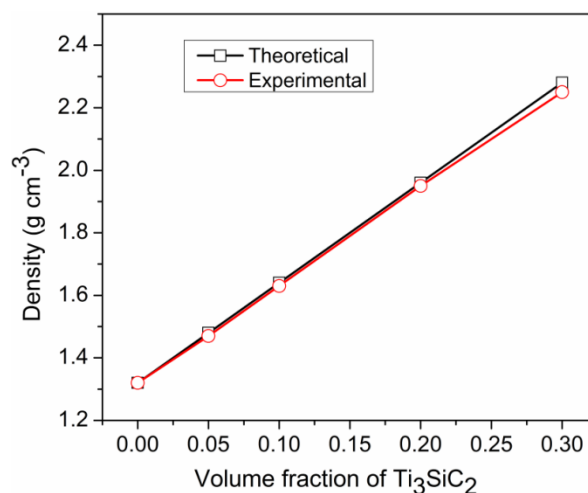
Figure 2.2: Density of the PAEK/Ti$_3$SiC$_2$ composites

2.4.1 Microstructure Analysis

The morphological features of PAEK and Ti$_3$SiC$_2$ powders before ball milling are presented in Figure 2.3 (A) and (B), respectively. The PAEK powder is spherical with an average particle size of 2 μm. The high magnification SEM image of Ti$_3$SiC$_2$ particle confirms the nanolaminated arrangement, where stacking of many nano-layered Ti$_3$SiC$_2$ sheet is clearly seen. The particles have an average size of 5 μm. The microstructural homogeneity of the PAEK-Ti$_3$SiC$_2$ and the distribution of Ti$_3$SiC$_2$ particles in PAEK matrix as observed under SEM are given in Figure 2.3(C)-(H). The SEM images show the uniform distribution of Ti$_3$SiC$_2$ phase through out the PAEK matrix. The extent of agglomeration is very less in all the composites. The microstructure confirms good interfacial interaction between Ti$_3$SiC$_2$ and PAEK matrix. The images at high magnification reveal no cracks, voids or debonding at the Ti$_3$SiC$_2$-PAEK interface (Figure 2.3(F-H)).
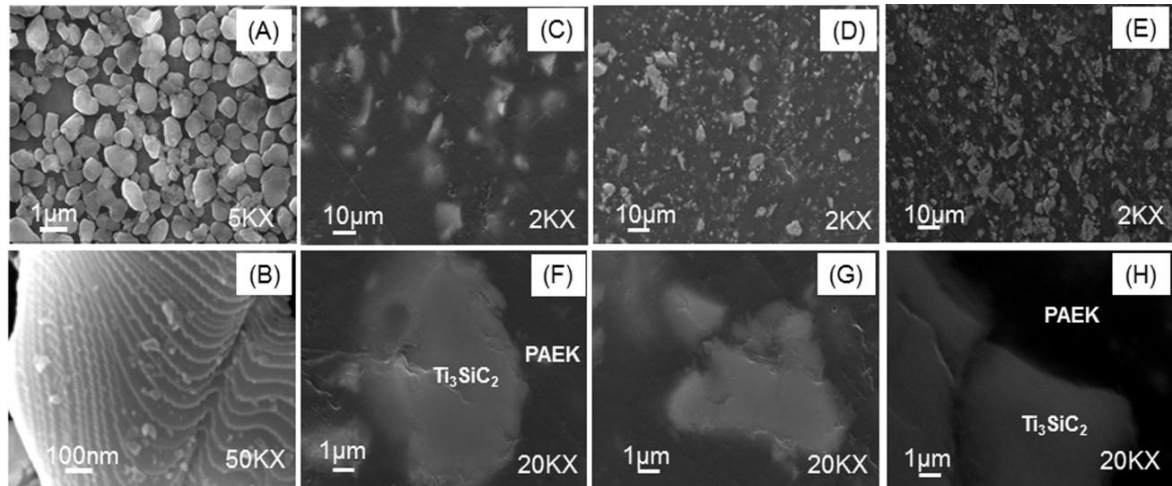
Figure 2.3: SEM images of PAEK, Ti$_3$SiC$_2$ and PAEK/Ti$_3$SiC$_2$ composites. (A) PAEK, (B) Ti$_3$SiC$_2$, (C) PT10, (D) PT20, (E) PT30 and (F)-(H) high maginfication images of C, D and E, respectively

The SEM images confirm that the given hot pressing conditions resulted in highly dense composites without any pull outs or delamination. In ceramic reinforced polymer matrix composites, the hard ceramic particles have a tendency to detach or pull out from the matrix if there is an improper wetting of ceramic particles with polymer melts. In this case, the polished images do not contain any processing defects even after a series of grinding, polishing and sliding against hard abrasives. The wet milling followed by hot pressing at a temperature close to melting point results in dense ceramic-polymer nanocomposites with good microstructural homogenity. It is well clear from the magnified SEM images that Ti$_3$SiC$_2$ sheets are randomly oriented and blended firmly with the PAEK matrix. At the given low temperature hot pressing conditions, only physical interaction is expected. They homogeneously distribute and bind properly with the matrix polymer ultimately producing defect free composite with good ceramic-polymer interfacial interaction.

2.4.2 Thermal Properties

The results on the thermal stability of PAEK-Ti$_3$SiC$_2$ nanocomposites analysed by TGA and DSC are given in Figure 2.4 and Figure 2.5, respectively. In order to eliminate weight changes due to oxidation of Ti$_3$SiC$_2$, the experiments were done in N$_2$ atmosphere. In TGA, a weight decrease corresponding to 10 % was taken as the the decomposition temperature (T$_d$) of the composites. From the TG curves

given in Figure 2.4, it was noticed that all the composites are thermally stable up to 500 °C. The PAEK polymer without any Ti_3SiC_2 phase shows the onset decomposition at 525 °C. The T_d slightly increased with increasing Ti_3SiC_2 contents. The composite PT30 which contains 0.3 V_f of Ti_3SiC_2 shows a T_d value of 565 °C with an advantage of 40 °C compared to pure PAEK. The increase in T_d might be due to the reduction in the segmental mobility of the polymer matrix induced by large number of restriction sites caused by nanolaminated Ti_3SiC_2 which reduces the C–C bond thermal vibration [Mishra *et al.* 2012; Wong *et al.* 1999]. As a result, composites require more thermal energy for the decomposition which eventually enhances the thermal stability. The TG analysis strongly supports the fact that the incorporation of Ti_3SiC_2 in PAEK significantly improved the thermal stability of the composites.
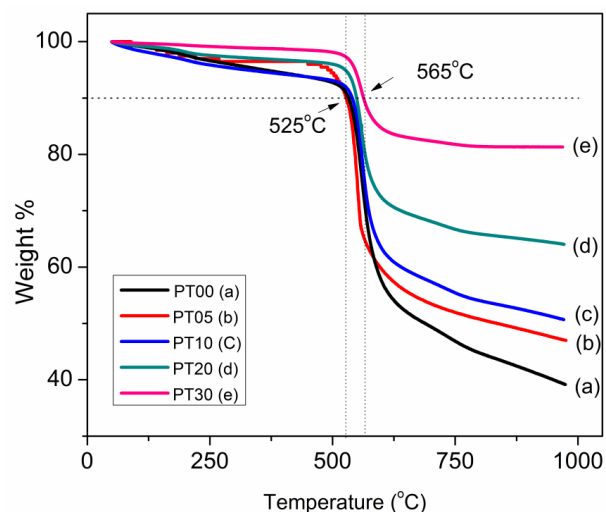
Figure 2.4: TGA of PAEK and PAEK/Ti_3SiC_2 composites under N_2 atmosphere

The DSC heating curves corresponding to all the composites are given in Figure 2.5(A). In DSC heating curves, two distinct thermal zones are seen. The first zone around 300 °C, where the polymer starts to soften, is designated as onset melting temperature (T_m^{on}). The second zone occurs in range 350-400 °C where the polymer completely melts and is designated as melting temperature (T_m). It was observed that the peak value, T_m is marginally increased with the addition of Ti_3SiC_2. The T_m of pure PAEK was increased by 1-2 °C on increasing the Ti_3SiC_2 loading. From the reported works, it can be inferred that the thermal properties of PEEK polymer composites largely depend upon the type of fillers, processing conditions

and matrix-filler interactions [Kuo *et al*. 2005; Goyal *et al*. 2006; Goyal *et al*. 2007a]. In the present work, even though there is no significant change in the T_m values, drastic change in the $T_m{}^{on}$ was observed with increase in V_f of Ti_3SiC_2. In pure PAEK polymer, the melting starts at 300 °C whereas, the PAEK reinforced with 0.3 V_f of Ti_3SiC_2, it starts at 344 °C. The melt temperature does not change unless a polymer is chemically modified at the molecular level. In this case, the Ti_3SiC_2 phase has only physical interaction with PAEK. The molecular nature of the polymer was unaffected. Therefore, much difference was not observed in the melting temperature. However, Ti_3SiC_2 filler particles can effectively retard the segmental movement of PAEK polymer chains thereby increasing the on-set melting of the composites. For all the composites, the corresponding DSC cooling curves are given in Figure 2.5 (B). PAEK is a semi-crystalline polymer and it usually crystallizes upon cooling. It was found that the Ti_3SiC_2 in PAEK enhanced the crystallization rate and there was a shift by 5 °C in crystallization temperature (T_c) at 0.3 V_f of Ti_3SiC_2. The same enhancement effect was also observed in onset crystallization temperature ($T_c{}^{on}$). There is an increase of 9 °C in $T_c{}^{on}$ when the filler amount was increased to 0.3 V_f.
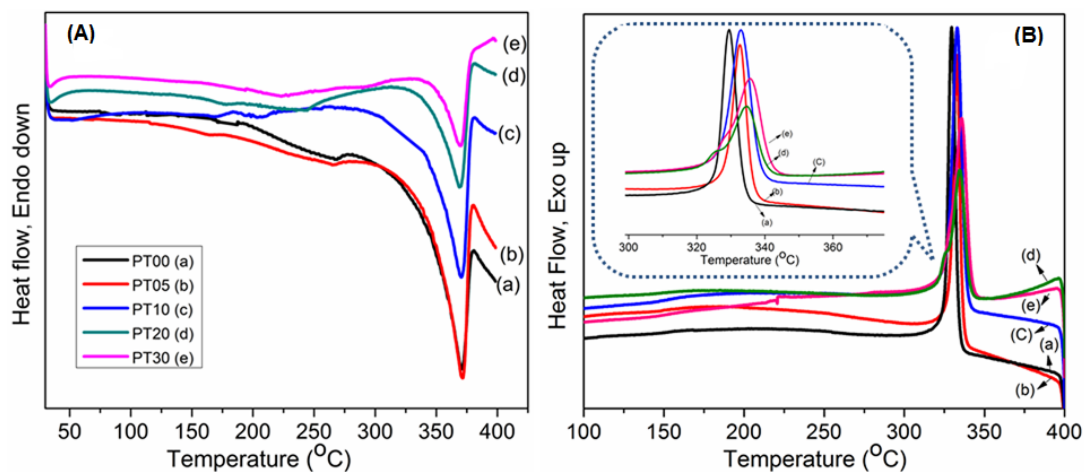
Figure 2.5: DSC heating (A) and cooling (B) curves of PAEK and PAEK/Ti_3SiC_2 composites

The overall thermal conductivity of a composite depends up on the intrinsic thermal conductivities of the matrix and fillers. Usually polymers show very low thermal conductivity which will increase when reinforced with ceramic fillers having fairly high thermal conductivity. In this work, thermal conductivities of the

composites in the temperature range 30-75 °C were measured using laser flash method and the results are depicted in Fig 2.6. The room temperature thermal conductivity and % enhancement in thermal conductivity with Ti_3SiC_2 loading are shown in Fig 2.6 (A). It was observed that the unfilled PAEK possess a thermal conductivity of 0.3 W $m^{-1}K^{-1}$. The thermal conductivity of bulk Ti_3SiC_2 is ~ 43 W $m^{-1}K^{-1}$ [Barsoum and El-Raghy 1996]. The addition of relatively high thermal conductive Ti_3SiC_2 fillers improved the thermal conductivity of the composites and this increase is more prominent with increase in filler loading. At room temperature, 3 times increase in thermal conductivity of PAEK matrix was observed with an addition of $0.3V_f$ of Ti_3SiC_2. At lower concentration of filler, the particles stay apart and the numbers of particle contact points are very low and therefore a minimal increase in thermal conductivity was observed. However, as the filler loading increases, the particles come closer and an effective thermal conductive path is created which resulted in enhanced thermal conductivity. Figure 2.6 (B) shows the temperature dependent thermal conductivity of the composites. It was observed that all the composites show slight increase in thermal conductivity with temperature.
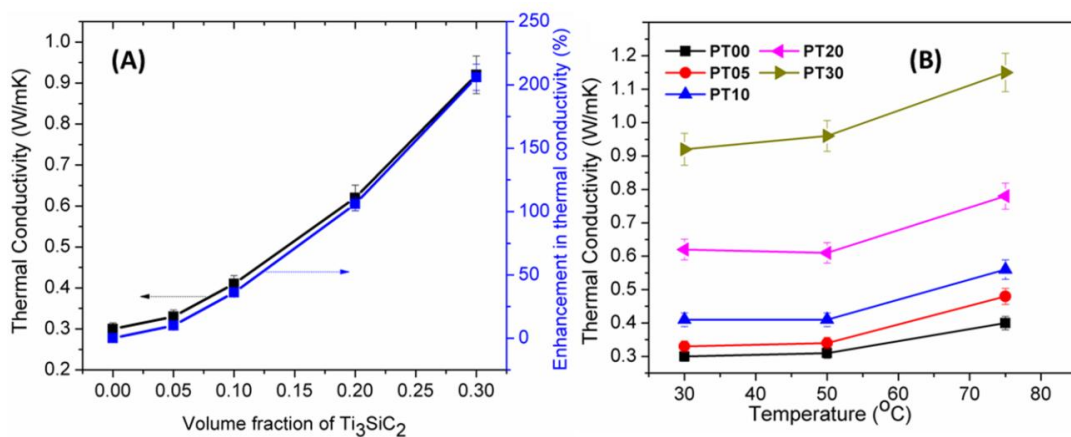
Figure 2.6: (A) Thermal conductivity values and % enhancement in thermal conductivity of PAEK/Ti₃SiC₂ composites at room temeprature and (B) Thermal condcutivity as a function of temeprature

Dimensional stability with temperature is very crucial while designing a structural material. The thermal expansion property of the hot pressed composites was studied by TMA and is given in Figure 2.7. It is observed that the linear expansion was largely reduced by the addition of Ti_3SiC_2. The CTE is showing a

sharp decrease with increasing amounts of Ti_3SiC_2. The unmodified PAEK shows a CTE value as $127 \times 10^{-6}/°C$ which was reduced to $79 \times 10^{-6}/°C$ by the addition of 0.3 V_f of Ti_3SiC_2. During hot pressing, the mechanically delaminated Ti_3SiC_2 particles randomly aligned in both lateral and horizontal directions within the PAEK matrix which preferably prevents the expansion of PAEK matrix. Moreover, decrease in PAEK V_f in the composite with respective filler loading might decrease the free volume of PAEK which in turn reduces the expansion. As discussed before, the ceramic fillers are well known to reduce the segmental movement of the polymer chains. This also contributes to the lowering of thermal expansion. In ceramic polymer composites, the ceramic particles are surrounded by tightly bound (constrained) polymer chains and loosely bound (unconstrained) polymer chains. With the addition of more reinforcement particles, unconstrained polymer chains get converted to constrained chains as a result of reduction in the inter-particle distance. The increase in volume of the constrained polymer chains retards the thermal expansion of the polymer composites [Tsagaropoulos *et al*. 1995; Goyal *et al*. 2007b]. It was reported that the bulk CTE of Ti_3SiC_2 is only $9.1(\pm 0.2) \times 10^{-6}/°C$ [Barsoum *et al*. 1999]. It is much less than the pure PAEK. This may also be a probable reason for reduction in CTE upon Ti_3SiC_2 addition.
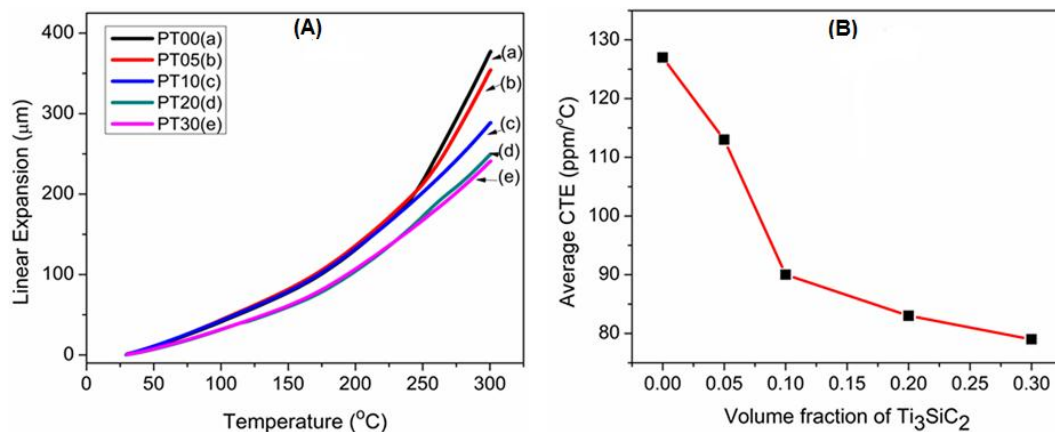
Figure 2.7: (A) Thermal expansion and (B) CTE curves of PAEK and PAEK/Ti_3SiC_2 composites

2.4.3 Mechanical Properties

The effect of Ti_3SiC_2 addition on microhardness of the composites was studied and the results are given in Figure 2.8 (A). It shows a linear trend with the V_f

of Ti_3SiC_2. However, only a marginal change in the hardness values is seen in the composites. The PAEK without any Ti_3SiC_2 has the hardness value of 35 Hv, whereas the same is 52 H_v when it was reinforced with 0.3 V_f of Ti_3SiC_2. The overall increase in the composite hardness is below 50%. As mentioned earlier, Ti_3SiC_2 is a metallic-ceramic with moderate Vickers hardness of 2-8 GPa [Barsoum *et al*. 2011] and is relatively soft than any other hard ceramics such as Al_2O_3, ZrO_2, SiC etc. In the present work, the mild increase in the hardness is only seen due to comparatively soft nature of Ti_3SiC_2. The representative indentation images are given as inset in Figure 2.8(A). It can be seen that the nature of the intender impression is almost same in their dimensions for both the PT00 (unmodified PAEK) and PT30 composites. Even though, the PAEK filled Ti_3SiC_2 shows enhanced hardness; it does not spoil the plastic nature of the parent matrix material. Usually, high hard ceramic reinforcements in soft-polymers like PAEK make them more brittle. In such cases, the crack initiation and propagation are clearly demonstrated at high loads. It is worth noticing that even at a high load of 19.6 N, the PAEK composite reinforced with 0.30 V_f of Ti_3SiC_2 (PT30) does not show any micro/macro cracks at the indentation site. The induced stress in composites is absorbed by the nanolaminated Ti_3SiC_2 sheets and the composite is plastically deformed. The moderate increase in the hardness does not affect the inherent soft nature of the PAEK.

Figure 2.8 (B) illustrates the flexural and compressive strengths of the PAEK with different Ti_3SiC_2 loading. It is observed that the composite flexural strength steeply increases as the amount of Ti_3SiC_2 in PAEK matrix increases. This might be due to the ductile Ti_3SiC_2 interface in the PAEK matrix. The increase in flexural strength is more when the composite contains above 0.1 V_f of the Ti_3SiC_2. Similar trend is also seen in compressive strength tests. The composite PT30 showed the maximum compressive strength. Ti_3SiC_2 is a material that deforms due to the net effect of kink band formation within the nanostructured interlayers. It possesses a compressive strength of 600 MPa and on varying the grain size the material fails gracefully, i.e. the material does not shatter [Barsoum *et al*. 2011]. In PAEK-Ti_3SiC_2 composites, the plastic deformation is controlled by the bridging ligaments and kink band formation by which the stress is either absorbed or deflected through the Ti_3SiC_2 interface and this causes delayed fracture. As a result, mechanical strength is

enhanced. Upon reinforcement, the ductile nature of the Ti_3SiC_2 reduces the tendency of brittleness in the bulk PAEK composites, which is not the case with other ceramic fillers. This is a unique benefit when such high damage tolerant Ti_3SiC_2 is used as reinforcement.
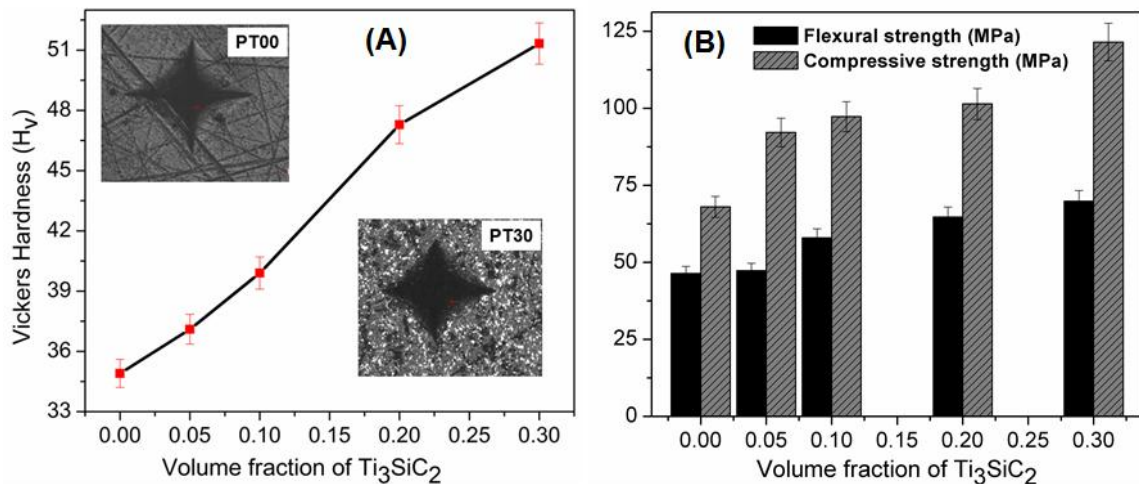
Figure 2.8: Mechanical properties of PAEK/Ti_3SiC_2 composites. (A) Microhardness (Optical images of the intendation mark for PT00 and PT30 are given as insets) and (B) flexural and compressive strength

2.4.4 Tribological Properties

Wear is one of the major hurdles in ensuring the reliability of materials. Wear causes the materials wastage and leads to the reduction in mechanical performance. So a reduction in wear by any means is envisaged as economically beneficial and help in substantial energy saving. Friction is the primary cause of wear. So ensuring lubrication and reducing friction is the preliminary step in preventing wear loss. However, adding external lubricating agents; solid or liquid lubricants are not economically viable and also not practically possible in certain applications. So a material with inherent lubricity is most preferred for applications ranging from household appliances to spacecraft.

In this work, the tribological performance of PAEK/Ti_3SiC_2 composites was assessed from wear and friction studies and the results are presented in Figure 2.9(A). It was observed that the friction coefficient, μ, decreases linearly with increase in Ti_3SiC_2 volume fractions. The PAEK without any Ti_3SiC_2 showed a μ value of 0.45 which was decreased to 0.33 in the composite PT30. This suggests that the

nanolaminated Ti_3SiC_2 is offering a sort of lubricating nature to PAEK polymer. The planar shearing of Ti_3SiC_2 layers possibly reduces friction. Normally, organic lubricants are applied for minimizing the friction between two surfaces during sliding. In this work, tribology was monitored in dry conditions. The following two events are only expected to occur. Firstly, both Ti_3SiC_2 and PAEK are soft and smooth in nature. In composites they offer the surface hardness of 52 H_v. When PAEK/Ti_3SiC_2 composite work specimen was abraded against EN 31 metallic base, possibly a composite atomic layer from the surface was forced to come out. Secondly, the abrasion always produces thermal heating during sliding. Under such micro thermal gradients, the PAEK polymer in the composite layers thermally softens. As a result, thermally stable Ti_3SiC_2 nanosheets are forced to embed and form a nano tribofilm. Formation of this sort of solid state lubricating film ultimately offers reduction in frictional force between the specimens and counter face material. Barsoum, a pioneer in MAX phase research, proposed that that Ti_3SiC_2 is reminiscent to graphite and can offer solid-lubrication character [Barsoum *et al*. 1996]. Zhang *et al.* studied the tribological properties of Ti_3SiC_2 against Ti_3SiC_2 and also between Ti_3SiC_2 and diamond by an oscillating pin-on-disc method with loads in the range of 1-10 N [Zhang *et al.* 2002]. The former couple showed a μ value of 1-1.5 and at the same time the latter showed $\mu \approx 0.1$. They proposed that low μ in the latter case was due to the formation of a lubricating tribofilm. This suggests that Ti_3SiC_2 can easily form tribofilm when abraded against hard surfaces. From the reported literatures, it is very clear that Ti_3SiC_2 shows a varying μ value depending upon the test conditions.

It is evidenced from the wear rate values that the PAEK wear rate was decreased with the V_f of Ti_3SiC_2. The wear resistance reaches maximum for the sample PT10 which corresponds to 0.10 V_f. A slight decrease was then observed for high Ti_3SiC_2 loadings. At such excessively high volume fractions, the Ti_3SiC_2 nanosheets align horizontally in the top-planar surface causing weak matrix–filler interaction that finally increases the wear rate. Still the wear rate is well below in PAEK-Ti_3SiC_2 composites than that in the unreinforced PAEK counterpart. The high thermal conducting characteristic of Ti_3SiC_2 plays a role in deciding the wear resistance. Such high thermal conductive ceramic fillers carry away the frictional

heat and reduce the chance of heat accumulation in the low thermal conductive PAEK matrix. The Ti_3SiC_2 surface atoms dissipate the frictional heat energy readily and decrease the wear. A strong matrix-filler interaction provides high thermally conducting interface network within the matrix which is responsible for the high thermal transport and increased thermal stability.
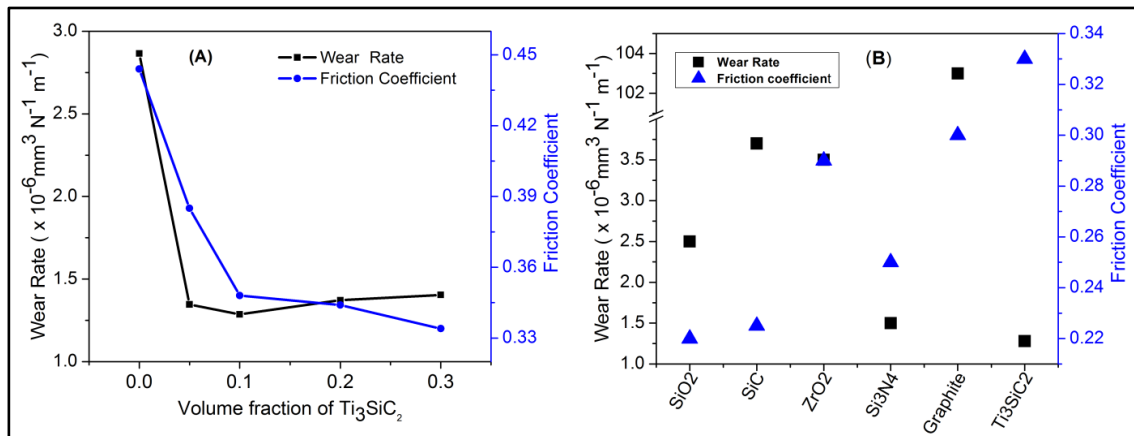
Figure 2.9: (A) Variation of coefficient of friction and wear rate of PAEK/Ti₃SiC₂ composites with filler loading. (B) Comparative plot of kinetic coefficient of friction and wear coefficient of various ceramic fillers (against steel ring hardened to 48-50 HRc) with the present study

For validating the tribological performance of PAEK/Ti_3SiC_2 composites, a comparison was made with known ceramic reinforcements like SiO_2, ZrO_2, SiC, and Si_3N_4 reported in various studies [Wang *et al.* 1997b; Wang *et al.* 1998; Wang *et al.* 1996; Xue *et al.* 1997]. Since Ti_3SiC_2 is very much reminiscent to graphite and PAEK composite with graphite was not studied and reported so far, we prepared a reference PAEK/graphite composite with 0.1 V_f of graphite so as to compare the wear and friction properties. All the results are presented in Figure 2.9 (B) for evaluating the comparable performance of Ti_3SiC_2. It was seen that the Ti_3SiC_2 has the lowest wear rate than any other filler. The coefficient of friction (μ) value is also close to other ceramic systems. When compared to graphite, Ti_3SiC_2 is shows approximately 100 times wear resistance with almost same μ value.

Further, the worn-out surfaces of PAEK-Ti_3SiC_2 composites were also analyzed by SEM and the images are given in Figure 2.10. It was observed from SEM images that the ploughed marks on the wear scar of pure PAEK are more severe than that of the composites. The samples prepared with 0.1 V_f of Ti_3SiC_2 (PT10), the

scuffing in the wear traces is very mild and less intense (Figure 2.10(C) and (D). There are also a few surface marks to understand the wearing of Ti_3SiC_2 nanosheets from the top-planar surface. This observation is in accordance with the wear rate result. In the composite PT30, the plough depth is less even though there is an evidence for the removal of material. Also, the wear traces confirm that the material was removed in layered manner. No significant pull-outs and deep pits are seen.
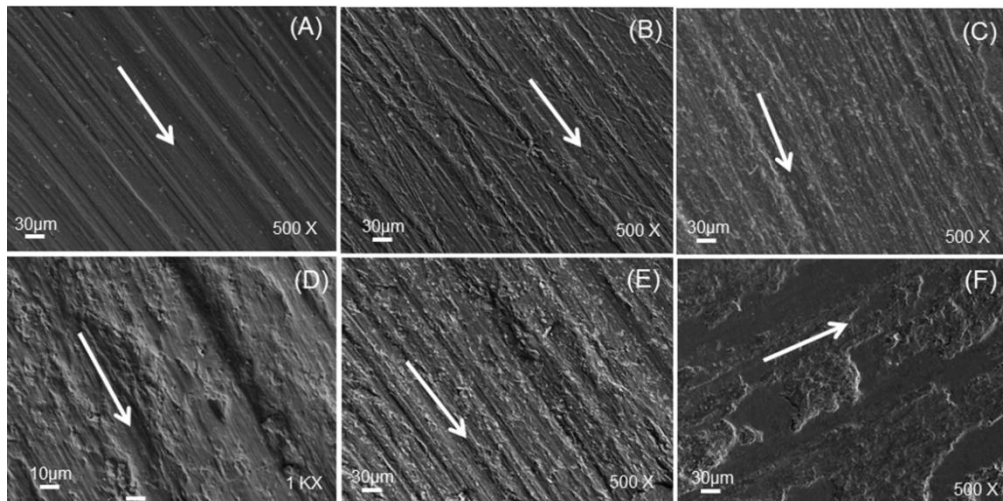
Figure 2.10: SEM images of worn surfaces of PAEK and PAEK/Ti$_3$SiC$_2$ composites with filler loading. (A) PT00 (B) PT05 (C) PT10 (D) high magnification image of PT10 (E) PT20 and (F) PT30. The arrow is showing the wear direction

This observation is further confirmed by recording the surface profile of worn out surface. The obtained surface profile is depicted in Figure 2.11. It is clear that wear scar in unmodified PAEK is deeper than that of composites. PT10 possesses the lowest wear depth among all the composites, confirming that the wear resistance is more with an optimum composition of 0.1V$_f$ of Ti$_3$SiC$_2$. It is also noticed that there was a continuous decrease in the coefficient of friction with respect to the volume fraction of Ti$_3$SiC$_2$. It is also observed that the debris mainly contains Ti$_3$SiC$_2$ which possibly stays on the wear track and acts as a third body solid lubricant and forms a tribofilm that finally reduces the coefficient of friction. This can be the reason for this composition to show lower μ value despite of its high wear rate. The XRD spectra of the debris collected after test was recorded and is given as Figure 2.12. It confirms that the debris mainly composed of Ti$_3$SiC$_2$ along with small amount of PAEK particles. No peaks for oxides of Ti or Si observed. This suggests a low frictional heat production during sliding and is beneficial in preventing the

oxidation both surfaces. Also the counter surface was protected from erosion as evidenced by the absence of any iron oxide peaks in XRD.
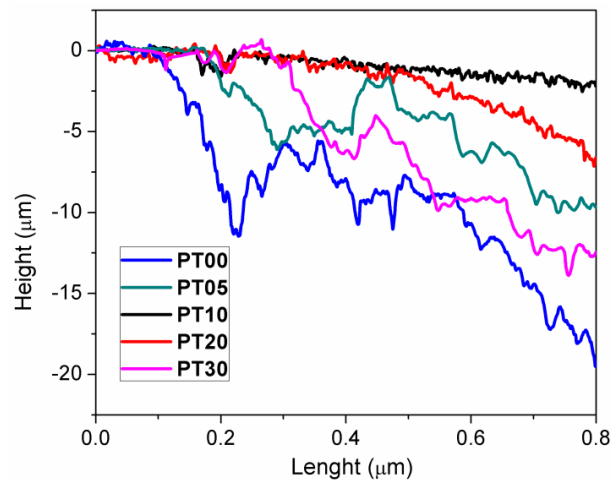
Figure 2.11: The surface profilometer curves of the worn-out surfaces of the PAEK and PAEK/Ti₃SiC₂ composites
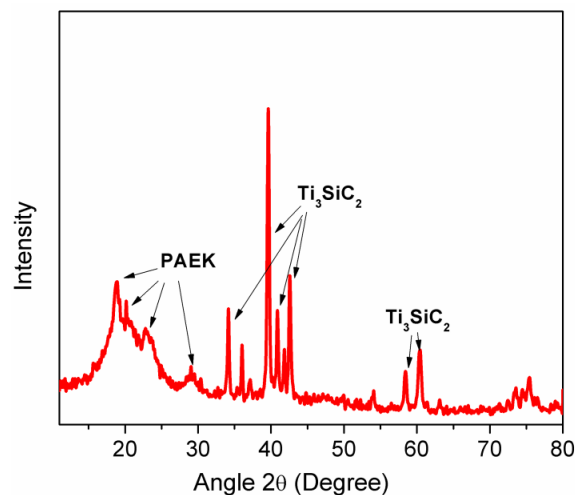
Figure 2.12: XRD spectrum of the debris collected after wear test

2.4.5 Machinability of the Composites

For any engineering applications, a machinable composite have added advantage since it can be made in to any complex shape without much difficulty. Polymers are generally machinable whereas ceramics are not. The incorporation of conventional ceramics in polymer matrix usually destroyed their inherent machinability. On the other hand, MAX phases are differing from other ceramics owing to its remarkable machinability. So it was envisaged a good machinability for PAEK-Ti₃SiC₂ composites. The machinability of the composites developed in this

work was tested by making a hole of 5mm diameter on a 40 mm diameter block made with PT20 composite, using conventional metallic drills. The results are as expected and the photograph of the machined composite is shown in Figure 2.13. A cleanly drilled hole with no scale cracking or chipping was easily made. This experiment shows that the addition of Ti_3SiC_2 do not spoiled the inherent machinability of PAEK polymer. To our surprise, PT20 composite showed machinability better than pure PAEK. Some micro level chipping was observed around the hole-edge in pure PAEK whereas the hole was perfect for the sample PT20.
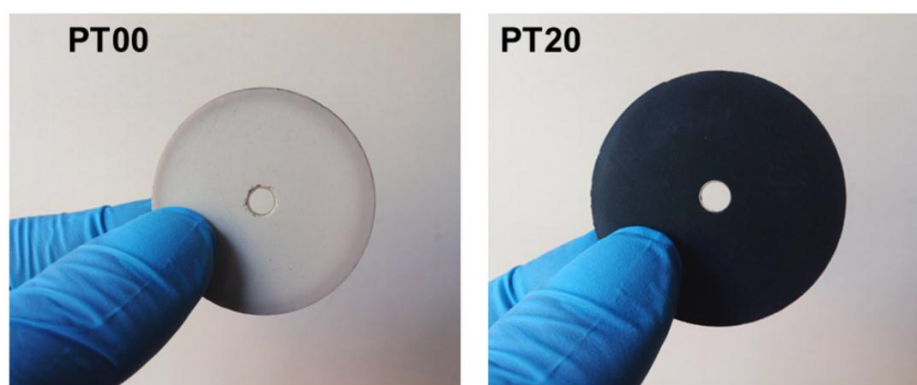
Figure 2.13: A perfect hole drilled on the 40 mm diameter composite block by a metallic tool (x = 0.2). Pure PAEK (Left) and PAEK-Ti_3SiC_2 composite (right)

2.5 Conclusions

A novel MAX phase nanolaminate was employed as multifunctional reinforcement for the first time to obtain thermally stable, low friction, low wear PAEK polymer composite without compromising the inhererent machinability. The beneficial properties realised with Ti_3SiC_2 nanolaminates include increased thermal decomposition and recrystallisation temperature, at least 50% enhancement in the mechanical hardness, flexural and compressive strengths and ~40% reduction in the thermal expansion values. The PAEK-Ti_3SiC_2 composites showed progressive wear resistance and low coefficient of friction suitable for developing thermo-mechanically stable engineeirng components. The formation of solid-lubrication tribofilm by Ti_3SiC_2 nanolaminates was a probable mechanism in enhancing the tribological performance.

CHAPTER 3

MAXene: A New 2D Material
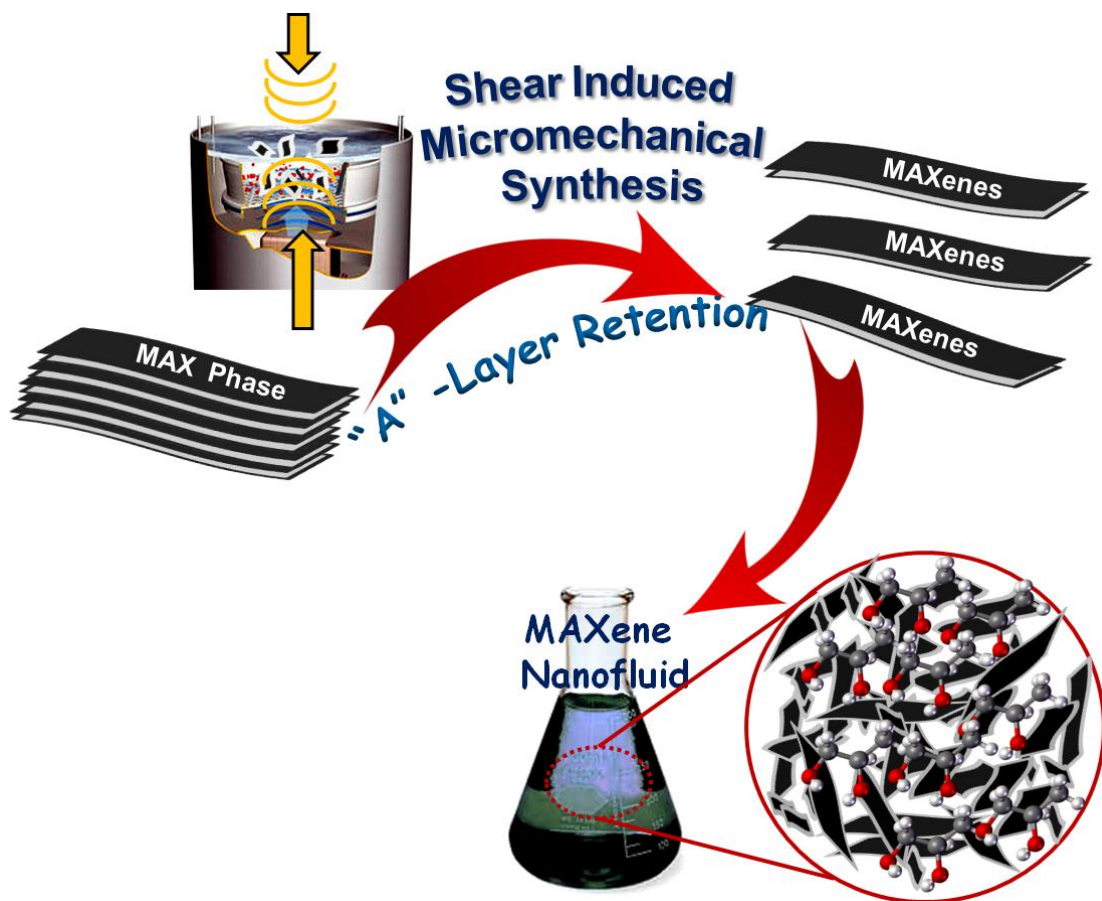
3.1: Shear Induced Micromechanical Synthesis of Ti$_3$SiC$_2$ MAXene Nanosheets for Functional Applications

3.1.1 Abstract

Herein, we report the synthesis of ultrathin 2D Ti$_3$SiC$_2$ (MAXene) nanosheets via a facile shear induced micromechanical cleavage strategy. The very high dispersion stability, the UV absorption properties, high electrical conductivity and castability into thin films makes the newly derived Ti$_3$SiC$_2$ nanosheets, an ideal candidate for many functional applications.

3.1.2 Introduction

The discovery of graphene and its unique nanostructures *via* mechano-chemical/sonication techniques triggered interest in the processing of similar kinds of 2D nanolayered materials *via* any novel strategies [Novoselov *et al.* 2005]. Recently synthesis of 2D nanostructures from metal chalcogenides (MoS$_2$, WS$_2$ etc.), BN, and double layered hydroxides have been successfully demonstrated through exfoliation of their 3D counterparts [Deepesh *et al.* 2014; Joensen *et al.* 1986; Seo *et al.* 2007; Miremadi *et al.* 1988; Pacile *et al.* 2008; Zeng *et al.* 2012]. These materials garnered great attention because they showed enhanced optical, thermal, mechanical and electrical properties compared to their bulk counterparts. They have been suggested for the applications in thermal fluids, light emitting diodes, super capacitors, thermoelectricity, Li-ion batteries, and also as reinforcements in composites [Yang *et al.* 2013; Soon *et al.* 2007; Song *et al.* 2007; Reynolds *et al.* 2003; Heising *et al.* 1999; Feng *et al.* 2009; Dresselhauset *et al.* 2007; Chunyi *et al.* 2011; Jaime *et al.* 2012].

As we discussed in chapter 1, now MAX phase also started getting 2D as well. Unlike graphene, MAX phase materials are composed of two type layers formed by three types of atoms and this opened up the door to get two types 2D MAX phase. One is by retaining all the atoms, and the other is by removal of A layer atoms. The latter one end up in MX phase. Very recently, Naguib *et al.* demonstrated an experiment to obtain 2D MX layers by selective etching of Al atoms from the selected

MAX phase material [Naguib *et al.* 2011; Naguib *et al.* 2012a]. This newly derived materials were named as MXenes to spotlight their similarity with graphene. Further, MXenes are explored for the applications in Li-ion batteries, Lead ion absorption, and photo catalysis [Xiaohong *et al.* 2013; Qiuming *et al.* 2013; Mashtalir *et al.* 2014; Naguib *et al.* 2012b]. However, the method proposed by Naguib *et al.* is success only when A layer is Al atoms. The loss of A elements from the crystal structure can probably alter the intrinsic properties of MAX phases.

A relatively strong inter atomic-bonding between MX and A layers of MAX phase makes the simple exfoliation techniques inappropriate for the delamination of the nanolayers into a single MAX phase nanosheets. Recently, Zhang *et al.* synthesized ultrathin nanosheets of MAX phases by substitutional solid solution method [Zhang *et al.* 2013]. They fabricated doped phases $Ti_3Si_{0.75}Al_{0.25}C_2$ and $Ti_3Al_{0.9}Si_{0.1}C_2$ by high-temperature self-propagation synthesis and ultrasonically exfoliated these phases which finally ended up with the same composition as the parent MAX phase i.e with two types of A atoms. Also the bulk level synthesis is very difficult by this methods. To the best of our knowledge, the preparation of phase pure MAX phase nano sheets is yet to be reported. Herein, we attempted a modified micromechanical cleavage strategy for obtaining single phase 2D MAX phase nanosheets. The newly processed nanosheets were named as MAXenes to highlight their 2D morphology. Micromechanical cleavage is reported to be a successful technique for the exfoliation of MoS_2, BN, $NbSe_2$, $Bi_2Sr_2CaCu_2O_x$, and graphite [Novoselov *et al.* 2005]. In these materials, a simple rubbing technique was used to delaminate the layered structures. Unfortunately, adopting such technique directly gives great failures, and delamination of MAX phase is not seen. Among the various properties discussed in chapter 1, we have seen that the weakest strength of MAX phase is its shear strength. Application of shear force for a long time may result delamination of layers at the kink band. Therefore by utilizing this property, we put forward this new idea, shear-induced micromechanical cleavage, wherein a simultaneous application of compressive and rotational shear force along with mechanical grinding in order to induce shearing of MAX phase layers. To the best of our knowledge, this is the first report on such shear-induced micromechanical cleavage for exfoliated MAX phase nanosheets.

3.1.3 Experimental Details

3.1.3.1 Synthesis of Nanosheets of Ti₃SiC₂ MAXenes by Micromechanical Cleavage Technique

Micronic Ti_3SiC_2 particles having an average size of 13 μm were procured from the 3-ONE-2 company, USA. Micromechanical milling was performed using Ultra-Fine mortar grinder (Retsch-RM 200, Germany) which works on pressure-friction principle. It consists of a mortar, pestle and a scraper. The role of the scraper is to feed the material in the area between the pestle and mortar. N,N Dimethyl formamide (DMF, Spectrochem, India), N-methyl pyrolidinone (NMP, Spectrochem, India) and distilled water were used as the solvent bath. Ti_3SiC_2 was first dispersed in 15 mL polar solvents. A highly polar chemical medium was employed based on a reason to prevent a reverse agglomeration of the exfoliated nanostructures which is critically important. In order to compensate for the natural evaporation of solvent, its level was maintained by the addition of small fractions of solvent during milling. The temperature was also monitored periodically to know the thermal-heating during milling. The dispersion after 24 h milling was then ultrasonicated for 1 h using ultrasonic processor (Sonics Vibra Cell, 20 kHz). The milled dispersion was then centrifuged at 8000 rpm. Finally, a nanodispersion of exfolaited Ti_3SiC_2 nanosheets was obtained and was characterized for the physical morphology, crystallinity, and chemical stoichiometry.

3.1.3.2 Characterization

Powder X-ray diffraction (X'Pert Pro, Philips X-ray diffractometer) with a monochromator on the diffraction beam side (Cu Kα radiation, λ=0.154 nm) is used for analyzing the crystalline nature. Crystallite size was calculated by Scherrer's formula:

D_{XRD}= 0.9λ/ β cosθ

where λ is the X-ray wavelength, θ the Bragg angle and β the full-width at half-max.

The microstructure of bulk TSC before exfoliation was recorded using ZEISS EVO 18 Scanning Electron Microscopy (SEM). Transmission Electron Microscopy (TEM) and high resolution TEM (HRTEM) images were carried out using FEI Tecnai 30G2S-TWIN, operated at an accelerating voltage of 300 kV, and coupled with EDAX

facility. The zeta potential value was measured using Malvern Zetasizer 3000H. The stability of the MAXene dispersion was monitored with a Nephelometer (CL 52D, ELICO) by measuring the intensity of transmitted visible light through the fluid against time. The surface chemistry of the exfoliated MAXene nanosheets was examined by X-ray photoelectron spectroscopy (XPS) using SPECS GmbH spectrometer (Phoibos100MCD Energy Analyzer) with Mg Kα radiation (1253.6 eV) as the excitation source. The peak of C1s at 284.6 eV was taken as the reference energy position. UV/Vis spectrum of the TSC dispersion was recorded with spectrophotometer Shimadzu (UV 240 IPC). The resistivity of the green pellets was measure by standard spring loaded pressure contact four probe conductivity meter, Keithley 6221 DC current source and 2182 A nanovoltmeter at 30 °C.

3.1.4 Results and Discussion

Figure 3.1.1 depicts the present strategy wherein we explained the simultaneous application of compressive and rotational forces, one in parallel, and another in the perpendicular direction to the basal planes for the exfoliation. Application of shear-induced mechanical grinding within a chemical bath is found to be quite successful to design 2D MAX phase nanostructures.
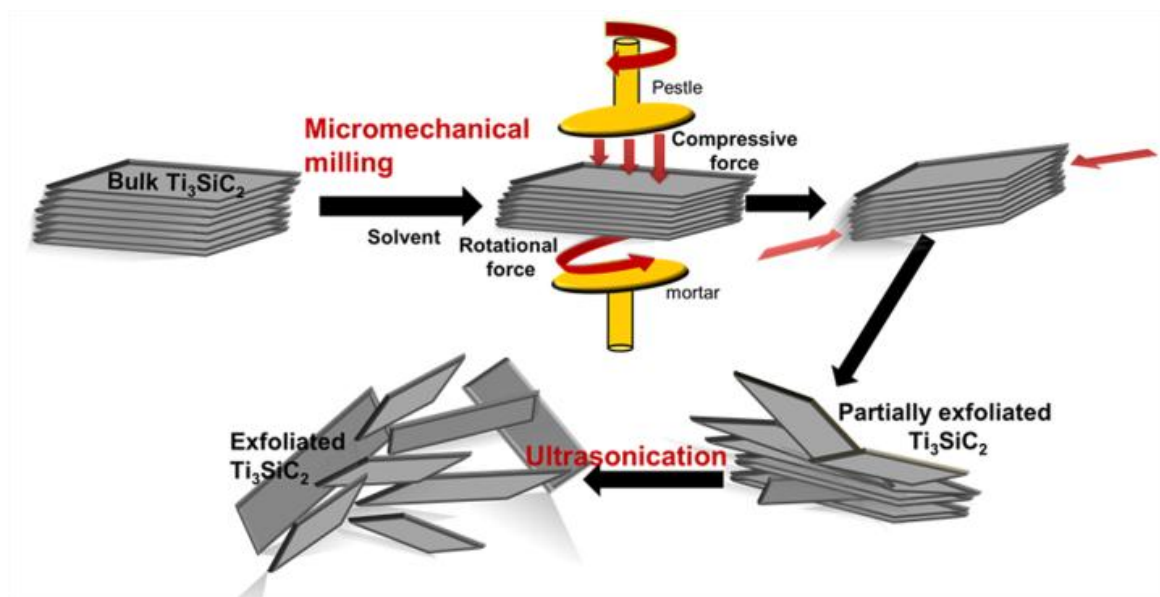
Figure 3.1.1: Schematic representation of the synthesis procedure to obtain ultrathin MAXene nanosheets using shear induced micromechanical cleavage technique

In a dense MAX phase bulk material, mechanical deformation is studied systematically, and said to be mediated by anisotropic basal dislocations which resulted in partial delaminations, and produce lamellas with a few tens to hundred nanometers thickness [Barsoum *et al.* 2004]. However, mechanical delamination in micrometer size MAX phase particles in the presence of prolonged shear force is not documented before. Herein, we have investigated the effect of shear induced micromechanical delamination of micronic Ti_3SiC_2 (hereafter denoted as bulk TSC) MAX phase and examined the evolution and properties of exfoliated nanostructures (hereafter denoted as MAXene nanosheets). The nanolayered ternary transition metal carbides consist of M-X slabs interleave with A atom layers. In Ti_3SiC_2, Ti-C slabs are intercalated with planar packed Si layers. Ti and C atoms are connected through strong covalent bonds, which are mechanically rigid. On the other hand, the Ti-Si bonds are relatively weaker than Ti-C bonds, and are prone to compression, and stretching under shear deformation [Jingyang *et al.* 2009; Barsoum *et al.* 2011]. These characteristics favours easy basal plane slip and offer low shear deformation resistance. The ab initio calculations reported by Medvedeva *et al.* also support the weak coupling between Ti_3C_2, and Si layers [Medvedeva *et al.* 1998]. However, the bond strength between Ti-C and Si layers is not as weak as in the case of graphite, and its analogues, where weak van der Waals force holds the layers together [Deepesh *et al.* 2014; Zhi *et al.* 2009]. A simple ultrasonication can mechanically break the weakly bonded graphite layers and produce freestanding individual graphite sheets. However, such a technique is inadequate to cleave the covalently bonded TiC-Si layers. Application of directionally varied shear force is expected to show advantages in shearing or the cleavage of the stacked nanolayers.

Retsch mortar grinder offers provision for applying both pressure, and friction simultaneously. In Retsch grinder, ceramic mortar is rotating at a speed of 100 rpm, and ceramic pestle can induce constant mechanical pressure. The pestle is situated not in the center of the mortar, but is offset. Mortar and the pestle rotating in opposite directions (pestle in clockwise and the mortar in anticlockwise directions) caused friction and compressive forces upon the bulk TSC particles dispersed in polar solvents. During grinding, the compressive and frictional forces resulted in mechanical shearing along the TSC basal planes. Each contact point of

the pestle and mortar acted as micro-scale cleavage points. Ultimately shearing occurs effectively in bulk TSC nanolayers. The polar medium helps to keep the separated or partially delaminated nanolayers in colloidal range from the micronic parent particle.

3.1.4.1 Morphological Features of the Ti$_3$SiC$_2$ MAXene Nanosheets

The electron microscopic images of the TSC particle observed before, and after micromechanical cleavage clearly show different morphological features, and the same are presented in Figure 3.1.2. The SEM image in Figure 3.1.2 (a) shows the morphology of bulk TSC material before micromechanical cleavage. The stacking of multiple numbers of TSC nanolayers is apparently seen in the SEM image.
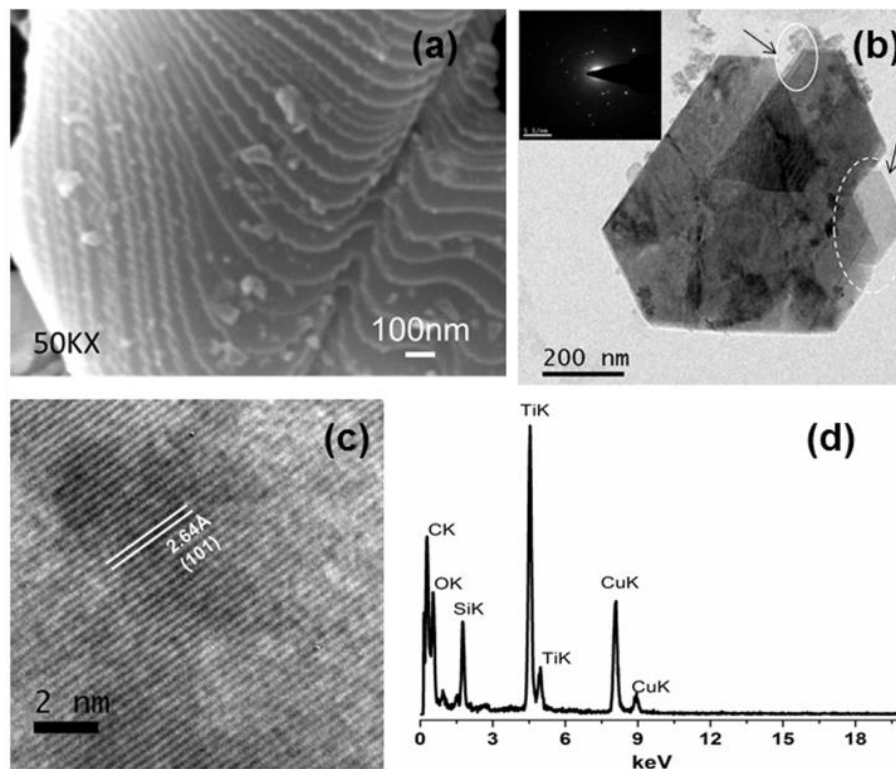
Figure 3.1.2: The morphological features of bulk and exfoliated MAXene nanosheets (a) SEM image of bulk TSC (b) TEM image of exfoliated MAXene nanosheets (c) HRTEM image of exfoliated MAXene nanosheets showing respective lattice spacing and (d) corresponding EDX spectrum.

Figure 3.1.2 (b) gives the representative TEM morphology of exfoliated MAXene nanosheets. This clearly confirms the effective exfoliation of TSC stacks into ultrathin TSC nanosheets. The microstructure of the exfoliated MAXene nanosheets consist only few layers. Single layered (dotted white circle) sheets are also clearly

identified in the micrograph. The SAED pattern of the corresponding image is given as inset in Figure 3.1.2 (b) that confirms the crystalline nature of the exfoliated MAXene nanosheets. Figure 3.1.2 (c) represents the corresponding high resolution TEM (HRTEM) image, which reveals the (101) plane of single MAXene nanosheets, indicating that nanosheets exposed the XZ plane. It is clear from the TEM images that the exfoliated MAXene nanosheets possess sheet length lower than its bulk counterpart. The dimensional decrease in nanosheets is obvious due to the grinding effect where particle size reduction is expected. Other than this, the formation of micro-scale kink bands may also be expected during mechanical deformation. The kink band is reported to obstruct the propagation of delamination in MAX phase materials, and prevent the full-scale delamination of the particle [Barsoum *et al.* 2004]. However, the continuous application of shear force for longer hours resulted in micro scale peeling of nanostacks at the kink junctions that finally yielded delaminated nanosheets.
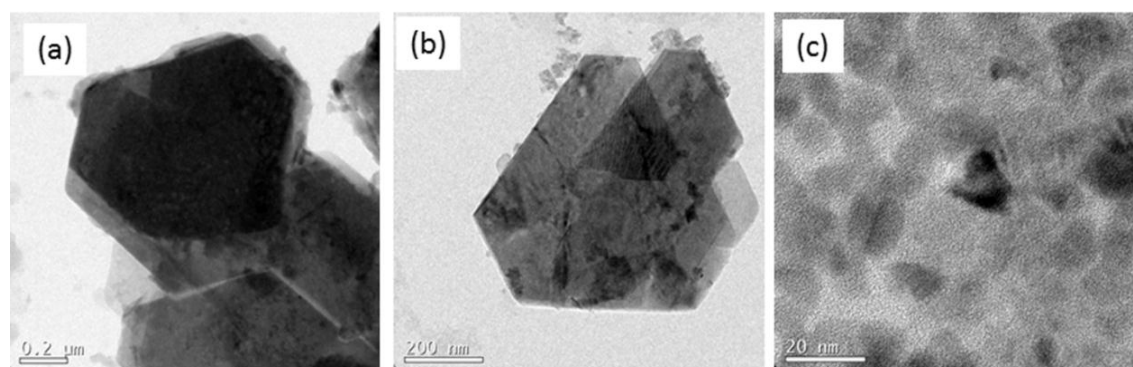
Figure 3.1.3: TEM images of MAXene nanosheets obtained after micromechanical milling time of (a) 12h, (b) 24 h, and (c) 30h

In oder to understand the role of milling time on morphology of the MAXene nanosheets, we performed the experiments at 12 h and 30 h aslo. The TEM images of the products obtained after various milling time is depicted in Figure 3.1.3. It was observed that the product obtained after 12 h milling consists of partially delaminated large sheets with relatively large number of layers, and that of 30 h consists of ultrasmall(~10 nm) sheets resulted by breakdown of nanostructures due to excessive milling. The EDX spectrum (Figure 3.1.2 (d)) shows the chemical composition of exfoliated MAXene nanosheets obtained by 24 h milling. It confirms that the stoichiometry is identical to that of the bulk TSC. However, the presence of

trace amounts of surface oxygen is also evident. It is envisaged a microthermal heating during mechanical milling that can cause atomic-level oxidation.

3.1.4.2 Role of Solvent on Exfoliation

In this work high boiling point solvents are used for the exfoliation to avoid evaporative loss of solvents during milling for extended hours. It was observed that the exfoliation is comparatively effective in polar solvents. We also conducted the identical experiments in non-polar solvents such as toluene, and o-dichlorobenzene (o-DCB) to understand the role of polarity in exfoliation efficiency. Photographs showing the stability of MAXene dispersion in diffrent solvents are shown in Figure 3.1.4. In non-polar medium, the particle settling is repeatedly observed. Whereas, the nanolamellar bulk TSC delaminated effectively in polar solvents and formed a stable MAXene dispersion. In fact, it is a surprise to see the dispersion is stable even after four months duration. Figure 3.1.5 (a) shows the dispersion stability of MAXene nanosheets processed at different particle concentrations in DMF medium over a period of 100 days. It is noticed that the stability of MAXene exfoliates is irrespective of the concentration. It is likely that the extensive milling in polar medium generates chemically identical charged surface functional groups on the nanosheets which in turn give stability *via* long range attraction or short range repulsive force by the interaction with the polar groups in the solvent. This was confirmed by measuring the zeta potential of the MAXene dispersion using the Malvern Zetasizer. The MAXene exfoliates in DMF is found to have a zeta potential value of ~ -29.2 mV. Whereas, the same for bulk TSC is only ~ 0.08 mV. A surface hydroxylation is expected because the mechanical milling in polar solvents was carried out in the open atmosphere. The extended milling time given for the effective dissemination generated a temperature of ~ 60 °C and such micro-thermal effect is the probable reason for the surface –OH group formation. This surface -OH layer is helping the nanosheets to form a stable dispersion in polar solvents. Probable interaction with the polar groups of solvent with the oxide layer may be the reason for extended stability of the MAXene nanosheets in polar solvents.

Figure 3.1.5 (b) confirms further the typical Tyndall effect which is observed by allowing the laser beam to pass through the MAXene dispersions prepared with different solid concentrations. The photographs in Figure 3.1.5 (b & c) taken at an

angle perpendicular to the direction of the laser beam is clearly showing a well intense Tyndall effect in both dilute as well as concentrated dispersions. The dilute dispersion is physically transparent which ascertains that the MAXene exfoliates have ultrathin dimensions. In order to check the aggregation property of the MAXene dispersion, turbidity values were recorded using Nephelometer for a period of three months at 15 days interval. The turbidity values shown in Figure 3.1.5 (d) does not show any significant change with time, confirming that there is no agglomeration occurring in nano dimensional MAXene dispersions, and are very stable without any settling of nanosheets.
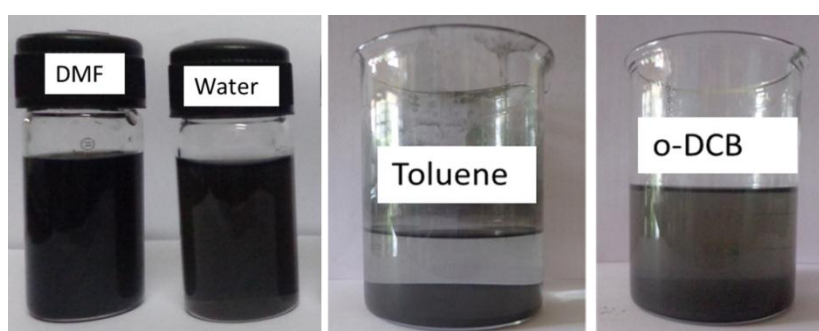
Figure 3.1.4: Photographs showing the stability and extent of exfoliation in different solvents.
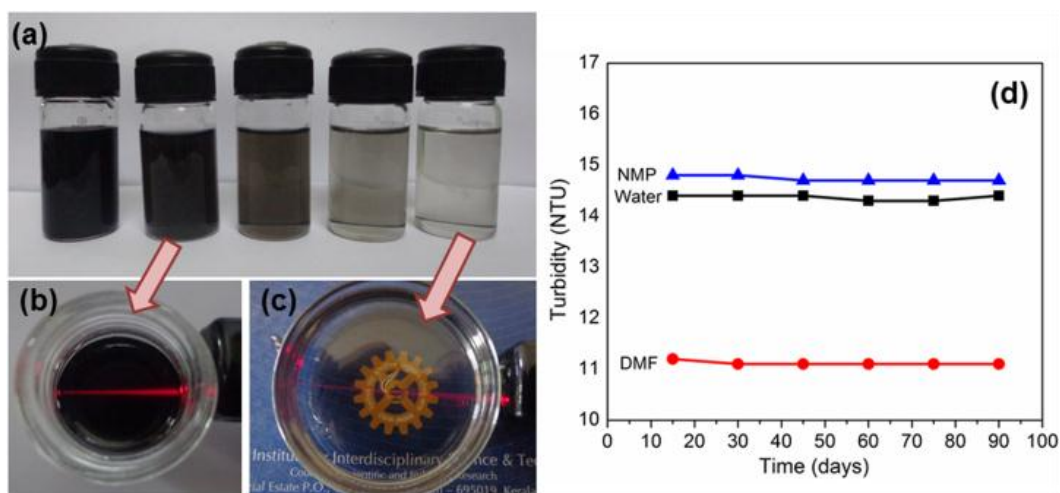
Figure 3.1.5: MAXene nanosheets prepared in DMF medium *via* micromechanical cleavage. The photographs of the (a) dispersion of MAXene nanosheets at different concentrations, (b) & (c) Tyndall effect shown by the dispersions, and (d) the turbidity values of the dispersions showing the stability in various polar solvents.

3.1.4.3 Structural Analysis Using Powder X-Ray Diffraction

Figure 3.1.6 depicts the powder X-ray diffraction patterns of the bulk TSC before and after micromechanical exfoliation. The XRD pattern indicates a change in the crystallinity of the TSC upon exfoliation. The intense, high order peaks correspond to the planes (006), (008), (107), (108), and (109) present in the bulk TSC are disappeared during exfoliation, indicating the occurrence of delaminated TSC nanolamellar superstructure. As expected, the peaks are also broadened and down shifted to lower angles with a slight increase in the c lattice parameter. The crystallite size of the delaminated MAXene nanosheets was calculated by the well-known Scherrer equation and it was noticed that the crystallite size is reduced to ~13 nm upon exfoliation from the bulk crystallite size of ~ 60 nm.
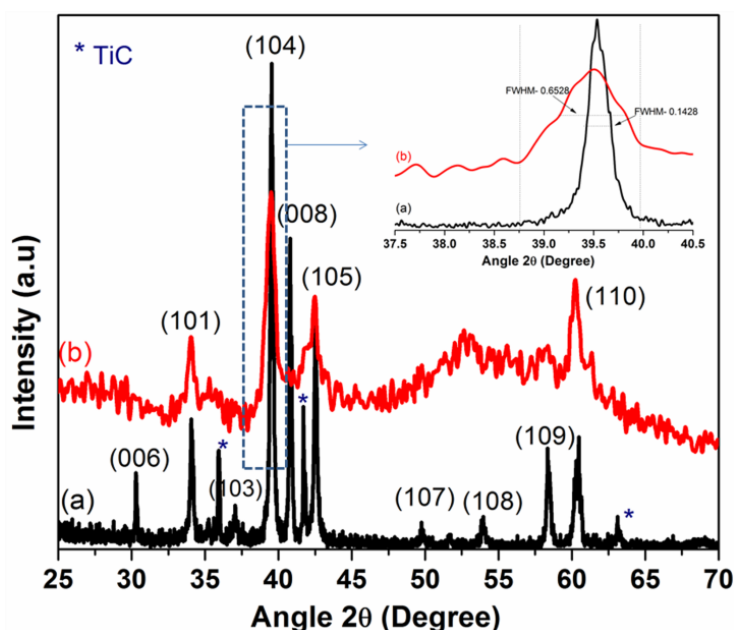
Figure 3.1.6: The powder X-ray diffraction patterns of TSC before (a) and after (b) micromechanical cleavage. The broadening of the peaks on exfoliation is shown in the inset.

3.1.4.4 Surface Analysis Using X-ray Photoelectron Spectroscopy

The surface chemical compositions of the MAXene nanosheets were examined by X-ray photoelectron spectroscopy (XPS), and the spectra are given in Figure 3.1.7. It supports strongly the atomic level oxidation of TSC during milling. The survey spectrum (Figure 3.1.7(A)) reveals that the surface of MAXene nanosheets consist of Ti, Si, and C atoms along with O atom.
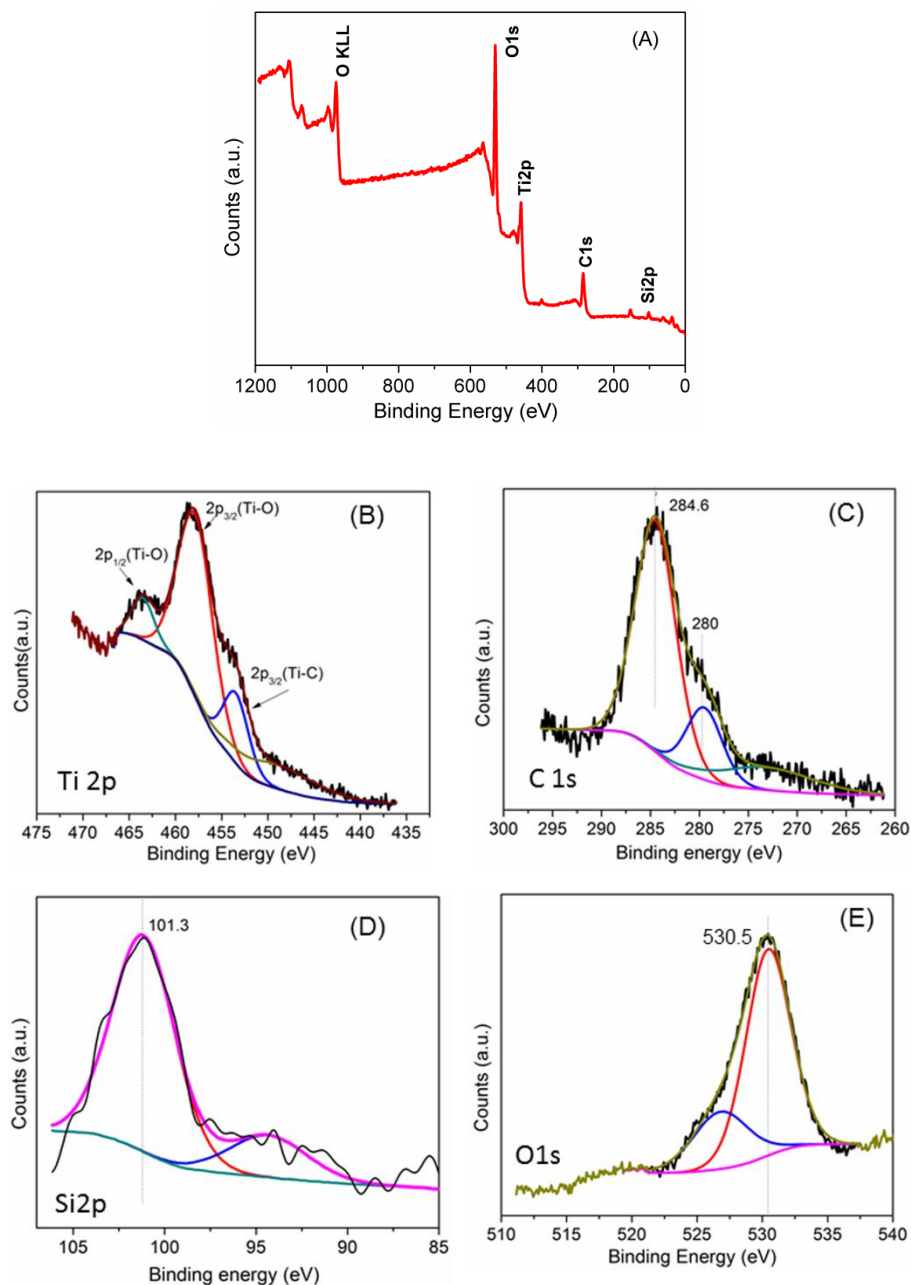
Figure 3.1.7: XPS of exfoliated MAXene nanosheets. (A) The survey spectrum showing all the elements present on the surface and high resolution spectra of (B) Ti 2p, (C) C 1s (D) Si 2p, and (E) O1s.

The high resolution spectra of Ti, Si, and C indicate a deviation from the surface chemical composition reported earlier for the bulk TSC [Myhra *et al.* 2001; Kisi *et al.* 1998]. As evidenced from the high resolution XPS spectra of Ti 2p (Figure 3.1.7(B)), that the O contribution mainly comes from the TiO_x fractions. The peak at *ca.* 458.2 eV and 463.6 eV corresponds to the Ti-O bonds [Sordello *et al.* 2014]. The peak at 454 eV represents carbide contribution from Ti-C bonds [Kisi *et al*. 1998].

The C1s spectra (Figure 3.1.7(C)) indicate the existence of graphitic carbon (ca. 284.6 eV) and carbide contribution (*ca.* 280 eV) which is identical to the values seen for the bulk TSC. The presence of SiO_x was also identified by the peak at *ca.* 101 eV in the Si2p spectra. The O1s spectra (Figure 3.1.7(D)) represents that the oxide contribution from M-O (M= Ti, Si) bonds. The absence of metal oxide peaks corresponding to TiO_2 and SiO_2 in the powder X-ray pattern (Figure 3.1.7(E)) suggests that the functionalization occurs only at the surface and not in the bulk of the TSC nanosheets.

3.1.4.5 UV-Visible Spectroscopy

It was noticed that the exfoliated MAXene nanosheets possess UV absorption properties. UV/visible absorption spectra of the as exfoliated MAXene dispersion prepared in DMF medium is given in Figure 3.1.8. It is clear from the spectra that the bulk TSC has no absorption in the UV/visible region, whereas the exfoliated TSC nanosheets exhibit high absorption in the UV region with an onset absorption at 410 nm with a strong band centered at 290 nm. This corresponds to band gap energy of 3.05 eV. It suggests that the exfoliated TSC nanosheets are becoming semiconducting in nature. The spectrum is reminiscent to that reported for graphene oxide (Zhang et al. 2010). The presence of surface TiO_x groups can probably contribute to the UV absorption at $\lambda< 400$ nm. It is important to note that these are only preliminary results and further studies are required before understanding this property.

Separation of the exfoliated MAXene nanosheets from the DMF medium is a trivial task as in the case of most of the 2D materials, because the separation by simple evaporation results in restacking of layers. In the present work, we have successfully extracted the exfoliated MAXene nanosheets from the solvent by precipitation with chloroform, a less polar volatile solvent. On dilution with excess chloroform, the nanosheets settle at the bottom. The decantation of the solvent followed by freeze drying gives the MAXene nanosheets devoid of restacking. The different stages of this method are shown in Figure 3.1.9 (A). It was also noticed that the exfoliated MAXene nanosheets can be easily compressed into definite cylindrical pellets which is difficult in 2D graphene and SWCNTs. The photographs of the green

pellets are given in Figure 3.1.9 (B). The exfoliated MAXene possesses a good green strength than bulk TSC.
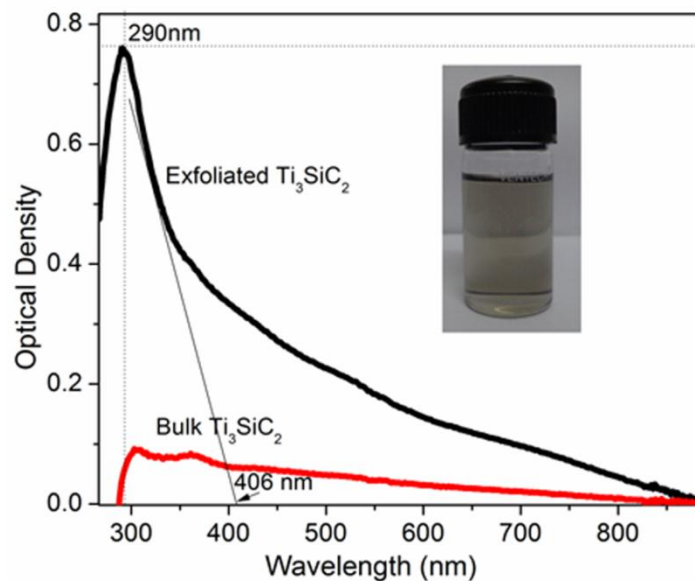
Figure 3.1.8: UV-Visible spectra of bulk TSC and exfoliated MAXene nanosheets in DMF
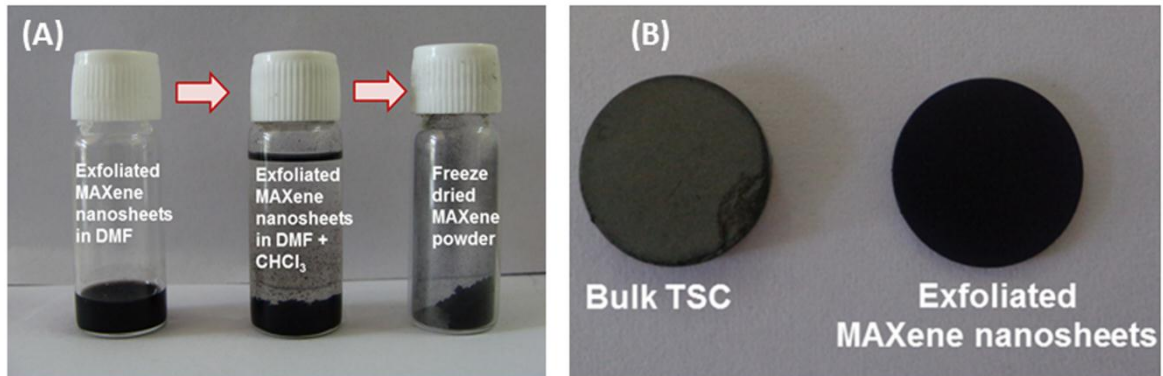
Figure 3.1.9: Photographs showing (A) the easy extraction of exfoliated MAXene nanosheets from dispersions using solvation technique, and (B) the green pellets of bulk Ti$_3$SiC$_2$ as well as exfoliated MAXene nanosheets.

The resistivity and conductivity of the exfoliated MAXene nanosheets compressed into a cylindrical disc of thickness < 1 mm and a diameter of 10 mm are given in Table 3.1.1. It is worth to note that the resistivity values mentioned in the table is not exactly the value of a single MAXene layer but a bulk resistivity of the green compact [Naguib et al. 2012a]. It is noticed that the MAXene nanosheets

possess conductivity six times higher than that of the bulk TSC. Such a comparison has earlier been reported between graphene and bulk graphite. Graphene sheets have increased conductivity than the parent graphite. Similar kind of comparable conductivity is seen with exfoliated MAXene and the bulk TSC.

The viability of making MAXene membrane using the exfoliated MAXene nanosheets was also demonstrated. For this, the dispersion of MAXene nanosheets was injected through a Nylon 6,6 membrane having a pore size of ~ 0.2 μm. While passing through this nylon membrane, the MAXene nanosheets were deposited, and formed a crack free thin film membrane module. The newly developed MAXene membrane is flexible as demonstrated in Figure 3.1.10.

Table 3.1.1 Resistivity, electrical conductivity, and green density of cold- pressed MAXene disc

Property	Bulk TSC	Exfoliated TSC (MAXene)
Resistivity (Ω m)	0.00847	0.00158
Conductivity (S m-1)	1.18 x 102	6.30 x 102
Density of cold pressed disc (% of theoretical density)	2.46 (55%)	1.45 (32%)

Figure 3.1.10 Photograph of flexible MAXene film prepared by deposition on Nylon 6,6 membrane.

3.1.5 Conclusions

In this work, a modified micromechanical cleavage strategy was successfully demonstrated to produce 2D derivatives of Ti_3SiC_2, the most famous member among the MAX phase ternary carbides. The exfoliation by micromechanical cleavage is more effective in polar solvents which resulted in 2D Ti_3SiC_2 (MAXene) dispersion stable for several months. TEM images confirmed that the ultrathin MAXene nanosheets possess only a few layer thicknesses. The presence of surface oxide groups formed during the milling process enhanced the dispersion stability. The UV activity makes the nanosheets a new semiconducting material. The exfoliated nanosheets compact has the electrical conductivity six times higher than the bulk counterpart. Thus, this work presented a design of nanostructured 2D carbides via a simple, innovative method for the first time and this new class of 2D functional material can be utilized to make stable thermal fluids, conducting ink, fuel cell electrodes, and conducting membranes. Also, the method developed in this work is a general technique which can be effective in delamination of all the MAX phases irrespective of the type of 'A' atoms.

3.2: High Thermal Conducting, Rheo-Controlled MAXene Nanofluids as a Potential Nanocoolant

3.2.1 Abstract

'Nanocoolants' offering extraordinary heat transport property demand new and exotic nanostructures as fillers that can display enhanced thermal conductivity and thermochemical stability for efficient thermal management operations. Herein we report for the first time, the processing of stable MAXene nanofluids using 2D MAXene nanosheets derived from the bulk nanolaminated Ti_3SiC_2 MAX phase ternary carbides via shear induced micromechanical delamination technique. The beneficial multifunctional physical properties of MAXene colloid such as thermal conductivity, viscosity, and lubrication effect are assessed and reported.

3.2.2 Introduction

Management of heat is critically important in various fields such as electronics, automobiles, solar cells, medical, food industries, and nuclear plants. The considerably large heat production during operation deteriorates the performance of the electrical and engine components used in these fields, and consume more energy. The miniaturization and efficiency improvement of the functioning components in such areas demand satisfactory control of heat. Heat transfer fluids play a significant role in this context. The need for energy conservation added importance to these fluids. Conventional heat transfer fluids included mineral oil, white/paraffinic oils, silicones, water, ethylene/ propylene glycols etc. Thermal conductivity, viscosity, and pumpability are the primary parameters that determine the quality and performance of a heat transfer fluid. A summary of the demand for heat transfer fluids in the market is presented in Figure 3.2.1.(A). It can be seen that almost all the industries relevant sectors depend on heat transfer fluids to ensure reliable performance. Figure 3.2.1 (B) shows the market analysis of various kinds of heat transfer fluids in this decade. It is reported that the global market for all types of fluids is increasing year by year, which indicates the importance of developing new types of high performing fluids.
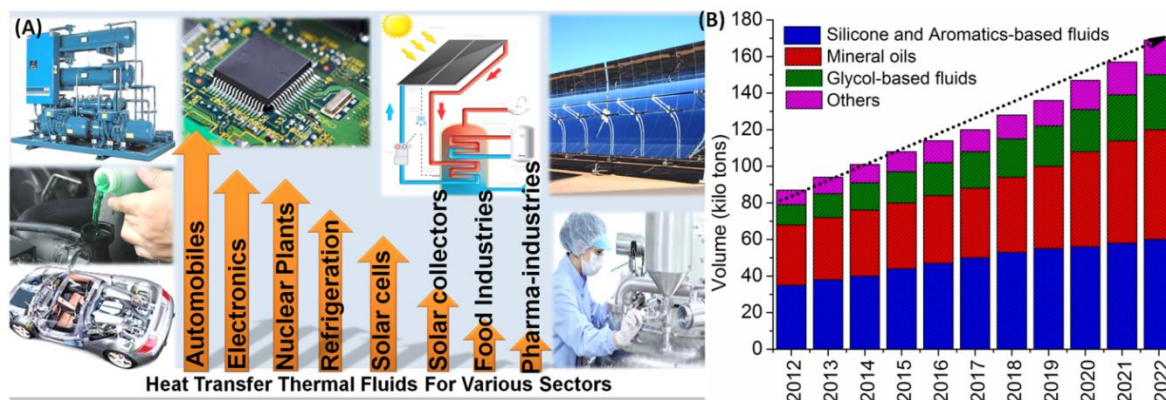
Figure 3.2.1 (A) Insight on the usage of heat transfer thermal fluids in various industrial sectors; (B) Global market analysis of heat transfer thermal fluids by type with a forecast of the global consumption rate. [Grand View Research, Market Research Report, February 2016]

Heat transfer fluids exhibiting non-reactivity and exceptional thermal dissipation characteristics in addition to good thermochemical stability over a range of service temperatures have high demand in thermal management operations [Zhi *et al.* 2011; Yu *et al.* 2010; Dey *et al.* 2015]. Over the years, many attempts were reported to enhance the performance of conventional heat transfer fluids. Adding metallic particle into classical fluids was initially regarded as a promising method to improve the thermal conductivity. Practically, clogging in microchannels and poor fluid stability are the very common technical issues realized with conventional thermal fluids prepared with micronic size metallic particles [Jonggan *et al.* 2012; Prasad *et al.* 2014; Sreeremya *et al.* 2014a]. This prompted researchers to develop 'nanofluids' by dispersing engineered nanopaticles possessing high thermal conductivity in basefluids such as water [Jonggan *et al.* 2012], tranformer oil [Choi *et al.* 2008], mineral oil [Jose Jaime *et al.* 2014], ethylene glycol [Kumaresan *et al.* 2012; Reddy *et al.* 2013], propylene glycol [Manikandan *et al.* 2014; Suganthi *et al.* 2013a], silicone oil, etc. [Lifei *et al.* 2009]. Factors affecting the bulk heat transfer in a thermal management fluid are dispersion stability, surface charge characteristics, fluid viscosity and the morphology of nanoparticles. They are controlled by optimum use of particulate solid fraction, i.e., the filler fraction in the basefluid [Choi *et al.* 2009]. Apart from the usual settling and choking problems, high filler loading increases viscosity and reduces the pumping efficiency, which is essential for mechanical circulation of the nano-fluid coolants. In fact, the viscosity of thermal

fluids prepared with high thermal conducting Al_2O_3 [Jonggan *et al.* 2012], ZrO_2 [Sreeremya *et al.* 2014a], ZnO [Suganthi *et al.* 2013a], Fe_2O_3 [Shima *et al.* 2010], SiC [Singh *et al.* 2009; Li *et al.* 2015], and CeO_2 [Sreeremya *et al.* 2014b] etc. is quite high even at very low concentrations. Moreover, nano-particulates such as Al_2O_3, SiC and ZrO_2 dispersoids generate mechanical friction and associated frictional heat that finally caused damage to mechanical components [Pena Paras *et al.* 2015] Therefore, a balance between thermal conductivity, stability, and viscosity is imperative. It calls for new multifunctional nanostructures where desirable dispersion stability, viscosity, and thermal conductivity can be reached.

Successive to many oxides, carbides, and nitrides dispersed ceramic thermal nanofluids, research was then shifted to carbon based nanofluids involving CNT nanostructures [Aravind *et al.* 2011; Huaqing *et al.* 2011; Neetu *et al.* 2008]. The very high thermal conductivity (2000-4000 W/mK) make it attractive for application in nanofluids. Unfortunately, in such nanofluids, the non-reactive CNT surfaces, intrinsic van der Waals force, and geometrically high aspect ratios caused severe aggregation and made the system less stable. Surfactants were employed to overcome this drawback [Assael *et al.* 2005; Chen *et al.* 2008; Chen *et al.* 2010]. However, surfactant molecules cause foaming during heating and weaken the overall thermal properties. Moreover, the thermal resistance between CNTs and basefluid may increase due to surfactant molecules attached to the CNT surfaces [Huxtable *et al.* 2003]. Further, the entanglement and associated aggregation in CNT nanofluids causes an increase in viscosity and clogging in microchannels. To overcome this, Xie *et al.* introduced acid functionalization of CNTs to prepare surfactant free, stable CNT nanofluids [Xie *et al.* 2003]. Metal nanoparticle modification of CNTs is another method reported to improve the stability and performance of nanofluids [Neetu *et al.* 2008].

2D nanostructures like graphene, fluorinated graphene oxide, and boron nitride are recently emerged as potentially high thermal conducting, heat dissipative dispersoids in nanofluids to be used as nanocoolants [Balandin *et al.* 2011; Sudeep *et al.* 2014; Tessy Theres *et al.* 2010]. Theres *et al.* reported an enhancement of ca. 28% in thermal conductivity of water at 25 °C using metal oxide decorated graphene nanosheets [Tessy Theres *et al.* 2011a]. A hybrid approach in which functionalized

multiwalled CNTs are attached to functionalized graphene was also reported to prepare stable composite nanofluids with enhanced thermal properties [Tessy Theres *et al.* 2011b]. Jaime et al. explored BN nanosheets as electrically insulating thermal conductive fillers in transformer oil [Jaime *et al.* 2012].

In this series, design of new 2D nanostructures is quickly growing. In the fist part of this chaper we showed that we could produce 2D Ti_3SiC_2 MAXene nanosheets via shear induced micromechanical delamination technique. A few layers thick Ti_3SiC_2 MAXene nanosheets were found to be very well stable in polar solvents. Since these newly derived Ti_3SiC_2 MAXene nanosheets contain surface terminated hydroxyl groups, they are a promising candidate for obtaining water based thermal-fluids where high thermal conductivity, low viscosity, and high lubricating properties can be expected.

While considering the basefluids, ethylene glycol and propylene glycol are two commonly used water- based fluid in thermal management [Kumaressan *et al.* 2012; Suganthi *et al.* 2013; Manikandan *et al.* 2013]. Even though ethylene glycol has better heat transport properties, propylene glycol is more non-toxic and environment-friendly than ethylene glycol [Dow Chemical Company; Canter N. 2009]. The excellent antifreeze properties make propylene glycol based fluids one of the fastest growing product segment in heat transfer fluids. Thus, they are used as antifreeze agents in food and beverage industry [Dow Chemical Company]. Moreover, a liquid with a freezing point less than -40 °C is preferred for electronics cooling. Propylene glycol meets all these requirements.

In the present study, we have successfully prepared a novel high thermal conducting Ti_3SiC_2 MAXene nanofluid in the propylene glycol medium. To the best of our knowledge, this is the first report demonstrating the application of 2D MAX phase nanosheets as heat carriers for heat transfer fluids. Interestingly, we also found unique rheological and lubricating properties in this newly designed MAXene thermal fluid. It is envisaged that the application of this multifunctional rheo-controlled 'MAXene nanocoolant' can contribute to the development of next generation heat transfer fluids.

3.2.3 Experimental Details

3.2.3.1 Materials and Methods

Nanolayered Ti_3SiC_2 MAX phase (particle size D_{av} = 13 μm) was procured from 3-ONE-2 LLC, USA. Micromechanical milling was performed using the Ultra-Fine mortar grinder (Retsch-RM 200, Germany) which works on pressure-friction principle. Propylene glycol (Merck India Ltd.) was used as the basefluid. An overview of the experimental procedure adopted in the present work is shown in Figure 3.2.2. In a typical experiment 1 g of bulk Ti_3SiC_2 was taken in 15 mL propylene glycol. It was transferred into the ceramic Retsch mortar, and subjected to micromechanical milling for 24 h. Before the last hour milling, the volume of propylene glycol was raised to 100 mL. After 24 h, the milled dispersion was transferred to a container, and subjected to ultrasonication for 1h using the ultrasonic processor (Sonics Vibra Cell, 20 kHz). The resultant dispersion was then centrifuged at 8000 rpm to settle down the un-exfoliated large particles. The delaminated Ti_3SiC_2 nanostructures stay suspended in the basefluid was collected for the preparation of nanofluid. The delaminated MAXene nanosheets required for morphological and structural characterization was collected by the removal of propylene glycol through solvent extraction method. For this, the nanofluid was diluted with an excess amount of chloroform, and kept for few hours. The nanosheets settled at the bottom were collected by freeze drying. Conventional drying was avoided because it causes restacking of nanosheets. The separated nanosheets were preserved for further characterization.

To prepare the nanofluids with various concentrations of Ti_3SiC_2 MAXenes, the solid content of the as processed dispersion was first determined gravimetrically by solid matter determination set up. For this thermal stability of the propylene glycol basefluid was first determined using Thermogravimetric analysis (TGA), and it was found that complete evaporation/decomposition of propylene glycol occurred at *ca.* 200 °C as shown Figure 3.2.3. Hence, to determine the solid content, 10 mL of the as prepared nanofluid was taken in a clean, pre-weighed quartz crucible and then heated to 200 °C in a temperature controlled muffle furnace, and kept at this temperature for 1 h. The weight of the crucible after cooling to room temperature was noted, and the solid concentration of the nanofluid was determined from the

weight difference. The as prepared nanofluid was then diluted with sufficient amount of propylene glycol followed by 30 min ultrasonication to make homogeneous dispersions containing different volume concentrations of Ti_3SiC_2 MAXene nanosheets. The corresponding MAXene nanofluid is designated as PG-TSC-x Vol % (where, x = 0.01, 0.02, 0.1, 0.2, and 0.25)
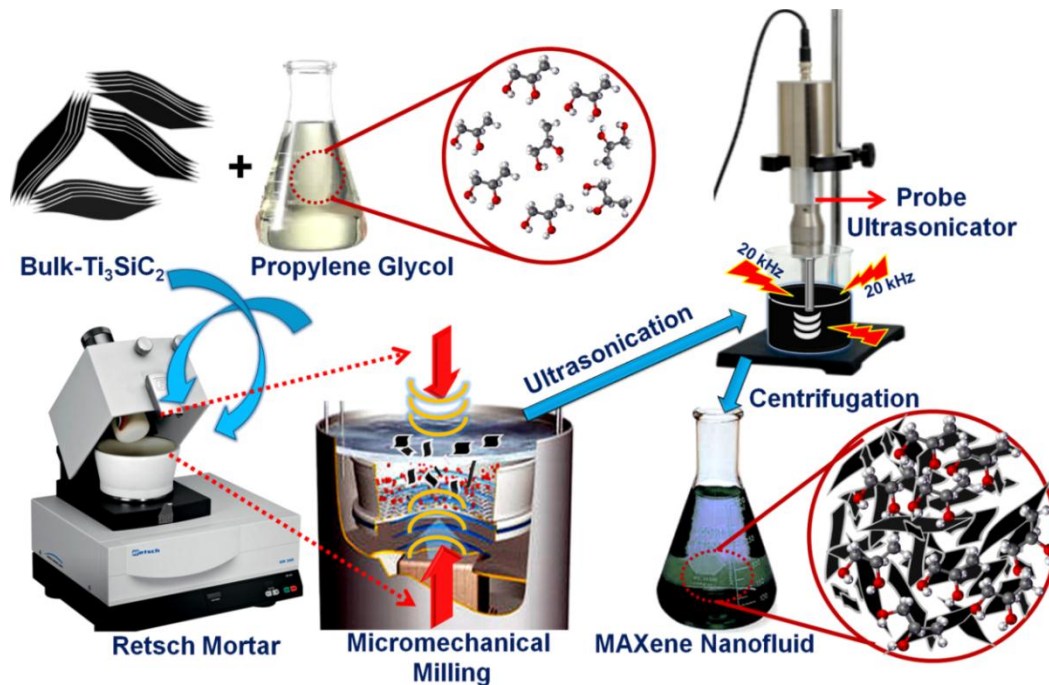
Figure 3.2.2: Schematic representation of the processing of Ti_3SiC_2 MAXene nanofluids.
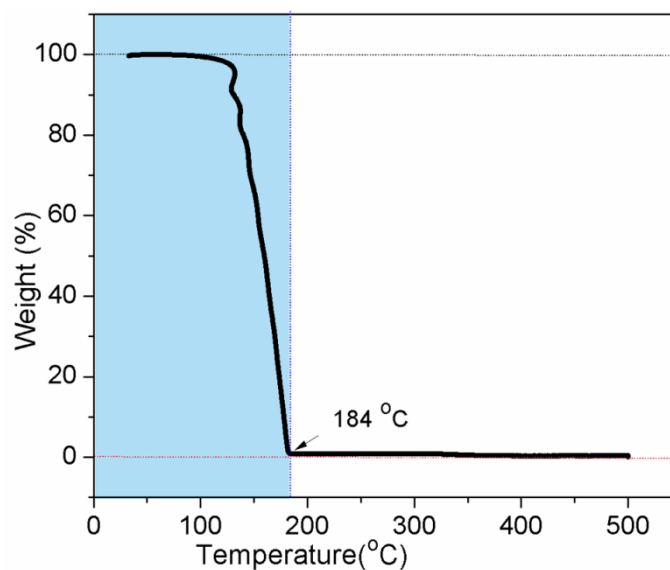
Figure 3.2.3: TGA of the pure propylene glycol. The complete decomposition taken place at temperature ~184 °C.

3.2.3.2 Characterization

The microstructure of bulk Ti_3SiC_2 before exfoliation was analyzed using ZEISS EVO 18 Scanning Electron Microscopy (SEM). The morphological features of delaminated Ti_3SiC_2 MAXene sheets were examined by FEI Tecnai 30G2S-TWIN Transmission Electron Microscopy (TEM), operated at an accelerating voltage of 300 kV, coupled with EDX facility. The powder X-ray diffraction (XRD) pattern of the MAXene nanosheets was recorded using X'Pert Pro, Philips X-ray diffractometer with a monochromator on the diffraction beam side (Cu Kα radiation, λ=0.154 nm). Size and zeta potential measurements for the nanofluids were conducted at 25 °C by Dynamic Light Scattering (DLS) using Malvern Zetasizer 3000HSA. The colloidal stability of the nanofluid was evaluated using Shimadzu UV-2401PC UV-visible Spectrophotometer. The rheological properties of the nanofluids were examined by Anton Paar Modular Compact Rheometer (MCR 102) using a measuring parallel plate setup (PP75) with 75 mm diameter, and a gap of 1 mm. The rheo-experiments were conducted in flow (rotational) mode at a controlled rate with shear rates ranging from 0-1000 S^{-1}. The temperature dependent viscosity was measured in the temperature range 303-333 K at a constant shear rate of 200 S^{-1}

The thermal conductivity of the nanofluid was recorded using KD2 Pro Thermal properties analyzer (Decagon Devices, USA) working on the principle of transient hot-wire technique. The KS-1 probe having a diameter of 1.2 mm and a length of 6 cm was completely immersed in the nanofluid to determine the thermal conductivity. Typically, the probe consists of a needle with a heater and a temperature sensor inside. A current passes through the heater, and the system monitors the temperature of the sensor over time. Analysis of the sensor temperature determines the thermal conductivity. Before the measurements, the probe was calibrated using standard fluid; glycerol supplied by KD2 Pro. Measurement of thermal conductivity of liquids is difficult, and extreme care was taken to obtain accurate and repeatable results. The sample and the probe were kept absolutely still to eliminate any forced convection. The measurements were carried out in an isolated clean room that was free from any source of vibrations. The errors coming from convection mechanism were also reduced by aligning the sensor orientation in a vertical direction with the fluid container. Moreover, the high

viscosity of propylene glycol than water minimizes the error due to convection. The temperature dependent measurements of thermal conductivity were carried out using a water bath. Thermal conductivity up to 323 K was measured since the viscosity becomes too low above this temperature and free convection begins to affect the measurement. A schematic representation of the experimental setup used for the thermal conductivity measurement is depicted in Figure 3.2.4. The electrical conductivity of the nanofluids was measured using Jenway 3540 pH and Conductivity Meter with a cell constant of 1.02
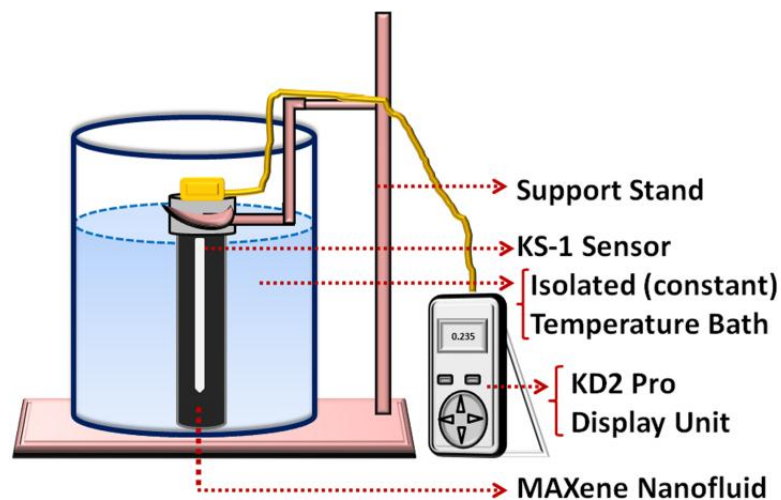
Figure 3.2.4: Schematic representation of the experimental setup used for the thermal conductivity measurement of nanofluids.

The tribological performance of the nanofluids was evaluated by ball-on-disc wear and friction technique (TR-201LE DUCOM, India). Steel balls (EN 31) having a diameter of 10 mm were used as standard test balls. A steel disc (EN 31 hardened to 62 HRc) having a diameter 100 mm and 8 mm thickness was used as the counterface material. A constant track diameter of 70 mm was given for all the measurements. The wear test was carried out with a normal load of 29.4 N and time of 900 s. The tests were conducted in an environmental chamber at ambient temperature. The nanofluid was applied on the wear track using a pump at a rate of 1 mL min^{-1}. A bare experiment was also conducted without the addition of any lubricants to determine the coefficient of friction of the steel ball. The frictional force was monitored by using a frictional force sensor, and was converted to the coefficient of friction (μ). The surface roughness of the wear scar formed on the steel balls was measured

using a surface roughness tester (Dektak XT Profilometer), with a measurement length of 0.8 mm.

3.2.4 Results and Discussion

3.2.4.1 Preparation of MAXene Nanofluids

The delamination of nanolayered, bulk MAX phase Ti_3SiC_2 particles into MAXene nanosheets and formation of nanofluids via mechanical shearing show a strong dependence on two processing parameters; milling time and initial mass. The gravimetric estimation of the solid fraction in the resultant MAXene nanofluids gives the percentage yield of the MAXene product at different processing conditions. Table 3.2.1 presents the effect of milling time and initial mass on the % yield of Ti_3SiC_2 MAXene nanosheets in a final volume of 100 mL propylene glycol. A maximum yield is obtained at a fixed time of 24 h milling for the initial feed of 1 g Ti_3SiC_2. It is seen that merely an increase in the initial mass of Ti_3SiC_2 feed could not improve the % yield though it is generally expected. Delamination of nanolayered Ti_3SiC_2 into MAXene nanosheets through mechanical means is possible by exfoliation, mechanical-peeling and thinning. In fact, factors such as inter- atomic bond strength, bulk hardness, and the dispersion stability of Ti_3SiC_2 in the given fluid medium are primarily controlled the effective mechanical exfoliation/delamination. Earlier reports on Ti_3SiC_2 clearly indicate that the TiC-Si bond is mechanically weak that can break and promote exfoliation/delamination when mechanical force is induced [Jingyang *et al.* 2009; Barsoum *et al.* 2011]. These reports confirm that the nanolaminated architectures can be mechanically separated from the original nanolayered stacked structure. In the first part of this chapter, we have studied the effect of various solvents on the mechanical exfoliation/delamination of bulk Ti_3SiC_2 and found that polar solvents are effective in dispersion stability and rate of delamination.

An operative mechanism in delamination of Ti_3SiC_2 is described schematically in Figure 3.2.2. As discussed earlier, the delamination of the Ti_3SiC_2 particle in the propylene glycol medium is mainly aided by the oppositional rotation of mechanical mortar and the ceramic pestle coupled with the compressive shear force on the particles. As the initial concentration increases, the particles move out

from the contact area from the vicinity of the mortar and pestle of the Retch milling equipment, and each particle is subjected to less milling process. As a result of this, the particle could not delaminate completely unless a proportional increase in the milling time is provided. This is the probable reason for the low yield even at high loading of Ti_3SiC_2. It was noticed that the centrifugation condition also influences the resultant yield of the MAXene product. We observed that the reduction of centrifugation time produced a dispersion of MAXene with a high % yield but with less stability. For example, at 4000 rpm/10 min duration, in addition to the colloidal size MAXene sheets, the centrifuged product also contains unexfoliated/partially exfoliated large and thick size MAXene sheets that make the dispersion less stable. At a given time of 24 h milling and 8000 rpm/10 min duration, the 1 g Ti_3SiC_2 feed produces completely exfoliated, stable MAXene nanofluid with 52 % yield of solids. Therefore, these conditions were finalized to produce well stable MAXene nanofluids. Upon dilution with appropriate amounts of propylene glycol, MAXene nanofluids containing 0.01, 0.02, 0.1, 0.02, and 0.25 Vol% of Ti_3SiC_2 MAXene was successfully obtained.

Table 3.2.1: Dependence of initial Ti_3SiC_2 loading and milling time on % yield of MAXene nanosheets in the nanofluids.

Ti_3SiC_2 mass (g)	Milling time (h)	Solid fraction mg mL^{-1}	% yield
1.0	12	1.2	12
2.0	12	4.6	23
1.0	24	5.2	52
2.0	24	9.2	46
2.5	24	9.8	39
5.0	24	12.4	25

3.2.4.2 Structural and Morphological Features of MAXene Nanosheets

SEM and TEM examinations further ascertained the structural characteristics of the MAXene nanosheets formed via mechanical shearing and the resultant

morphologies are depicted in Figure 3.2.5. The schematic representation of layered arrangements of atoms in bulk Ti_3SiC_2 is given in Figure 3.2.5 (a). The SEM images in Figure 3.2.5 (b and c) show the nanolayered nature of bulk Ti_3SiC_2 particles that upon micromechanical exfoliation turns to MAXene nanosheets. The microstructure indicates that the single Ti_3SiC_2 particle has a physical size below 10 μm. The particle also contains stacks of multiple nanometer thick inter-layers. Figure 3.2.5 (d1-d4) is the TEM morphologies of the exfoliated Ti_3SiC_2 MAXene nanosheets obtained in the propylene glycol medium. The TEM image describes three distinct nano morphologies of MAXene nanosheets in the nanofluids. In Figure 3.2.5 (d1) the TEM image shows a few layer thick, large size MAXene nanosheet with a sheet length of *ca*. 200 nm. A further examination reveals that the nanofluids also contain nanosheets with single layers, and such layered sheets have the length of *ca*. 30-150 nm. These single layer MAXene sheet are transparent to electron beam as evidenced from HRTEM image in Figure 3.2.5 (d3). The inset to Figure 3.2.5 (d3) is the magnified part of the single nanosheet revealing the orientation in (104) plane with a d spacing of 0.227 nm. The corresponding FFT pattern is also depicted in Figure 3.2.5 (f). In addition to these large size thick and single layer Ti_3SiC_2 MAXene nanosheets, the micro-mechanical exfoliation of bulk Ti_3SiC_2 also produced a significant amount of ultra-small Ti_3SiC_2 sheets with size *ca*.10 nm as seen in Figure 3.2.5 (d2). The parallel existence of Ti_3SiC_2 ultrasmall sheets is the result of the micromechanical grinding effect due to an extended period of mechanical shearing where the destruction of Ti_3SiC_2 readily occurred.

The EDX spectrum of the MAXene nanosheets is given as Figure 3.2.5 (e). The presence of OH functionalities on the surface of the MAXene nanosheets is distinguished in the spectrum. Formation of the surface oxygen group is due to the micro-thermal heat produced during mechanical milling in the polar solvent for long hours. The electrostatic interaction of these OH groups with the propylene glycol leads to the formation of very stable dispersions without any settling. A low magnification TEM image and the corresponding statistical analysis illustrating the distribution of MAXene nanosheets in the nanofluid is given as Figure 3.2.6. It is noticed that the nanofluid mainly contains nanosheets having length in the range 30-150 nm. Such mixed morphologies of nanosheets with different sheet lengths

are expected to offer increased inter-particle contacts and maintain the particle networking to have effective thermal transport.
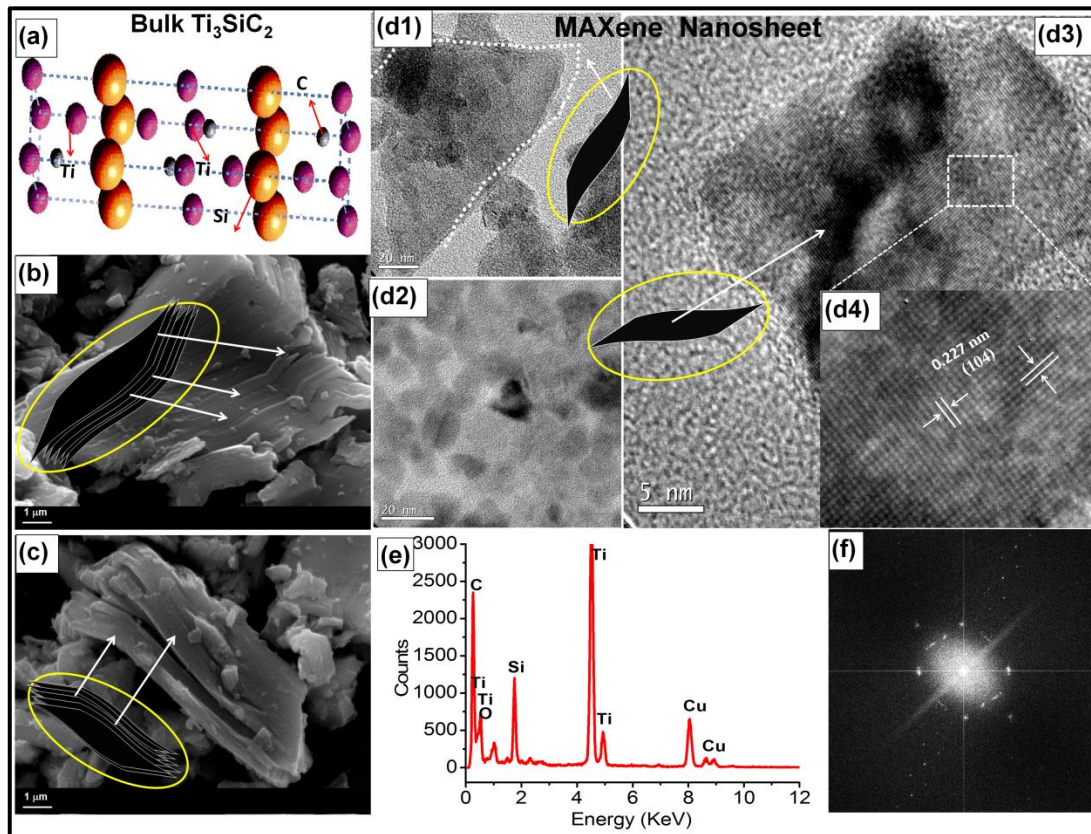
Figure 3.2.5: (a) Schematic representation of crystal structure of bulk Ti$_3$SiC$_2$ revealing the layered arrangement of atoms; (b & c) SEM images of bulk Ti$_3$SiC$_2$ showing the nanolayered characteristics; (d1-d3) TEM images of Ti$_3$SiC$_2$ MAXene nanosheets showing various size distribution in the nanofluids; (d4) magnified portion of HRTEM image of single MAXene nanosheets shown in d3; (e) the EDAX spectrum of the MAXene nanosheets; and (f) FFT corresponds to the TEM images shown in d3.

The phase purity and crystallinity of MAXene nanosheets can be understood from the corresponding powder X-ray diffraction patterns given in Figure 3.2.7. The XRD pattern of the bulk Ti$_3$SiC$_2$ was also presented to verify the crystal features of MAXene nanosheets. It is observed that the nanosheets retain its chemical identity, and the results are on par with the earlier result discussed in the first part of this chapter. As expected the nanosheets have highly broadened crystalline peaks and in such nanoscale, the peak intensity largely decreased. From the XRD, it is confirmed that the mechanically delaminated MAXene layers preferably have few layer thick

ultrathin dimensions. In fact the higher order peaks seen in bulk Ti_3SiC_2 is absent in the XRD spectrum of MAXene nanosheets confirming its 2D characteristics.
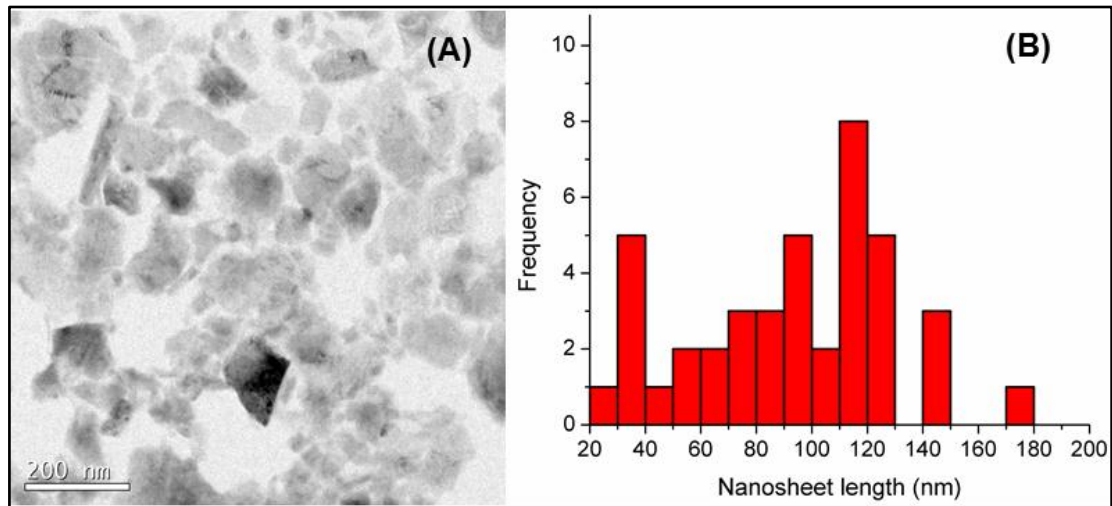
Figure 3.2.6: (A) Low magnification TEM image showing size disribution of MAXene nanosheets in the nanofluid, and (B) the statistical analysis illustrating the size distribution of MAXene nanosheets in the nanofluids.
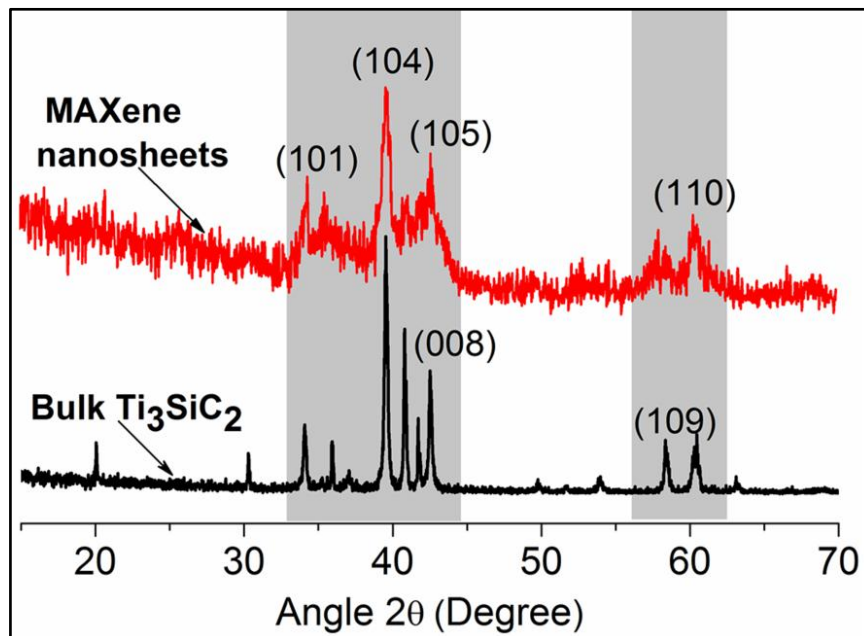
Figure 3.2.7: Powder X-ray spectra of MAXene nanosheets and bulk Ti_3SiC_2.

3.2.4.3 Stability of MAXene Nanofluids

Figure 3.2.8 represents the physical stability of the MAXene nanosheets in propylene glycol based fluids with different concentrations. Normally the main

challenge in obtaining a highly thermal conducting nanofluid is the dispersion and stabilization of nanoparticles. In many cases, nanoscale dispersoids easily stay dispersed at low concentrations. However, for effective thermal transport, a high solid fraction is important and at high solid concentrations, the dispersion stability is very poor. The addition of suitable surfactants is usually employed to overcome this problem. But unfortunately, the surfactants affect the bulk thermal transport characteristics. Here, the MAXene nanosheets form a very stable dispersion in propylene glycol even at high concentrations without the aid of any surfactants or stabilizers. Figure 3.2.8 shows the stability of MAXene nanofluids in comparison with the nanofluid prepared with unexfoliated bulk Ti_3SiC_2. Figure 3.2.8 (A) corresponds to the physical stability of 0.1 Vol% bulk Ti_3SiC_2 nanofluid processed by ultrasonication only. In propylene glycol, the bulk particles form dispersion, but they started settling immediately after preparation and completely settled in 3 days of period. The density of the Ti_3SiC_2 is 4.53 g cm^{-3}. The propylene glycol density and theoretical viscosity are 1.04 g cm^{-3} and 0.42 cPa.s, respectively. The bulk Ti_3SiC_2 used in the present study has an average particle size of 13 μm. The high density and particle size make it difficult to disperse it in the reasonably viscous glycol medium even at low solid loading. However, in the case of MAXene nanosheets, the nanofluids offer high stability even after keeping undisturbed for more than a month (Figure 3.2.8). The stability is not affected by the increase in the solid loading. It was observed that the cold pressed 2D MAXene nanosheets derived from the bulk Ti_3SiC_2 possess low density of ~1.45 g cm^{-3} only (determined from physical dimensions and weight).

Apart from the nanoscale dimensions, as evidenced by the EDX analysis, the presence of chemically interactive surface functional moieties favoring the high colloidal stability in MAXene nanofluids. When solids loading have gradually increased the tendency of interparticle aggregation is seen. Nevertheless, the aggregates exhibit good stability up to the solids loading of 0.2 Vol% MAXene. Above this range, a minimal settling was observed. However, it was observed that the sediment formed is reversible and a simple hand shaking is enough to make it again a stable dispersion.
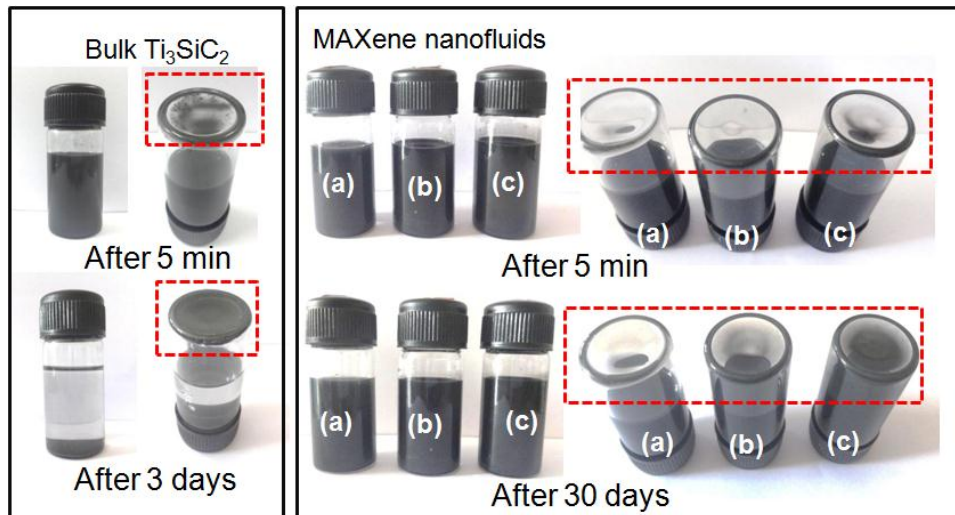
Figure 3.2.8: Photographs showing the dispersion stability of the MAXene nanofluids prepared with (left) bulk Ti$_3$SiC$_2$ and (right) Ti$_3$SiC$_2$ MAXene nanosheets; (a) PG-TSC-0.01 Vol%, (b) PG-TSC-0.2 Vol%, and (c) PG-TSC-0.25 Vol%.

The stability of the nanofluid is also analysed using UV-vis spectroscopy studies, and the results are depicted as Figure 3.2.9. UV-vis spectroscopy is a common tool for the sedimentation characteristics analysis of nanoparticles in a dispersion and for the evaluation the stability of nanofluids [Amiri *et al.* 2016]. According to Beer–Lambert law, the absorbance of a solution is directly proportional to the concentration of the absorbing species such as particles in a dispersion, and therefore this method is a unique technique to determine the particle concentration in a dispersion. The absorbance of the nanofluids was recorded immediately after synthesis, and after kept undisturbed for one month. No abrupt decrease in absorbance was observed which confirms that the dispersions are well stable even after kept undisturbed for more than 1 month. The relative concentration of the nanofluids was calculated from the absorabance values and are given in Figure 3.2.9. (B). Only about 13 % sedimentation was seen in the case of the highest concentration (0.25 Vol%). The sedimentation is negligible in the case of lower concentrations. We also measured the zeta potential values to validate the colloidal stability of MAXene nanofluids. It is seen that the zeta potential value increased from -24.1 to -38 mV when the amount of MAXene nanosheets is increased from 0.01 to 0.25 Vol%. The relatively high zeta potential value confirms the colloidal stability.
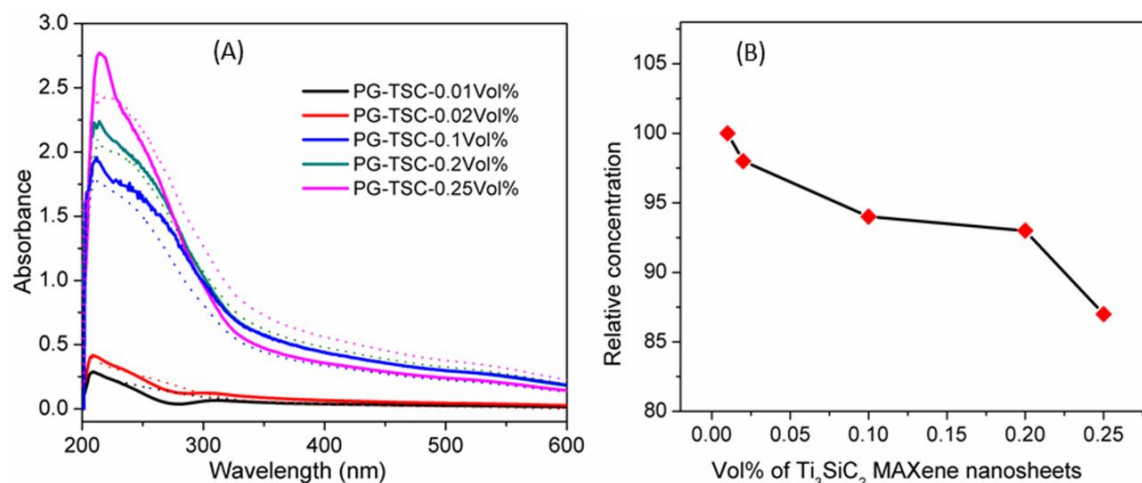
Figure 3.2.9: (A) UV-visible spectra of Ti₃SiC₂ MAXene nanofluids at diffrent concentrations. The dotted line represents the corresponding spectra obtained after 1 month; (B) Relative concentration of Ti₃SiC₂ MAXene nanofluids after 1 month shelf life time (calulated from UV- visible spectrum).

To get an insight of the particle-solvent interaction, the hydrodynamic diameter of the MAXene nanosheets with respect to their concentration in propylene glycol was monitored using DLS measurements, and the size distribution result is shown in Figure 3.2.10. In DLS technique for non-spherical particles, the size is interpreted as an equivalent spherical diameter equal to Stokes-Einstein hydrodynamic diameter. The hydrodynamic diameter includes both the inorganic core as well as the attached solvent layer. It was observed that the average hydrodynamic diameter increased from 120 nm to 310 nm with respect to the increase in MAXene loading from 0.01 Vol% to 0.25 Vol%. The increase in the hydrodynamic diameter indirectly indicates the strong interaction of the MAXene nanosheets with the dispersion medium. The high hydrodynamic diameter observed in the present case suggests a strong hydrophilic interaction between propylene glycol medium and MAXene nanosheets. It is interesting to note that unlike many 2D nanostructures, the MAXene nanosheets have advantages in two ways: it works well with mechanical dispersion technique, it produces dimensionally varying mixed morphologies, and finally high stability at high solid concentrations even in the absence of any surfactants which makes them potential candidate for the processing of multifunctional MAXene 'nanocoolant'.
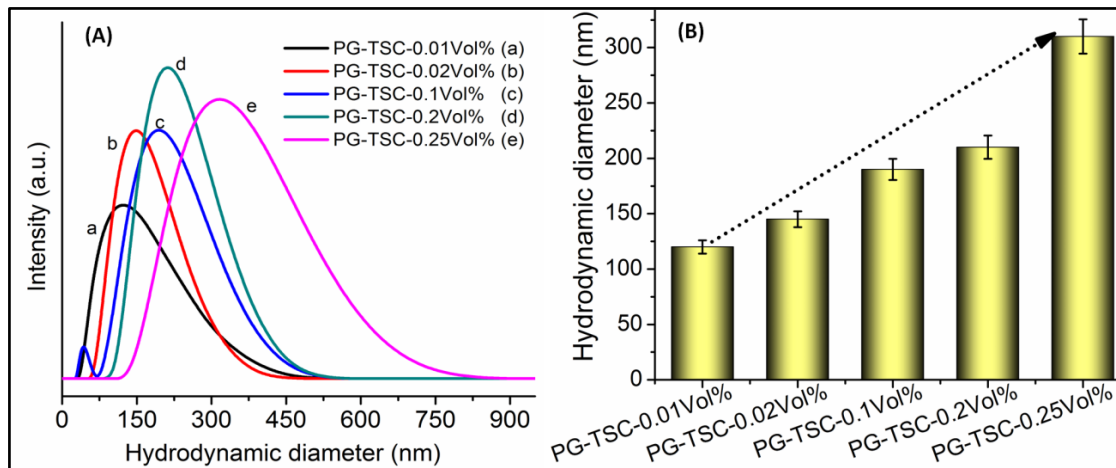
Figure 3.2.10: (A) The size distribution and (B) hydrodynamic diameter of of Ti₃SiC₂ MAXene nanosheets in the nanofluid at diffrent concentrations.

3.2.4.4 MAXene Nanocoolant Performance - Rheological Properties

Viscosity is very critical for a thermal fluid because the thermal fluids are mostly used under continuous flow applications. The flow characteristics of basefluid should not be increased when the active nanofillers are introduced. Earlier studies on the viscosity of nanofluids prepared with conventional metallic and ceramic nanoparticles for thermal management operations strongly indicate an increase in the viscosity with increasing nanofiller addition [Sreeremya *et al.* 2014a; Sreeremya *et al.* 2014b]. The aggregation effect and weak interactive surface forces with the fluid medium were said to be the reasons for the abrupt rise in the viscosity. In a shear flow, the hydrodynamic forces required to break the network of aggregated nanoparticles in to individual primary nanoparticles are insufficient. This casues an increase in viscosity of the system than that of the basefluid. Usually, a well dispersed nanofluid exhibit lower viscosity than that of a less stable, aggregated dispersion with equivalent solid loading, and several reports documented the need of steric or electrostatic stabilization techniques to control the aggregation effect and minimize the increase in viscosity [Chen *et al.* 2009; Suganthi *et al.* 2013b]. The rheology of MAXene nanofluids developed in the present work was evaluated using cone and plate rheometer. The variation of room temperature viscosity with the shear rate ranging between 0-1000 s⁻¹ was investigated with respect to MAXene loading, and the results are given in Figure 3.2.11. The flow curves clearly explain that the viscosity of the MAXene nanofluid is independent of

shear rate and is following the Newtonian flow behavior. The shear stress curves also follow the same patterns as depicted in Figure 3.2.11(b). This indicates that even though the inter-particle clustering occurs, they are feeble in nature and gets separated easily under applied mechanical stress.
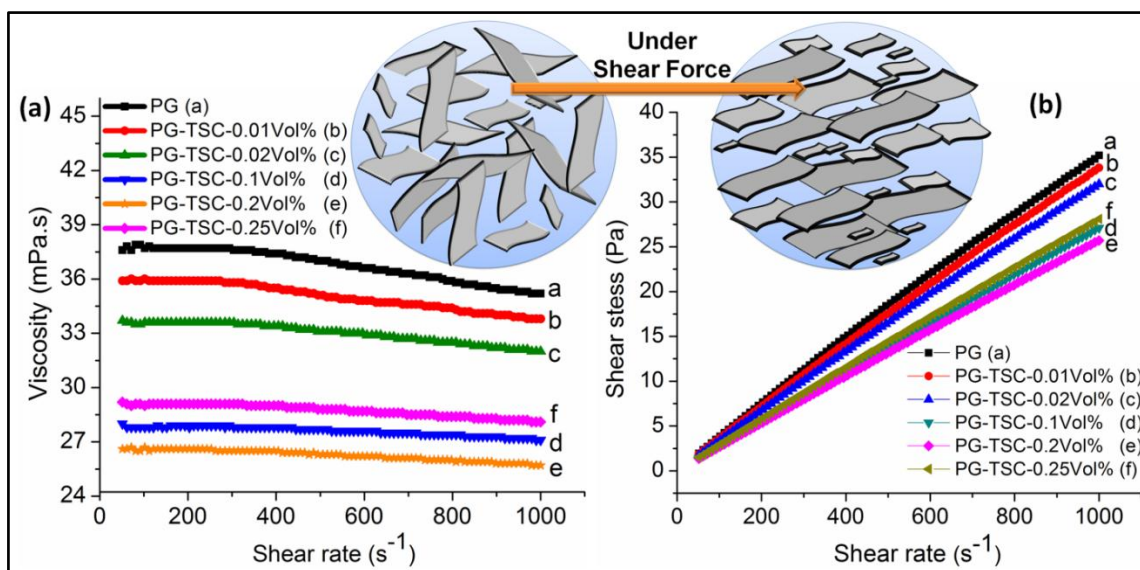
Figure 3.2.11: Rheological properties of the nanofluids: (a) variation in viscosity with shear rate, and (b) variation of shear stress with shear rate. Schematic representation showing the easy flow behavior of nanofluids under shear force is given as inset.

In MAXene nanofluid, the interesting factor to be noticed is the remarkable decrease in the viscosity values. The flow curve corresponds to the propylene glycol basefluid shows the value ~ 38 mPa.s. The intermolecular hydrogen bonding between the molecular chains is responsible for the viscosity of propylene. The viscosity value gradually decreases with the loading of MAXene up to 0.2 Vol%. Beyond this range, the viscosity appears to increase. However, the viscosity value is still well below that of the basefluid. The flow-property results confirm the good interfacial interaction among the nanosheets with the basefluid. Propylene glycol has chemically weak hydrogen bonding and due to the interfacial interaction with MAXene nanosheets, the weakening of hydrogen bonds has finally resulted in dropping of the fluid viscosity. The interfacial interaction is mainly governed by the hydrophilic surface functional groups present in the nanosheets. The surface hydroxyl groups present on MAXene nanostructure bridge with hydroxyl groups in the propylene glycol that possibly form weak hydrogen bonds and decreases the fluid viscosity. Tan *et al.* reported the formation of such kind of interactions in

reduced graphene oxide dispersion in polyvinyl alcohol [Tan *et al.* 2012]. The reduction in viscosity with MAXene loading may be due to three main factors: (1) at very low concentrations of nanosheets, the like charges repel each other and reduce the inter-particle interactions that in turn prevent associated increase in viscosity, (2) the hydrophilic MAXene nanosheets can easily bond with hydroxyl groups of propylene glycol, and thereby decrease the interaction between the fluid molecular chains and causes lowering of viscosity, and (3) the nanosheets can easily align themselves in the direction of shear force and act as lubricant materials and reduce the friction (between the particles as well as the fluid and the walls of the container) which will eventually result in a sharp decrease in viscosity and allows smooth flow of the fluids.

Figure 3.2.12 shows the temperature dependent rheological behavior of the MAXene nanofluids evaluated in the range 303-333 K at a constant shear rate of 200 s^{-1}. The flow curves confirm a decrease in viscosity with increasing temperatures in both basefluid as well as MAXene nanofluid. The propylene glycol viscosity decreases sharply from the value of 38 mPa.s to 8 mPa.s at 333 K. The nanofluids containing MAXene nanosheets also follow the same trend. Figure 3.2.12 (b) represents the relative viscosity (μ_r) of the nanofluids with respect to the basefluid calculated using the expression:

$$\mu_r = \mu_{nf}/ \mu_b \qquad\qquad (3.2.1)$$

where μ_{nf} and μ_b are the viscosities of nanofluid and the basefluid, respectively. In many nanofluid systems reported earlier, the viscosity of the nanofluid is greater than that of the basefluid and hence, the relative viscosity is always higher than the parent fluid used for the preparation of nanofluid. However, in this present work, a unique performance of MAXene nanofluid was observed. The results on the relative viscosities of the MAXene nanofluids confirm that the relative viscosity is < 1 at all the concentrations in the entire temperature range of 303-333 K. The relative viscosity of MAXene nanofluid prepared with 0.2 Vol% concentration is only about 0.70 at room temperature, which accounts for a reduction of 30 % in the viscosity compared to the basefluid. Such a substantial reduction in viscosity gives a great advantage in improved pumpability (easiness of pumping) and high thermal conductivity in the MAXene nanofluid. It is clear from the Figure 6b that the relative

viscosity is very less at low temperatures. At elevated temperatures, the relative viscosity is gradually increased. However, the value is still < 1.
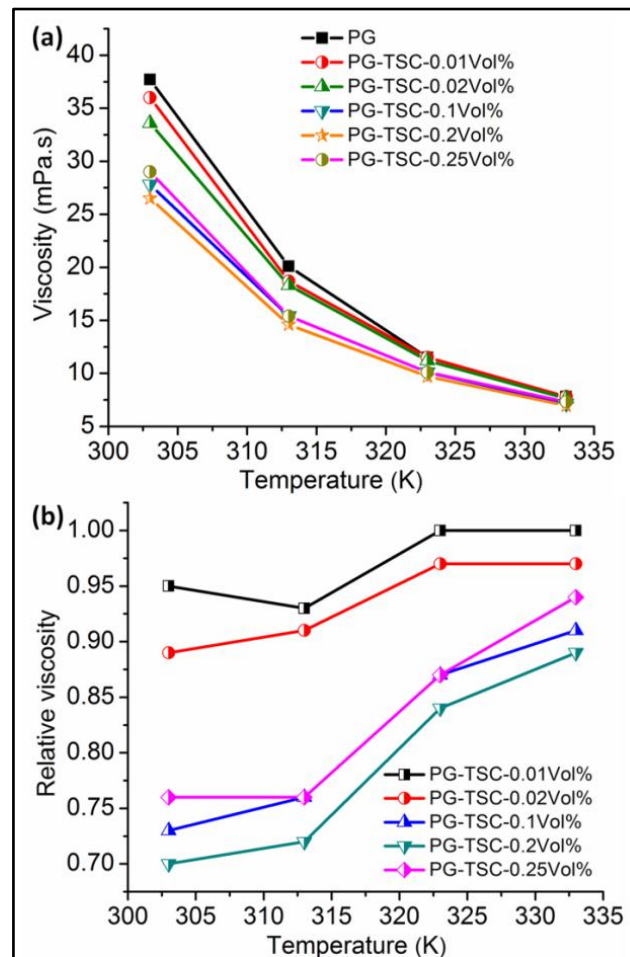
Figure 3.2.12: Dependence of (a) viscosity and (b) relative viscosity on temperature.

3.2.4.5 Thermal Conductivity Performance of MAXene Nanocoolants

The trend in the thermal conductivity enhancement of the MAXene nanofluids with different MAXene concentrations is presented in Figure 3.2.13. The enhancement in the thermal conductivity was computed from the equation:

$$k_{eff} = (k_{nf} - k_0) / k_0 \times 100 \qquad (3.2.2)$$

where k_{nf} and k_0 are the thermal conductivities of MAXene nanofluid and propylene glycol basefluid, respectively. Figure 3.2.13 (a) illustrates the concentration dependent thermal conductivity of MAXene nanofluid at two different temperatures, 303 K (30 °C) and 323 K (50 °C). It is observed that at both the temperatures, MAXene nanofluids show an increased thermal conductivity with increasing concentration of MAXene nano dispersoids. The thermal conductivity enhancement

is almost linear with an increase in the MAXene loading. It is noticed that at the given experimental temperatures of 303 K and 323 K, the thermal conductivity enhancement is apparently significant, and the percentage increase achieved is approximately 45 % when the MAXene concentration, as well as the applied temperatures, are at their maximum. More specifically, at 303 K, the MAXene concentration of 0.01Vol% accounts only 5 % increase in thermal conductivity which is further improved to 15 % when the MAXene loading is increased to 0.25 Vol%. At this identical concentration level, the thermal conductivity enhancement at an elevated temperature of 323 K is ~ 45 %. The increase in thermal conductivity with increasing filler content suggests that the percolation mechanism also significantly contributes to the thermal transport. This indicates that Maxwell's theory is not following at high filler concentrations. According to Maxwell's theory concentration have very small impact on thermal conductivity. We have earlier confirmed from the TEM images that the MAXene nanosheets in propylene glycol nanofluids exhibit morphologically varied nanostructures with varying dimensions. Such mixed morphologies can effectively maintain the percolative channel for maximizing the thermal transport at higher filler loading as shown schematically in Figure 3.2.13 (b).

Figure 3.2.13 (c) describes the influence of temperatures on the enhancement in thermal conductivity of MAXene nanofluids processed at different concentrations. The corresponding thermal conductivity data of the basefluid and MAXene nanofluids are given in Figure 3.2.14 for better understanding. As expected, in the absence of any active MAXene nanofillers, the thermal conductivity of propylene glycol does not show any dependence on temperature, and retain almost a constant value, ~ 0.191 W m^{-1} K^{-1} in the whole temperature ranges. However, upon dispersion of MAXene nanosheets, the nanofluids show a prominent increase in the thermal conductivity with increasing applied temperatures. For example, when the propylene glycol is loaded with 0.25 Vol% of MAXene fillers, the thermal conductivity is increased from 0.191 to 0.276 W m^{-1} K^{-1} at 323 K. This confirms that the concentration of MAXene nanofillers as well as fluid temperature play a key role in thermal transport property of the bulk nanofluid. More accurate measurements of thermal conductivity were hard to observe beyond 323 K and the values were

fluctuating due to free convection at higher temperatures. It resulted in statistically large errors and therefore, could not be included here. The increase in the effective thermal conductivity (k_{eff}) with temperature is a result of Brownian motion (the random motion of nanoparticles in a colloidal suspension) induced convection in the MAXene nano colloid, and is in accordance with predictions of Maxwell [Shima *et al.* 2010; Jaime *et al.* 2012]. The Brownian movement of the nanoparticles will be more with increase in temperature of the medium. The particle contact or collision resulted from this particle movement will be more when the concentration of nanoparticle is high in the medium. Moreover, the decrese in viscosity of the fluid with increase in temperature further helps the particels to move faster and aids the transport heat energy among the particles, and this will finally resulted in enhancement of thermal conductivity of the medium.
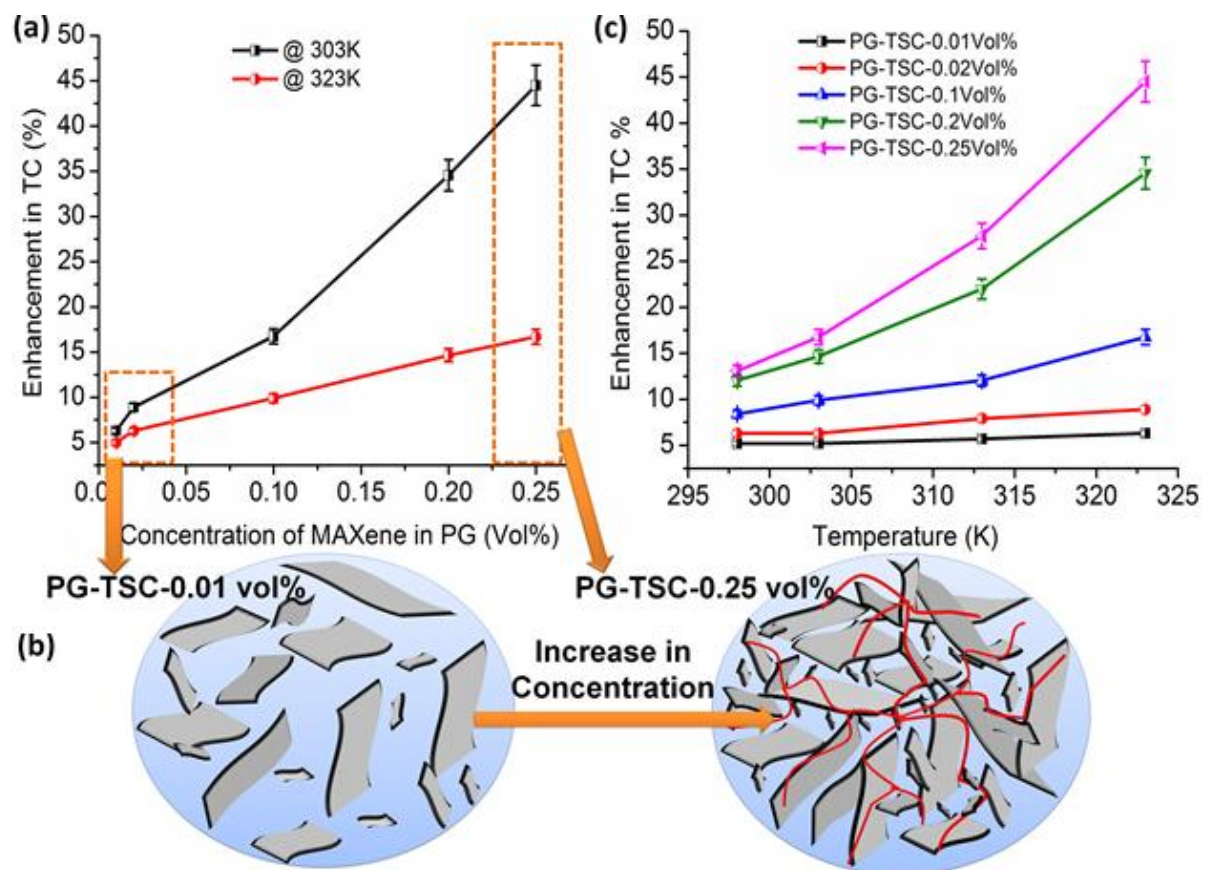
Figure 3.2.13: Variation of thermal conductivities of the nanofluids with (a) concentration, (b) Schematic representation of the role of Ti₃SiC₂ MAXene concentration on thermal conductivity and (c) Variation of thermal conductivities of the nanofluids with temperature.
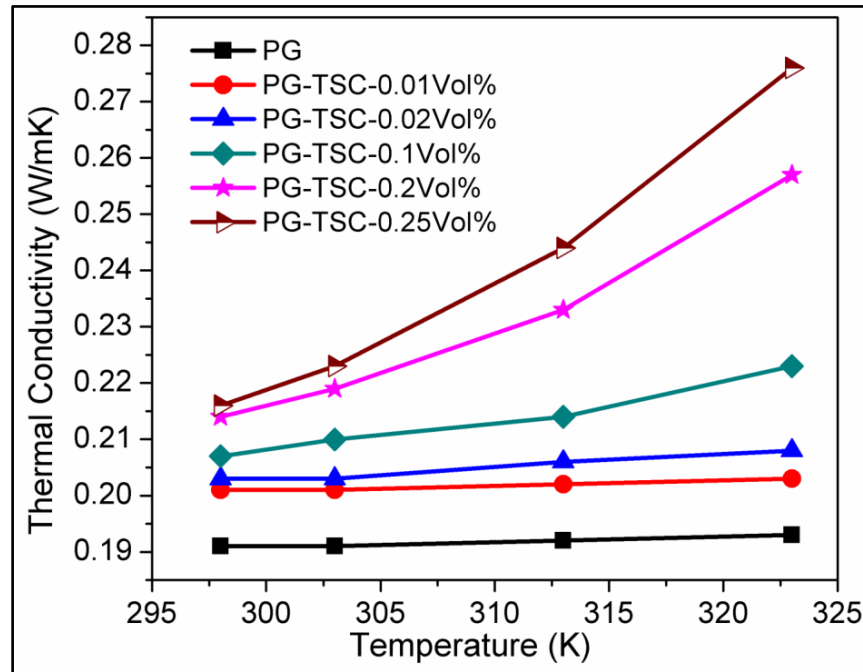
Figure 3.2.14: Thermal conductivity values of the nanofluids containing different Vol% of Ti₃SiC₂ MAXene nanosheets as a function of temperature. The thermal conductivity is increased with both concentration of Ti₃SiC₂ MAXene nanosheets and temperature.

As we discussed earlier, the hydrophilic nature of MAXenes provide good interaction with the basefluid and form effective liquid layering at MAXene-propylene glycol interface. The drastic decrease in the viscosity of propylene glycol in the presence of MAXene nanodispersoids is in fact, supporting the liquid layering effect. The liquid layering as well as the lowering of viscosity are the factors governing the improvement in the bulk thermal conductivity of the basefluid [Manikandan *et al.* 2014; Suganthi *et al.* 2013a]. The low viscosity possibly promotes the particle movement in the fluid much easier, and makes them as effective carriers of heat energy. One essential difference in this work to be worth indicating is that the MAXene nanosheets are dispersed in propylene glycol without the use of any surfactants or stabilizing agents. This adds to the advantage of present nanofluid design. Earlier studies confirmed that the surfactant layers reduced the thermal conductivity owing to defects created by them, which ultimately retard the free electron/phonon transportation. So surfactant free nanofluids, such as the one reported in this work, are always attractive for the sustainable thermal transport and thermal management applications.

Over the period, we also observed a weak clustering of the MAXene nanosheets as claimed from the marginal increase in the hydrodynamic particle size data. This clustering effect is in fact, one among many reasons reported earlier for the improvement in the thermal conductivity of nanofluids. Figure 3.2.15 depicts the increase in thermal conductivity with the hydrodynamic diameter of the MAXene nanofluid. It is clear that the thermal conductivity is increasing with the increase in the hydrodynamic size. The increase is more prominent at high temperatures due to the additive effect of both Brownian motion and percolation mechanism.
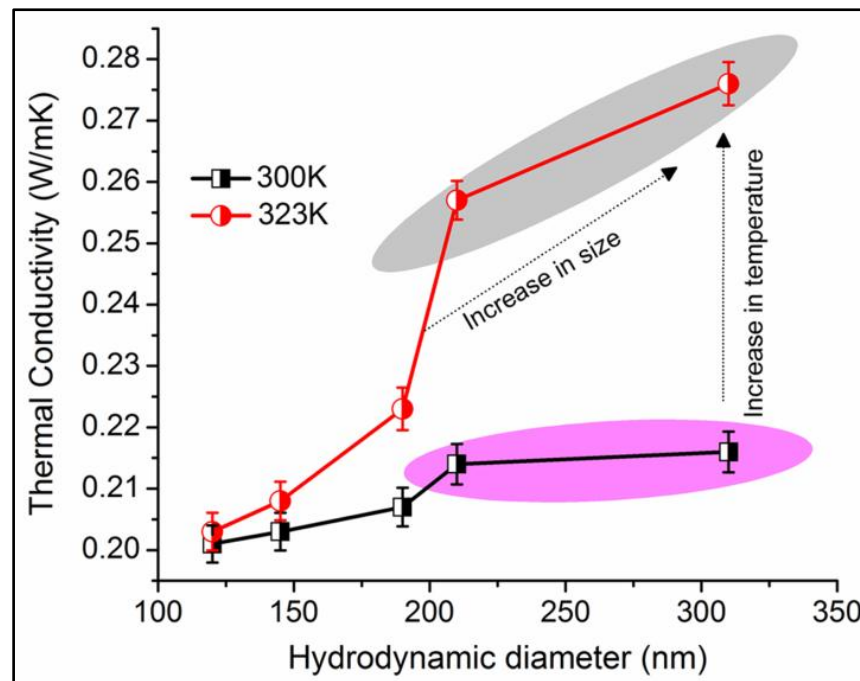
Figure 3.2.15: The dependence of thermal conductivity with the hydrodynamic diameter of the MAXene nanosheets at temperatures of 300 K and 323 K.

3.2.4.6 Efficiency of the Nanofluids

The performance of nanofluids also depends on the flow mode (laminar/turbulent) and in the case of laminar flow, for an ideal nanofluid; the ratio of viscous to thermal conductivity coefficients should be < 4 i.e. the increase in the viscosity is less than four times the increase in thermal conductivity [Sreeremya *et al.* 2014a; Prasher *et al.* 2006]. This is usually estimated using the dynamics relations by the equations:

$$\eta_{nf}/\eta_{bf} = 1 + C_\eta \qquad (3.2.3)$$

$$k_{nf}/k_{bf} = 1 + C_k \qquad (3.2.4)$$

$$C_\eta/C_k < 4 \qquad\qquad (3.2.5)$$

where η_{nf}/η_{bf} and k_{nf}/k_{bf} are respectively the ratios of experimental viscosity and thermal conductivity of nanofluids with the basefluid. C_η and C_k are the viscosity and thermal conductivity enhancement coefficients. The C_η/C_k values calculated for the MAXene nanofluids at temperatures 303 K and 323 K are given in Table 3.2.2. Usually, the addition of ceramic and metallic nanofillers in basefluids resulted in an increase in viscosity and therefore, C_η/C_k is always positive. In this MAXene nanofluid design, it can be understood from tabulated values, the ratio of viscosity and thermal conductivity enhancement coefficients is much lower than the critical limit of 4. In all concentrations (0.01 to 0.25. Vol%) of Ti_3SiC_2 MAXene nanosheets, the C_η/C_k values are not only lower than zero but also they fall in the negative range. The negative value is a result of the decreased viscosity of MAXene nanofluids with MAXene dispersoids.

Table 3.2.2: Ratio of viscosity and thermal conductivity enhancement coefficients as a function of Vol% of MAXenes at two different temperatures

Sample	C_η/C_k	
	303 K	323K
PG-TSC- 0.01Vol%	-0.86	-0.17
PG-TSC- 0.02Vol%	-1.73	-0.34
PG-TSC- 0.1Vol%	-2.64	-0.78
PG-TSC- 0.2Vol%	-2.03	-0.47
PG-TSC- 0.25Vol%	-1.38	-0.28

A performance comparison of rheological and thermal properties of MAXene nanofluid with other nanofluids reported in the literature is given as Table 3.2.3. It can be understood that 2D nanosheets such as born nitride and graphene is reported to have the maximum enhancement in thermal conductivity. However, their performance is limited by the unfavourable increase in viscosity. In the case of MAXene nanofluid, the viscosity is reduced by 30 % compared to the basefluid along

with comparatively higher enhancement in thermal conductivity. Both these properties make it an excellent nanocoolant.

Table 3.2.3: Nanocoolant performance comparison of various nanofluids with the MAXene nanofluid.

Nanofiller	basefluid	Vol/ Wt % of filler	Viscosity ratio	Thermal conductivity enhancement (%) at 323 K	Ref
Fe_3O_4	kerosene	9.5	3.4	23.0	[Shima *et al.* 2010]
TiO_2	ethylene glycol-water (50:50)	1	not reported	10.5	[Redy *et al.* 2013]
Graphene	water	0.056	not reported	64	[Tessy Theres et al. 2013]
MWCNT	ethylene glycol	0.03	1.3	40	[Aravind *et al.* 2011]
ZnO	propylene glycol	2	0.8	25	[Suganthi *et al.* 2013]
ZrO_2	transformer oil	1.7	40	12.4	[Sreeremya *et al.* 2014]
Boron nitride	water	6	7.2	160	[Zhi *et al.* 2011]
Al_2O_3	ethylene glycol-water (55:45)	2	3.50	7.5	[Kumaresan *et al.* 2012]
Boron nitride	mineral oil	0.1	>1	75	[Jaime *et al.* 2012]
CeO_2	transformer oil	0.7	14	14.6	[Sreeremya *et al.* 2014b]
Ti_3SiC_2 MAXene	propylene glycol	0.25	0.7	45	present study

3.2.4.7 Lubricating Performance of the Nanofluids

The lubrication effect by the well dispersed MAXene nanofluid is studied by ball on disc wear and friction technique, and the results are presented in Figure 3.2.16. In fact, in most of the earlier works, attempts were made only to report the thermal properties. Their tribological performance is seldom reported. The lubricating effect of the nanofluids is also significant like thermal conductivity since high friction, heat generation, increased viscosity, and high wear are interrelated

factors for deteriorating the performance of any structural component in a typical mechanical operation. From Figure 3.2.16 (a) it is seen that the frictional force is largely decreased when the MAXene functional nanofluid is introduced in the wear track. The bare steel ball is exerting a high frictional force against the steel disc in the absence of any MAXene nano lubricant. The frictional force falls approximately 4 times compared to the bare steel ball when the MAXene nanofluids are introduced. It is known that the propylene glycol basefluid possesses a considerable lubrication property. However, when the addition of conventional ceramic nanofillers with this basefluid is employed, it causes an increase in the fluid viscosity that deteriorates its inherent lubricating property. In spite of the increase in the thermal transport in a typical ceramic nanofluid, such a loss in the lubricating property due to the relatively high hardness of the ceramic nanomaterial and high viscosity of ceramic nanofluids makes most of the nanofluids unsuitable for the thermal fluid applications [Pena-Paras *et al.* 2015]. Surprisingly, the addition of Ti_3SiC_2 MAXene nanosheets does not seem to affect the lubricating characteristics of the basefluid, propylene glycol. MAX phase materials are already known to exhibit self-lubricating nature [Barsoum *et al.* 1996]. Several ceramic and polymer composites showed low coefficient of friction and excellent wear resistance than the matrix when Ti_3SiC_2 was used as active filler [Xiaoliang *et al.* 2013]. With this lubricating effect of propylene glycol-MAXene nanodispersion, the nanofluid not only tender the thermal management function but also retain the minimum frictional force, and thereby avoid the heat generation and wearing of the structural parts.

Figure 3.2.16 (b) demonstrates the decrease in the coefficient of friction (COF) values when the MAXene lubricating nano fluid is applied to the contact point between the ball and disc. When polypropylene glycol is introduced without any MAXene nanolubricant, the COF value decreased from 0.54 to 0.12. When nanofluid containing 0.2 Vol% MAXene nanosheets is employed, the coefficient of friction value decreased to a lower value of 0.1. It is worth noticing that the wear resistance is largely improved in the presence of MAXene nanofluids.

The optical microscopic images of the steel balls after wear tests at various conditions are given in Figure 3.2.17 which indirectly indicates the lubricating action of the MAXene nanocoolant. It is observed that in the absence of MAXene

nano lubricant, the surface of the test specimen reveals a strong and deep wear scar in the diameter of ~ 1450 µm. This was reduced to ~ 750 µm when propylene glycol is added without MAXene nanosheets. The wear diameter further decreased to 670 µm at 0.2 Vol% additions of MAXene nanosheets indicating the layered MAXene nanostructures offered lubricating effect and improved the wear resistance.
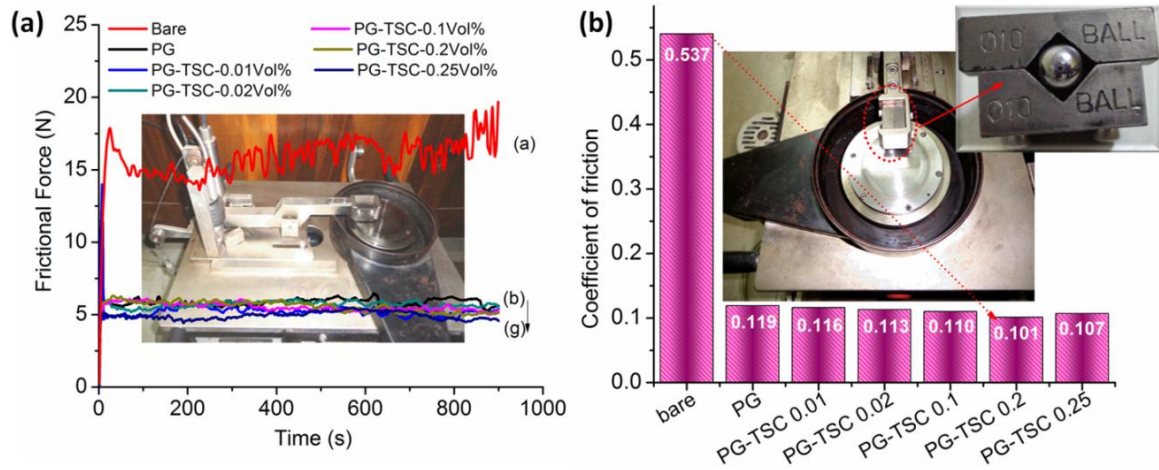
Figure 3.2.16: The tribological performance of the MAXene nanofluids (a) frictional force and (b) coefficient of friction with respect to different Ti₃SiC₂ MAXene loading.
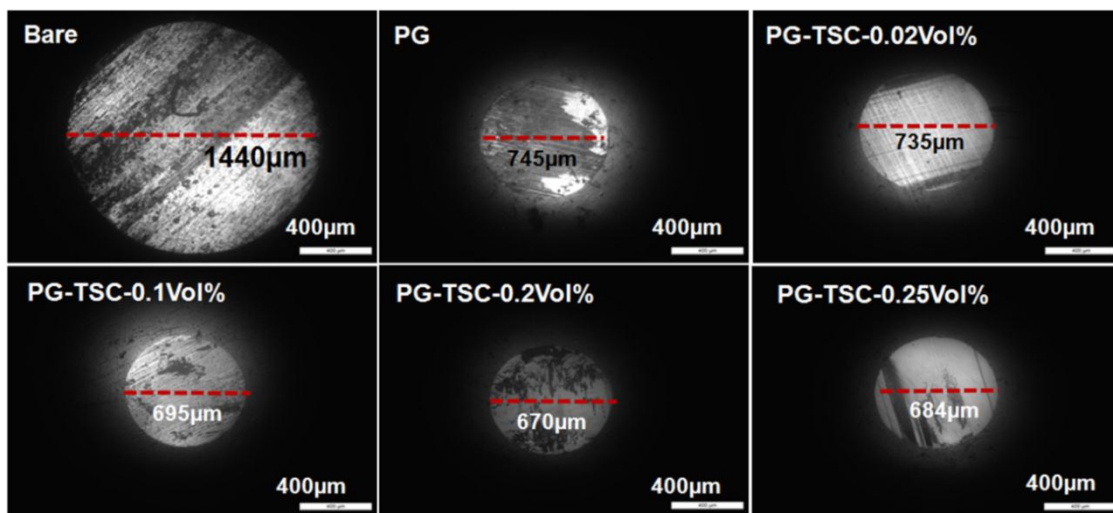
Figure 3.2.17: The optical microscopic images of the wear scar formed on the steel ball at different experimental conditions. The wear diameter in each case is marked as a red line.

The roughness of wear tracks were analysed by surface profilometry. The corresponding profilometer curves showing the hills and valleys on the wear scar

are given in Figure 3.2.18. It is seen that depth of the valleys and the height of the hills are more prominent in the absence of nanofluids. The surface appears smooth when the MAXene nanofluid is used. The wear scars on steel ball under no lubrication condition have a surface roughness of 765 nm. The value is estimated as 215 nm when propylene glycol is used. The surface roughness further decreased when nanofluid containing MAXene nanosheets is used. The wear scar of the steel balls with 0.1 and 0.2 Vol% MAXene nanosheets possess reduced roughness of 125 and 138 nm, respectively. All these observations reveal that the nanofluid developed in the present work is acting as a multifunctional nanofluid with controlled rheological performance, enhanced thermal transport properties, and improved lubrication properties.
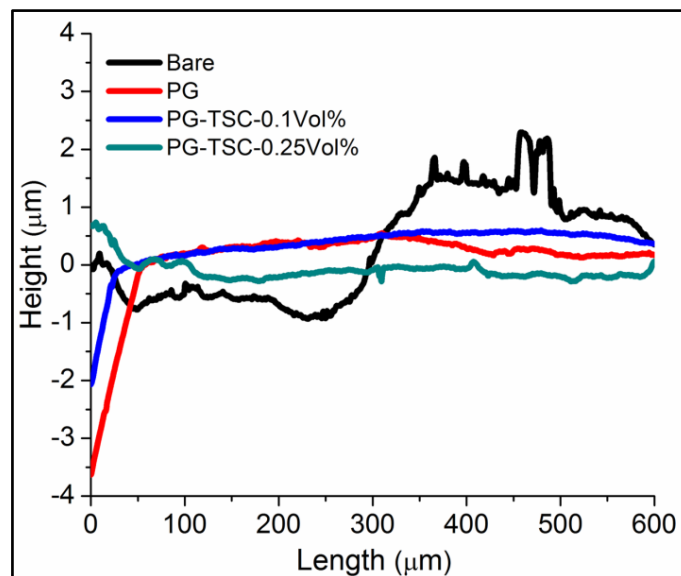
Figure 3.2.18: The Surface profilometer curves of the steel balls at different lubrication conditions.

3.2.4.8 Electrical Properties of the Nanofluids

The electrical conductivity of the nanofluid is also important since some applications required fluids with least electrical conductivity. The electrical conductivity of the nanofluids with respect to MAXene concentration was measured at room temperature, and the results are presented in Figure 3.2.19 The electrical conductivity of the nanofluid is increasing with an increase in the amount of MAXene nanosheets. The basefluid, propylene glycol exhibits an electrical conductivity of < 0.1 μS cm^{-1} which is increased to 2.5 μS cm^{-1} when the MAXene

content in the fluid increased to 0.25 Vol%. Since the volume fraction of the MAXene nanomaterial in the nanofluids is less, there is no abrupt increase seen in the electrical conductivity. The electrical conductivity increase in MAXene nanofluid is negligible when compared with graphene oxide based nanofluids [Tessy Theres *et al.* 2010].
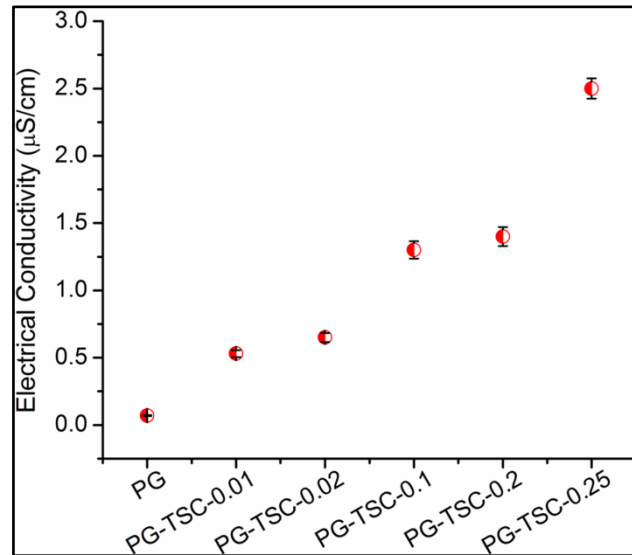
Figure 3.2.19: The electrical conductivity of the MAXene nanofluids at room temperature as a function of MAXene loading.

3.2.5 Conclusions

In this work, a new nanofluid is designed and systematically investigated for its promising beneficial properties. In situ processing of Ti_3SiC_2 MAXene nanosheets in propylene glycol medium via shear induced micromechanical cleavage technique resulted in highly stable surfactant-free thermal nanofluid. This new nanofluid qualifies all the necessary requirements for a heat-transport thermal management fluid. The salient features of the Ti_3SiC_2 MAXene nanofluids processed in this work are:

1. The shear-induced micromechanical cleavage technique successfully resulted in mixed morphologies of MAXene nanostructures consist of 10 nm size MAXene dots and 30-200 nm sized 2D-nanosheets with the surface associated OH-functional groups that eventually retain the colloidal stability.

2. The rheology study confirms that the MAXene dispersed polypropylene glycol nanofluid attains unusually decreased viscosity even when the solid fraction

of MAXene is increased. At a concentration of 0.2 Vol%, MAXene dispersion showed 30 % reduction in viscosity. The shear rate v/s viscosity flow curves strongly suggests the Newtonian flow behaviour of nanofluid. Such a control over viscosity favorably increases the pumpabilty (easiness of pumping) of MAXene nanofluid that is necessary for ideal circulation during cooling operations.

3. The thermal property studies strongly indicate the nanolayered; mixed morphologies of stable MAXene nanostructures significantly increase the bulk thermal conductivity due to percolation mechanism. The nanofluid prepared with 0.25 Vol% of MAXene dispersoids showed a 15 % increase thermal conductivity at room temperature, which was further enhanced to 45 % at a temperature of 323 K.

4. Interestingly, the MAXene-propylene glycol nanofluids offer a lubrication property that was confirmed by ball-on-disc wear and friction test. Under dry friction test condition, a coefficient of friction value 0.54 was seen which decreased to 0.1 when the fluid containing 0.2 Vol% MAXene dispersion was employed. The self-lubricating property of MAXene nanosheets and reduced viscosity are the key players in this phenomenon. Such lubrication effect decreases the wearing of structural parts, and thereby improves the efficiency when it is subjected to an actual application.

Ultimately, the study reveals that the MAXene nanofluid is an all-rounder with multifunctionalities with respect to rheo-control, thermal conductivity, and lubrication property that makes the system an effective nanocoolant for thermal management applications.

CHAPTER 4

MXenes- Unveiling the Hidden Versatility
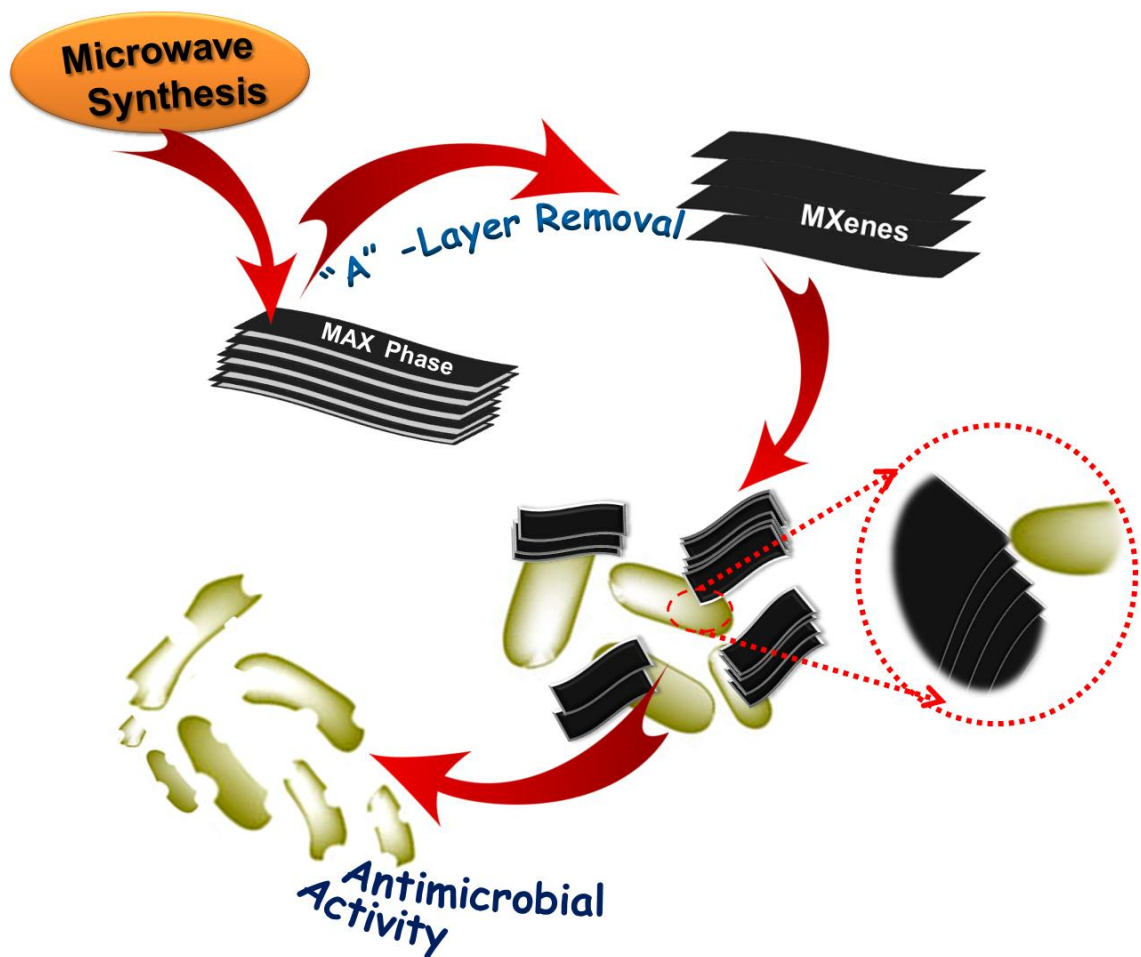
4.1: Microwave Synthesis of Ti$_3$AlC$_2$ MAX Phase

4.1.1 Abstract

In this chapter, processing of Ti$_3$AlC$_2$ MAX phase was sucessfully attempted via microwave heating of TiH$_2$/Al/C reactants. When the powder compacts made from these reactants are placed inside the microwave cavity and heat treated at temperatures 1000, 1100, and 1200 ℃, they interacted with microwaves readily and effectively so as to produce Ti$_3$AlC$_2$ powders with realtively high purity at a maximum reaction temperature of 1200 °C. Addition of nano SiC as *in situ* susceptor was also attempted to enhance the reaction kinetics. It was confirmed that the nano SiC accelerated the Ti$_3$AlC$_2$ formation and decreased the formation temperature from 1200 to 1100 °C with significantly low TiC content.

4.1.2 Introduction

Among the various MAX phase ternary carbides, titanium aluminum carbide (Ti$_3$AlC$_2$) is a promising structural ceramic material with technological importance, due to its reasonably good electrical conductivity, ready machinability, and better oxidation resistance over the temperature range from 1100 to 1350 ℃. Crystallographically, Ti$_3$AlC$_2$ MAX phase is isostructural with the well-known Ti$_3$SiC$_2$ MAX phase ceramics. It possess hexagonal unit cell with lattice parameters of $a \sim$ 0.307 nm and $c \sim$ 1.857 nm [Tzenov and Barsoum 2000]. The structure consists of hexagonal nets of Al-atoms which are separated by layers of edge-sharing Ti$_3$C$_2$. Ti$_3$AlC$_2$ MAX phase material is mechanically soft in nature with the Vickers microhardness value of ~3.5 GPa. However, it is elastically stiff. It's reported Young's modulus and shear modulus values are 297 GPa and 124 GPa, respectively. The compressive and flexural strength values measured for the dense Ti$_3$AlC$_2$ ceramics are ~560 and 375 MPa, respectively. The electrical resistivity value is ~0.35 μΩ m at room-temperature. The measured coefficient of thermal expansion, up to the temperature of 1200 °C is around 9.0×10^{-6} K^{-1} which is matching closely with alumina ceramics, a well accepted structural ceramics. It is known that alumina ceramics fail catastrophically due to poor thermal shock resistance. Since Ti$_3$AlC$_2$ has high damage tolerance and offer a kind of plasticity via shear-band formation,

and also has the matching coefficient of thermal expansion property over alumina, this is one of the emerging reinforcement materials to make reliable and high performance alumina composites.

Pietzka and Schuster processed this material successfully via sintering technique, for the first time [Pietzka *et al*. 1994]. Other high temperature processing methods like hot pressing, spark plasma sintering, and hot isostatic pressing etc. were also attempted successfully and well documented. Very recently, Naguib *et al.* synthesised 2D Ti_3C_2 nanosheets from bulk Ti_3AlC_2 by selective etching of Al layers with con. HF acid [Naguib *et al.* 2011]. These new class of 2D material was named as MXene. The Ti_3C_2 MXene quickly attracted great attention owing to their superior energy storage capacities. Scientists proposed Ti_3C_2 MXene as a candidate for Li-ion batteries and super capacitors [Naguib *et al.* 2012a; 2012a; Mashtalir *et al.* 2013; Naguib *et al.* 2013]. This changed the scenario entirely and created unlimited demand for Ti_3AlC_2 MAX phase as the base material for the synthesis of Ti_3C_2 MXenes. Thus, the development of simple process for the synthesis of Ti_3AlC_2 is extremely important due to its acceptance as potential damage tolerant reinforcement phase to industrial ceramics like alumina and zirconia, and also as material for energy storage.

Commercially Ti_3AlC_2 is produced and marketed only by a very few companies and the process know-how is patent protected. If we look into the national availability of this material, no company in India is producing this material. So the process know-how on the synthesis of high purity Ti_3AlC_2 through economically viable and cheaper way has national importance.

Microwave heating is today a well reported processing technique and recognized as a rapid method for obtaining ceramics within short durations [Clark and Sutton 1996]. Synthesis of Ti_3AlC_2 MAX phase *via* microwave synthesis route is not documented so far and this motivated us to explore the microwave technique for synthesizing Ti_3AlC_2 powders. Microwave energy is an electromagnetic energy which falls in the frequency range of 300 MHz to 300 GHz. In microwave heating, materials couple with microwaves and volumetrically absorb the electromagnetic energy, and convert it into heat. This type of heating is different from conventional approaches where heat transfer is governed by mechanisms like conduction, radiation, and convection. In conventional method, heating occurs first on the

material's surface followed by inward heat transport. Therefore, there is a temperature difference between the surface and core of the material. On the other hand, in microwave heating method, materials directly interact with microwave energy, and depending upon their dielectric nature they absorb microwaves and then convert it into heat energy. Microwave heating has several advantages over conventional heating. Microwave enables faster heating and thereby reduces the energy consumption [Yadoji *et al.* 2003; Clark *et al.* 2000; Oghbaei and Mirzaee 2010].

However, few limitations are encountered in microwave processing. Since the microwaves accelerate the reaction from bulk to the surface, the sintered ceramics were found to have poor microstructure homogeneity throughout the product. Another phenomena called temperature runaway (catastrophic overheating of specimen) is also seen while processing materials such as SiO_2, Al_2O_3, ZrO_2, Fe_3O_4, etc. [Sutton *et al.* 1989]. These issues promoted hybrid heating approach. This is performed by using a microwave susceptor material, which is a good microwave absorber at low temperatures, and facilitates initial heating by transferring its heat to the sample via conventional heating mechanisms. The heat profile of different heating system depicted in Figurer 4.1.1 shows advantage of microwave hybrid heating over other two methods.
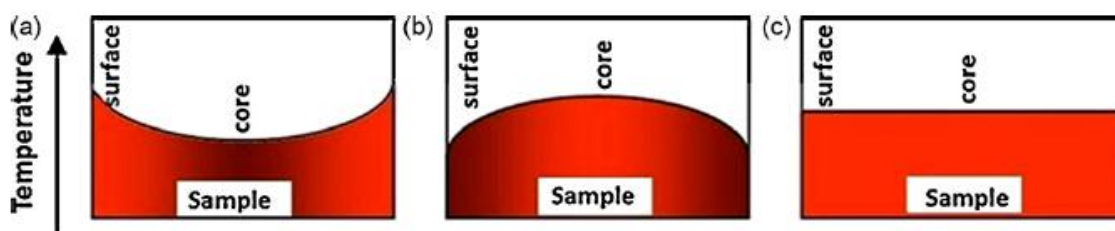
Figure 4.1.1: Temperature profile within the sample in: (a) conventional heating, (b) microwave heating, and (c) microwave hybrid heating [Oghbaei *et al.* 2010]

Microwave heating has been successfully utilized for the synthesis and densification of wide variety of ceramic materials, both oxide and non-oxide ceramics. However, use of microwave energy for the synthesis of MAX phase is seldom reported. Recently, Wang *et al.* used microwave heating method to synthesize high purity Ti_3SiC_2 from the mixtures of titanium, silicon, and graphitic

carbon. They achieved a purity of 98 vol% by a two-step heating process of initial heating to 1480 °C/ 30 min followed by dwelling at 1300 °C/ 60 min [Wang *et al.* 2014]. However, there is no report on the microwave synthesis of Ti$_3$AlC$_2$ and in this work, we aimed to achieve it. Graphitic carbon is a good microwave absorber even at low temperatures and similarly the loosely compacted metal powders are also highly receptive to microwaves at elevated temperatures. Hence, when TiH$_2$/Al/C powder mixture is subjected to microwaves, a good microwave interaction is envisaged that subsequently produce the desired reaction temperatures via dielectric heating. In this work, microwave hybrid heating is also followed in which SiC blocks were used as external susceptor material to ensure uniform volumetric heating. SiC is reported as excellent external susceptor for microwave sintering of ceramics [Janney *et al.* 1992]. In addition to the use of SiC blocks as external susceptor, we also adopted a new idea of adding SiC nanopowders as *in situ* susceptors to enhance the micro-thermal heating in localized environments and accelerate the reaction kinetics. For this, separate experiments were also carried out with 0.1 mol % nano SiC powder added to the Ti$_3$AlC$_2$ precursors. The effect of nano SiC on Ti$_3$AlC$_2$ phase formation is also briefly attempted for the first time and the results are discussed.

4.1.3 Experimental Details

4.1.3.1 Materials

Powders of Titanium hydride (TiH$_2$) (Sigma Aldrich), Aluminium (Al) (sd-Fine chemicals), and Graphite (C) (SRL chemicals), were used as precursors. Silicon carbide (SiC) powder (Sigma Aldrich) was used as *in situ* susceptors. Toluene (sd-Fine chemicals) was used as solvent medium for mixing the powders.

4.1.3.2 Synthesis of Ti$_3$AlC$_2$ by Microwave Hybrid Heating

TiH$_2$/Al/C with molar ratio of 3/1.2/2 was used for the synthesis of Ti$_3$AlC$_2$. Instead of Ti metal powders, TiH$_2$ was used considering its highly reactive nature. TiH$_2$ nanopowder was preferred because nanometric powders offer high surface area that might possibly increase the reaction kinetics. The 20 % excess Al was taken to compensate any evaporative loss at elevated temperatures. In a typical synthesis, the powders weighed in the required compositions were mixed well by ball milling in toluene

medium for 2 h. The mixture was then dried, and compacted to green pellets. The powder compacts were placed into quartz ampule, evacuated and sealed. The sealed quartz ampule was then subjected to microwave hybrid heating at 1000 °C, 1100 °C, and 1200 °C with a fast heating rate of 25 °C/min and a soaking time of 1 h. The effect of SiC as *in situ* susceptor was carried in the same way except that 0.1 mol% nano SiC powder was added to the reaction mixture during ball milling step. The microwave furnace used in this study was supplied by VB Ceramics, Chennai, which is equipped with micro-controller to conduct the experiment at controlled heating rates. The microwave power output is 2 KW @ 2.45 GHz. For comparing the efficiency of microwave synthesis with conventional sintering, an experiment was conducted in conventional inert tube furnace at 1200 °C/ 1 h with a heating rate of 10 °C/min. The obtained dense compact was powdered and characterized for the evolution of Ti_3AlC_2 phase. The experimental steps involved are schematically represented in Figure 4.1.2.

The experiments were conducted with much care taking into account of H_2 gas evolution during microwave heating of the reactants. Initial attempts clearly indicated the release of H_2 gas and sometimes resulted in the bursting of quartz ampule. Therefore, a dehydrogenation of TiH_2+Al+C reactant mixture was carried out at 400 ^{o}C in Ar atmosphere for about an hour before sealing the powder compacts in quartz tube.
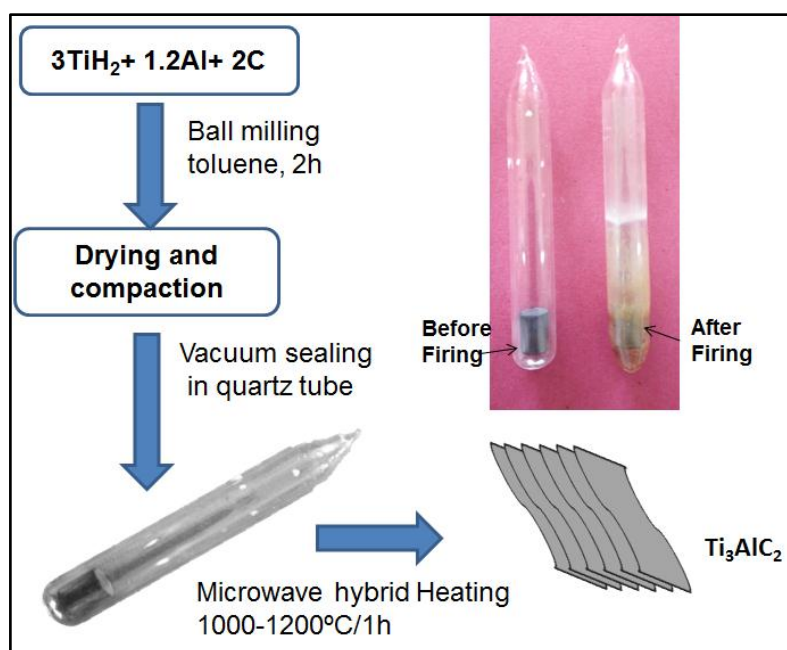
Figure 4.1.2: Schematic representation of the experimental steps involved in the synthesis of Ti_3AlC_2 by microwave hybrid heating

4.1.3.3 Characterizations of Microwave Synthesized Ti₃AlC₂

The phase formation and purity of Ti_3AlC_2 formed at various reaction conditions were systematically analysed using powder X-ray diffraction (X'Pert Pro, Philips X-ray diffractometer) with a monochromator on the diffraction beam side (Cu Kα radiation, λ=0.154 nm). The fractured microstructures of the sintered compacts were recorded using ZEISS EVO 18 Scanning Electron Microscopy (SEM) equiped with EDX facility. Transmission Electron Microscopy (TEM) images of the powdered samples were carried out using FEI Tecnai 30G2S-TWIN, operated at an accelerating voltage of 300 kV.

4.1.4 Results and Discussion

4.1.4.1 Powder X-ray Diffraction Analysis

Figure 4.1.3 shows the results on the different crystalline phases evolved from the compacted reactant mixtures while microwave heating was carried out at temperatures 1000 °C, 1100 °C, and 1200 °C under vacuum sealing conditions. The XRD pattern corresponding to the product obtained at 1000 °C/1 h confirmed that the initial reactant mixture in the molar ratio 3/1.2/2 produced crystalline Ti_2AlC, $Ti_3AlC_{2,}$ and TiC. The powder XRD further indicates that there are no peaks corresponding to the starting materials. In XRD pattern, the peaks at 2θ =13.05° and 39.57° ascertained that Ti_2AlC is the predominant phase formed at 1000 °C. The peaks are identical with the standard reference X-ray pattern published in ICDD file no 00-029-0095. However, the reaction condition resulted in the formation of considerable amount of TiC also. The formation of Ti_3AlC_2 was evident but the corresponding peak intensity is weak which suggests the Ti_3AlC_2 phase formation started at 1000 °C but has not completed. It is noteworthy to mention that the 2θ values corresponding to the intensity maximum reported for Ti_3AlC_2 and Ti_2AlC are very close, and it makes difficult to identify, as seen in Figure 4.1.3 (A). However, the magnified patterns of this region given in Figure 4.1.3(B) clearly distinguish the peaks corresponding to Ti_3AlC_2 and Ti_2AlC with clarity. When microwave heating is employed at 1100 °C, the phase formation is improved. The relative Ti_3AlC_2 peak intensity at 2θ = 9.5° and 39.04° is considerably enhanced. The peaks are well matched with ICDD file no. 00-052-0875. It is worthwhile to note that there is no peaks correspond to Ti_2AlC. However, the final product still has undesired TiC in a large amount suggesting that a temperature of 1100 °C not sufficient to accomplish maximum purity. When the reaction temperature is further increased to 1200

°C, an increased amount of Ti₃AlC₂ MAX phase formation is successfully obtained. It is worth to mention that relatively pure Ti₃AlC₂ is obtained at 1200 °C with a soaking time 1 h and fast heating rate of 25 °C/min.
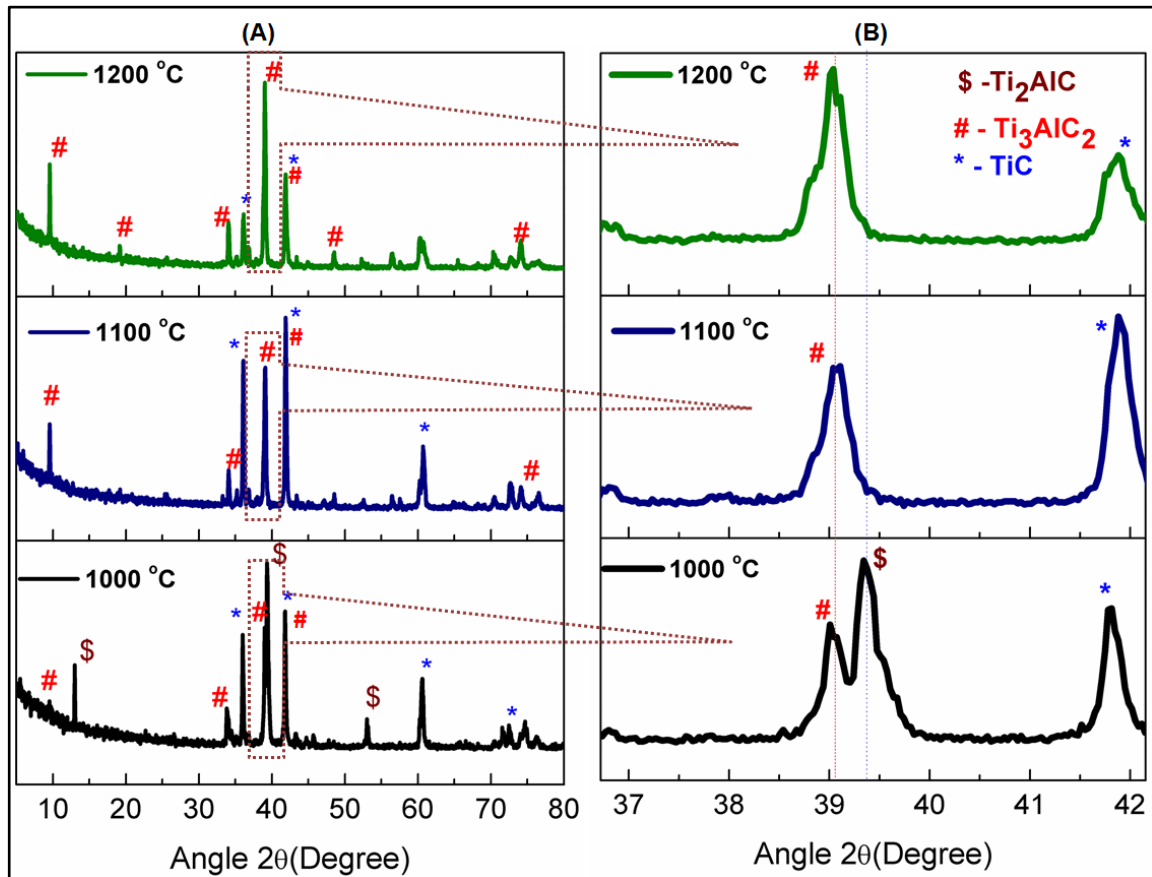
Figure. 4.1.3 (A) Powder X-ray diffraction patterns of the final products obtained after microwave hybrid heating at different temepratures, and (B) the enlarged portion showing change in the intensity and compostion with repect to temperature

Compared to the simple pressureless sintering technique, microwave technique appears to be even simpler and faster way to achieve Ti₃AlC₂ MAX phase reaction condition. The synthesis of Ti₃AlC₂ MAX phase with almost same purity by conventional pressureless sintering method required a temperature of 1350 °C with soaking time of 4-5 h with a slow heating rate of 3 °C/min. Under the given microwave heating condition, the undesirable TiC phase is also decreased to an unprecedented level. Ti₃AlC₂ was formed by the reaction between Ti₂AlC and TiC at higher temperatures. Since the peak locations corresponding to (105) plane of Ti₃AlC₂ and (200) plane of TiC are very close (2θ value 41.816° and 41.808°, respectively), it is very difficult to distinguish them. So the TiC peak at 2θ = 35° was considered for comparing the relative intensity of Ti₃AlC₂ and TiC

in the final product. The product phases evolved at different reaction temperatures is summarized in Table 4.1.1

Table 4.1.1: Summary of the phase analysis of the samples synthesised by microwave hybrid heating at different temperatures

Temperature	Phases present
1000 °C	Ti_2AlC, TiC, Ti_3AlC_2
1100 °C	Ti_3AlC_2, TiC
1200 °C	Ti_3AlC_2, TiC

Based on these observations, the following reaction sequences are proposed for the formation of Ti_3AlC_2 from the precursor powders of TiH_2, Al and C. It is envisaged that at around 660 °C melting of Al occurred, and then the Al melt reacted with Ti to form Ti–Al intermetallics such as Ti_3Al and TiAl at around 800 °C. When the temperature is increased, Ti_2AlC, Ti_3AlC_2, and TiC were formed by the diffusion of carbon into Ti–Al intermetallics and finally at higher temperature, these phases reacted to form Ti_3AlC with minor TiC impurity.

$$4Ti_{(s)} + 2Al_{(l)} \rightarrow Ti_3Al_{(s)} + TiAl_{(s)} \qquad (4.1.1)$$

$$Ti_3Al_{(s)} + 2C_{(s)} \rightarrow Ti_2AlC_{(s)} + TiC_{(s)} \qquad (4.1.2)$$

$$TiAl_{(s)} + Ti_3Al_{(s)} + TiC_{(s)} + 2C_{(s)} \rightarrow Ti_2AlC_{(s)} + Ti_3AlC_{2(s)} \qquad (4.1.3)$$

$$Ti_2AlC_{(s)} + 2TiC_{(s)} \rightarrow Ti_3AlC_{2(s)} \qquad (4.1.4)$$
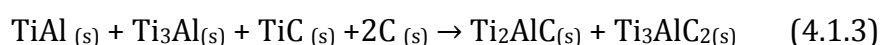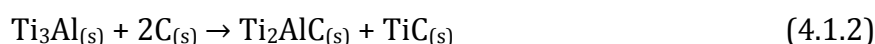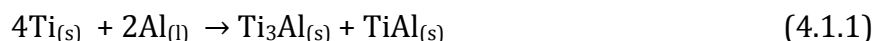
A comparison of microwave heating with the conventional solid state reaction synthesis for obtaining Ti_3AlC_2 MAX phase under identical heating temperature of 1200 °C is monitored using powder X-ray technique and the results are presented in Figure 4.1.4 (A). As discussed earlier, the microwave heated samples showed Ti_3AlC_2 MAX phase at 1200 °C with relatively high purity. Whereas, the conventional sintering at identical reaction temepraturs failed to produce phase pure Ti_3AlC_2. It is observed that the reaction is still in the initial stage and the presence of only Ti_2AlC phase is noticed in the final product. Ti_2AlC and TiC are the major phases formed in this case. The XRD pattern, however indicates, the evolution

of Ti_3AlC_2 as observed by a small peak at $2\theta \sim 39°$ in the maginified XRD pattern and the same is shown in Figure 4.1.4 (B).
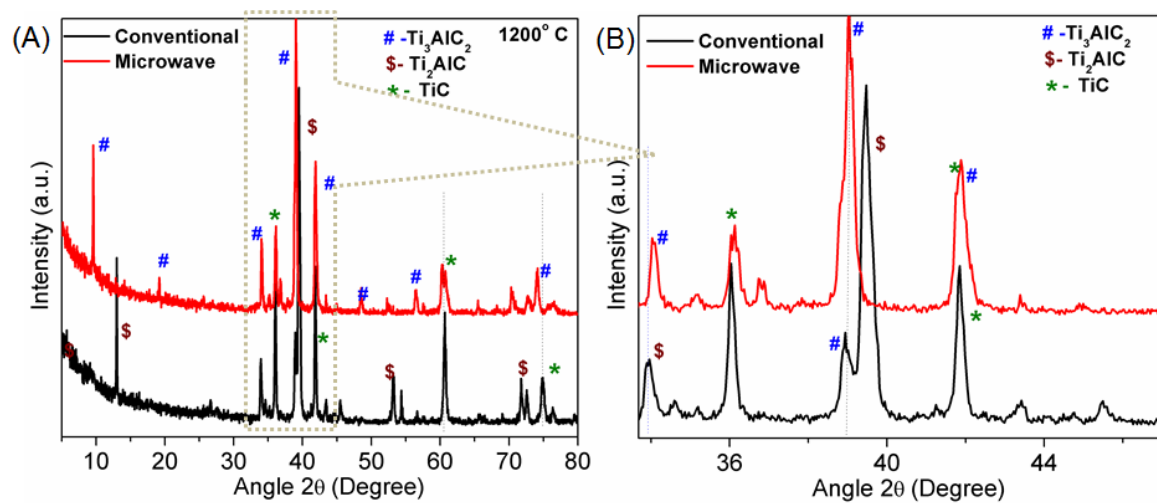
Figure 4.1.4 Powder X-ray diffraction patterns the final Ti_3AlC_2 products obtained via microwave hybrid heating and conventional pressureelss sintering at 1200 °C/1 h

4.1.4.2 Microstructure Analysis

Figure 4.1.5 shows the microstuctures of the final products obtained via microwave heating at variuos temperatures. It can bee seen that the characteristic layered structures started to form even at 1000 °C (shown by white arrow in Figure 4.1.5 (A)). The presence of loosely packed particles with limited grain growth are also evident. As the tempearture is increased further to 1100 °C, the grain size as well as the dimensions of the MAX phase layers is also increased gradually (Figure 4.1.5 (B)). When the temperature was raised to 1200 °C, a compact, dense layered microsturcture is clealrly seen (Figure 4.1.5 (C)). The grains are intact and induvidual layers are more apparent. However, the sample subjected to conventional sintering at 1200 °C/1 h for the sake of comparison failed to show any such dense layered morphology (Figure 4.1.5 (D)).

A high magnification SEM micrographs of the sample recieved from microwave heating at 1200 °C is presented in Figure 4.1.6. It shows the nanolayered arrangement of Ti_3AlC_2 bulk material. The EDX spectrum of the marked area confirm the composition of Ti_3AlC_2. The powdered sample was further analysed with TEM and the images are given in Figure 4.1.7. The TEM also supported the results obtained from SEM (layeres shown by the red arrow).
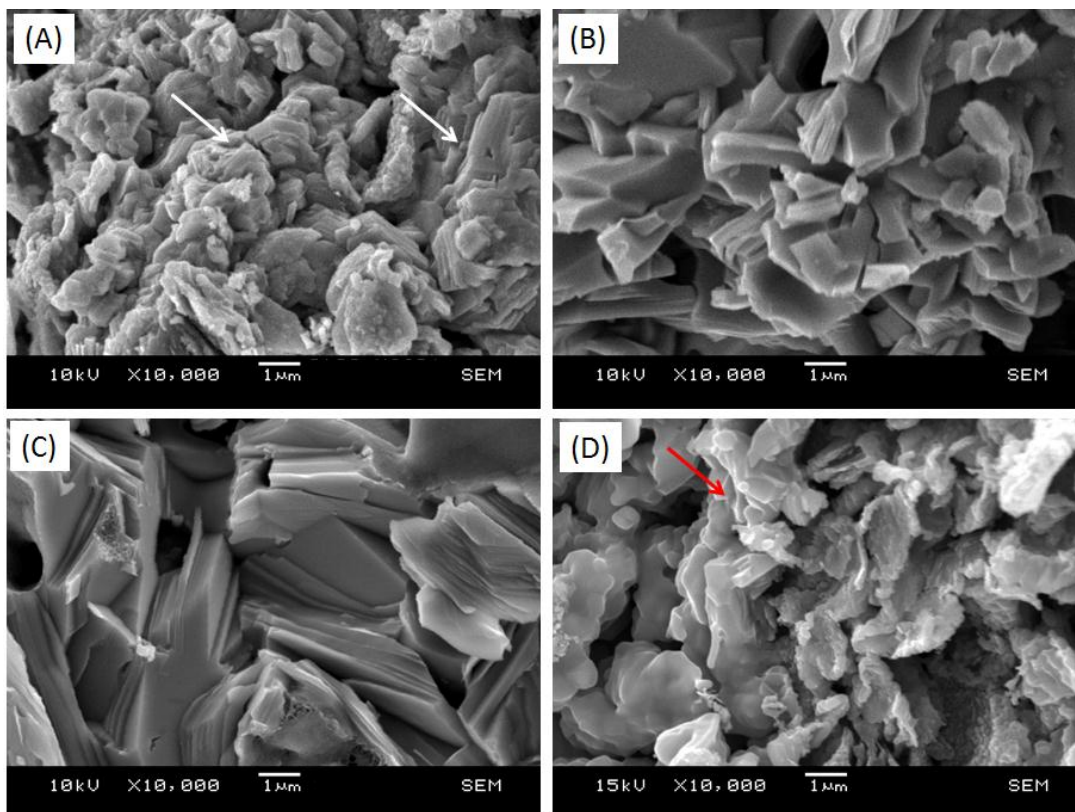
Figure. 4.1.5 SEM micrographs of final products obtained after microwave hybrid heating at (A) 1000 °C/1h, (B) 1100 °C/1h, (C) 1200 °C/1h, and (D) conventional heating at 1200 °C/1h
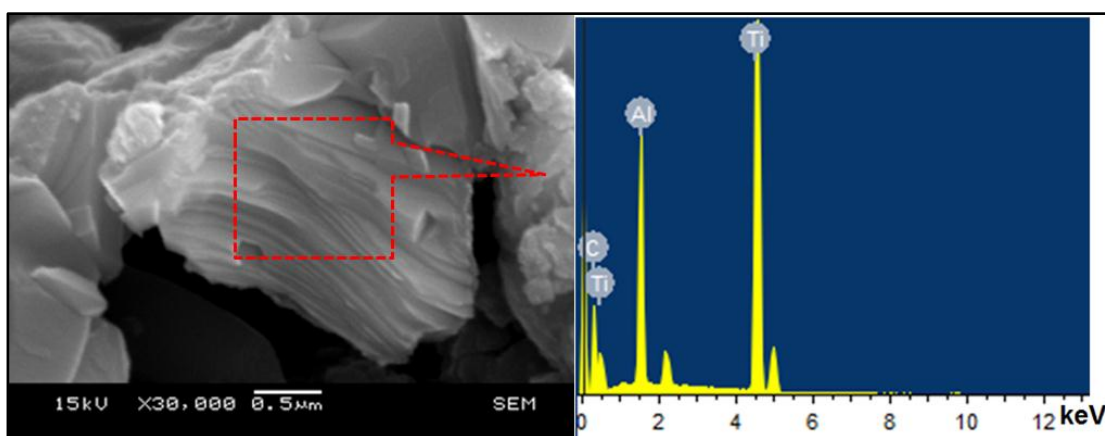
Figure. 4.1.6: High magnification SEM micrographs of Ti$_3$AlC$_2$ obtained after microwave hybrid heating 1200 °C/1 h, and the EDX spectra of the marked area
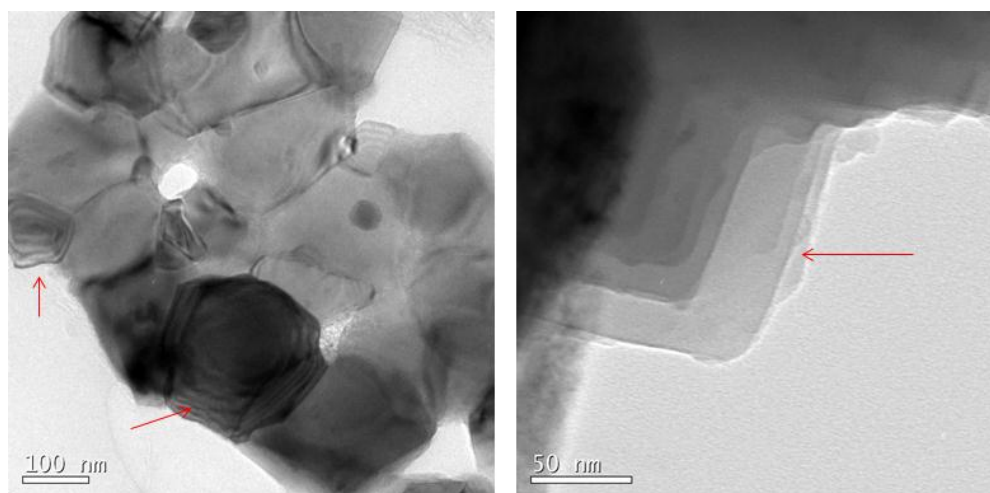
Figure. 4.1.7: TEM image of Ti$_3$AlC$_2$ obtained after microwave heating 1200 °C/1h

4.1.4.3 Effect Addition of SiC as an *in situ* Susceptor

To further promote the formation of Ti$_3$AlC$_2$ phase and accelerate the reactions at temperatures as low as 1100 ℃, the addition of nano SiC as *in situ* microwave absorber was employed and the attempt yielded promising results. Only 0.1 mol% SiC was added along with the desired precursors. SiC has dielectric constant as high ε$_r$ ~ 9.66, that makes this material a good absorber of microwave and the absorption generates heat up to 600 °C within few minutes once it is microwave irradiated. This aids faster diffusion pathways and enhanced mass transport. Surprisingly, we observed a reduction of 100 °C in the formation temperature compared to the normal microwave synthesis attempted without nano SiC. This is confirmed from the XRD analysis and the results are given in Figure 4.1.8. Ti$_3$AlC$_2$ with relatively high purity is seen at 1100°C. As seen in the XRD pattern corresponds to 1100 °C sintered sample, there is no Ti$_2$AlC formed and the intensity of TiC is also relatively less and also the results are comparable with that obtained at 1200 °C without SiC addition. When we raised the temperature to 1200 °C, the phase purity of Ti$_3$AlC$_2$ is increased to a large extent as evidenced by the large reduction in the intensity of TiC. As we pointed out earlier, the peak at 2θ ~ 41.8° is a combination of both Ti$_3$AlC$_2$ and TiC and the intensity reduction in this peak at 1200 °C suggests that contribution from TiC is negligible. This is also evidenced from the reduction in peak intensity of TiC peak at 2θ ~35°. In both the cases no peaks for SiC is observed since it is added in only 0.1 mol%. So it can be concluded that nano SiC addition further improved the phase formation at relatively low temperature compared to the conventional methods.
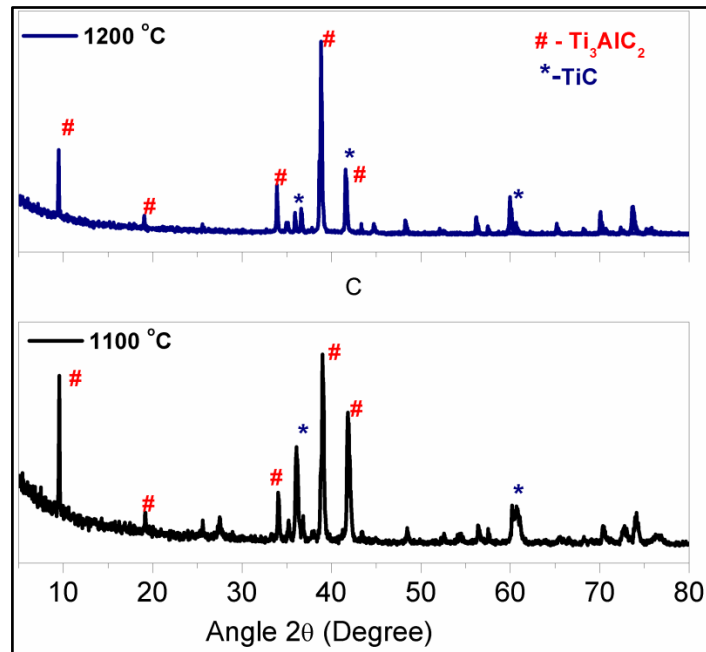
Figure. 4.1.8: (A) Powder X-ray diffraction patterns the final products ontained after microwave hybrid heating in presence of SiC as internal susceptor

The SEM images further confirmed the formation of nanolayered Ti_3AlC_2 and the images are depicted in Figure 4.1.9. It can be see that the phase formation was completed at 1000 °C itself, and at 1200 °C dense Ti_3AlC_2 layers are formed.
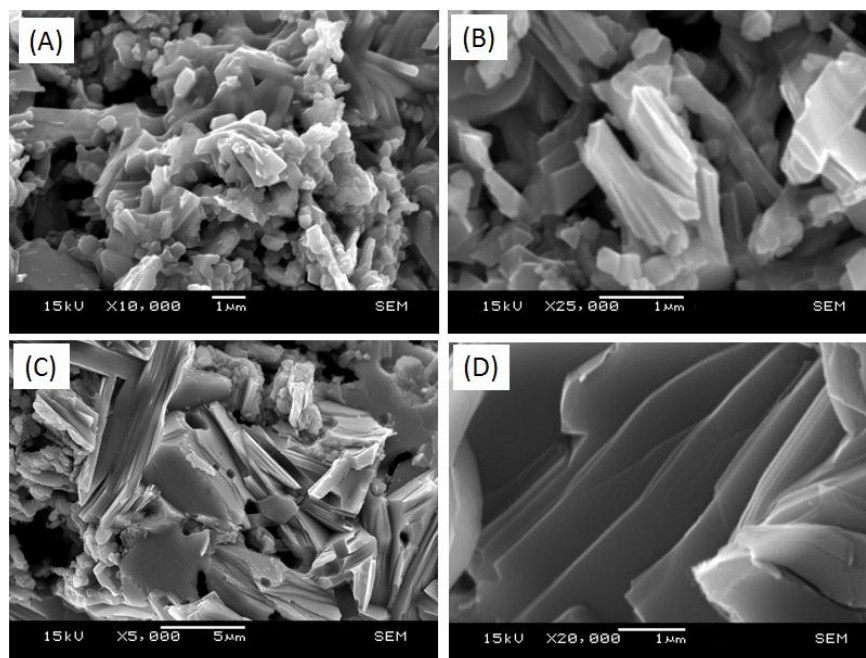
Figure 4.1.9: SEM micrographs of final products obtained after microwave hybrid heating in presence of nano SiC as *in situ* susceptor: (A and B) 1000 °C/1h, and (C and D) 1200 °C/1h

4.1.5 Conclusions

Microwave heating was successfully employed for obtaining Ti_3AlC_2 MAX phase with considerbaly low TiC impurity. The reaction mixture (TiH_2/Al/C) is readily interacting with microwaves and the system is capable of yielding significanlty pure Ti_3AlC_2 at 1200 °C with a soaking time of only 1 h and at a fast heating rate of 25 °C/min. When compared to conventional heating technique like pressureless sintering where the Ti_3AlC_2 is produced between 1350 to 1400 °C, microwave heating offers benefit by decreasing the phase formation temperature at least by 200 °C less, and also reduced the reaction time. Additionaly, use of nano SiC as *in situ* susceptor was introdcued for enhancing the reaction kinetics, that decreased the formation temperature further by 100 °C. In summary, a simple but faster way for obtaining Ti_3AlC_2 MAX phase is successfully accomplished in this work.

4.2: Antimicrobial, Antibiofilm and Cytotoxicity Properties of $Ti_3C_2T_x$ MXenes

4.2.1 Abstract

$Ti_3C_2T_x$ MXene derived from Ti_3AlC_2 MAX phases have been recently emerged as a potential material for desalination and purification membranes. The success of any water treatment system relied on its resistance against biological pathogens. In this study a detailed investigation was made on the antimicrobial and antibiofilm properties of $Ti_3C_2T_x$ MXene. The study reveals that $Ti_3C_2T_x$ MXene show time and concentrated dependent antimicrobial activity. The contact killings as well as intracellular reactive oxygen species are responsible for the antimicrobial activity. The material show excellent resistance against biofilm formation. The preliminary cytotoxicity studies conducted confirm that $Ti_3C_2T_x$ MXene is not toxic to mammalian cells.

4.2.2 Introduction

Studies on the biological viability and environmental feasibility of the newly invented nanostructured materials are essential and in fact inevitable before recommending these materials for any biotechnological and biomedical applications. For example, 2D graphene based nanosheets *(Graphene, Graphene oxide, Reduced Graphene oxide etc.)* are emerging fastly for the biomedical applications. By this time, attempts such as magnetic resonance imaging [Cong *et al.* 2009], photothermal therapy of cancer [Yang *et al.* 2010] and gene transfection [Feng *et al.* 2010] were already reported on the graphene nanostructures in the literature. Today, convincingly, graphene nanosheets are found to be non-toxic toward mammalian cell, which encourages the use of graphene in bio-related applications [Hu *et al.* 2010]. Another new 2D nanomaterial, MoS_2 nanosheets, has been recently proposed as NIR photothermal agent to kill Hela cells by utilizing its near-infrared (NIR) absorbance property [Chou *et al.* 2013]. Similarly, WSe_2 synthesized by DNA assisted exfoliation is also reported for its higher antibacterial activity against *Escherichia coli* K-12 MG1655 cells than graphene oxide [Bang *et al.*

2016]. Since nanomaterials are increasingly preferred for the betterment of human health, biomedical instrumentation and also for bioinert drug supports, enzyme and protein immobilization, biomedical experts strongly insist and recommend systematic studies on the bio-response behavior like antimicrobial efficiency/cytotoxicity for the newly proposed 2D nanomaterials.

2D $Ti_3C_2T_x$ *MXene* nanostructures (T represents surface termination groups such as –OH, -O, or –F) in the MAX phase family is a very recent innovation. While considering the environmental impact of these nanostructures, the biological properties mainly the cytotoxicity and their resistance against microbial attack are truly crucial and the science behind the biological response of this material received great attention for its complete exploration. At present, this material is, in a limited way, recognized for energy storage applications, particularly in electrochemical energy storage devices like Li- ion batteries. Research efforts are also being initiated to explore the possibility of using $Ti_3C_2T_x$ MXene for supercapacitors. Development of $Ti_3C_2T_x$ membranes for water purification through charge and size selective sieving of ions is recently demonstrated successfully. Ren *et al.* developed supported membranes by assembling 2D- Ti_3C_2Tx MXene nanosheets and studied the charge and size selective rejection of the ions and molecules through MXene membrane structures. It was found to offer high flexibility, mechanical strength, electrical conductivity and hydrophilic surface characteristics. The hydrophilic nature in combination with the hydrated interlayer spacing enabled ultrafast water flux through $Ti_3C_2T_x$ membranes. The differential sieving capability of this membrane on the single and multi-charged metal cations was also proved successfully [Ren *et al.* 2015]. It surpassed the graphene oxide on the performance towards the separation of cations with higher charges. Peng *et al.* attempted preferential adsorption of Pb(II) ions on 2D-$Ti_3C_2T_x$ MXene nanosheets. He had shown this by tailoring the surface functional groups, preferably via alkalization. The selectivity towards Pb(II) ions was found better even when competing cations (Ca- (II)/Mg(II)) coexisted at high levels [Peng *et al.*2014]. $Ti_3C_2T_x$ MXene is also tried for protein immobilization primarily aimed to design biosensors [Liu *et al.* 2015]. Most of the above applications have direct impact on human health and environment safety. Hence, the cytotoxicity and resistance against microbial attack are truly critical in order to

unambiguously select $Ti_3C_2T_x$ MXene as a biomaterial. To the best of our knowledge, the antimicrobial properties of Ti_3C_2Tx MXene are not well reported, except one by Rasool *et al.*, very recently in the March 2016 on antibacterial properties of $Ti_3C_2T_x$ [Rasool *et al.* 2016]. This chapter is devoted to study the antimicrobial, antibiofilm and cytotoxicity properties of Ti_3C_2Tx MXenes and validate the applicability of MXenes as a novel biomaterial.

In previous studies, the investigation was mostly centered to determine the physical/biological interactions of the nanomaterial with bacteria and fungi to understand the operating mechanisms involved in the antimicrobial activity. In graphene oxide (GO) nanomaterial, the direct contact with the bacteria itself was found to be the reason for microbial killing. The physical stress persuaded by the edges of GO nanosheets leads to the damage of cell membranes. The production of reactive oxygen species (ROS) is another responsible mechanism reported for the antibacterial activity of metal and metal oxide nanoparticles. The interaction of ROS with sulphur containing proteins and phosphorous containing DNA possibly leads to cell death. The antibacterial properties of MXenes against *Escherichia coli* and *Bacillus subtilis* was also attributed to the direct-contact mechanism [Rasool *et al.* 2016]. So far, this is the only report available on the antimicrobial activity of MXenes. A detailed study on their performance against various microbes is needed to prove the MXenes can act as a biocide. Their cytotoxicity also should be evaluated to predict the health and environmental compatibility. In this study, due attention was paid to address these issues. We had tested the biocidal properties of $Ti_3C_2T_x$ MXenes against bacteria such as *Escherichia coli, Klebsella pneumonia, Staphylococcus aureus*, and *Staphylococcus epidermidis* as well as with a few selective fungi species; *Candida albicans, Candida tropicalis, Candida glabrata* and *Candida parapsilosis* . We had also tested the antibiofilm and cytotoxicity properties of $Ti_3C_2T_x$ MXenes and the results are discussed in detail.

4.2.3 Experimental Details

4.2.3.1 Synthesis of $Ti_3C_2T_x$ MXenes

Ti_3AlC_2, the starting material for the synthesis of Ti_3C_2 MXene was synthesized via the microwave hybrid heating described in the first part of this

chapter. In a typical synthesis, titanium hydride, graphite and aluminium powders were taken in the molar ratio 3:1.2:2. The reactant mixture was milled well in toluene medium for 2h to get a homogenous mixture. Toluene was used as solvent to avoid any surface oxidation of reactants while grinding. The reactant mixture was then dried and uniaxially compacted in to cylindrical pellets. The pellets were then placed in quartz ampule and vacuum sealed. The sealed quartz ampule was subsequently subjected to microwave hybrid heating at 1200 °C/1h in a high temperature microwave furnace (VB ceramics, Chennai). The fired pellet was mechanically grounded and ball milled again in toluene medium for 24 h and finally very fine powders of Ti_3AlC_2 was obtained. It was further used as the precursor material for the synthesis of $Ti_3C_2T_x$ MXenes.

About 5 g of Ti_3AlC_2 power was immersed in 50 mL of 48 % HF solution and stirred for 15 h. Then it was centrifuged and washed several times with distilled water until the pH is > 4. The $Ti_3C_2T_x$ MXenes wet powder thus obtained was then dried in vacuum at 80 °C for 12 h. The schematic representation of the synthesis of $Ti_3C_2T_x$ from Ti_3AlC_2 is shown in Figure 4.2.1
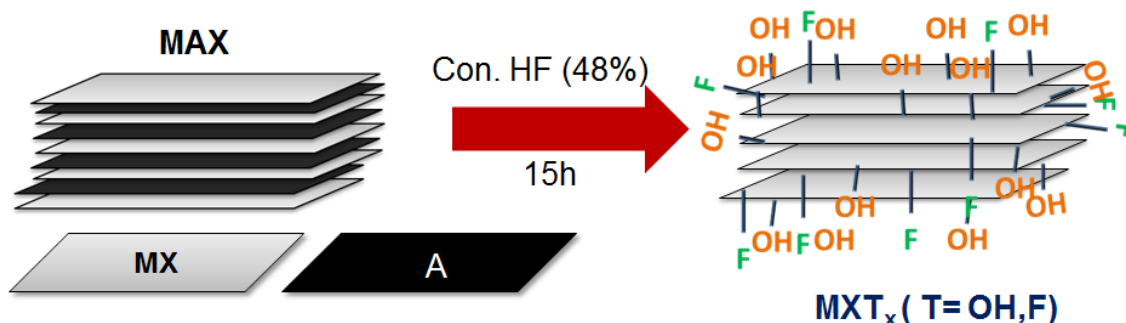
Figure 4.2.1: Schematic representation of the synthesis of $Ti_3C_2T_x$

4.2.3.2 Characterization of $Ti_3C_2T_x$ MXenes

The microstructures of bulk T_3AlC_2 and $T_3C_2T_x$ was recorded using ZEISS EVO 18 Scanning Electron Microscopy (SEM). Transmission Electron Microscopy (TEM) images were carried out using FEI Tecnai 30G2S-TWIN, operated at an accelerating voltage of 300 kV. Phase analysis of $T_3C_2T_x$ was monitored by Powder X-ray diffraction (X'Pert Pro, Philips X-ray diffractometer) with a monochromator on the diffraction beam side (Cu Kα radiation, λ=0.154 nm). The surface chemistry of the exfoliated MAXene nanosheets was examined by X-ray photoelectron spectroscopy

(XPS) using SPECS GmbH spectrometer (Phoibos100MCD Energy Analyzer) with Mg Kα radiation (1253.6 eV) as the excitation source. The peak of C1s at 284.6 eV was taken as the reference energy position. The peaks were deconvoluted using CasaXPS software. The conductivity of $Ti_3C_2T_x$ was measured by standard spring loaded pressure contact four probe conductivity meter, Keithley 6221 DC current source and 2182 A nanovoltmeter at 30 °C.

4.2.3.3 Antimicrobial Activity Studies

4.2.3.3.1 Reagents, Bacterial Strains, and Culture Conditions

All the chemicals and media used for microbiological assays were purchased from Sigma-Aldrich (USA) unless otherwise stated. Gram positive bacteria; *Staphylococcus aureus* MTCC 902 and *Staphylococcus epidermidis* MTCC 3382, Gram negative bacteria; *Escherichia coli* MTCC 2622, *Klebsiella pneumoniae* MTCC 109; medically important fungi: *Candida albicans* MTCC 277, *Candida tropicalis* MTCC 230, *Candida glabrata* MTCC 3019 and *Candida parapsilosis* MTCC 6510 were used for the antimicrobial studies. All the test microorganisms were procured from Microbial Type Culture Collection Centre (MTCC), IMTECH, Chandigarh, India. The test bacteria were maintained in nutrient agar (NA) slants and test fungi were maintained in potato dextrose agar (PDA) slants.

Bacterial culture and media preparation were carried out according to the standard Clinical and Laboratory Standards Institute (CLSI) methods. Briefly, bacteria were grown aerobically at 37 °C in nutrient broth (NB) and fungi were grown in potato dextrose broth (PDB) at 37 °C. The cultures were maintained by streaking the organisms on nutrient agar and potato dextrose agar slants and also sub-culturing was done in every 15 days. Pure colonies were isolated and stored at -80 °C for future use. Cells were harvested by centrifugation at 5000 rpm for 15 min at 4 °C and re-suspended in sterile NB and PDB medium to obtain an optical density of 1.0 at 600 nm.

4.2.3.3.2 Determination of Zone of Inhibition of $Ti_3C_2T_x$ by Disc Diffusion Assay

An agar diffusion assay was performed as reported previously, using Muller Hinton Agar (MHA) (Gurunathan S. 2015). A single colony of each test strain was grown overnight in NB/PDB on a rotary shaker (200 rpm) at 37 °C. The inocula

were prepared by diluting the overnight cultures with 0.85 % NaCl to a 0.5 McFarland standard. Inocula were applied to the MHA (for bacteria)/PDA (for *Candida*) plates along with control discs. After incubation at 37 °C for 24 h, zones of inhibition (ZOIs) were determined by measuring the diameter of zone of clearance and it was expressed in mm. The experiments were performed in triplicates.

4.2.3.3.3 Determination of Minimum Inhibitory Concentrations of $Ti_3C_2T_x$

To determine the minimum inhibitory concentrations (MICs) of $Ti_3C_2T_x$, bacterial strains were cultured in NB/PDB. Cell suspensions were adjusted to obtain standardized populations by measuring the turbidity with a spectrophotometer (Shimadzu). Susceptibility tests were performed by two fold microdilution of $Ti_3C_2T_x$ in standard broth according to the CLSI guidelines (CLSI, 2003). The bacterial strains were grown in Muller Hinton broth (MHB) and fungal strains were grown in PDB to mid-log phase (1×10^6 cells/mL) and diluted in fresh NB and PDB for bacteria and fungi, respectively, and 0.1 mL of the diluted cell suspension was dispensed into each well of a 96-well microliter plate. The test bacteria/fungi were then exposed to different concentrations of $Ti_3C_2T_x$ (0.5 to 500 µg/mL). Growth was assayed by monitoring absorbance at 600 nm using a microplate reader. The MICs of the $Ti_3C_2T_x$ were determined as the lowest concentrations that inhibited visible growth of the microbes. The experiments were performed in triplicates.

4.2.3.3.4 Detailed Antifungal Studies of $Ti_3C_2T_x$

Based on the MIC results, we have selected the Fungi *Candida* species, *C. albicans* and *C. tropicalis* for more detailed studies since these species recorded more sensitivity towards $Ti_3C_2T_x$. Antifungal activity of $Ti_3C_2T_x$ against *Candida* strains was determined by the colony count method and also by measuring the OD(optical density). Multilayer $Ti_3C_2T_x$ concentration of 50 µg/mL was applied to both *Candida* strains and cell survival rate was counted by CFU/mL. A second set of antifungal activity tests was conducted by spread plate CFU counting. The fungi (about 10^7 CFU/mL were incubated with different concentrations (0.5–100 µg/mL) of $Ti_3C_2T_x$ for 4 h. Aliquots of the samples were withdrawn and CFU were counted by plating 50 µL of 10-fold serial dilutions onto PDA plates. Colonies were counted after

incubation at 37 °C and the cell survival rate was expressed as the percentage of control and log reduction.

The following equation was used to represent relative viability of cells:

$$Relative\ cell\ viability = [Fc/Fm] \times 100$$

Where Fc is fungal colonies of the control sample and Fm are colonies for cells treated with $Ti_3C_2T_x$.

To examine the effect of compound on bacterial regrowth, the batch assays were subjected to 1, 2, 10, 25, 50, 100, and 200 μg/mL $Ti_3C_2T_x$. The batch assays were subjected to continuous shaking at 150 rpm and constant temperature of 37 °C for 4 h. Controls experiments were conducted without adding $Ti_3C_2T_x$. The reaction mixture was then transferred to 10 mL tubes, each containing 5 mL of PDB medium, and the tubes were inoculated on a shaking incubator at 150 rpm and 37 °C. Aliquots of the samples were withdrawn at specific time intervals and the value of OD (optical density) at a wavelength of 600 nm was measured on an UV–Vis spectrophotometer. Fungal regrowth curves were created by plotting OD values versus time and bacterial growth kinetics were studied. All experiments were performed as triplicates and average values were reported. Antifungal activity of $Ti_3C_2T_x$ in PDB growth media was assessed by exposing the fungi (about 10^5 CFU/mL) to 200 μg/mL of $Ti_3C_2T_x$ for 4 h. Aliquots of the samples were withdrawn and CFU were counted as described earlier.

4.2.3.3.5 Mechanism of Antifungal Action of $Ti_3C_2T_x$

4.2.3.3.5.1 Detection of ROS Production

The effects of $Ti_3C_2T_x$ on intracellular ROS generation in *Candida* cells were monitored by DCF-DA assay. Briefly, the bacterial cells were harvested by centrifugation, washed twice with PBS, and incubated with 10 mM CM-H2DCFDA [5-(and -6)-chloromethyl-2',7'-dichlorodihydrofluorescein diacetate acetyl ester] in PBS at 37 °C for 30 min. The cells were then incubated with 10 μg/mL $Ti_3C_2T_x$ composites at 37 °C for 24 h. The intracellular ROS level was examined under a fluorescence microscope with the excitation and emission wavelengths at 495 nm and 525 nm, respectively, and the ROS level was examined by confocal laser scanning microscopy (CLSM)(BD Biosciences) images. CM-H2DCFDA immediately

diffuses through the cell membrane, and intracellular esterases present in the cells hydrolyzed it to a non-fluorescent dichlorofluorescein (DCFH), which is then quickly oxidized to highly fluorescent 2',7'-dichlorofluorescein (DCF) by any one of the intracellular ROS, aside from H_2O_2. The fluorescence intensity of the DCF formed is proportional to the amount of ROS generated intracellularly.

4.2.3.3.5.2 Membrane Integrity Assay

Propidium iodide (PI) staining was used for checking the integrity of fungal plasma membrane following treatment with $Ti_3C_2T_x$. Propidium iodide (PI) has been found to be an excellent membrane impermeable nucleic acid staining fluorescent dye. PI enters the cells with compromised permeability only and it binds to the double stranded nucleic acids thus producing a red fluorescence when excited at 480 nm (Figure 4.2.2). *Candida* cells were harvested at the logarithmic phase and 1×10^6 cells/mL were added in phosphate buffer saline (PBS, 0.1 mM, pH 7.2), containing inhibitor. The tubes were incubated at 37 °C for 2 h. Cells were separated by centrifugation and washed with PBS. Subsequently, they were incubated with 3 mM of PI for 10 min, harvested by centrifugation, washed (using PBS) and suspended in PBS. PI stained cells were counted using CLSM images.
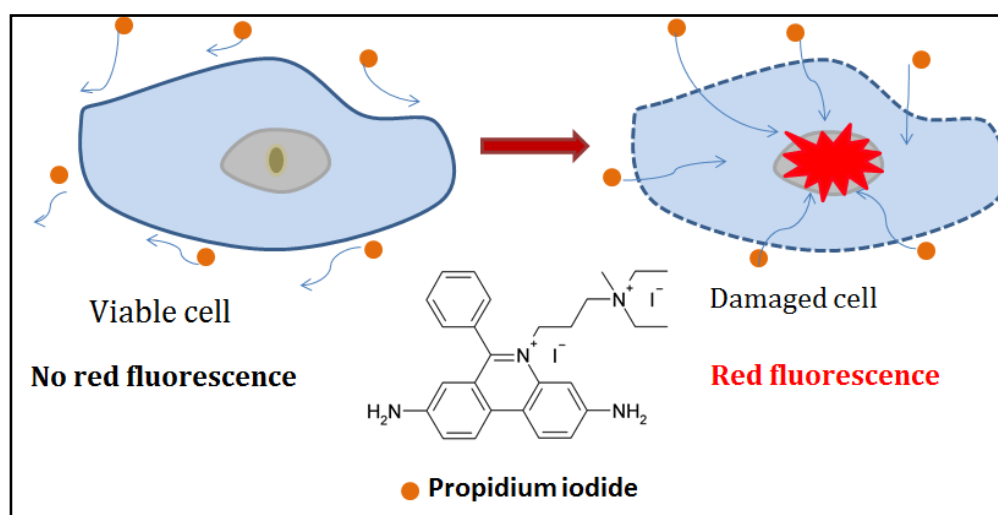
Figure 4.2.2: Mechanism of Propidium Iodide assay

4.2.3.3.5.3 Measurement of Mitochondrial Membrane Potentials (mtΔψ)

The effect of $Ti_3C_2T_x$ on the mtΔψ of *Candida* strains was measured by fluorescence microscopy using rhodamine 123 (Rh123) according to the procedure as described previously with some modifications [Chen et al., 2013]. Cells exposed to

various doses of $Ti_3C_2T_x$ at 30 °C for 12 h were harvested by centrifugation, washed twice, and resuspended to $1–3×10^5$ CFU/ml with cold distilled water. Rh123 was added to a final concentration of 100 ng/ml, incubated for 30 min in the dark at room temperature and observed with a fluorescent microscope (BD Bioscience) equipped with a 60X lens.

4.2.3.4 Antibiofilm Potential of $Ti_3C_2T_x$

To determine the efficacy of $Ti_3C_2T_x$ on the formation of biofilm, 96-well microtiter plate method was applied [Kalishwaralal et al. 2010]. Individual wells of the sterile microtiter plate were filled with 150 μL of PD broth and inoculated with 20 μL of overnight grown culture. To this mixture, 30 μg of $Ti_3C_2T_x$ was added from the stock solution so that the final concentration is 2.5, 5, 10 μg/mL. The microtiter plates were incubated for 24 h at 37 °C. After incubation, content of each well was gently removed and washed with 0.2 mL of phosphate buffer saline (PBS, pH 7.2) three times, to remove free-floating 'planktonic' yeast cells. Biofilms formed by adherent 'sessile' organisms on the wall of the plate were fixed with sodium acetate (2 %, w/v) and stained with crystal violet dye (0.1 %, w/v). Excess stain was rinsed off by thorough washing with sterilized Millipore water and plates were kept for drying. After drying, 200 μL of 95 % (v/v) ethanol was added to the wells. The absorbance at 600 nm was measured on an ELISA reader, and values obtained were considered as an index of *Candida* adhering to the surface of well wall for developing biofilms. The percentage of biofilm inhibition was calculated using the equation:

% biofilm inhibition = [1 – (OD_{600} of cells treated with $Ti_3C_2T_x$/OD_{600} of non-treated control) ×100].

Experiment was performed in triplicate, the data were then averaged, and the standard deviation was calculated.

4.2.3.5 Cytotoxicity Studies of $Ti_3C_2T_x$ MXene in Mammalian cells

H9c2 cell lines (rat embryonic cardiomyoblasts) were obtained from ATCC (American Type Culture Collection, USA). For the maintenance of cell lines, Dulbeccos Modified Eagle's Medium (DMEM) (Sigma) containing 10 % fetal bovine serum (FBS) (Gibco), antibiotics (100 U/mL Penicillin and 100 μg/mL streptomycin) and amphotericin (0.25 μg/mL) (Hi-Media) were employed. The cells were

maintained in cell culture flasks in CO_2 incubators at 37 ℃ with 5 % CO_2 in air and 99% humidity. Passaging of cells when confluent was carried out using 0.25% trypsin and 0.02 % EDTA (Hi-Media) in phosphate buffered saline (PBS).

Cell viability after incubating the cells with different concentrations of the $Ti_3C_2T_x$ was determined by methyl thiazolyl tetrazolium (MTT) assay. It is a colorimetric assay based on the ability of live cells to reduce MTT (yellow) to a formazan (purple) product. The cells were spread in the 96-well plates at 5×10^3 cells/well. After 36 h of seeding, they were incubated with different concentrations of the test substance individually for 24 h. Subsequently, the cells were exposed to MTT at a concentration of 50 µg/well for 2.5 to 3 h at 37 °C in CO_2 incubator. The working solution of MTT was prepared in Hanks balanced salt solution (HBSS). After viewing formazan crystals under the microscope, the crystals were solubilized by treating the cells with DMSO: isopropanol at a ratio of 1:1 for 20 min at 37°C. Plate was read at an absorbance of 570 nm. The relative cell viability in percent was calculated as: (Absorbance of treated /Absorbance of control) ×100. Control samples used were cells without having any treatment with $Ti_3C_2T_x$ MXene. Cell viability of control cells was kept as 100%.

4.2.4 Results and Discussion

4.2.4.1 Synthesis and Characterization of $Ti_3C_2T_x$

The Ti_3AlC_2 powders were treated with concentrated HF acid for about 15 h to remove the 'A' layer atoms as much as possible through etching, followed by vacuum drying, then it was first subjected to powder x-ray analysis for examining the crystalline structural variation, phase stability, crystal structure distortion and chemical compositional changes.

Figure 4.2.3 presents the powder diffraction analyses of the Ti_3AlC_2 before and after HF etching. Compared to the parent Ti_3AlC_2 MAX phase, the following visible differences have been observed with the X-ray pattern of Ti_3AlC_2 treated with HF (i) disappearance of most non-basal plane peaks present in the Ti_3AlC_2, (ii) broadening of peaks corresponding to basal plane (002), and (iii) shifting of the peaks to lower angles from their original 2θ values. The intense peak at 2θ = 39° for the parent Ti_3AlC_2 disappeared in the XRD pattern of $Ti_3C_2T_x$. The untreated Ti_3AlC_2

possess the *d* spacing of 9.32 Å and *c* lattice parameter of 18.64 Å which is well matched with the value reported earlier (Table 1.1). A slight increase in the *'d'* spacing from ~9.32 Å to 10.05 Å is seen with the HF treated Ti_3AlC_2. Accordingly, the *c* lattice parameter is increased to 20.10 Å from 18.64 Å. When the Al atoms are removed from the structure, the two neighboring Ti atoms per unit formula get exposed. These sites are satisfied by hydroxyl and fluorine ligands. The DFT modeling studies suggest that the *c* lattice parameter should be 19.494 Å if all these exposed sites are occupied by OH groups alone and it should be 21.541 Å if is fully satisfied by fluorine atoms. However, here we obtained the *c* lattice parameter of 20.10 Å which indicates that $Ti_3C_2T_x$ product may have both hydroxyl and fluorine functional groups.
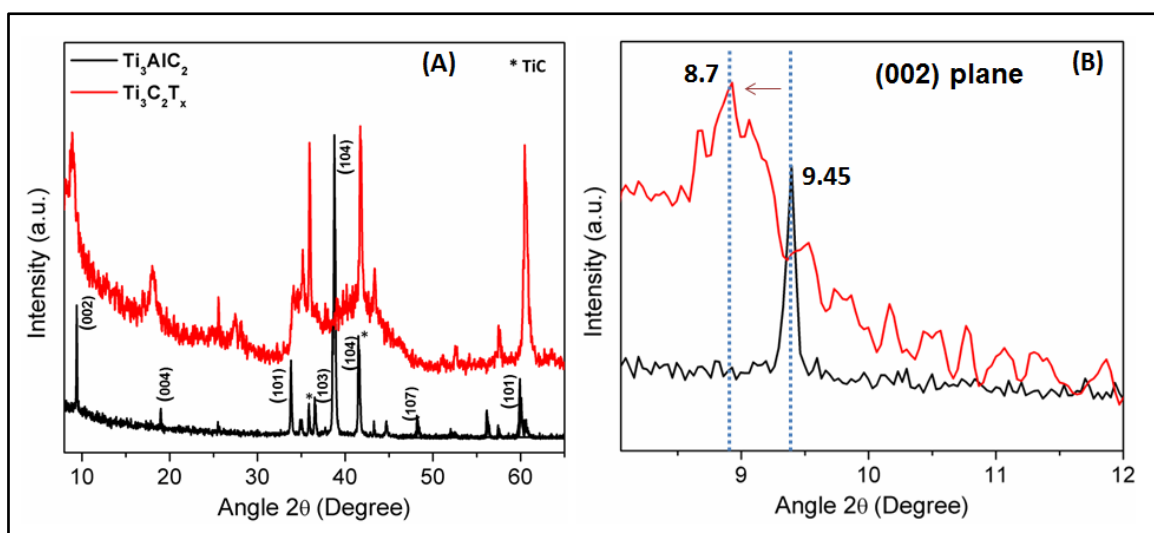
Figure 4.2.3: (A) XRD pattern of Ti_3AlC_2 before and after HF treatment; (B) the magnified XRD spectrum showing the shift and broadening of (002) plane after HF etching

SEM and TEM images in Figure 4.2.4 reveal the effects of HF etching on the texture / morphology features on the bulk Ti_3AlC_2 MAX phase. Figure 4.2.4 (A) depicts the particle morphology of Ti_3AlC_2 before any etching. Here the characteristic stacking of dense multilayer arrangement is very clear. The microstructural changes occurred during the transformation of Ti_3AlC_2 to MXene $Ti_3C_2T_x$ can be seen from the SEM images in Figure 4.2.4 (B) and (C). It shows the tightly stacked MAX phase layers are de-bonded and separated from each other. It confirms the successful etching of Al layers from the parent MAX phase. The SEM

and TEM images show how basal planes spread apart as result of HF treatment. It is expected that HF treatment produced Ti_3C_2 layers with abundant OH and F groups on the surface.
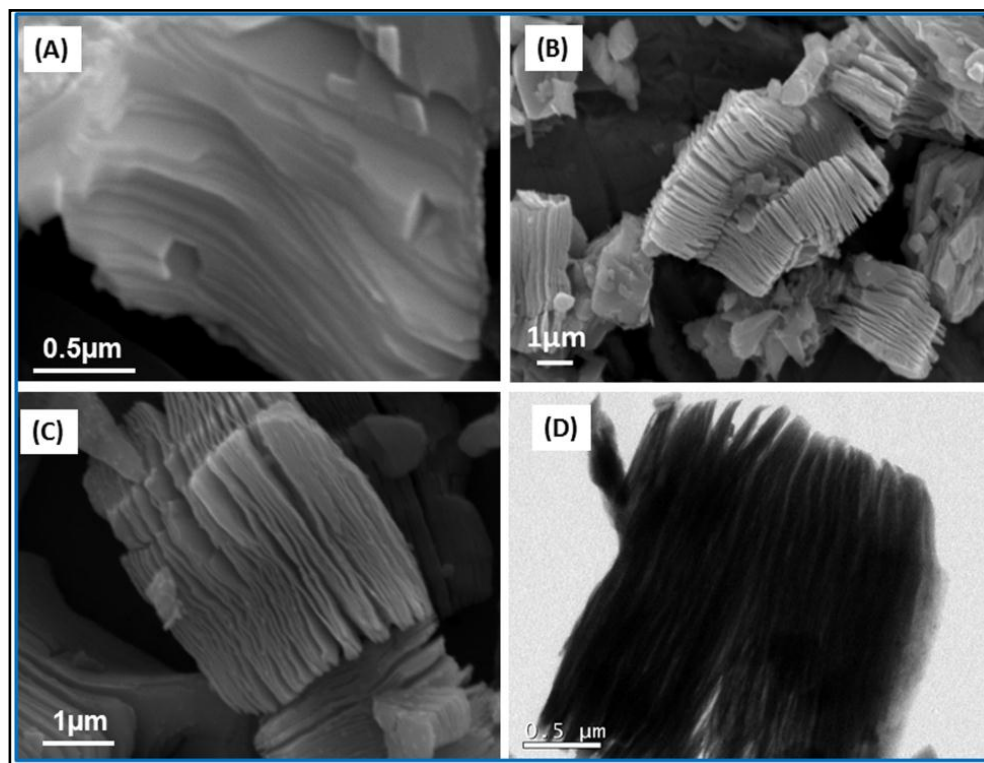
Fig 4.2.4: SEM images of (A) bulk Ti_3AlC_2 before HF treatment, (B and C) $Ti_3C_2T_x$ obtained after HF treatment and (D) the TEM image of $Ti_3C_2T_x$ typically showing the spread apart of single layers

The surface chemistry of the $Ti_3C_2T_x$ MXene was studied using XPS analysis and the results are shown in Figure 4.2.5. It is reported that depending upon the reaction time, washing efficiency and final pH, the following chemical moieties are possible in the final product [Halim *et al.* 2016] ;

   i) $Ti_3C_2O_x$: Ti atoms are bonded to C atoms and one oxygen

   ii) $Ti_3C_2(OH)_x$:Ti atoms bonded to C atoms as well as to an OH group

   iii) $Ti_3C_2F_x$: Ti atoms bonded to both C and F atoms,

   iv) $Ti_3C_2OH\text{-}H_2O$ (or H_2O_{ads}): physisorbed H_2O molecules on $Ti_3C_2(OH)_x$
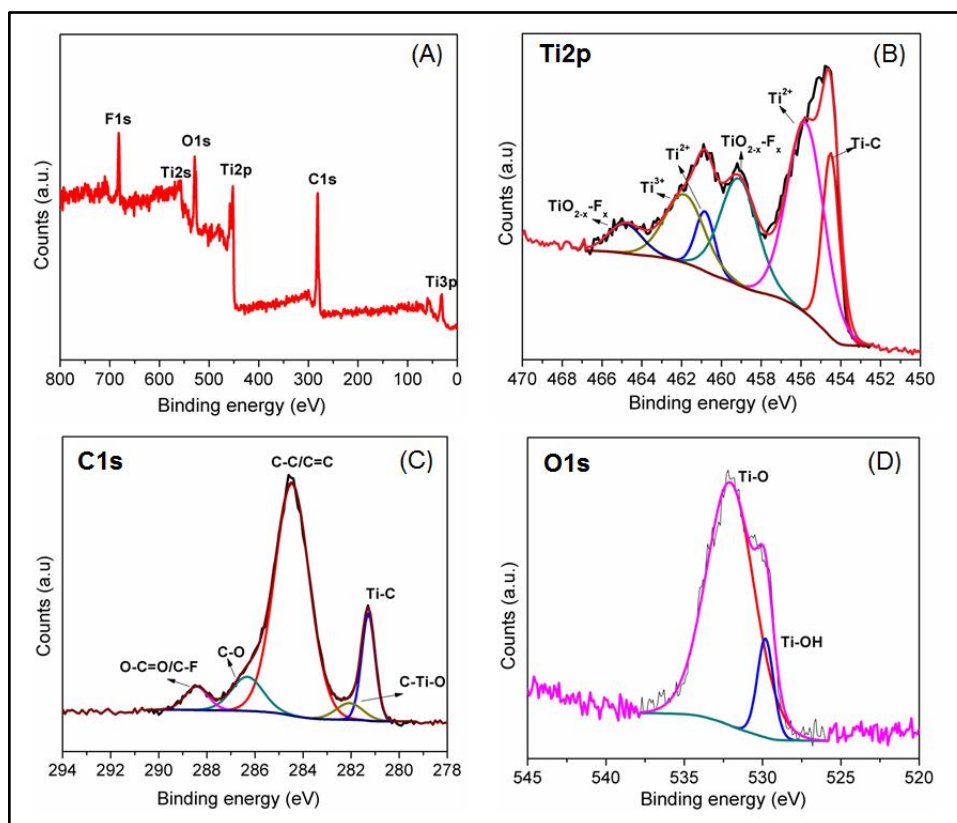
Figure 4.2.5: XPS spectra of Ti₃C₂Tₓ : (A) the survey spectrum showing all the elements present in Ti₃C₂T; high resolution of spectra of (B) Ti2p, (C) C1s, and (D) O1s

The XPS survey spectrum in Figure 4.2.5 (A) corresponds to the HF treated $Ti_3C_2T_x$. Here it shows, in bulk $Ti_3C_2T_x$ contains the presence of Ti, C, O and F atoms on the surface. The absence of peaks correspond to Al atom confirm that the Al layers are completely removed from the structure. The detailed high resolution spectra corresponding Ti, C, O elements further explains the details on difference moieties present. The high resolution Ti2p spectra given in Figure 4.2.5 (B) indicate the presence of Ti_3C_2 with OH and F groups attached. Figure 4.2.5 (C) represents the high resolution C1s spectra. Here five distinguishable peaks for C atoms are observed. The peak at 281.3 and 284.4 eV corresponds to Ti-C and graphitic carbon, respectively. Presence of C-O, C-F moieties are also seen and are likely formed from the HF acid and aqueous solvents used in etching process. It is worth to note that their percentage is very low. The high resolution of O1 spectrum (Figure 4.2.2.5 (D)) confirms the formation of C-Ti-OH and C-Ti-Oₓ moieties. From the X-ray pattern and XPS analyses, the selective etching of 'A' atom layers to form $Ti_3C_2T_x$ MXenes with the surface functional groups OH and F are confirmed.

4.2.4.2 Antimicrobial Activities of Ti$_3$C$_2$T$_x$

4.2.4.2.1 Zone of Inhibition (ZOIs) and Minimum Inhibition Concentration (MIC)

As preliminary study to assess the antimicrobial properties of Ti$_3$C$_2$T$_x$, disc diffusion experiments were conducted with a series of bacteria and fungi cells as per the standard procedure outlined in the experimental part. To have a clear understanding on the antimicrobial property of Ti$_3$C$_2$T$_x$ with the parent MAX phase, the experiments were made also with un-etched Ti$_3$AlC$_2$. In both MXene and MAX phase, the zones of inhibition (ZOIs) were determined after the incubation for a period of 24 h at 37 °C by measuring the diameter of zone of clearance and expressed in mm. The experimental results could be seen from the photographs of the agar plates prepared with the Ti$_3$C$_2$T$_x$ and T$_3$AlC$_2$ discs (0.2 g, 10 mm diameter) given in Figure 4.2.6 and 4.2.7 respectively. The agar plates containing MXene discs demonstrated a very good inhibition against both test-bacteria and fungi. In the case of bacteria the diameter of zone of clearance is about 30 mm which is higher than that of a conventional oxide based antimicrobial agents [Wang et al. 2014].
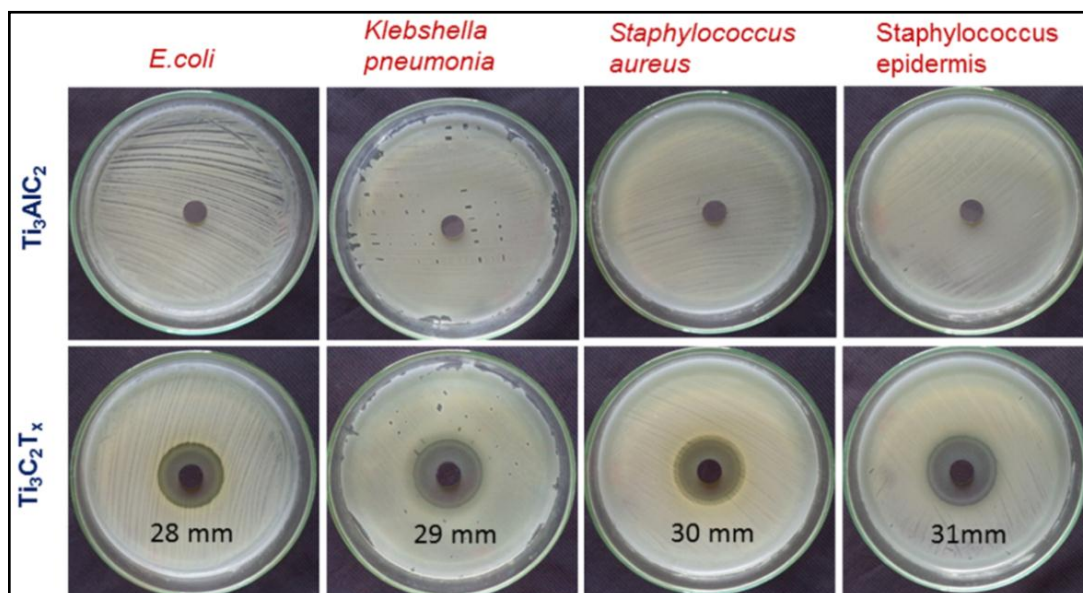
Figure 4.2.6: Photograph of inhibition zone of Ti$_3$AlC$_2$ and Ti$_3$C$_2$T$_x$ against various bacteria by disc diffusion assay.

The Ti$_3$C$_2$T$_x$ samples showed significantly high inhibition against all the tested fungi species. The measured diameter of zone of inhibition is more than 35 mm. The highest values of 47 mm and 45 mm were determined with the fungi

species *candida albicans* and *candida tropicalis,* respectively. Comparatively very poor zone of inhibition (or even we can say no zone of inhibiton) on the samples treated with bulk Ti_3AlC_2. It shows the MXene nanomaterial exhibits better antimicrobial activity.
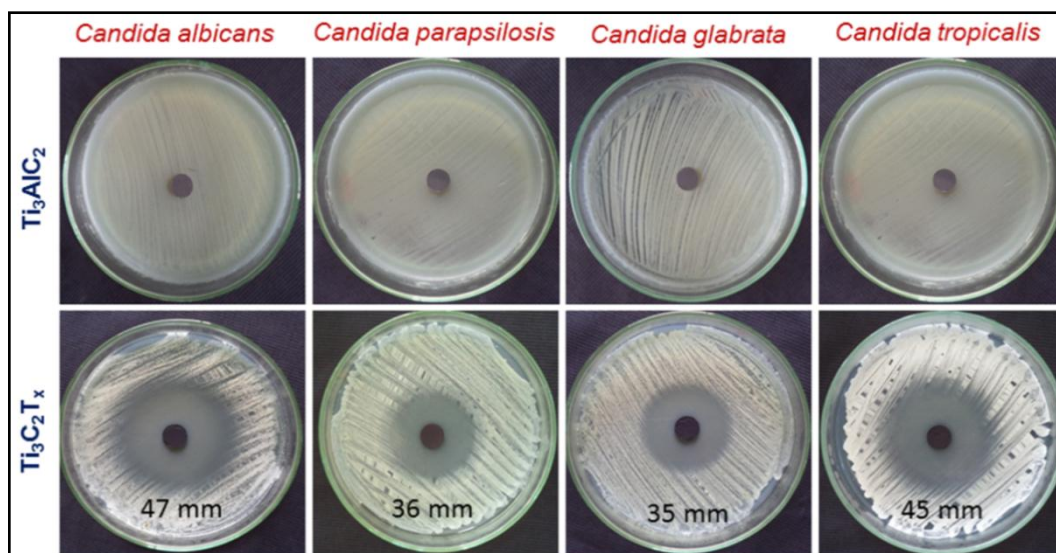
Figure 4.2.7: Photograph of inhibition zone of Ti_3AlC_2 and $Ti_3C_2T_x$ against various fungi by disc diffusion assay.

Table 4.2.1: Zone of inhibition and MIC values of $Ti_3C_2T_x$ against various bacteria and fungi (no measurable zone of inhibition/ or no bio-activity in Ti_3AlC_2)

Test bacteria	Zone of inhibition (mm)		MIC (µg/mL)	
	$Ti_3C_2T_x$	Ti_3AlC_2	$Ti_3C_2T_x$	Ti_3AlC_2
E. Coli	28±1.77	-	32	-
K. Pneumoniae	29±2.11	-	64	-
S. Aureus	30±1.72	-	32	-
S. Epidermis	31±1.52	-	16	-
Test fungi				
C. Albicans	47±2.75	-	4	-
C. Tropicalis	45±1.52	-	8	-
C. Glabrata	35±1.12	-	16	-
C. Parapsilosis	36±1.12	-	16	-

Table 4.2.1 showcase the ZOI and MIC (lowest concentrations that inhibited visible growth of microbes) values of $Ti_3C_2T_x$ against the tested microbes. It was observed that ultra-small quantities of $Ti_3C_2T_x$ are enough to trigger the

antimicrobial properties. Among the different types of microbes tested, the antimicrobial effect of $Ti_3C_2T_x$ was more effective in fungi than bacteria. The MIC value of 4 μg/mL itself was found to have excellent activity in the case of *C. albicans*. Based on these preliminary observations, the detailed antimicrobial studies were conducted with *C. albicans* and *C. tropicalis*. As we seen in disc diffusion test, Ti_3AlC_2 did not show antimicrobial activity even with high dosage limits.

4.2.4.2.2 Dose-Dependent Antifungal Activity of $Ti_3C_2T_x$

To study the effect of $Ti_3C_2T_x$ concentrations on the antifungal activity, the dose dependent activity tests were performed by measuring the growth curve and cell viability of the fungi, *C. albicans* and *C. tropicalis after* exposed to $Ti_3C_2T_x$ concentrations in the range 5-100 μg/mL for 4 h. In order to compare the activity, the experiments were also conducted with corresponding concentrations of Ti_3AlC_2. The control experiment lacks $Ti_3C_2T_x$ nanoparticle. It was once again confirmed that the parent Ti_3AlC_2 has no activity even at higher concentrations. Figure 4.2.8 depicts the cell viability of *Candida albicans* (Figure 4.2.8 A) and *Candida tropicalis* (Figure 4.2.8 B) seen with different concentrations of $Ti_3C_2T_x$. The results confirm an excellent antifungal activity of $Ti_3C_2T_x$ against both the fungi and the activity are ascending with increase in the concentration of $Ti_3C_2T_x$. At a very low concentration of 5 μg/mL, *Candida albicans* and *Candida tropicalis* showed a survival rate of 79 % and 85 %, respectively. With an increase in the $Ti_3C_2T_x$ addition, the cell death seems to happen more prominently. At 100 μg/mL concentration of $Ti_3C_2T_x$, the cell viability appears to drop to 2 % and 4 % for *Candida albicans* and *Candida tropicalis*, respectively. In other words, the fungal growth inhibition was increase to 98 % and 96 % respectively. Among the two fungi species tested, $Ti_3C_2T_x$ show more toxicity towards *Candida albicans* but the difference is not too high. The Ti_3AlC_2 bulk material showed no activity, at all concentrations. A negligible activity was observed against *Candida albicans*, at high concentrations.

The efficiency of $Ti_3C_2T_x$ as an antimicrobial agent was further evaluated using fungal regrowth curves in a second assay. The experimental results on the OD growth curves correspond to *C. albicans and C. tropicalis* cells incubated with different $Ti_3C_2T_x$ concentrations are shown in Figure 4.2.9. It is observed that the inhibition of fungi regrowth is dose dependent. The rate of regrowth was decreased

with increase in concentration of $Ti_3C_2T_x$. The control shows almost linear increase in fungal growth with time whereas the growth was inhibited when $Ti_3C_2T_x$ is present. The effect was more at higher concentrations. At 200 µg/mL concentration, there was no significant growth. In this case the growth and kill rates are possibly in equilibrium.
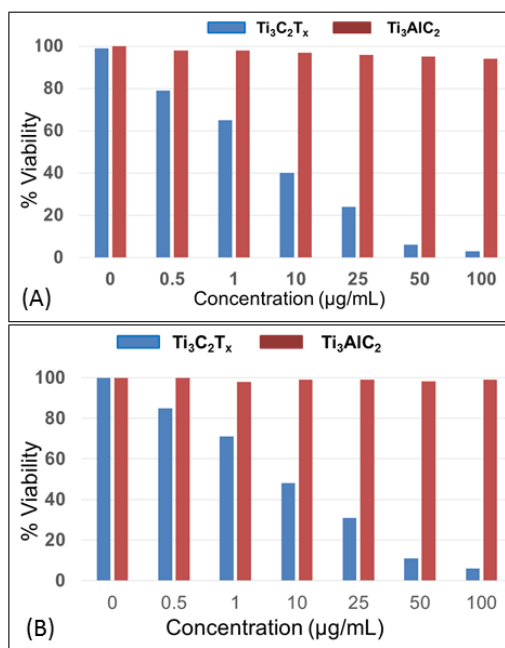
Figure 4.2.8: Dose dependent antifungal activities of $Ti_3C_2T_x$ and Ti_3AlC_2 against A) *candida albicans* **and B)** *tropicalis.*
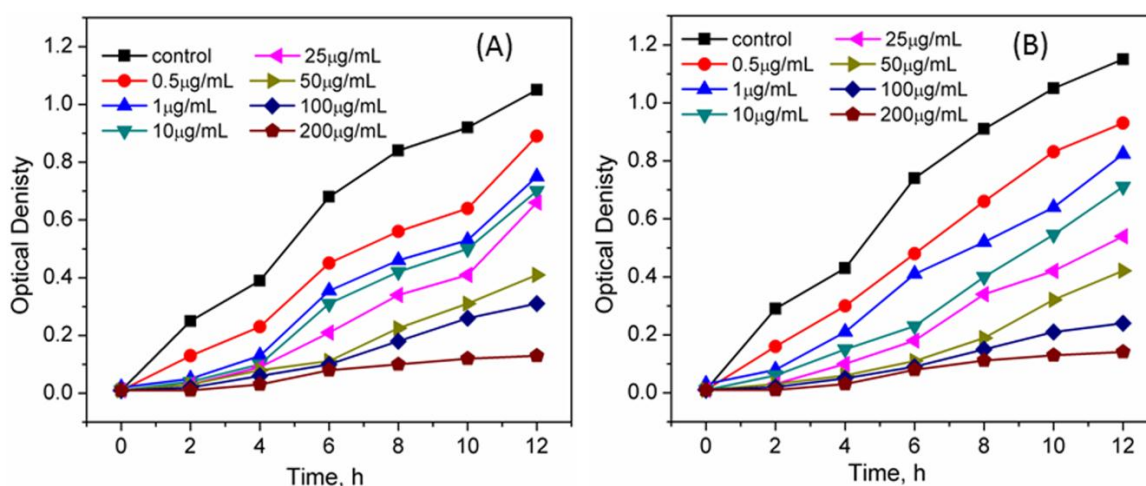
Figure 4.2.9: Regrowth curves of A) *C. albicans* **and B)** *C. tropicalis.* **The fungal suspensions were treated with different concentrations of $Ti_3C_2T_x$ at 37 °C for 4 h and then the reaction mixture was transferred in to tubes containing LB medium followed by inoculation on a shaking incubator at 37 °C with 150 rpm. The optical density of fungi at specific time interval was measured.**

4.2.4.2.3 Morphology Change of Fungal Cells after Exposed to Ti$_3$C$_2$T$_x$

The effect of Ti$_3$C$_2$T$_x$ treatment on the morphology and membrane integrity of *C. albicans* and *C. tropicalis* fungal cells was further investigated using SEM and TEM. Microscopic images of these fungal cells were taken before and after treatment with Ti$_3$C$_2$T$_x$. For this, the fungi cells treated with 100 µg/mL Ti$_3$C$_2$T$_x$ and were separated by centrifugation at 5000 rpm for 3 min. The condensed pellets were washed with 0.1 M phosphate buffer solution (pH-7) and centrifuged again to separate the pellet. It was then fixed with 2.5 % glutaraldehyde solution and again washed with phosphate buffer. Microliter quantity of this fungi solution was dropped on the SEM stub using a metallic loop and dried in ambient condition. Finally the cell morphology was observed with SEM. The control sample was prepared with untreated cells. The corresponding SEM images are depicted in Figure 4.2.10.
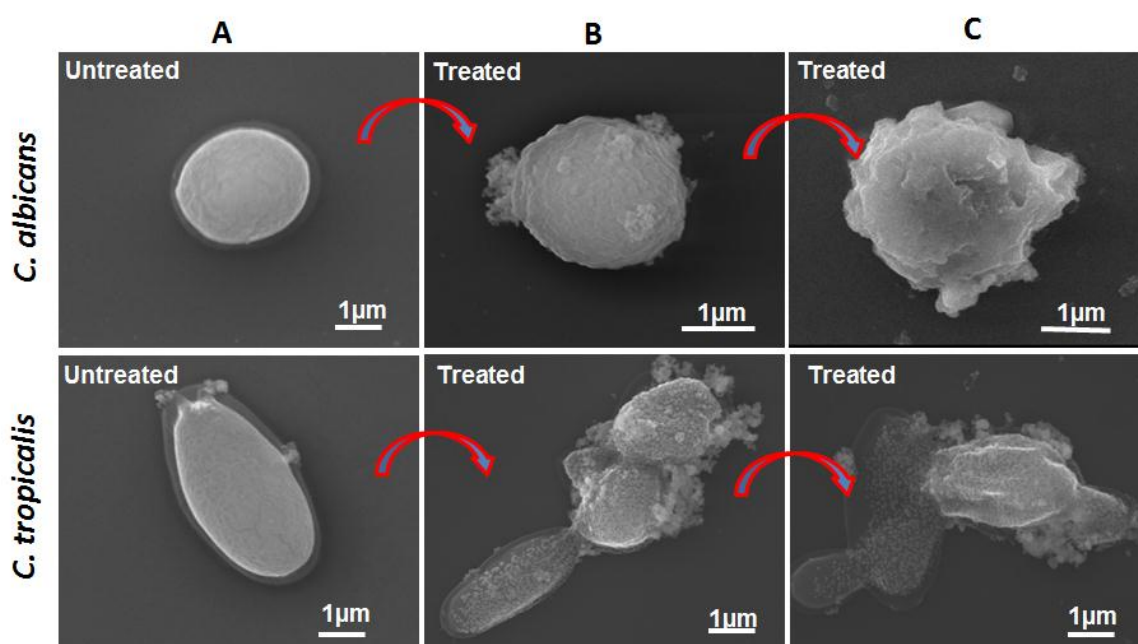
Figure 4.2.10: SEM images of *C. albicans* and *C. tropicalis* before (A) and after (B & C) incubation with Ti$_3$C$_2$T$_x$.

The SEM images of untreated fungal cells reveal no observed membrane damage or cell death. As seen in the Figure 4.2.10 (A), spherical shape morphology of *C. albicans* and oval shape morphology of *C. tropicalis* was undisturbed and protected by intact cytoplasmic membrane. Whereas, the cell viability is lost and the morphology of the fungi cells significantly changed once they are exposed to Ti$_3$C$_2$T$_x$

nanostructures and the membrane damage is very clear in the SEM microstructures. Figure 4.2.10 (B) and (C) shows the partially damaged and fully damaged fungi cells, respectively. The complete collapse of the cell membrane and leakage of cytoplasm for both *C. albicans* and *C. tropicalis* can be apparently seen from the Figure 4.2.10 (C). SEM observations confirm that $Ti_3C_2T_x$ is toxic to the candidal pathogens and induces growth inhibition and cell death. The morphological change of *Candida* cells could be attributed to direct contact through adsorption or trapping of $Ti_3C_2T_x$ nanosheets onto the cell wall. Similar mechanism was reported for CNTs and graphene based materials [Li *et al.* 2014; Liu *et al.* 2011; Li *et al.* 2012; Kang *et al.* 2007].
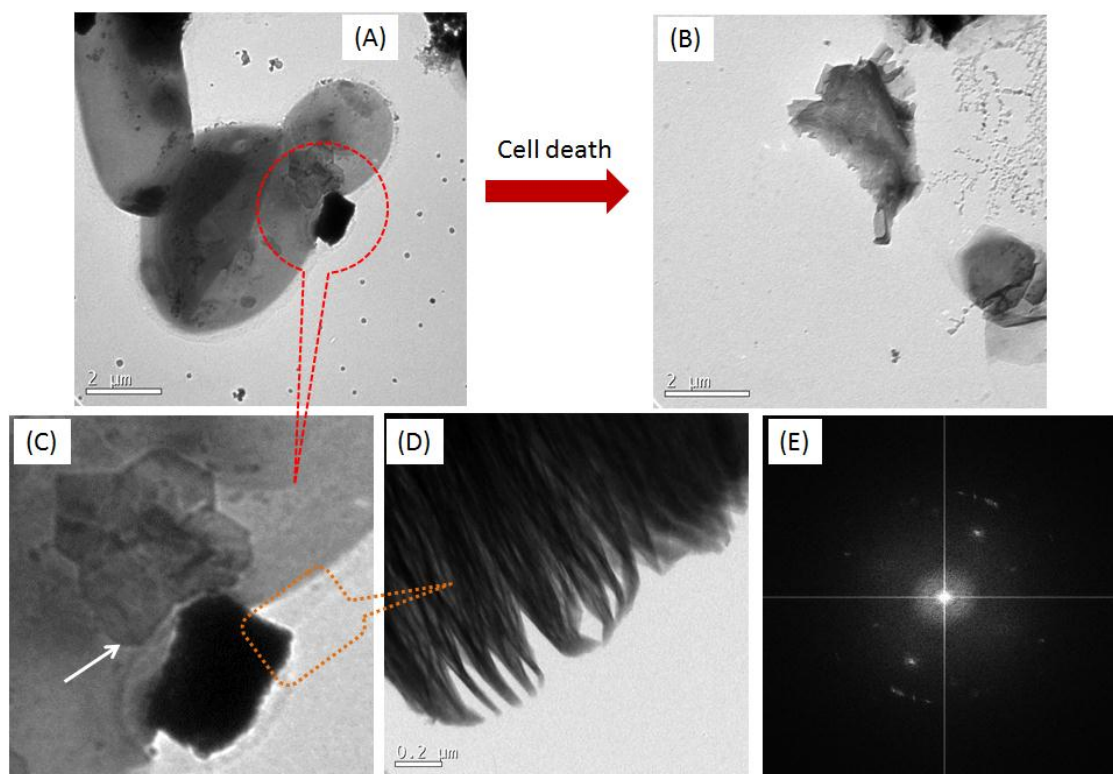
Figure 4.2.11: TEM images of *C. albicans* after exposed to 100 μg/mL $Ti_3C_2T_x$ MXene. (A) a partially damaged cell showing the adsorbed $Ti_3C_2T_x$ MXene on the cellular membrane, (B) a completely destructed *C. albicans* cell, (C) magnified portion of part marked in red circular arrow in (C) showing the initiation damage due to adsorbed $Ti_3C_2T_x$ MXene, (D) High magnification TEM images showing nano-knives of $Ti_3C_2T_x$ MXene, and (E) corresponding FFT pattern

The direct contact killing mechanism of $Ti_3C_2T_x$ was further analyzed by TEM studies. The TEM images shown in Figure 4.2.11 illustrates the morphology change

of *C. albicans* after exposed to 100 μg/mL $Ti_3C_2T_x$ MXene. Figure 4.2.11 (A) represents the morphology of a partially damaged *C. albicans* cell, where the adsorption of $Ti_3C_2T_x$ on to the cell wall could be clearly seen. This finally leads to the complete loss of membrane integrity and cytoplasm leakage and eventually leads to cell death (Figure 4.2.11 (B)). The adherence of $Ti_3C_2T_x$ caused notable deformations on the cell wall as shown in the red circle. The respective magnified image is given as Figure 4.2.11 (C & D). It is clear that the $Ti_3C_2T_x$ MXene consist of nanolayered sheets with very sharp edges. This kind of sharp edge possibly acts as nano-knife which is piercing the cell wall and in turn causes the cell death. The adhesion of $Ti_3C_2T_x$ MXene to cell membrane of *C. albicans* was further evaluated by the corresponding FFT pattern obtained and is shown in Figure 4.2.11 (E). It confirms the presence of crystalline $Ti_3C_2T_x$ MXene on *C. albicans* cells.

4.2.4.2.4 Role of Intracellular Reactive Oxygen Species (ROS) on Antifungal Activity of $Ti_3C_2T_x$ MXene

While considering the mechanism of antimicrobial activity of materials, the oxidative stress was proposed as a dominant cause. Oxidative stress induced antimicrobial activity was reported extensively on the metal oxides and carbon based nanomaterials [Li *et al.* 2014; Liu *et al.* 2011; Li *et al.* 2012]. Exposure to free radicals such as $O_2^{\cdot-}$, $\cdot OH$, and H_2O_2 generates oxidative stress in cells. However, a generalization is difficult since this is highly dependent on treatment conditions. For example, some researchers proposed the ROS production in TiO_2 under dark conditions, [Long *et al.* 2006] but some of the other studies do not support this mechanism [Xia *et al.* 2006]. The level of oxidative stress on the microbes is proportional to the quantity of reactive oxygen species (ROS) generated.

In this work, the intra cellular ROS production was determined by DCFH-DA assay. The green florescence observed through confocal microscope is shown in Figure 4.2.12. The incubation with the dosage of 10 μg/ml $Ti_3C_2T_x$ MXene nanostructures increases DCFH-DA fluorescence, displayed a significant increase in the intracellular ROS concentration compared to the untreated cell counterpart. The ROS generation is indicated by the green florescence in the confocal images.

Confocal green florescence supports the cell death can be mediated by intracellular ROS generation.
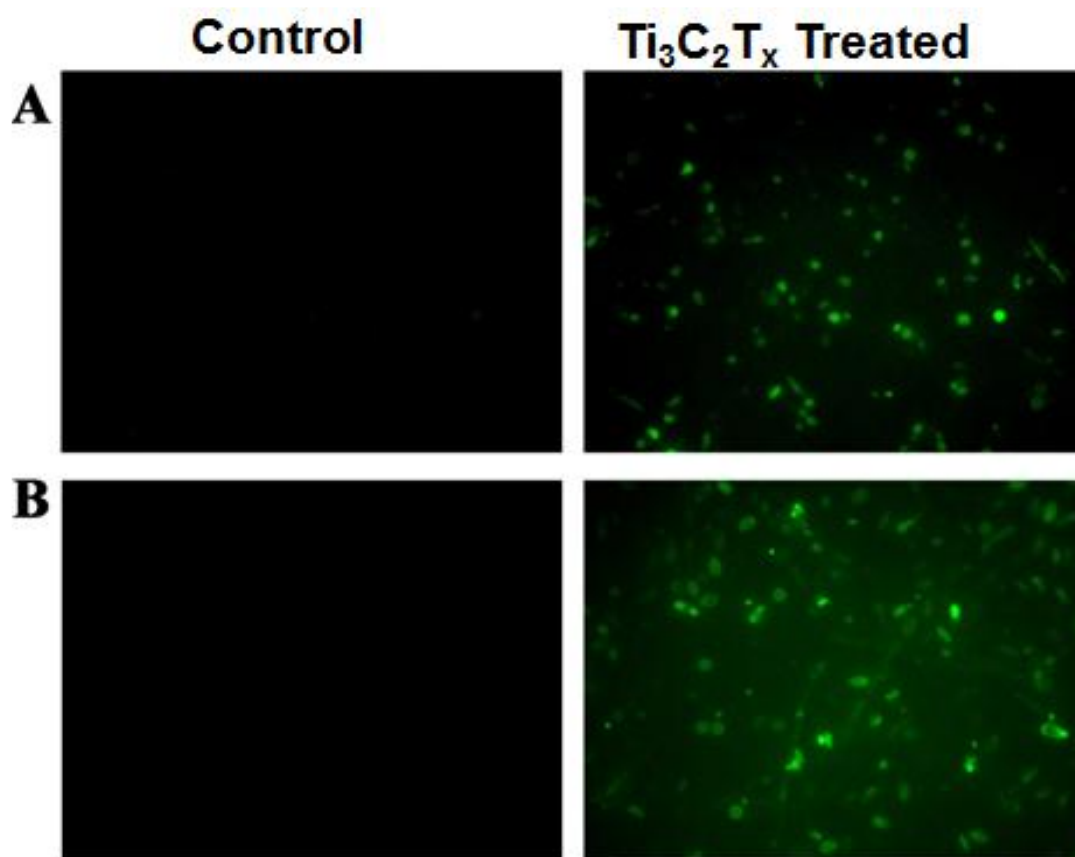
Figure 4.2.12 Effect of Ti$_3$C$_2$T$_x$ on intracellular ROS formation in *Candida* species assayed by fluorescent microscopy stained with DCFHDA. Cells exposed to Ti$_3$C$_2$T$_x$ and cells were collected, stained with DCFHDA and visualized by fluorescent microscope. (A) *C. albicans* and (B) *C. tropicalis*

4.2.4.2.5 Loss of Membrane Integrity by Ti$_3$C$_2$T$_x$

To investigate the disruptive effect of Ti$_3$C$_2$T$_x$ on the membrane of *Candida* species, the Propidium iodide (PI) influx was assessed by fluorescence microscopy (Figure 4.2.13). PI is a membrane impermeable dye exhibiting a red fluorescence upon binding with nucleic acid. Normally PI cannot cross the barrier created by undamaged cell membrane. But dying cells with damaged membrane are prone to PI penetration and it easily allow PI to enters inside and interact with nucleic acid. So the extent of membrane permeability induced by Ti$_3$C$_2$T$_x$ MXene was carefully examined by PI staining. The intense red florescence observed in *Candida* cells treated with Ti$_3$C$_2$T$_x$ MXenes is shown in Figure 4.2.13. The increased red

fluorescence level observed in the treated cells compared to its untreated counterpart suggests that $Ti_3C_2T_x$ MXene creates severe membrane damage and resulted in membrane integrity loss and cell death.
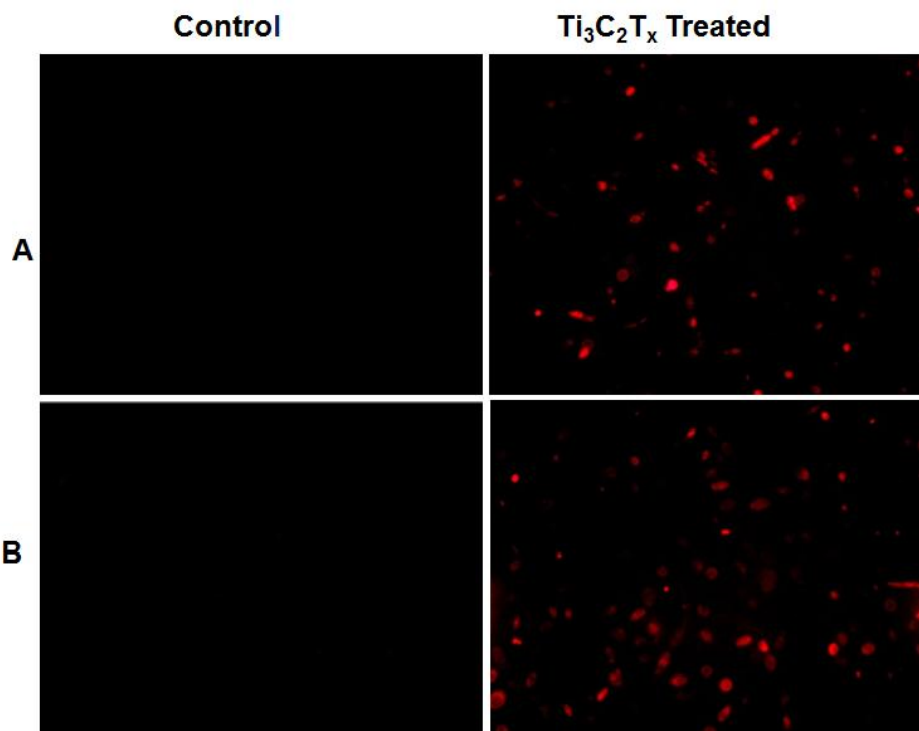
Figure 4.2.13: Confocal laser scanning microscopy (CLSM) images of membrane permeabilization by propidium iodide (PI). [A] *C. albicans* **and [B]** *C. tropicalis*

4.2.4.2.6 Measurement of Mitochondrial Membrane Potentials (mtΔψ)

The mtΔψ, in situ, is a sensitive indicator for the energetic state of the mitochondria and the cell [Wu et al., 2009], and can be used to assess the activity of the mitochondrial proton pumps, electrogenic transport systems, and the activation of the mitochondrial permeability transition [Wu et al., 2009]. Therefore, the effect of $Ti_3C_2T_x$ on mtΔψ of cells was measured by fluorescence microscopy and the corresponding images are depicted in Figure 4.2.14

In the present study, Rh123 was used to examine the effect of $Ti_3C_2T_x$ on mitochondrial potentials. Rh123 is a cationic and lipophilic dye that permeates the negatively charged mitochondria and reflects mtΔψ. Exposure to different concentrations of $Ti_3C_2T_x$ for 12 h showed significant hyperpolarization of *Candida* species mtΔψ, suggesting mitochondrial dysfunction. The results suggest that these

Ti$_3$C$_2$T$_x$ MXenes may obstruct the mitochondrial respiratory function, and cause the collapse of Δψm.
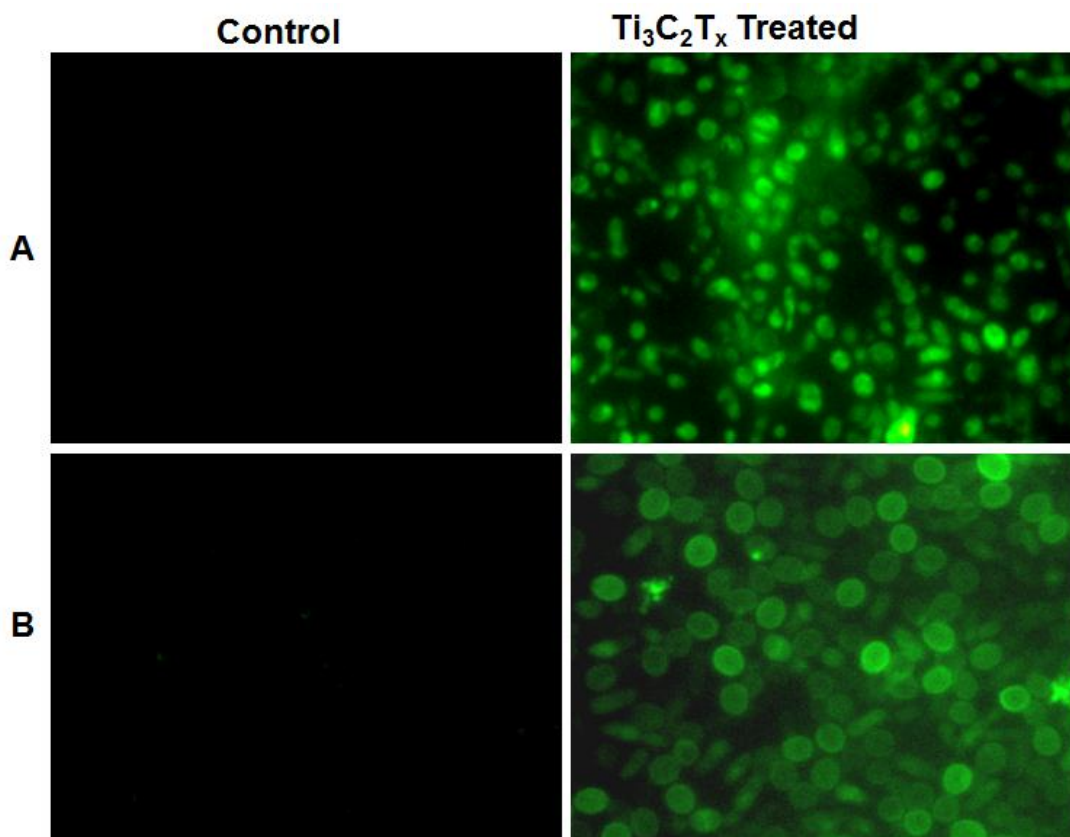
Figure 4.2.14: Confocal laser scanning microscopy (CLSM) images showing the change in mitochondrial potentials (A) *C. albicans* **and (B)** *C. tropicalis.*

4.2.4.2.7 Proposed Antimicrobial Mechanism of Ti$_3$C$_2$T$_x$ MXenes

From all these experimental evidences, a multistep mechanism may be proposed on the biocidal activity of Ti$_3$C$_2$T$_x$ MXene nanomaterial. The SEM and TEM observations support that the contact killing may be a prevalent mechanism. The Ti$_3$C$_2$T$_x$ MXene is rich in negatively charged surface groups and this anionic nature may be partially contributed to the antimicrobial property. Reports claim that Ti$_3$C$_2$T$_x$ MXene nanostructures have hydrophilic nature and this favors the firm adhesion Ti$_3$C$_2$T$_x$ MXene nanosheet on microbes [Rasool *et al.* 2016]. The strong physical binding and adherence tendency of Ti$_3$C$_2$T$_x$ MXene with the microbial membrane convincingly indicate direct contact mechanism is possibly leading to the cell damage [Figure 4.2.11]. The effect of nano-knives morphology as seen in the TEM images offered by the Ti$_3$C$_2$T$_x$ MXene nanolayers can also be accounted.

Moreover, the abundant oxygenated groups present on the surface of $Ti_3C_2T_x$ MXene may form hydrogen bonds with lipopolysaccharides stings present in cell membrane. This could prevent the nutrient intake and which in turn leads to cell death. This type of mechanism was earlier proposed for graphene oxide [Akhavan *et al.* 2010].

The exposure to $Ti_3C_2T_x$ MXene creates intracellular ROS generation and associated oxidative stress in microbes. The PI assay confirms the membrane integrity loses. Occurrence of mitochondrial damage was also evidenced. It was also reported that MXenes is a good reducing agent [Mashtalir *et al.* 2014]. All these observations suggest that there are some interactions taking place between $Ti_3C_2T_x$ MXene and the microbial cell, and more detailed study is required to uncover the real mechanism. Earlier studies on rGO and CNTs nanostructures mentioned the high electrical conductivities can also enhance the antimicrobial property by creating a conductive bridge over the insulating lipid bilayer and facilitating electron transfer from intracellular components to the surroundings. It was reported earlier that $Ti_3C_2T_x$ MXene thin film possesses conductivity as high as 2.4×10^5 S/m [Ling *et al.* 2014]. We have determined the electrical conductivity of green pellets made with $Ti_3C_2T_x$ MXene nanosheets using Four probe electrical conductivity meter and found that the conductivity is more than 8.67×10^2 S/m. The actual conductivity is much more than this, but the porous nature of the compacted MXene pellets may cause lowering of measured conductivity. Such reasonably high electrical conductivity can also be an important reason for the antimicrobial property of $Ti_3C_2T_x$ MXene.

4.2.4.3 Inhibition of Candidal Biofilm Formation by $Ti_3C_2T_x$ MXenes

Candida species are capable of triggering a large number of infections from mucosal to disseminated candidiasis in human. The later remains the most common and the third-to-fourth most frequent nosocomial infection in hospitals worldwide. *C. albicans* is the major fungus that colonizes indwelling medical devices (dental implants, vascular bypass grafts, ocular lenses, catheters, heart valves, central nervous system, shunts artificial joints, etc.) and producing device-associated infections with high mortality [Pierce *et al.* 2015]. Even though *Candida albicans* was considered as the main source of candidiasis, other non-*C. albicans* species also have been identified as common human pathogens. Infections from the medical devices

are in fact one of the probable cause in many occasions and generally necessitate the replacement or removal of the device. A situation that complicates the elimination of *C. albicans* infections is its ability to form biofilms, i.e. formation of co-operative, aggregated microbial communities on biological or inert surfaces. It is a protected niche for fungal cells and acts as a reservoir for recurring sources of persistent infections. Fully grown biofilms are huge threat due to their high levels of resistance against most of the common antifungal agents.

In this scenario, materials capable of retarding the microbial biofilm formation are extremely important. Recently, nanomaterials such as gold, silver, bismuth oxide, etc., were reported as antibiofilm agents [Yu *et al.* 2016; Lara *et al.* 2015; Hernandez-Delgadillo *et al.* 2013]. In this study, the experimental evidences strongly indicate the $Ti_3C_2T_x$ MXenes have excellent antifungal properties against a wide range of fungal pathogens. It was found that $Ti_3C_2T_x$ MXenes capable of killing most of the pathogens within a short duration effectively. After exploring the bioactive property, the capability of antibiofilm capacity of $Ti_3C_2T_x$ MXenes is also considered.

The efficiency of $Ti_3C_2T_x$ MXenes as an antibiofilm agent is documented by measuring the OD values and microscopic images. The bar chart in Figure 4.2.15 shows the observed OD values with respect to the $Ti_3C_2T_x$ MXenes concentration. The OD values undoubtedly reveal that the $Ti_3C_2T_x$ nanomaterial offers significant inhibition against biofilm formation. Both *C. albicans* and *C. tropicalis* when treated with $Ti_3C_2T_x$ nanomaterials, the rate of inhibition high and it is proportional to the concentration of $Ti_3C_2T_x$ MXenes. More than 95% inhibition was observed with 10 µg/mL $Ti_3C_2T_x$ MXenes. Microscopic images in Figure 4.2.16 shows the extent of the biofilm formed when 10 µg/mL $Ti_3C_2T_x$ MXenes is dosed. It also shows the performance in absence of $Ti_3C_2T_x$ MXenes. A visible difference is seen between these two samples. In the absence of $Ti_3C_2T_x$ MXenes, a dense layer of biofilm is formed with both the pathogens. The microbial filament formations are clearly observed. Whereas, in the case of $Ti_3C_2T_x$ MXenes treated samples, the formation of biofilm is prevented to a greater extent. Only a few isolated cells are observed in localized manner. It demonstrates the excellent biofilm resistance property of $Ti_3C_2T_x$ MXenes. Thus the study confirms that $Ti_3C_2T_x$ MXenes can be an ideal

candidate for antibiofilm coatings as well as they can act as functional fillers in biological implants.
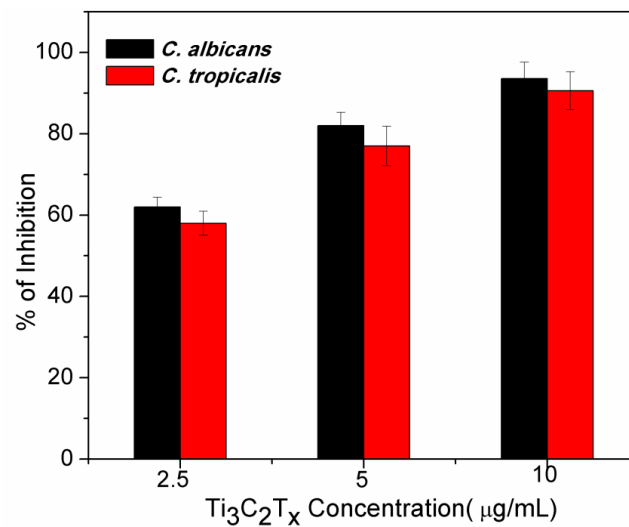
Figure 4.2.15 The effect of different concentration of Ti$_3$C$_2$T$_x$ MXenes on biofilm formation
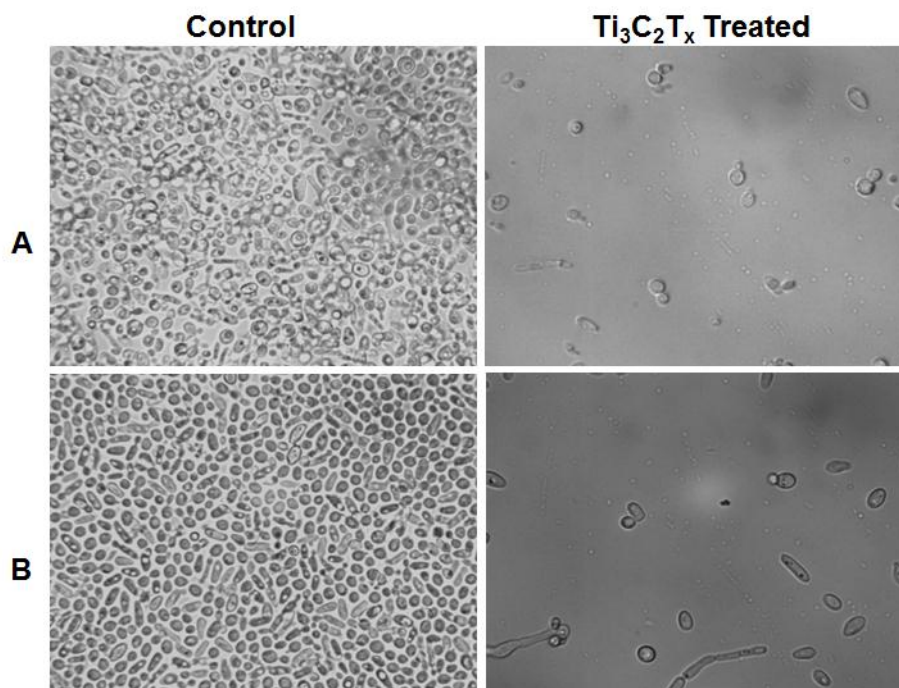
Figure 4.2.16 Opitcal microscope images showing the inhibition biofilm formation in presence of Ti$_3$C$_2$T$_x$ MXenes. (A) *C. albicans* **and (B)** *C. tropicalis*

4.2.4.4 *In vitro* Cytotoxicity of Ti$_3$C$_2$T$_x$ MXene by MTT Assay

The promising antimicrobial properties opened a new window for new biomaterial. So in order to get an insight in to the cytotoxicity of Ti$_3$C$_2$T$_x$ MXene on

mammalian cells, we have conducted an initial study using MMT assay. The experiment was conducted as per procedure given in experimental part. MTT results are directly related to the number of living cells. MMT is yellow in color which will be converted to purple colored formazan by living cells. So the absorbance of formazan crystals directly gives the number viable cells. The results are depicted in Figure 4.2.17. It was observed that $Ti_3C_2T_x$ MXene is not showing any toxicity towards mammalian cells even at the higher concentration of 200µg/mL. As seen in Figure 4.2.17 the intensity of formazan is not showing any decrease with increase in concentration of $Ti_3C_2T_x$ MXene. This suggests that $Ti_3C_2T_x$ MXene is a new biocompatible material.
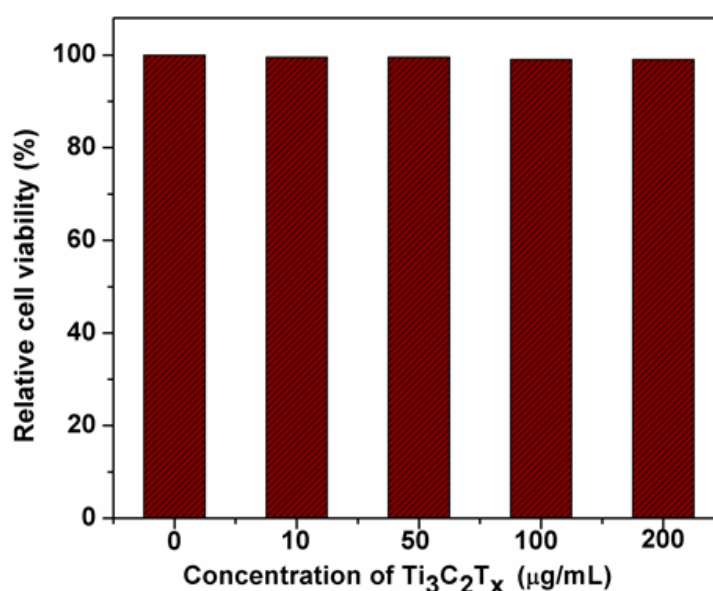
Figure 4.2.17: The cell viabilty in presence of $Ti_3C_2T_x$ MXene determined from the absorbance of formazan generated by living cell

The results were further confirmed with the microscopic images taken and are shown in Figure 4.2.18. It is well clear that there is an observable cell death occurs. This is only a preliminary study and much effort is required in future to have a detailed study on cellular uptake and cytotoxicity of $Ti_3C_2T_x$ MXene for understanding the biological impact of this material.
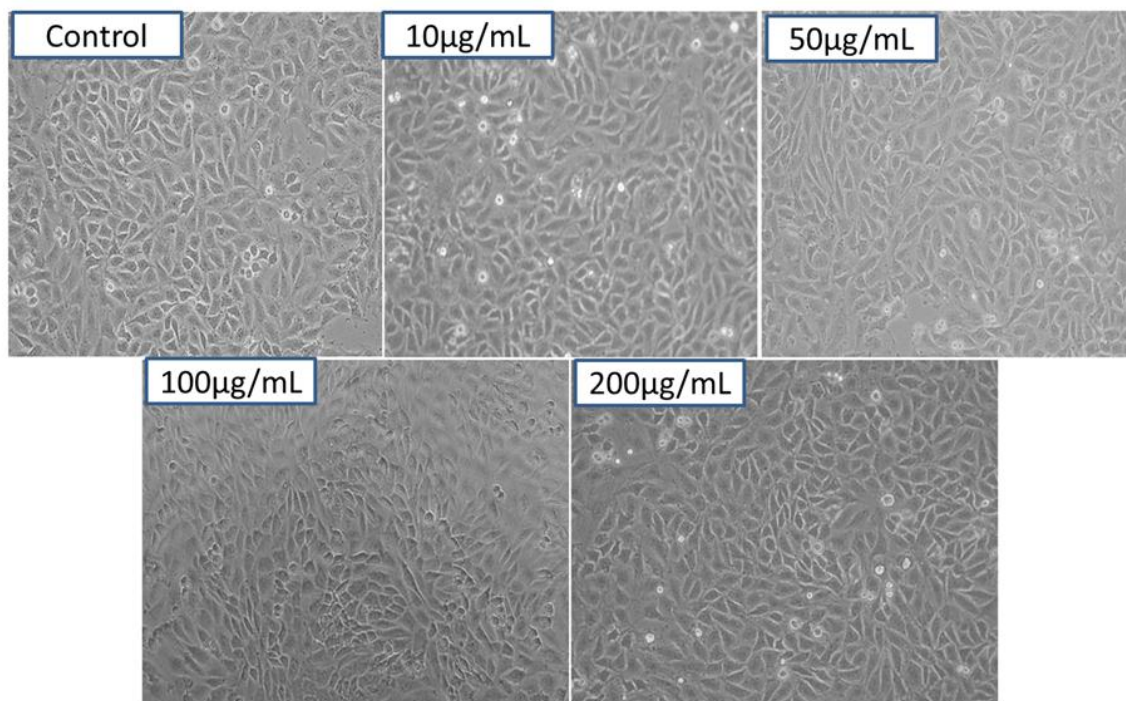
Figure 4.2.18: **The microscopic image showing the cell viabilty in presence of different concentarion of Ti$_3$C$_2$T$_x$ MXene**

4.2.5 Conclusions

The studies carried out in this chapter, clearly brought out the bio-response behaviour of Ti$_3$C$_2$T$_x$ nanostructures. This study is in fact generated a first-hand scientific knowledge on the bio-properties of MXene nanostructures. Interestingly, it can be said that MXene nanostructures are very effective and is a novel antimicrobial agent which can act as both bactericide and fungicide with extraordinary microbial killing and growth retardation capacity. The antimicrobial activity of Ti$_3$C$_2$T$_x$ MXene nanomaterial is both time and concentration dependent. Direct contact with cellular membrane and geraration of intracellualr ROS can be the possible driving force for the antimicrobial activity in Ti$_3$C$_2$T$_x$ MXene. It also possesses excellent resistance against biofilm formation. The cytotoxicity study reveals that Ti$_3$C$_2$T$_x$ MXene is a promising biomaterial. However, for convincing the biomedical expetrs, more detailed work is necessary on the cellular upatake and cytotoxicty properties.

CHAPTER 5

Summary and Future Prospects

CHAPTER 5

Summary and Future Prospects

5.1 Summary

Materials possessing exceptional functional properties have always been received much interest to develop reliable and more efficient engineering structural components, electronic devices and biomedical gadgets. In the family of layered materials, recently discovered nano laminated MAX phase materials are seriously considered for developing innovative engineering and electronic components. The attractive reason for this is, the MAX phase offers both ceramic as well as metallic properties which are truly uncommon in many conventional layered materials.

In this Ph.D. thesis, investigations have been made on MAX phase materials, primarily to explore the scientific knowledge which has not been brought out by earlier researchers. The work for this investigative study is carefully designed to bridge the technical gaps exist in certain areas like; (i) new synthesis techniques like microwave processing, (ii) application of these nanolayered MAX phase to develop new nanocomposites in order to bring out the exciting new properties, (iii) delamination characteristics of MAX phase via a simple mechanical energy to produce novel 2D nanostructures and (iv) application studies of such 2D nanostructures which are not disclosed in the earlier research attempts.

In summary, the working chapters covered; 1) experimental exploration of the beneficial properties of MAX phase reinforcements in polymer matrix composites; 2) synthesis of 2D Ti_3SiC_2 MAX phase nanosheets *via* mechanical exfoliation; 3) rapid synthesis of Ti_3AlC_2 MAX phase though microwave heating ; 4) unveiling the antimicrobial, antibiofilm and cytotoxicity properties of $Ti_3C_2T_x$ MXenes.

The major research findings and accomplishments arrived in this research study can be concluded as follows:

➢ MAX phase Ti_3SiC_2 was employed as reinforcement phase in polyaryletherketone (PAEK), an engineering soft-polymer, to produce PAEK-Ti_3SiC_2 nanocomposite for the first time. The composite was processed by hot pressing technique. The effect of different volume fractions of Ti_3SiC_2 over thermal, mechanical and tribological properties was investigated. The study showed that the Ti_3SiC_2 reinforcement offers significant control over the high thermal expansion behavior of PAEK polymer. The addition of Ti_3SiC_2 in PAEK polymer resulted in at least 50 % enhancement in the flexural and compressive strengths without affecting its inherent machinability. The composites were easily machinable. Further the composites showed progressive wear resistance and low coefficient of friction. The wear resistance is in fact much superior than the graphite reinforced PAEK composites. The coeffiecient of friction is less than that of the other comonly studied ceramic reinforcements with PAEK. A conclusion can be drawn from this part of study that a new, thermo-mechanically stable PAEK-TI_3SiC_2 composite is possible for developing structural components for any engineeirng applications.

➢ A chapter is devoted to investigate the synthesis of 2D Ti_3SiC_2 MAX phase nanostructures. A new shear induced micromechanical cleavage technique was newly conceived and successfully demonstrated. The study revealed that the exfoliation efficiency is higher in polar solvents and that ultimately produced few layer thick 2D MAX phase nanosheets. We named this 2D MAX phase derivative as '*MAXenes'* to emphasize its similarity with graphene. It can be concluded that the MAXenes offered surfactant free stable dispersions. The dispersion stability in polar solvents is attributed to the hydrophilic interaction between solvent molecules and the surface oxide groups formed on the 2D MAXene. The electrical conductivity of the 2D MAXene was six times higher than that of the bulk Ti_3SiC_2.

➢ This process was further extended successfully to design stable MAXene nanofluid by *in situ* dispersion of 2D Ti_3SiC_2 MAXene in propylene glycol base fluid. The surface associated –OH functional groups helped in retaining the colloidal stability. The nanofluids were found to be stable even after kept undisturbed for several months. Nanofluid consists of MAXene nanosheets

with varying dimensions was attempted subsequently to determine the rheology and thermal conductivity properties. The rheology study confirmed the MAXene dispersed polypropylene glycol nanofluid attains unusually decreased viscosity even when the solid fraction of MAXene is increased. At a concentration of 0.2 Vol%, MAXene dispersion results in 30 % reduction in the viscosity. Such a control over viscosity favourably increases the pumpabilty (easiness of pumping) of MAXene nanofluid that is necessary for ideal circulation during cooling operations. The MAXene nanofluid exhibits enhanced thermal transport properties compared to its basefluid. The nanofluid prepared with 0.25 vol% of MAXene dispersoids showed a 15 % increase in thermal conductivity at room temperature, which was further enhanced to 45 % at a temperature of 323 K. It is also seen that the nanofluid offered a kind of lubrication to minimize the friction. Such lubricating effect is beneficial and in fact MAXene lubricant may be an alternate to heat sensitive organic-lubricants.

➢ Microwave hybrid heating was another noteworthy contribution made in this thesis. Microwave energy was employed for the first time to synthesize Ti_3AlC_2 MAX phase. This is the best starting material for developing exotic layered Ti_3C_2 MXene 2D nanostructures. The microwave processing produced phase pure Ti_3AlC_2 successfully at relatively low temperatures.

➢ The microwave derived Ti_3AlC_2 was further explored to obtain 2D $Ti_3C_2T_x$ MXene nanostructure and an attempt was made to reveal the bio response of $Ti_3C_2T_x$ MXene over some of the selective microbial pathogens. The study found that $Ti_3C_2T_x$ MXene exhibits extraordinary antimicrobial properties. The contact killing mechanism and intracellular ROS generation was noticed as the main driving force for its antimicrobial activity. The efficiency of $Ti_3C_2T_x$ MXene as antibiofilm agent was also confirmed. The preliminary cytotoxicity studies suggest that $Ti_3C_2T_x$ MXene is not toxic to mammalian cells.

The investigations carried out in this PhD work are in fact 'first-of-its-kind' and from these research components a good numbers of publications are successfully realized in high impact factor journals, which is the notable outcome of this thesis work. The study also put forward some future directions.

5.2 Future Prospects

Most of the works attempted and demonstrated in this thesis are studied and reported for the first time. One of the researchers in this field of MAX phase is Prof. Barsoum and his co-workers. Their team is in fact the first to study the engineering aspects of this material for aerospace and structural coatings, bulk components applications. They have completely omitted the functional applications of MAX phase materials. Herein we have selected systematic studies on functional properties and thrilled with the various exciting functional characteristics of MAX phases.

However, still a good amount of work is needed to utilize the MAX phase materials completely for the electronics, energy and structural applications. Some of the aspects are left out in this thesis due to time constraints and lack of specific experimental as well as characterization facilities. They are projected here as future perspectives.

☞ Fabrication and industrial validation of PAEK-Ti_3SiC_2 composites.

☞ Investigation on the 2D Ti_3SiC_2 MAXene nanosheets as functional membranes for gas separation and desalination due to its atomic level interlayer spacing and plentiful surface functional groups that may offer selectivity to specific ions. Due to better electrical conductivity, bio-film formation resistance, antibacterial and antifungal properties combined with the good dispersion stability, a new concept for separating gas molecules and water soluble ions can be possibly conceived.

☞ MXene and MAXene applications for the transparent conductors, conducting inks, supercapacitor electrodes etc. are also quite interesting and important and hence can be considered in future.

☞ The optical properties such as UV absorption and IR transmittance/reflectance for MAX phase and its derivatives have not been known till date. It is also an avenue for further research.

☞ Utilization of 2D MAXenes for developing solar thermal fluids to harvest solar thermal energy is also essential and hence this kind of study is recommended.

Research Highlights
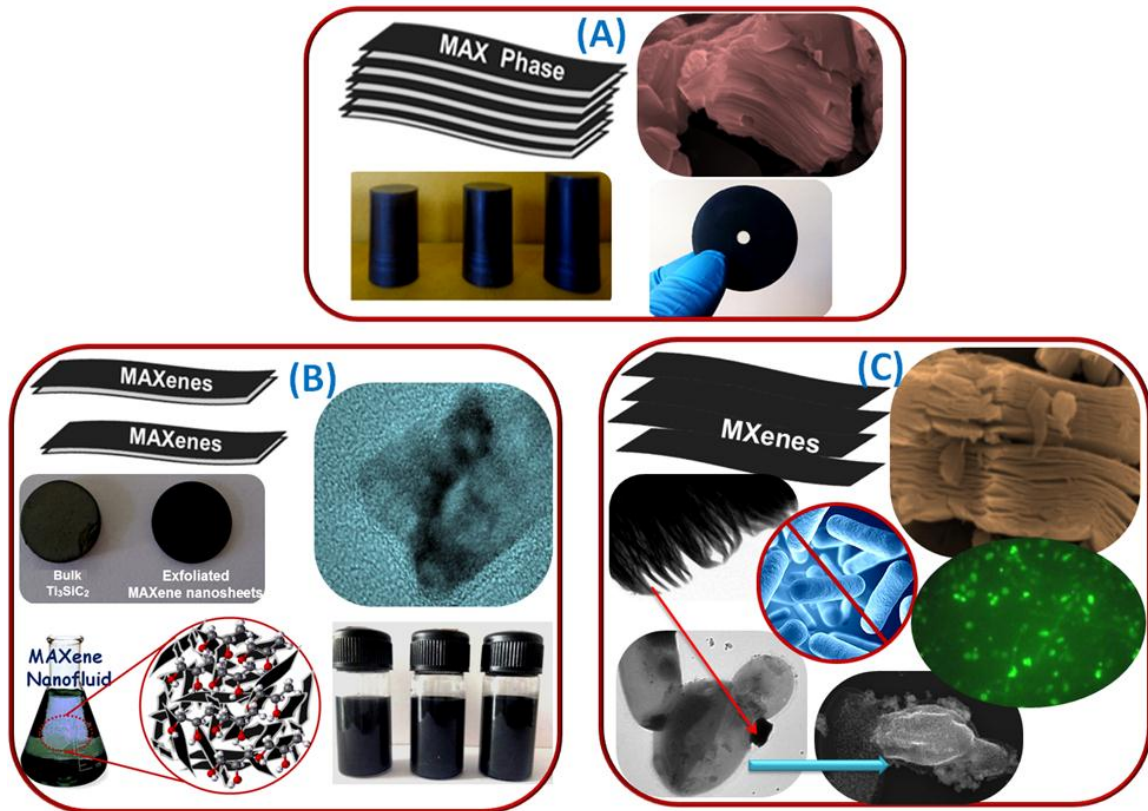
(A) Demonstration of PAEK-Ti$_3$SiC$_2$ machinable composites reported in chapter 2;(B) MAXene and MAXene nanofluids reported in chapter 3, and (C) demonstration of antimicrobial property of Ti$_3$C$_2$T$_x$ MXene reported in chapter 4

List of Publications

From the Thesis:

1. **K.V. Mahesh**, Vazhayal Linsha, A. Peer Mohamed, S. Ananthakumar "Processing of 2D-MAXene nanostructures and design of high thermal conducting, rheo-controlled MAXene nanofluids as a potential nanocoolant" **Chemical Engineering Journal,** 297, **2016**,158–169

2. **K.V. Mahesh**, R. Rashada, M. Kiran, A. Peer Mohamed and S. Ananthakumar "Shear induced micromechanical synthesis of Ti_3SiC_2 MAXene nanosheets for functional applications" **RSC Advances**, 5, **2015**, 51242

3. **K.V. Mahesh**, S. Balanand, R. Raimond, A. Peer Mohamed, S. Ananthakumar "Polyaryletherketone polymer nanocomposite engineered with nanolaminated Ti_3SiC_2 ceramic fillers" **Materials and Design**, 63, **2014**, 360–367

4. **K.V. Mahesh**, Akhil s. Nair, S. Ananthakumar, Microwave - an ultra-fast synthetic method for Ti_3AlC_2 MAX phase (communicated)

5. **K.V. Mahesh**, S. Nishanth Kumar, Vazhayal Linsha, S. Ananthakumar, Unveiling the antimicrobial properties of $Ti_3C_2T_x$ MXenes (communicated)

Outside Thesis:

6. Linsha Vazhayal, K. A. Shuhailath, **K.V. Mahesh**, A. Peer Mohamed, Ananthakumar Solaiappan "Biocatalytic conversion efficiency of steapsin lipase immobilized on hierarchically porous biomorphic aerogel supports", **ACS Sustainable Chemistry & Engineering** (under revision), **2016**

7. S.S. Vaisakh, **K.V. Mahesh**, S. Balanand, R. Metz, M. Hassanzadeh and S. Ananthakumar "MAX phase ternary carbide derived 2-D ceramic nanostructures [CDCN] as chemically interactive functional fillers for damage tolerant epoxy polymer nanocomposites" **RSC Advances**, 5, **2015**, 16521

8. Sasidharan Pillai Rahul, **K.V. Mahesh**, S. S. Sujith, Mathews Jeen Maria , S. Ananthakumar, 'Processing of La_2O_3 based rare earth non-linear resistors via combustion synthesis" **Journal of Electroceramics** 32, **2014**, 292-300.

9. R. Metz, M. Hassanzadeh, **K.V. Mahesh**, S. Ananthakumar "Quasi-ideal Nonlinear Electrical Behavior of Polycrystalline SnO_2 Ceramic Varistors Doped with SiO_2" **Journal of Electronic Materials** 43, **2014**, 1411-1418

10. S.S. Sujith, S.L. Arun Kumara, **K.V. Mahesh**, A. Peer Mohamed and S. Ananthakumar "Sintering and thermal shock resistance properties of $LaPO_4$ based composite refractories" **Transactions of Indian Ceramic Soceity**, 73, **2014**,161-164.

11. **K.V. Mahesh**, S. Anas, S. Rahul, S. Ananthakumar "Effect of two-stage sintering on rare earth (RE=Y_2O_3, Pr_6O_{11}) doped ZnO-Bi_2O_3 varistors processed from 'nano-precursor' powders", **Journal of Materials Science: Materials in Electronics**, 24, **2013**, 1495–1504

12. S. Anas, **K.V. Mahesh**, V. Jobin, S. Prasanth and S. Ananthakumar "Nanofillers in ZnO based materials: a 'smart' technique for developing miniaturized high energy field varistors, **Journal of Materials Chemistry C**,1, **2013**, 6455-6462

13. P.K. Sanoop, **K.V. Mahesh**, K.M. Nampoothiri, R.V. Mangalaraja, S. Ananthakumar, Multifunctional ZnO-Biopolymer Nanocomposite Coatings for Health-Care Polymer Foams and Fabrics, **Journal of Applied Polymer Science**, 126, **2012**, E233–E244.

14. S. Anas, **K.V. Mahesh**, K.J. Ambily, M.R. Chandran, K. Uma, K.G.K. Warrier, S. Ananthakumar, New insights on physico-chemical transformations of ZnO: From clustered multipods to single crystalline nanoplates, **Materials Chemistry and Physics**, 134, **2012**, 435-442.

Book Chapters

1. **Book:** Biomedical Application of Biopolymeric Materials. **Chapter:** Functionally Engineered Sol-Gel Derived Inorganic Gels and Hybrid Nanoarchitectures for Biomedical Applications. Linsha Vazhayal, **K.V. Mahesh** and S. Ananthakumar. **John Wiley & Sons,** 2016, pp.261-301

2. **Book:** Sol-Gel Materials for Energy, Environment and Electronic Applications. **Chapter:** Sol Gel Materials for Varistor Devices. S. Anas, **K.V. Mahesh,** Jeen Maria Mathews and S. Ananthakumar. **Springer International Publishing,** 2016, pp.23-59

Papers Presented in International/National Conferences

1. **K.V. Mahesh**, T. S. Krishnakumar, A. Peer Mohamed, M. Jose Prakash, S. Ananthakumar "A Novel Thermal Fluid Based on Ti_3SiC_2 MAX phase Ternary Carbide", **International Conference on Aerospace and Mechanical Engineering**, December 2015, TKM College of Engineering, Kollam, India. **Oral presentation**

2. **K.V. Mahesh,** Balanand Santhosh, A. Peer Mohamed, S. Ananthakumar "Ultrathin MAXene Nanostructures for Multifunctional Applications" **National Seminar on Advances in Materials Chemistry,** October 2014, Christian College, Chengannur, Kerala. **(Best Oral Presentation Award)**

3. **Mahesh K.V.,** Ananthakumar S. "MAX phase ternary carbides: a mechanical wonder" **MRSI Annual Technical day Meeting**, November 2013, Trivandrum. **Oral presentation**

4. **K.V. Mahesh, Balanand Santhosh, A. Peer Mohamed, R. Raimond, S. Ananthakumar** "Ultrathin MAXene Nanosheets:- A competitive Nanostructure for Self Lubricating Ceramic Applications" 77th annual Session of Indian Ceramic Society, December 2013, Jamshedpur, Jharkhand. **Oral presentation**

5. **Mahesh K.V.,** Ananthakumar S. "2D MAXene Nano Thermal Fluids by Ultrasonic Assisted Shear Induced Micromechanical Cleavage" January 2015, SASTRA University, Thanjavur, Tamilnadu.

6. **Mahesh K.V.,** Rahul S., Soumya S., Babitha K.B., Linsha V., Peer Mohamed, Ananthakumar S. "Microwave synthesis of nanocrystalline ZnO, it's hybrids and composites for UV/IR-shielding paints and functional cosmetics", **Chemical Research Society of India.** February 2012,Trivandrum, India

7. **Mahesh K.V**., Rahul S., Anas S., Sanoop P.K., Ananthakumar S." Medium to high voltage varistors from rare earths for surge-protection applications". **Platinum Jubilee session of Indian Ceramic Society,** December, 2011, Agra, India

8. **K. V. Mahesh,** S. Anas, S. Ananthakumar "Nanocomposite approach for high-energy field Smart-ZnO varistors: - Effect of nano fillers, two-stage sintering and microwave aging" **74th Annual session of Indian ceramic society,** January 2011, Kolkatta, India

References

Ai, M. X.; Zhai, H. X.; Zhou, Y.; Huang, Z. Y.; Zhang, Z. L.; Guan, M. L.; Li, S. B. "Fabrication and properties of Al/Ti$_3$SiC$_2$ composites" *Rare Metal Materials and Engineering* 34, **2005,** 397.

Akhavan, O.; Ghaderi, E. "Toxicity of graphene and graphene oxide nanowalls against bacteria" *ACS Nano* 4, **2010,** 5731.

Amini, S.; Barsoum, M. W.; El-Raghy, T. "Synthesis and mechanical properties of fully dense Ti$_2$SC" *Journal of the American Ceramic Society* 90, **2007,** 3953.

Amiri, A.; Shanbedi, M.; Chew, B. T.; Kazi, S. N.; Solangi, K. H. "Toward improved engine performance with crumpled nitrogen-doped graphene based water-ethylene glycol coolant" *Chemical Engineering Journal* 289, **2016,** 583.

Aravind, S. S. J.; Prathab, B.; Tessy Theres, B.; Sabareesh, R. K.; Sumitesh, D.; Ramaprabhu, S. "Investigation of structural stability, dispersion, viscosity, and conductive heat transfer properties of functionalized carbon nanotube based nanofluids" *The Journal of Physical Chemistry C* 115, **2011,** 16737.

Arunajatesan, S.; Carim, A. H. "Synthesis of titanium silicon carbide" *Journal of the American Ceramic Society* 78, **1995,** 667.

Assael, M. J.; Metaxa, I. N.; Arvanitidis, J.; Christofilos, D.; Lioutas, C. "Thermal conductivity enhancement in aqueous suspensions of carbon multi-walled and double-walled nanotubes in the presence of two different dispersants" *International Journal of Thermophysics* 26, **2005,** 647.

Balandin, A. A. "Thermal properties of graphene and nanostructured carbon materials" *Nature Materials* 10, **2011,** 569.

Bang, G. S.; Cho, S.; Son, N.; Shim, G. W.; Cho, B.-K.; Choi, S.-Y. "DNA-assisted exfoliation of tungsten dichalcogenides and their antibacterial effect" *ACS Applied Materials & Interfaces* 8, **2016,** 1943.

Bao, Y.; Zhang, H.; Zhou, Y. "Punch-shear tests and size effects for evaluating the shear strength of machinable ceramics" *Zeitschriftfur Metallkunde* 95, **2004,** 372.

Bao, Y. W.; Wang, X. H.; Zhang, H. B.; Zhou, Y. C. "Thermal shock behavior of Ti_3AlC_2 from between 200 °C and 1300 °C" *Journal of the European Ceramic Society* 25, **2005,** 3367.

Bao, Y. W.; Zhou, Y. C. "Low shear strength and shear-induced failure in Ti_3SiC_2" *Journal of Materials Science & Technology* 19, **2003,** 197.

Bao, Y. W.; Zhou, Y. C.; Zhang, H. B. "Investigation on reliability of nanolayer-grained Ti_3SiC_2 via Weibull statistics" *Journal of materials Science* 42, **2007,** 4470.

Barsoum, M. W. "The $M_{N+1}AX_N$ phases: a new class of solids: thermodynamically stable nanolaminates" *Progress in Solid State Chemistry* 28, **2000,** 201.

Barsoum, M. W. "Physical properties of the MAX phases, Encyclopedia of Materials: Science and Technology" *Physical properties of the MAX phases, Encyclopedia of Materials: Science and Technology* **2006**.

Barsoum, M. W. *MAX phases: properties of machinable ternary carbides and nitrides.* John Wiley & Sons: **2013**.

Barsoum, M. W.; Brodkin, D.; El-Raghy, T. "Layered machinable ceramics for high temperature applications" *Scripta Materialia* 36, **1997b,** 535.

Barsoum, M. W.; El-Raghy, T. "A progress report on Ti_3SiC_2, Ti_3GeC_2, and the H-phases, M_2BX" *Journal of Materials Synthesis and Processing* 5, **1997,** 197.

Barsoum, M. W.; El-Raghy, T. "Room-temperature ductile carbides" *Metallurgical and Materials Transactions A* 30, **1999,** 363.

Barsoum, M. W.; El-Raghy, T. "The MAX Phases: unique new carbide and nitride materials: ternary ceramics turn out to be surprisingly soft and machinable, yet also heat-tolerant, strong and lightweight" *American Scientist* 89, **2001,** 334.

Barsoum, M. W.; El-Raghy, T.; Rawn, C. J.; Porter, W. D.; Wang, H.; Payzant, E. A.; Hubbard, C. R. "Thermal properties of Ti_3SiC_2" *Journal of Physics and Chemistry of Solids* 60, **1999a,** 429.

Barsoum, M. W.; El-Raghy, T. "Synthesis and characterization of a remarkable ceramic: Ti_3SiC2" *Journal of the American Ceramic Society* 79, **1996,** 1953.

Barsoum, M. W.; El-Raghy, T.; Ogbuji, L. U. J. T. "Oxidation of Ti_3SiC_2 in air" *Journal of the Electrochemical Society* 144, **1997c,** 2508.

Barsoum, M. W.; Farber, L.; Levin, I.; Procopio, A.; El-Raghy, T.; Berner, A. "High Resolution Transmission Electron Microscopy of Ti_4AlN_3, or $Ti_3Al_2N_2$ Revisited" *Journal of the American Ceramic Society* 82, **1999b,** 2545.

Barsoum, M. W.; Ho-Duc, L. H.; Radovic, M.; El-Raghy, T. "Long time oxidation study of Ti_3SiC_2, Ti_3SiC_2/SiC, and Ti_3SiC_2/TiC composites in air" *Journal of the Electrochemical Society* 150, **2003,** B166.

Barsoum, M. W.; Radovic, M. Elastic and Mechanical Properties of the MAX Phases. In *Annual Review of Materials Research, Vol 41*, D.R. Clarke, P. Fratzl, Eds. **2011**; Vol. 41, pp 195.

Barsoum, M. W.; Zhen, T.; Kalidindi, S. R.; Radovic, M.; Murugaiah, A. "Fully reversible, dislocation-based compressive deformation of Ti_3SiC_2 to 1 GPa" *Nature Materials* 2, **2003b,** 107.

Barsoum, M. W.; Zhen, T.; Zhou, A.; Basu, S.; Kalidindi, S. R. "Microscale modeling of kinking nonlinear elastic solids" *Physical Review B* 71, **2005,** 134101.

Barsoum, M. W. R., M. Mechanical Properties of the MAX phases. In *Encyclopedia of Materials Science and Technology*, K.H.J.C. Buschow, R. W.; Flemings, M. C.; Kramer, E. J.; Mahajan, S.; Veyssiere, P., Ed. Elsevier Science: Amsterdam, **2004**; pp 1.

Beckers, M.; Schell, N.; Martins, R. M. S.; Mucklich, A.; Moller, W. "Phase stability of epitaxially grown Ti_2AlN thin films" *Applied Physics Letters* 89, **2006,** 74101.

Benko, E.; Klimczyk, P.; Mackiewicz, S.; Barr, T. L.; Piskorska, E. "cBN-Ti_3SiC_2 composites" *Diamond and Related materials* 13, **2004,** 521.

Canter, N. Heat Transfer Fluids: Selection, maintenance & new applications. In *Tribology & Lubrication Technology*, **2009**; Vol. 65, pp 28.

Chen, H.; Witharana, S.; Jin, Y.; Kim, C.; Ding, Y. "Predicting thermal conductivity of liquid suspensions of nanoparticles (nanofluids) based on rheology" *Particuology* 7, **2009,** 151.

Chen, L.; Xie, H. Q.; Li, Y.; Yu, W. "Applications of cationic gemini surfactant in preparing multi-walled carbon nanotube contained nanofluids" *Colloids and Surfaces a-Physicochemical and Engineering Aspects* 330, **2008,** 176.

Chen, L. F.; Xie, H. Q. "Properties of carbon nanotube nanofluids stabilized by cationic gemini surfactant" *Thermochimica Acta* 506, **2010,** 62.

Chen, Y.; Zeng, H.; Tian, J.; Ban, X.; Ma, B.; Wang, Y. "Antifungal mechanism of essential oil from Anethum graveolens seeds against Candida albicans" *Journal of medical microbiology* 62, **2013,** 1175.

Choi, C.; Yoo, H. S.; Oh, J. M. "Preparation and heat transfer properties of nanoparticle-in-transformer oil dispersions as advanced energy-efficient coolants" *Current Applied Physics* 8, **2008,** 710.

Choi, S. U. S. "Nanofluids: From vision to reality through research" *Journal of Heat Transfer* 131, **2009,** 033106.

Chou, S. S.; Kaehr, B.; Kim, J.; Foley, B. M.; De, M.; Hopkins, P. E.; Huang, J.; Brinker, C. J.; Dravid, V. P. "Chemically Exfoliated MoS_2 as Near-Infrared Photothermal Agents" *Angewandte Chemie International Edition* 52, **2013,** 4160.

Chunfeng, H.; Yanchun, Z.; Yiwang, B.; Detian, W. "Tribological Properties of Polycrystalline Ti_3SiC_2 and $Al_2O_3 \bullet$ Reinforced Ti_3SiC_2 Composites" *Journal of the American Ceramic Society* 89, **2006,** 3456.

Chunyi, Z.; Yibin, X.; Yoshio, B.; Dmitri, G. "Highly thermo-conductive fluid with boron nitride nanofillers" *ACS nano* 5, **2011,** 6571.

Clark, D. E.; Folz, D. C.; West, J. K. "Processing materials with microwave energy" *Materials Science and Engineering: A* 287, **2000,** 153.

Clark, D. E.; Sutton, W. H. "Microwave processing of materials" *Annual Review of Materials Science* 26, **1996,** 299.

Cong, H.-P.; He, J.-J.; Lu, Y.; Yu, S.-H. "Water-soluble magnetic-functionalized reduced graphene oxide sheets: in situ synthesis and magnetic resonance imaging applications" *Small* 6, **2009,** 169.

Cote, L. J.; Kim, F.; Huang, J. "Langmuir Blodgett assembly of graphite oxide single layers" *Journal of the American Chemical Society* 131, **2009,** 1043.

Crossley, A.; Kisi, E. H.; Summers, J. W. B.; Myhra, S. "Ultra-low friction for a layered carbide-derived ceramic, investigated by lateral force microscopy (LFM)" *Journal of Physics D: Applied Physics* 32, **1999,** 632.

de Heer, W. A.; Berger, C.; Wu, X.; First, P. N.; Conrad, E. H.; Li, X.; Li, T.; Sprinkle, M.; Hass, J.; Sadowski, M. L.; Potemski, M.; Martinez, G. r. "Epitaxial graphene" *Solid State Communications* 143, **2007,** 92.

Deepesh, G.; Dijo, D.; Manikoth, M. S. "MoS$_2$ quantum dot-interspersed exfoliated MoS2 nanosheets" *ACS nano* 8, **2014,** 52975303.

Dey, K.; Bhatnagar, D.; Srivastava, A.; Wan, M.; Singh, S.; Yadav, R.; Yadav, B.; Deepa, M. "VO$_2$ nanorods for efficient performance in thermal fluids and sensors" *Nanoscale* 7, **2015,** 6159.

Dikin, D. A.; Stankovich, S.; Zimney, E. J.; Piner, R. D.; Dommett, G. H. B.; Evmenenko, G.; Nguyen, S. T.; Ruoff, R. S. "Preparation and characterization of graphene oxide paper" *Nature* 448, **2007,** 457.

DowChemicalCompany   http://www.dow.com/heattrans/support/selection/ethylene-vs-propylene.htm (accessed 03.02.2016)

Dresselhaus, M. S.; Chen, G.; Tang, M. Y.; Yang, R.; Lee, H.; Wang, D.; Ren, Z.; Fleurial, J.-P.; Gogna, P. "New directions for low-dimensional thermoelectric materials" *Advanced Materials* 19, **2007,** 1043.

Du, Y. L.; Sun, Z. M.; Hashimoto, H.; Tian, W. B. "First-principles study of polymorphism in Ta$_4$AlC$_3$" *Solid State Communications* 145, **2008a,** 461.

Du, Y. L.; Sun, Z. M.; Hashimoto, H.; Tian, W. B. "First-principles study on electronic structure and elastic properties of Ti$_2$SC" *Physics Letters A* 372, **2008b,** 5220.

Ebbesen, T. W.; Hiura, H. "Graphene in 3-dimensions: Towards graphite origami" *Advanced Materials* 7, **1995,** 582.

Eklund, P.; Beckers, M.; Jansson, U.; Hagberg, H.; Hultman, L. "The M$_{n+1}$AX$_n$ phases: Materials science and thin-film processing" *Thin Solid Films* 518, **2010,** 1851.

Eklund, P.; Virojanadara, C.; Emmerlich, J.; Johansson, L. I.; Hagberg, H.; Hultman, L. "Photoemission studies of Ti$_3$SiC$_2$ and nanocrystalline-TiC/amorphous-SiC nanocomposite thin films" *Physical Review B* 74, **2006,** 045417.

El-• Raghy, T.; Barsoum, M. W.; Zavaliangos, A.; Kalidindi, S. R. "Processing and mechanical properties of Ti$_3$SiC$_2$: II, effect of grain size and deformation temperature" *Journal of the American Ceramic Society* 82, **1999b,** 2855.

El-Raghy, T.; Barsoum, M. W. "Processing and mechanical properties of Ti3SiC2: I, reaction path and microstructure evolution" *Journal of the American Ceramic Society* 82, **1999,** 2849.

El-Raghy, T.; Blau, P.; Barsoum, M. W. "Effect of grain size on friction and wear behavior of Ti_3SiC_2" *Wear* 238, **2000b,** 125.

El-Raghy, T.; Chakraborty, S.; Barsoum, M. W. "Synthesis and Characterization of Hf 2 PbC, Zr_2PbC and M_2SnC (M= Ti, Hf, Nb or Zr)" *Journal of the European Ceramic Society* 20, **2000,** 2619.

Emmerlich, J.; Hagberg, H.; Sasvari, S.; Persson, P.; Hultman, L.; Palmquist, J.-P.; Jansson, U.; Molina-Aldareguia, J. M.; Czigany, Z. "Growth of Ti_3SiC_2 thin films by elemental target magnetron sputtering" *Journal of applied physics* 96, **2004,** 4817.

Emmerlich, J.; Music, D.; Eklund, P.; Wilhelmsson, O.; Jansson, U.; Schneider, J. M.; Hagberg, H.; Hultman, L. "Thermal stability of Ti_3SiC_2 thin films" *Acta Materialia* 55, **2007,** 1479.

Etzkorn, J.; Ade, M.; Kotzott, D.; Kleczek, M.; Hillebrecht, H. "Ti_2GaC, Ti_4GaC_3 and Cr_2GaC-synthesis, crystal growth and structure analysis of Ga-containing MAX-phases $M_{n+1}GaC_n$ with M= Ti, Cr and n= 1, 3" *Journal of Solid State Chemistry* 182, **2009,** 995.

Farber, L.; Levin, I.; Barsoum, M. W.; El-Raghy, T.; Tzenov, T. "High-resolution transmission electron microscopy of some $Ti_{n+1}AX_n$ compounds (n= 1, 2; A= Al or Si; X= C or N)" *Journal of applied physics* 86, **1999,** 2540.

Feng, C.; Ma, J.; Li, H.; Zeng, R.; Guo, Z.; Liu, H. "Synthesis of molybdenum disulfide (MoS_2) for lithium ion battery applications" *Materials Research Bulletin* 44, **2009,** 1811.

Feng, L.; Zhang, S.; Liu, Z. "Graphene based gene transfection" *Nanoscale* 3, **2010,** 1252.

Finkel, P.; Barsoum, M. W.; El-Raghy, T. "Low temperature dependencies of the elastic properties of Ti_4AlN_3, $Ti_3Al_{1.1}C_{1.8}$, and Ti_3SiC_2" *Journal of applied physics* 87, **2000,** 1701.

Finkel, P.; Seaman, B.; Harrell, K.; Palma, J.; Hettinger, J. D.; Lofland, S. E.; Ganguly, A.; Barsoum, M. W.; Sun, Z.; Li, S. "Electronic, thermal, and elastic properties of $Ti_3Si_{(1-x)}Ge_xC_2$ solid solutions" *Physical Review B* 70, **2004,** 085104.

Frodelius, J.; Sonestedt, M.; Bjarklund, S.; Palmquist, J.-P.; Stiller, K.; Hagberg, H.; Hultman, L. "Ti_2AlC coatings deposited by high velocity oxy-fuel spraying" *Surface and Coatings Technology* 202, **2008,** 5976.

Gil, A., Korili, S.A., Trujillano, R., Vicente, M.A. *Pillared Clays and Related Catalysts*. Springer New York: **2010**.

Gilbert, C. J.; Bloyer, D. R.; Barsoum, M. W.; El-Raghy, T.; Tomsia, A. P.; Ritchie, R. O. "Fatigue-crack growth and fracture properties of coarse and fine-grained Ti_3SiC_2" *Scripta Materialia* 42, **1999**.

Goesmann, F.; Wenzel, R.; Schmid• Fetzer, R. "Preparation of Ti_3SiC_2 by Electron• Beam• Ignited Solid• State Reaction" *Journal of the American Ceramic Society* 81, **1998,** 3025.

Goto, T.; Hirai, T. "Chemically vapor deposited Ti_3SiC_2" *Materials Research Bulletin* 22, **1987,** 1195.

Goyal, R. K.; Negi, Y. S.; Tiwari, A. N. "High performance polymer composites on PEEK reinforced with aluminum oxide" *Journal of Applied Polymer Science* 100, **2006**.

Goyal, R. K.; Tiwari, A. N.; Mulik, U. P.; Negi, Y. S. "Effect of aluminum nitride on thermomechanical properties of high performance PEEK" *Composites Part A: Applied Science and Manufacturing* 38, **2007a**.

Goyal, R. K.; Tiwari, A. N.; Mulik, U. P.; Negi, Y. S. "Novel high performance Al_2O_3/poly(ether ether ketone) nanocomposites for electronics applications" *Composites Science and Technology* 67, **2007b,** 1802.

Grand View Research, Market Research Report on "Heat Transfer Fluids Market Analysis By Product (Silicones & Aromatics, Mineral Oils, Glycol), By Application (Oil & Gas, Chemical Industry, Concentrated Solar Power (CSP), Food & Beverages, Plastics, Pharmaceuticals, HVAC) And Segment Forecasts To 2022" http://www.grandviewresearch.com/industry-analysis/heat-transfer-fluids-market/toc (accessed March 2016).

Gupta, S.; Filimonov, D.; Palanisamy, T.; Barsoum, M. W. "Tribological behavior of select MAX phases against Al_2O_3 at elevated temperatures" *Wear* 265, **2008**.

Gurunathan, S. "Biologically synthesized silver nanoparticles enhances antibiotic activity against Gram-negative bacteria" *Journal of Industrial and Engineering Chemistry* 29, **2015,** 217.

Halim, J.; Cook, K. M.; Naguib, M.; Eklund, P.; Gogotsi, Y.; Rosen, J.; Barsoum, M. W. "X-ray photoelectron spectroscopy of select multi-layered transition metal carbides (MXenes)" *Applied Surface Science* 362, **2016,** 406.

He, X.; Bai, Y.; Zhu, C.; Barsoum, M. W. "Polymorphism of newly discovered Ti_4GaC_3: A first-principles study" *Acta Materialia* 59, **2011,** 5523.

Heising, J.; Kanatzidis, M. G. "Exfoliated and restacked MoS_2 and WS_2: Ionic or neutral species? Encapsulation and ordering of hard electropositive cations" *Journal of the American Chemical Society* 121, **1999,** 11720.

Hernandez-Delgadillo, R.; Velasco-Arias, D.; Jose Martinez-Sanmiguel, J.; Diaz, D.; Zumeta-Dube, I.; Arevalo-Nino, K.; Cabral-Romero, C. "Bismuth oxide aqueous colloidal nanoparticles inhibit *Candida albicans* growth and biofilm formation" *International Journal of Nanomedicine* 8, **2013,** 1645.

Hettinger, J. D.; Lofland, S. E.; Finkel, P.; Meehan, T.; Palma, J.; Harrell, K.; Gupta, S.; Ganguly, A.; El-Raghy, T.; Barsoum, M. W. "Electrical transport, thermal transport, and elastic properties of M_2AlC (M= Ti, Cr, Nb, and V)" *Physical Review B* 72, **2005,** 115120.

Hu, C.; Zhang, J.; Bao, Y.; Wang, J.; Li, M.; Zhou, Y. "In-situ reaction synthesis and decomposition of Ta_2AlC" *International Journal of Materials Research* 99, **2008,** 8.

Hu, C.; Zhou, Y.; Bao, Y.; Wan, D. "Tribological Properties of Polycrystalline Ti_3SiC_2 and $Al_2O_3•$ Reinforced Ti_3SiC_2 Composites" *Journal of the American Ceramic Society* 89, **2006,** 3456.

Hu, W.; Peng, C.; Luo, W.; Lv, M.; Li, X.; Li, D.; Huang, Q.; Fan, C. "Graphene-based antibacterial paper" *ACS Nano* 4, **2010,** 4317.

Huaqing, X.; Lifei, C. "Review on the Preparation and Thermal Performances of Carbon Nanotube Contained Nanofluids" *Journal of Chemical & Engineering Data* 56, **2011,** 1030.

Huxtable, S. T.; Cahill, D. G.; Shenogin, S.; Xue, L. P.; Ozisik, R.; Barone, P.; Usrey, M.; Strano, M. S.; Siddons, G.; Shim, M.; Keblinski, P. "Interfacial heat flow in carbon nanotube suspensions" *Nature Materials* 2, **2003,** 731.

Iijima, S. "Helical microtubules of graphitic carbon" *Nature* 354, **1991,** 56.

Ismadji, S.; Soetaredjo, F. E.; Ayucitra, A. Natural clay minerals as environmental cleaning agents. In *Clay Materials for Environmental Remediation*, Springer International Publishing: Cham, **2015**; pp 5.

Ivchenko, V. I.; Kosolapova, T. Y. "Conditions of preparation of ternary Ti-Al-C alloy powders" *Powder Metallurgy and Metal Ceramics* 14, **1975,** 431.

Ivchenko, V. I.; Lesnaya, M. I.; Nemchenko, V. F.; Kosolapova, T. Y. "Preparation and some properties of the ternary compound Ti_2AlN" *Porosh. Metall.* 160, **1976a,** 60.

Ivchenko, V. I.; Lesnaya, M. I.; Nemchenko, V. F.; Kosolapova, T. Y. "Some physical properties of ternary compounds in the system Ti-Al-C." *Porosh. Metall.* 161, **1976b,** 45.

Jacques, S.; Di-Murro, H.; Berthet, M. P.; Vincent, H. "Pulsed reactive chemical vapor deposition in the C-Ti-Si system from $H_2/TiCl_4/SiCl_4$" *Thin Solid Films* 478, **2005,** 13.

Jaime, T.-T.; Tharangattu, N. N.; Guanhui, G.; Matthew, R.; Dmitri, A. T.; Matteo, P.; Pulickel, M. A. "Electrically insulating thermal nano-oils using 2D fillers" *ACS nano* 6, **2012,** 1214.

Jaime, T.-T.; Tharangattu, N. N.; Guanhui, G.; Matthew, R.; Dmitri, A. T.; Matteo, P.; Pulickel, M. A. "Electrically insulating thermal nano-oils using 2D fillers" *ACS nano* 6, **2012** 1214.

Janney, M. A.; Calhoun, C. L.; Kimrey, H. D. "Microwave sintering of solid oxide fuel cell materials: I, Zirconia/8 mol% Yttria" *Journal of the American Ceramic Society* 75, **1992,** 341.

Jeitschko, W.; Nowotny, H. "Die Kristallstruktur von Ti_3SiC_2 ein neuer Komplex carbid-Typ" *Monatsheftefur Chemie undverwandte Teile anderer Wissenschaften* 98, **1967,** 329.

Jingyang, W.; Yanchun, Z. "Recent progress in theoretical prediction, preparation, and characterization of layered ternary transition-metal carbides" *Annual Review of Materials Research* 39, **2009,** 415.

Joensen, P. F., Rf; Morrison, Sr. "Single-layer MoS_2" *Materials Research Bullettin* 21, **1986,** 457.

Jonggan, H.; Dongsik, K. "Effects of aggregation on the thermal conductivity of alumina/water nanofluids" *Thermochimica Acta* 542, **2012,** 2832.

Jose Jaime, T.-T.; Tharangattu Narayanan, N.; Chandra Sekhar, T.; Karen, L.; Mircea, C.; Pulickel, M. A. "Nanodiamond-based thermal fluids" *ACS Applied Materials & Interfaces* 6, **2014,** 4778.

Kalishwaralal, K.; BarathManiKanth, S.; Pandian, S. R. K.; Deepak, V.; Gurunathan, S. "Silver nanoparticles impede the biofilm formation by *Pseudomonas aeruginosa* and *Staphylococcus epidermidis*" *Colloids and Surfaces B: Biointerfaces* 79, **2010,** 340.

Kang, S.; Pinault, M.; Pfefferle, L. D.; Elimelech, M. "Single-walled carbon nanotubes exhibit strong antimicrobial activity" *Langmuir* 23, **2007,** 8670.

Kim, K. S.; Zhao, Y.; Jang, H.; Lee, S. Y.; Kim, J. M.; Kim, K. S.; Ahn, J.-H.; Kim, P.; Choi, J.-Y.; Hong, B. H. "Large-scale pattern growth of graphene films for stretchable transparent electrodes" *Nature* 457, **2009,** 706.

Kisi, E. H.; Crossley, J. A. A.; Myhra, S.; Barsoum, M. W. "Structure and crystal chemistry of Ti_3SiC_2" *Journal of Physics and Chemistry of Solids* 59, **1998a,** 1437.

Kisi, E. H.; Crossley, J. A. A.; Myhraa, S. "Structure and crystal chemistry of Ti_3SiC_2" *Journal of Physics and Chemistry of Solids* 59, **1998b,** 1437.

Klemm, H.; Tanihata, K.; Miyamoto, Y. "Gas pressure combustion sintering and hot isostatic pressing in the Ti-Si-C system" *Journal of materials Science* 28, **1993,** 1557.

Koh, Y.-H.; Kim, H.-W.; Kim, H.-E.; Halloran, J. W. "Thermal shock resistance of fibrous monolithic Si_3N_4/BN ceramics" *Journal of the European Ceramic Society* 24, **2004,** 2339.

Kroto, H. W.; Heath, J. R.; O'Brien, S. C.; Curl, R. F.; Smalley, R. E. "C60: Buckminsterfullerene" *Nature* 318, **1985a,** 162.

Kroto, H. W.; Heath, J. R.; O'Brien, S. C.; Curl, R. F.; Smalley, R. E. "C 60: buckminsterfullerene" *Nature* 318, **1985b,** 162.

Kumaresan, V.; Velraj, R. "Experimental investigation of the thermo-physical properties of water-ethylene glycol mixture based CNT nanofluids" *Thermochimica Acta* 545, **2012,** 180186.

Kuo, M. C.; Tsai, C. M.; Huang, J. C.; Chen, M. "PEEK composites reinforced by nano-sized SiO_2 and Al_2O_3 particulates" *Materials Chemistry and Physics* 90, **2005**.

Kuroda, Y.; Low, I. M.; Barsoum, M. W.; El-Raghy, T. "Indentation responses, wear and damage characteristics of hot-isostatically-pressed Ti_3SiC_2" *Journal of the Australasian Ceramic Society* 37, **2001,** 95.

Kwon, S.-Y.; Ciobanu, C. V.; Petrova, V.; Shenoy, V. B.; Bareao, J.; Gambin, V.; Petrov, I.; Kodambaka, S. "Growth of semiconducting graphene on palladium" *Nano Letters* 9, **2009,** 3985.

Lane, N. J.; Naguib, M.; Lu, J.; Hultman, L.; Barsoum, M. W. "Structure of a new bulk $Ti_5Al_2C_3$ MAX phase produced by the topotactic transformation of Ti_2AlC" *Journal of the European Ceramic Society* 32, **2012,** 3485.

Lara, H. H.; Romero-Urbina, D. G.; Pierce, C.; Lopez-Ribot, J. L.; Arellano-Jimenez, M. J.; Jose-Yacaman, M. "Effect of silver nanoparticles on Candida albicans biofilms: an ultrastructural study" *Journal of Nanobiotechnology* 13, **2015**.

Lee, D. B.; Park, S. W. "Oxidation of Ti_3SiC_2 between 900 °C and 1200 °C in air" *Oxidation of metals* 67, **2007,** 51.

Li, H.; Peng, L. M.; Gong, M.; He, L. H.; Zhao, J. H.; Zhang, Y. F. "Processing and microstructure of Ti_3SiC_2/M (M= Ni or Co) composites" *Materials Letters* 59, **2005a,** 2647.

Li, J.-F.; Matsuki, T.; Watanabe, R. "Fabrication of highly dense Ti$_3$SiC$_2$ ceramics by pressureless sintering of mechanically alloyed elemental powders" *Journal of materials Science* 38, **2003,** 2661.

Li, J.; Wang, G.; Zhu, H.; Zhang, M.; Zheng, X.; Di, Z.; Liu, X.; Wang, X. "Antibacterial activity of large-area monolayer graphene film manipulated by charge transfer" *Scientific reports* 4, 4359.

Li, J.; Wang, G.; Zhu, H.; Zhang, M.; Zheng, X.; Di, Z.; Liu, X.; Wang, X. "Antibacterial activity of large-area monolayer graphene film manipulated by charge transfer" *Scientific reports* 4, **2014,** 4359.

Li, J. F.; Matsuki, T.; Watanabe, R. "Combustion reaction during mechanical alloying synthesis of Ti$_3$SiC$_2$ ceramics from 3Ti/Si/2C powder mixture" *Journal of the American Ceramic Society* 88, **2005b,** 1318.

Li, J. F.; Pan, W.; Sato, F.; Watanabe, R. "Mechanical properties of polycrystalline Ti$_3$SiC$_2$ at ambient and elevated temperatures" *Acta Materialia* 49, **2001,** 937.

Li, K.; Yeung, C.Y.; Yeung, K. W. K.; Tjong, S. C. "Sintered hydroxyapatite/polyetheretherketone nanocomposites: mechanical behavior and biocompatibility" *Advanced Engineering Materials* 14, **2012a,** B155.

Li, S.-B.; Xie, J.-X.; Zhang, L.-T.; Cheng, L.-F. "In situ synthesis of Ti$_3$SiC$_2$/SiC composite by displacement reaction of Si and TiC" *Materials Science and Engineering: A* 381, **2004,** 51.

Li, X.; Cai, W.; An, J.; Kim, S.; Nah, J.; Yang, D.; Piner, R.; Velamakanni, A.; Jung, I.; Tutuc, E. "Large-area synthesis of high-quality and uniform graphene films on copper foils" *Science* 324, **2009,** 1312.

Li, X.; Zou, C.; Wang, T.; Lei, X. "Rheological behavior of ethylene glycol-based SiC nanofluids" *International Journal of Heat and Mass Transfer* 84, **2015,** 925.

Li, Y.; Zhang, W.; Niu, J.; Chen, Y. "Mechanism of photogenerated reactive oxygen species and correlation with the antibacterial properties of engineered metal-oxide nanoparticles" *ACS Nano* 6, **2012b,** 5164.

Lifei, C.; Huaqing, X. "Silicon oil based multiwalled carbon nanotubes nanofluid with optimized thermal conductivity enhancement" *Colloids and Surfaces A: Physicochemical and Engineering Aspects* 352, **2009,** 136.

Ling, Z.; Ren, C. E.; Zhao, M. Q.; Yang, J.; Giammarco, J. M.; Qiu, J. S.; Barsoum, M. W.; Gogotsi, Y. "Flexible and conductive MXene films and nanocomposites with high capacitance" *Proceedings of the National Academy of Sciences of the United States of America* 111, **2014,** 16676.

Lis, J.; Pampuch, R.; Piekarczyk, J.; Stobierski, L. a. "New ceramics based on Ti$_3$SiC$_2$" *Ceramics international* 19, **1993,** 219.

Lis, J.; Pampuch, R.; Rudnik, T.; Wegrzyn, Z. "Reaction sintering phenomena of self-propagating high-temperature synthesis-derived ceramic powders in the Ti,-Si-C system" *Solid State Ionics* 101, **1997,** 59.

Liu, H.; Duan, C.; Yang, C.; Shen, W.; Wang, F.; Zhu, Z. "A novel nitrite biosensor based on the direct electrochemistry of hemoglobin immobilized on MXene-Ti$_3$C$_2$" *Sensors and Actuators B: Chemical* 218, **2015,** 60.

Liu, S.; Zeng, T.; Hofmann, M.; Burcombe, E.; Wei, J.; Jiang, R.; Kong, J.; Chen, Y. "Antibacterial activity of graphite, graphite oxide, graphene oxide, and reduced graphene oxide: membrane and oxidative stress" *ACS Nano* 5, **2011,** 6971.

Liya, Z.; Fangzhi, L.; Yanchun, Z.; Koc, R. "Preparation, mcrostructure, and mechanical properties of TiB$_2$ Using Ti$_3$AlC$_2$ as a Sintering Aid" *Journal of the American Ceramic Society* 95, **2012**.

Long, T. C.; Saleh, N.; Tilton, R. D.; Lowry, G. V.; Veronesi, B. "Titanium Dioxide (P25) produces reactive oxygen species in immortalized brain microglia (BV2): implications for nanoparticle neurotoxicity" *Environmental Science & Technology* 40, **2006,** 4346.

Low, I. M. "Vickers contact damage of micro-layered Ti$_3$SiC$_2$" *Journal of the European Ceramic Society* 18, **1998,** 709.

Low, I. M.; Lee, S. K.; Lawn, B. R.; Barsoum, M. W. "Contact damage accumulation in Ti$_3$SiC$_2$" *Journal of the American Ceramic Society* 81, **1998,** 225.

Luo, Y.; Li, S.; Pan, W.; Chen, J.; Wang, R. "Machinable and mechanical properties of sintered Al$_2$O$_3$-Ti$_3$SiC$_2$ composites" *Journal of materials Science* 39, **2004,** 3137.

Luo, Y.; Pan, W.; Li, S.; Wang, R.; Li, J. "Fabrication of Al$_2$O$_3$-Ti$_3$SiC$_2$ composites and mechanical properties evaluation" *Materials Letters* 57, **2003a**.

Luo, Y. M.; Li, S. Q.; Chen, J.; Wang, R. G.; Li, J. Q.; Pan, W. "Preparation and characterization of Al_2O_3-Ti_3SiC_2 composites and its functionally graded materials" *Materials Research Bulletin* 38, **2003b,** 69.

Manikandan, S.; Rajan, K. S. "Rapid synthesis of MgO nanoparticles & their utilization for formulation of a propylene glycol based nanofluid with superior transport properties" *RSC Advances* 4, **2014,** 51830.

Manoun, B.; Saxena, S. K.; El-Raghy, T.; Barsoum, M. W. "High-pressure x-ray diffraction study of Ta_4AlC_3" *Applied Physics Letters* 88, **2006,** 201902.

Mashtalir, O.; Cook, K. M.; Mochalin, V. N.; Crowe, M.; Barsoum, M. W.; Gogotsi, Y. "Dye adsorption and decomposition on two-dimensional titanium carbide in aqueous media" *Journal of Materials Chemistry A* 2, **2014,** 14334.

Mashtalir, O.; Naguib, M.; Mochalin, V. N.; Dallaagnese, Y.; Heon, M.; Barsoum, M. W.; Gogotsi, Y. "Intercalation and delamination of layered carbides and carbonitrides" *Nature communications* 4, **2013,** 1716.

Medvedeva, N. I.; Novikov, D. L.; Ivanovsky, A. L.; Kuznetsov, M. V.; Freeman, A. J. "Electronic properties of Ti_3SiC_2-based solid solutions" *Physical Review B* 58, **1998a,** 16042.

Medvedeva, N. I.; Novikov, D. L.; Ivanovsky, A. L.; Kuznetsov, M. V.; Freeman, A. J. "Electronic properties of Ti_3SiC_2-based solid solutions" *Physical Review B* 58, **1998b,** 16042.

Miremadi, B. K.; Morrison, S. R. "The intercalation and exfoliation of tungsten disulfide" *Journal of Applied Physics* 63, **1988,** 4970.

Mishra, T. K.; Ashish, K.; Vishal, V.; Pandey, K. N.; Vijai, K. "PEEK composites reinforced with zirconia nanofiller" *Composites Science and Technology* 72, **2012**.

Mogilevsky, P.; Mah, T. I.; Parthasarathy, T. A.; Cooke, C. M. "Toughening of SiC with Ti_3SiC_2 particles" *Journal of the American Ceramic Society* 89, **2006,** 633.

Morgiel, J.; Lis, J.; Pampuch, R. "Microstructure of Ti_3SiC_2-based ceramics" *Materials Letters* 27, **1996,** 85.

Myhra, S.; Summers, J. W. B.; Kisi, E. H. "Ti_3SiC_2-a layered ceramic exhibiting ultra-low friction" *Materials Letters* 39, **1999,** 6.

Naguib, M.; Come, J. r. m.; Dyatkin, B.; Presser, V.; Taberna, P.-L.; Simon, P.; Barsoum, M. W.; Gogotsi, Y. "MXene: a promising transition metal carbide anode for lithium-ion batteries" *Electrochemistry Communications* 16, **2012a,** 61.

Naguib, M.; Halim, J.; Lu, J.; Cook, K. M.; Hultman, L.; Gogotsi, Y.; Barsoum, M. W. "New two-dimensional niobium and vanadium carbides as promising materials for Li-ion batteries" *Journal of the American Chemical Society* 135, **2013,** 15966.

Naguib, M.; Jeremy, C.; Boris, D.; Volker, P.; Pierre-Louis, T.; Patrice, S.; Michel, W. B.; Yury, G. "MXene: a promising transition metal carbide anode for lithium-ion batteries" *Electrochemistry Communications* 16, **2012b,** 61.

Naguib, M.; Kurtoglu, M.; Presser, V.; Lu, J.; Niu, J.; Heon, M.; Hultman, L.; Gogotsi, Y.; Barsoum, M. W. "Two-dimensional nanocrystals produced by exfoliation of Ti_3AlC_2" *Advanced materials (Deerfield Beach, Fla.)* 23, **2011,** 4248.

Naguib, M.; Mashtalir, O.; Carle, J.; Presser, V.; Lu, J.; Hultman, L.; Gogotsi, Y.; Barsoum, M. W. "Two-dimensional transition metal carbides" *ACS nano* 6, **2012c,** 1322.

Naguib, M.; Mochalin, V. N.; Barsoum, M. W.; Gogotsi, Y. "25th Anniversary Article: MXenes: A new family of two dimensional materials" *Advanced Materials* 26, **2014,** 992.

Neetu, J.; Ramaprabhu, S. "Synthesis and thermal conductivity of copper nanoparticle decorated multiwalled carbon nanotubes based nanofluids" *The Journal of Physical Chemistry C* 112, **2008,** 9315.

Ngai, T. L.; Zheng, W.; Li, Y. "Effect of sintering temperature on the preparation of Cu-Ti_3SiC_2 metal matrix composite" *Progress in Natural Science-Materials International* 23, **2013,** 70.

Nickl, J. J.; Schweitzer, K. K.; Luxenberg, P. "Gasphasenabscheidung im system Ti- Si -C" *Journal of the Less Common Metals* 26, **1972,** 335.

Novoselov, K. S.; Geim, A. K.; Morozov, S. V.; Jiang, D.; Zhang, Y.; Dubonos, S. V.; Grigorieva, I. V.; Firsov, A. A. "Electric field effect in atomically thin carbon films" *Science* 306, **2004,** 666.

Novoselov, K. S.; Jiang, D.; Schedin, F.; Booth, T. J.; Khotkevich, V. V.; Morozov, S. V.; Geim, A. K. "Two-dimensional atomic crystals" *Proceedings of the National Academy of Sciences of the United States of America* 102, **2005,** 10451.

Nowotny, V. H. "Strukturchemie einiger verbindungen der Ã¼bergangsmetalle mit den elementen C, Si, Ge, Sn" *Progress in Solid State Chemistry* 5, **1971,** 27.

Nowotony, H.; Schuster, J.; Rogl, P. "Structural chemistry of complex carbides and related compounds" *J. Solid State Chem.* 44, **1982,** 126.

Oghbaei, M.; Mirzaee, O. "Microwave versus conventional sintering: A review of fundamentals, advantages and applications" *Journal of Alloys and Compounds* 494, **2010a,** 175.

Oghbaei, M.; Mirzaee, O. "Microwave versus conventional sintering: a review of fundamentals, advantages and applications" *Journal of Alloys and Compounds* 494, **2010b,** 175.

Oo, Z.; Low, I. M.; OConnor, B. H. "Dynamic study of the thermal stability of impure Ti_3SiC_2 in argon and air by neutron diffraction" *Physica B: Condensed Matter* 385, **2006,** 499.

Pacile, D.; Meyer, J. C.; Girit, C. O.; Zettl, A. "The two-dimensional phase of boron nitride: few-atomic-layer sheets and suspended membranes" *Applied Physics Letters* 92, **2008**.

Paek, S.-M.; Yoo, E.; Honma, I. "Enhanced cyclic performance and lithium storage capacity of SnO2/graphene nanoporous electrodes with three-dimensionally delaminated flexible structure" *Nano Letters* 9, **2009,** 72.

Palmquist, J. P.; Li, S.; Persson, P. O. A.; Emmerlich, J.; Wilhelmsson, O.; Hagberg, H.; Katsnelson, M. I.; Johansson, B. r.; Ahuja, R.; Eriksson, O. "$M_{n+1}AX_n$ phases in the Ti-Si-C system studied by thin-film synthesis and *ab initio* calculations" *Physical Review B* 70, **2004,** 165401.

Pampuch, R.; Lis, J.; Stobierski, L.; Tymkiewicz, M. "Solid combustion synthesis of Ti_3SiC_2" *Journal of the European Ceramic Society* 5, **1989,** 283.

Pasumarthi, V.; Chen, Y.; Bakshi, S. R.; Agarwal, A. "Reaction synthesis of Ti_3SiC_2 phase in plasma sprayed coating" *Journal of Alloys and Compounds* 484, **2009,** 113.

Pena-Paras, L.; Taha-Tijerina, J.; Garza, L.; Maldonado-Cortas, D. f.; Michalczewski, R.; Lapray, C. "Effect of CuO and Al_2O_3 nanoparticle additives on the tribological behavior of fully formulated oils" *Wear* 332, **2015,** 1256.

Peng, L. "Fabrication and properties of Ti$_3$AlC$_2$ particulates reinforced copper composites" *Scripta Materialia* 56, **2007,** 729.

Peng, Q.; Guo, J.; Zhang, Q.; Xiang, J.; Liu, B.; Zhou, A.; Liu, R.; Tian, Y. "Unique lead adsorption behavior of activated hydroxyl group in two-dimensional titanium carbide" *Journal of the American Chemical Society* 136, **2014,** 4113.

Pierce, C. G.; Chaturvedi, A. K.; Lazzell, A. L.; Powell, A. T.; Saville, S. P.; McHardy, S. F.; Lopez-Ribot, J. L. "A novel small molecule inhibitor of Candida albicans biofilm formation, filamentation and virulence with low potential for the development of resistance" *Npj Biofilms And Microbiomes* 1, **2015,** 15012.

Pietzka, M. A.; Schuster, J. C. "Summary of constitutional data on the Aluminum-Carbon-Titanium system" *Journal of Phase Equilibria* 15, **1994,** 392.

Prasad, G.; Naik, S. S.; Komel, A.; Srinath, S.; Kishore, K. A.; Setty, Y. P.; Shirish, S. "Stable colloidal copper nanoparticles for a nanofluid: Production and application" *Colloids and Surfaces A: Physicochemical and Engineering Aspects* 441, **2104,** 589597.

Prasher, R.; Song, D.; Wang, J.; Phelan, P. "Measurements of nanofluid viscosity and its implications for thermal applications" *Applied Physics Letters* 89, **2006,** 133108.

Qiuming, P.; Jianxin, G.; Qingrui, Z.; Jianyong, X.; Baozhong, L.; Aiguo, Z.; Riping, L.; Yongjun, T. "Unique lead adsorption behavior of activated hydroxyl group in two-dimensional titanium carbide" *Journal of the American Chemical Society* 136, **2013,** 4113.

R. R. Haering, J. A. R. S., K. Brandt. Lithium molybdenum disulphide battery cathode. US **1980**; Vol. 4224390.

Racault, C.; Langlais, F.; Naslain, R. "Solid-state synthesis and characterization of the ternary phase Ti$_3$SiC$_2$" *Journal of materials Science* 29, **1994,** 3384.

Radhakrishnan, R.; Henager, C. H.; Brimhall, J. L.; Bhaduri, S. B. "Synthesis of Ti$_3$SiC$_2$-SiC and TiSi2-SiC composites using displacement reactions in the Ti- Si- C system" *Scripta Materialia* 34, **1996,** 1809.

Radovic, M.; Barsoum, M. W. "MAX phases: bridging the gap between metals and ceramics" *American Ceramics Society Bulletin* 92, **2013,** 20.

Radovic, M.; Barsoum, M. W.; El-Raghy, T.; Seidensticker, J.; Wiederhorn, S. "Tensile properties of Ti$_3$SiC$_2$ in the 25-1300 °C temperature range" *Acta Materialia* 48, **2000,** 453.

Radovic, M.; Barsoum, M. W.; El-Raghy, T.; Wiederhorn, S. M. "Tensile creep of coarse-grained Ti$_3$SiC$_2$ in the 1000-1200 °C temperature range" *Journal of Alloys and Compounds* 361, **2003,** 299.

Radovic, M.; Barsoum, M. W.; El-Raghy, T.; Wiederhorn, S. M.; Luecke, W. E. "Effect of temperature, strain rate and grain size on the mechanical response of Ti$_3$SiC$_2$ in tension" *Acta Materialia* 50, **2002,** 1297.

Rampai, T.; Lang, C. I.; Sigalas, I. "Investigation of MAX phase/c-BN composites" *Ceramics International* 39, **2013,** 4739.

Rao, C. N. R.; Nag, A. "Inorganic Analogues of Graphene" *European Journal of Inorganic Chemistry* 2010, **2010,** 4244.

Rasool, K.; Helal, M.; Ali, A.; Ren, C. E.; Gogotsi, Y.; Mahmoud, K. A. "Antibacterial Activity of Ti$_3$C$_2$T$_x$ MXene" *ACS Nano* 10, **2016,** 3674.

Reddy, M. C. S.; Rao, V. V. "Experimental studies on thermal conductivity of blends of ethylene glycol-water-based TiO$_2$ nanofluids" *International Communications in Heat and Mass Transfer* 46, **2013,** 3136.

Ren, C. E.; Hatzell, K. B.; Alhabeb, M.; Ling, Z.; Mahmoud, K. A.; Gogotsi, Y. "Charge- and Size-Selective Ion Sieving Through Ti$_3$C$_2$T$_x$ MXene Membranes" *The Journal of Physical Chemistry Letters* 6, **2015,** 4026.

Reynolds, K. J.; Frey, G. L.; Friend, R. H. "Solution-processed niobium diselenide as conductor and anode for polymer light-emitting diodes" *Applied Physics Letters* 82, **2003,** 1123.

Riley, D. P.; Kisi, E. H.; Hansen, T. C.; Hewat, A. W. "Self propagating high• temperature synthesis of Ti$_3$SiC$_2$: I, Ultra high speed neutron diffraction study of the reaction mechanism" *Journal of the American Ceramic Society* 85, **2002,** 2417.

Riley, D. P.; Kisi, E. H.; Phelan, D. "SHS of Ti$_3$SiC$_2$: ignition temperature depression by mechanical activation" *Journal of the European Ceramic Society* 26, **2006,** 1051.

Rosen, J.; Ryves, L.; Persson, P. O. A.; Bilek, M. M. M. "Deposition of epitaxial Ti$_2$AlC thin films by pulsed cathodic arc" *Journal of applied physics* 101, **2007.**

S. Myhra, J. A. A. C., M.W. Barsoum. "Crystal-chemistry of the Ti$_3$AlC$_2$ and Ti$_4$AlN$_3$ layered carbide/nitride phases characterization by XPS" *Journal of Physics and Chemistry of Solids* 62, **2001,** 811817.

Sanjay, G.; Sugunan, S. "Glucoamylase immobilized on montmorillonite: Synthesis, characterization and starch hydrolysis activity in a fixed bed reactor" *Catalysis Communications* 6, **2005,** 525.

Sarkar, S. J.; Cho, M. C.; Chu, S. S.; Hwang, S. W. "Park, and B. Basu, Fretting Wear Properties of Ti3SiC2, *Journal of American Ceramic Society* 88, **2005,** 3245.

Sato, F.; Li, J.-F.; Watanabe, R. "Reaction synthesis of Ti$_3$SiC$_2$ from mixture of elemental powders" *Materials Transactions, JIM* 41, **2000,** 605.

Scabarozi, T. H.; Amini, S.; Finkel, P.; Leaffer, O. D.; Spanier, J. E.; Barsoum, M. W.; Drulis, M.; Drulis, H.; Tambussi, W. M.; Hettinger, J. D. "Electrical, thermal, and elastic properties of the MAX-phase Ti$_2$SC" *Journal of applied physics* 104, **2008,** 033502.

Schedin, F.; Geim, A. K.; Morozov, S. V.; Hill, E. W.; Blake, P.; Katsnelson, M. I.; Novoselov, K. S. "Detection of individual gas molecules adsorbed on graphene" *Nat Mater* 6, **2007,** 652.

Seo, J.-W.; Jun, Y.-W.; Park, S.-W.; Nah, H.; Moon, T.; Park, B.; Kim, J.-G.; Kim, Y. J.; Cheon, J. "Two-dimensional nanosheet crystals" *Angewandte Chemie-International Edition* 46, **2007,** 8828.

Shi, S.-L.; Pan, W.; Fang, M.-H.; Fang, Z.-Y. "Electrical and dielectric behaviors of Ti$_3$SiC$_2$/Yttria-stabilized zirconia composites" *Applied Physics Letters* 87, **2005**.

Shima, P. D.; John, P.; Baldev, R. "Synthesis of aqueous and nonaqueous iron oxide nanofluids and study of temperature dependence on thermal conductivity and viscosity" *J. Phys. Chem. C* 114, **2010,** 18825.

Sik Hwang, W.; Remskar, M.; Yan, R.; Protasenko, V.; Tahy, K.; Doo Chae, S.; Zhao, P.; Konar, A.; Xing, H.; Seabaugh, A.; Jena, D. "Transistors with chemically synthesized layered semiconductor WS$_2$ exhibiting 105 room temperature modulation and ambipolar behavior" *Applied Physics Letters* 101, **2012,** 013107.

Singh, D.; Timofeeva, E.; Yu, W.; Routbort, J.; France, D.; Smith, D.; Lopez-Cepero, J. M. "An investigation of silicon carbide-water nanofluid for heat transfer applications" *Journal of Applied Physics* 105, **2009,** 64306.

Song, W.-L.; Wang, P.; Cao, L.; Anderson, A.; Meziani, M. J.; Farr, A. J.; Sun, Y.-P. "Polymer/Boron nitride nanocomposite materials for superior thermal transport performance" *Angewandte Chemie-International Edition* 51, **2012,** 6498.

Soon, J. M.; Loh, K. P. "Electrochemical double-layer capacitance of MoS_2 nanowall films" *Electrochemical and Solid State Letters* 10, **2007,** A250.

Sordello, F.; Zeb, G.; Hu, K.; Calza, P.; Minero, C.; Szkopek, T.; Cerruti, M. "Tuning TiO_2 nanoparticle morphology in graphene-TiO_2 hybrids by graphene surface modification" *Nanoscale* 6, **2014,** 6710.

Souchet, A.; Fontaine, J.; Belin, M.; Le Mogne, T.; Loubet, J.-L.; Barsoum, M. W. "Tribological duality of Ti_3SiC_2" *Tribology Letters* 18, **2005,** 341.

Spotz, M. S.; Skamser, D. J.; Johnson, D. L. "Thermal stability of ceramic materials in microwave heating" *Journal of the American Ceramic Society* 78, **1995,** 1041.

Stankovich, S.; Dikin, D. A.; Dommett, G. H. B.; Kohlhaas, K. M.; Zimney, E. J.; Stach, E. A.; Piner, R. D.; Nguyen, S. T.; Ruoff, R. S. "Graphene-based composite materials" *Nature* 442, **2006,** 282.

Stankovich, S.; Dikin, D. A.; Piner, R. D.; Kohlhaas, K. A.; Kleinhammes, A.; Jia, Y.; Wu, Y.; Nguyen, S. T.; Ruoff, R. S. "Synthesis of graphene-based nanosheets via chemical reduction of exfoliated graphite oxide" *Carbon* 45, **2007,** 1558.

Sudeep, P. M.; Taha-Tijerina, J.; Ajayan, P. M.; Narayanan, T. N.; Anantharaman, M. R. "Nanofluids based on fluorinated graphene oxide for efficient thermal management" *RSC Advances* 4, **2014,** 24887.

Suganthi, K. S.; Anusha, N.; Rajan, K. S. "Low viscous ZnO-propylene glycol nanofluid: a potential coolant candidate" *Journal of Nanoparticle Research* 15, **2013**.

Sui Lin, S.; Wei, P. "Machinable Ti_3SiC_2/Hydroxyapatite bioceramic composites by spark plasma sintering" *Journal of the American Ceramic Society* 90, **2007,** 3331.

Sun, Z.; Zhang, Z.; Hashimoto, H.; Abe, T. "Ternary Compound Ti_3SiC_2: Part I. Pulse discharge sintering synthesis" *Materials Transactions* 43, **2002a,** 428.

Sun, Z.; Zhou, Y. "Ab initio calculation of titanium silicon carbide" *Physical Review B* 60, **1999,** 1441.

Sun, Z.; Zhou, Y.; Zhou, J. "The anomalous flow behaviour in the layered Ti_3SiC_2 ceramic" *Philosophical magazine letters* 80, **2000,** 289.

Sun, Z.; Zou, Y.; Tada, S.; Hashimoto, H. "Effect of Al addition on pressureless reactive sintering of Ti_3SiC_2" *Scripta Materialia* 55, **2006,** 1011.

Sun, Z. M. "Progress in research and development on MAX phases: a family of layered ternary compounds" *International Materials Reviews* 56, **2011,** 143.

Sun, Z. M.; Yang, S.; Hashimoto, H.; Tada, S.; Abe, T. "Synthesis and consolidation of ternary compound Ti_3SiC_2 from green compact of mixed powders" *Materials Transactions* 45, **2004,** 373.

Sun, Z. M.; Zhou, Y. C.; Li, S. "Tribological behavior of Ti_3SiC_2-based material" *Journal of Materials Science & Technology* 18, **2002b,** 142.

Sun, Z. M.; Zhou, Y. C.; Li, S. "Tribological behavior of Ti_3SiC_2-based material" **2002c**.

Sutton, W. H. "Microwave processing of ceramic materials" *American Ceramic Society Bulletin* 68, **1989,** 376.

Tan, Y. Q.; Song, Y. H.; Zheng, Q. "Hydrogen bonding-driven rheological modulation of chemically reduced graphene oxide/poly(vinyl alcohol) suspensions and its application in electrospinning" *Nanoscale* 4, **2012,** 6997.

Tang, Y.; Wu, D.; Mai, Y.; Pan, H.; Cao, J.; Yang, C.; Zhang, F.; Feng, X. "A two-dimensional hybrid with molybdenum disulfide nanocrystals strongly coupled on nitrogen-enriched graphene via mild temperature pyrolysis for high performance lithium storage" *Nanoscale* 6, **2014,** 14679.

Tenne, R.; Margulis, L.; Genut, M.; Hodes, G. "Polyhedral and cylindrical structures of tungsten disulphide" *Nature* 360, **1992a,** 444.

Tenne, R.; Margulis, L.; Genut, M. e. a.; Hodes, G. "Polyhedral and cylindrical structures of tungsten disulphide" *Nature* 360, **1992b,** 444.

Tessy Theres, B.; Ramaprabhu, S. "Investigation of thermal and electrical conductivity of graphene based nanofluids" *Journal of Applied Physics* 108, **2010,** 124308.

Tessy Theres, B.; Ramaprabhu, S. "Synthesis and transport properties of metal oxide decorated graphene dispersed nanofluids" *The Journal of Physical Chemistry C* 115, **2011,** 85278533.

Tessy Theres, B.; Sundara, R. "Experimental investigation of the thermal transport properties of a carbon nanohybrid dispersed nanofluid" *Nanoscale* 3, **2011,** 2208.

Thadathil, S. S.; Asha, K.; Lakshmi Narayan, S.; Swapankumar, G. "Facile synthetic strategy of oleophilic zirconia nanoparticles allows preparation of highly stable thermo-conductive coolant" *RSC Advances* 4, **2014a,** 28020.

Thadathil, S. S.; Asha, K.; Mohamed, A. P.; Hareesh, U. S.; Swapankumar, G. "Synthesis and characterization of cerium oxide based nanofluids: An efficient coolant in heat transport applications" *Chemical Engineering Journal* 255, **2014b,** 282.

Tian, W.; Sun, Z.; Du, Y.; Hashimoto, H. "Synthesis reactions of Cr_2AlC from $CrAl_4C_3C$ by pulse discharge sintering" *Materials Letters* 62, **2008a,** 3852.

Tian, W.; Wang, P.; Kan, Y.; Zhang, G. "Oxidation behavior of Cr_2AlC ceramics at 1,100 and 1,250 C" *Journal of materials Science* 43, **2008b,** 2785.

Tong, X.; Okano, T.; Iseki, T.; Yano, T. "Synthesis and high temperature mechanical properties of Ti_3SiC_2/SiC composite" *Journal of materials Science* 30, **1995,** 3087.

Tsagaropoulos, G.; Eisenberg, A. "Dynamic-mechanical study of the factors affecting the 2 glass-transition behavior of filled polymers - similarities and differences with random ionomers" *Macromolecules* 28, **1995,** 6067.

Tzenov, N. V.; Barsoum, M. W. "Synthesis and characterization of Ti_3AlC_2" *Journal of the American Ceramic Society* 83, **2000,** 825.

Wang, J.-Y.; Zhou, Y.-C. "Polymorphism of Ti_3SiC_2 ceramic: first-principles investigations" *Physical Review B* 69, **2004,** 144108.

Wang, J.; Wang, J.; Zhou, Y.; Lin, Z.; Hu, C. "*Ab initio* study of polymorphism in layered ternary carbide M_4AlC_3 (M= V, Nb and Ta)" *Scripta Materialia* 58, **2008,** 1043.

Wang, Q.-H.; Xue, Q.-J.; Liu, W.-M.; Chen, J.-M. "The friction and wear characteristics of nanometer SiC and polytetrafluoroethylene filled polyetheretherketone" *Wear* 243, **2000.**

Wang, Q.; Hu, C.; Cai, S.; Sakka, Y.; Grasso, S.; Huang, Q. "Synthesis of High purity Ti$_3$SiC$_2$ by microwave Sintering" *International Journal of Applied Ceramic Technology* 11, **2014,** 911.

Wang, Q.; Xu, J.; Shen, W.; Xue, Q. "The effect of nanometer SiC filler on the tribological behavior of PEEK" *Wear* **1997a**.

Wang, Q.; Xue, Q.; Liu, H.; Shen, W.; Xu, J. "The effect of particle size of nanometer ZrO$_2$ on the tribological behaviour of PEEK" *Wear* **1996a**.

Wang, Q.; Xue, Q.; Shen, W. "The friction and wear properties of nanometre SiO$_2$ filled polyetheretherketone" *Tribology International* 30, **1997b**.

Wang, Q.; Xue, Q.; Shen, W.; Zhang, J. "The friction and wear properties of nanometer ZrO$_2$-filled polyetheretherketone" *Journal of Applied Polymer Science* 69, **1998**.

Wang, Q. H.; Xu, J. F.; Shen, W. C.; Liu, W. M. "An investigation of the friction and wear properties of nanometer Si$_3$N$_4$ filled PEEK" *Wear* 196, **1996b,** 82.

Wang, X.; Zhou, Y. "Solid-liquid reaction synthesis of layered machinable Ti$_3$AlC$_2$ ceramic" *Journal of Materials Chemistry* 12, **2002a,** 455.

Wang, X. H.; Zhou, Y. C. "Microstructure and properties of Ti$_3$AlC$_2$ prepared by the solid-liquid reaction synthesis and simultaneous in-situ hot pressing process" *Acta Materialia* 50, **2002b,** 3143.

Wang, X. H.; Zhou, Y. C. "Stability and selective oxidation of aluminum in nano-laminate Ti$_3$AlC$_2$ upon heating in argon" *Chemistry of materials* 15, **2003,** 3716.

Wolfsgruber, H.; Nowotny, H.; Benesovsky, F. "Die Kristallstruktur von Ti$_3$GeC$_2$" *Monatshefte fur Chemie/Chemical Monthly* 98, **1967,** 2403.

Wong, C. P.; Bollampally, R. S. "Thermal conductivity, elastic modulus, and coefficient of thermal expansion of polymer composites filled with ceramic particles for electronic packaging" *Journal of Applied Polymer Science* 74, **1999,** 3396.

Wu, J.; Becerril, H. c. A.; Bao, Z.; Liu, Z.; Chen, Y.; Peumans, P. "Organic solar cells with solution-processed graphene transparent electrodes" *Applied Physics Letters* 92, **2008a,** 263302.

Wu, J.; Tang, Q.; Sun, H.; Lin, J.; Ao, H.; Huang, M.; Huang, Y. "Conducting film from graphite oxide nanoplatelets and poly (acrylic acid) by layer-by-layer self-assembly" *Langmuir* 24, **2008b,** 4800.

Wu, J.; Zhou, Y.; Yan, C. "Mechanical and electrical properties of Ti2SnC dispersion-strengthened copper" *Zeitschrift fur Metallkunde* 96, **2005,** 847.

Wu, X.-Z.; Cheng, A.-X.; Sun, L.-M.; Sun, S.-J.; Lou, H.-X. "Plagiochin E, an antifungal bis (bibenzyl), exerts its antifungal activity through mitochondrial dysfunction-induced reactive oxygen species accumulation in Candida albicans" *Biochimica et Biophysica Acta (BBA)-General Subjects* 1790, **2009,** 770.

Xia, T.; Kovochich, M.; Brant, J.; Hotze, M.; Sempf, J.; Oberley, T.; Sioutas, C.; Yeh, J. I.; Wiesner, M. R.; Nel, A. E. "Comparison of the abilities of ambient and manufactured nanoparticles to induce cellular toxicity according to an oxidative stress paradigm" *Nano Letters* 6, **2006,** 1794.

Xiaohong, X.; Siguo, C.; Wei, D.; Yao, N.; Zidong, W. "An extraordinarily stable catalyst: Pt NPs supported on two-dimensional $Ti_3C_2X_2$ (X = OH, F) nanosheets for oxygen reduction reaction" *Chemical Communications* 49, **2013,** 10112.

Xiaoliang, S.; Mang, W.; Wenzheng, Z.; Zhiwei, Z.; Zengshi, X.; Qiaoxin, Z.; Siyuan, S.; Jie, Y.; Abid Qamar ud, D. "Friction and wear behavior of NiAl/10 wt% Ti_3SiC_2 composites" *Wear* 303, **2013a,** 9.

Xiaoliang, S.; Wenzheng, Z.; Mang, W.; Zengshi, X.; Jie, Y.; Siyuan, S.; Abid Qamar ud, D.; Qiaoxin, Z. "Tribological performance of $Ni_3Al/15$ wt% Ti_3SiC_2 composites against Al_2O_3, Si_3N_4 and WC-6Co from 25 to 800 °C" *Wear* 303, **2013b**.

Xie, H. Q.; Lee, H.; Youn, W.; Choi, M. "Nanofluids containing multiwalled carbon nanotubes and their enhanced thermal conductivities" *Journal of Applied Physics* 94, **2003,** 4967.

Xue, Q.; Wang, Q. "Wear mechanisms of polyetheretherketone composites filled with various kinds of SiC" *Wear* **1997**.

Xuekun, L.; Minfeng, Y.; Hui, H.; Rodney, S. R. "Tailoring graphite with the goal of achieving single sheets" *Nanotechnology* 10, **1999,** 269.

Y.M. Luo; W. Pan; S.I. Li; J. Chen; R.G. Wang; Li, J. Q. *Materials Letters* 52, **2002,** 245.

Yadoji, P.; Peelamedu, R.; Agrawal, D.; Roy, R. "Microwave sintering of Ni/Zn ferrites: comparison with conventional sintering" *Materials Science and Engineering: B* 98, **2003,** 269.

Yang, K.; Zhang, S.; Zhang, G.; Sun, X.; Lee, S.-T.; Liu, Z. "Graphene in Mice: ultrahigh in vivo tumor uptake and efficient photothermal therapy" *Nano Letters* 10, **2010,** 3318.

Yang, L.; Wang, S.; Mao, J.; Deng, J.; Gao, Q.; Tang, Y.; Schmidt, O. G. "Hierarchical MoS$_2$/polyaniline nanowires with excellent electrochemical performance for lithium-ion batteries" *Advanced Materials* 25, **2013,** 1180.

Yang, S.; Sun, Z. M.; Hashimoto, H. "Reaction in Ti$_3$SiC$_2$ powder synthesis from a TiSi/TiC powder mixture" *Journal of Alloys and Compounds* 368, **2004,** 312.

Yang, S. L.; Sun, Z. M.; Hasimoto, H.; Park, Y. H.; Abe, T. "Oxidation of Ti$_3$SiC$_2$ at 1000 °C in Air" *Oxidation of metals* 59, **2003,** 155.

Yang, X.; Li, J.; Liang, T.; Ma, C.; Zhang, Y.; Chen, H.; Hanagata, N.; Su, H.; Xu, M. "Antibacterial activity of two-dimensional MoS$_2$ sheets" *Nanoscale* 6, **2014,** 10126.

Yongming, L.; Wei, P.; Shuqin, L.; Jian, C.; Ruigang, W.; Jianqiang, L. "Synthesis of high-purity Ti3SiC2 polycrystals by hot-pressing of the elemental powders" *Materials Letters* 52, **2002,** 245.

YongMing, L.; Wei, P.; ShuQin, L.; RuiGang, W.; JianQiang, L. "Fabrication of Al2O3â€"Ti3SiC2 composites and mechanical properties evaluation" *Materials Letters* 57, **2003**.

Yongming, L.; Zhimin, Z.; Caihong, X.; Xuening, M. "Polycarbosilane derived Ti$_3$SiC$_2$" *Materials Letters* 62, **2008,** 3570.

Yu, Q.; Li, J.; Zhang, Y.; Wang, Y.; Liu, L.; Li, M. "Inhibition of gold nanoparticles (AuNPs) on pathogenic biofilm formation and invasion to host cells" *Scientific reports* 6, **2016**.

Yu, W.; Xie, H. Q.; Bao, D. "Enhanced thermal conductivities of nanofluids containing graphene oxide nanosheets" *Nanotechnology* 21, **2010,** 7.

Yuan-Liang, C.; Wei-Hsing, T. "Contribution of plastic deformation of Ti$_3$SiC$_2$ to the crack deflection in the Al$_2$O$_3$/Ti$_3$SiC$_2$ composites" *Materials Science and Engineering: A* 528, **2011**.

Zeng, Z.; Sun, T.; Zhu, J.; Huang, X.; Yin, Z.; Lu, G.; Fan, Z.; Yan, Q.; Hng, H. H.; Zhang, H. "An effective method for the fabrication of few-layer-thick inorganic nanosheets" *Angewandte Chemie-International Edition* 51, **2012,** 9052.

Zhang, H. B.; Bao, Y. W.; Zhou, Y. C. "Current status in layered ternary carbide Ti_3SiC_2, a review" *J. Mater. Sci. Technol* 25, **2009,** 1.

Zhang, H. B.; Zhou, Y. C.; Bao, Y. W.; Li, M. S. "Abnormal thermal shock behavior of Ti_3SiC_2 and Ti_3AlC_2" *Journal of materials research* 21, **2006,** 2401.

Zhang, X.; Coleman, A. C.; Katsonis, N.; Browne, W. R.; van Wees, B. J.; Feringa, B. L. "Dispersion of graphene in ethanol using a simple solvent exchange method" *Chemical Communications* 46, **2010,** 7539.

Zhang, X.; Xu, J.; Wang, H.; Zhang, J.; Yan, H.; Pan, B.; Zhou, J.; Xie, Y. "Ultrathin nanosheets of max phases with enhanced thermal and mechanical properties in polymeric compositions: $Ti_3Si_{0.75}Al_{0.25}C_2$" *Angewandte Chemie-International Edition* 52, **2013,** 4361.

Zhang, Y.; Ding, G. P.; Zhou, Y. C.; Cai, B. C. "Ti_3SiC_2 - a self-lubricating ceramic" *Materials Letters* 55, **2002a,** 285.

Zhang, Y.; Small, J. P.; Pontius, W. V.; Kim, P. "Fabrication and electric-field-dependent transport measurements of mesoscopic graphite devices" *Applied Physics Letters* 86, **2005,** 073104.

Zhang, Y.; Zhou, Y. C. "Mechanical properties of Ti_3SiC_2 dispersion-strengthened copper" *Zeitschrift Fur Metallkunde* 91, **2000,** 585.

Zhang, Z. F.; Sun, Z. M.; Hashimoto, H. "Rapid synthesis of ternary carbide Ti_3SiC_2 through pulse-discharge sintering technique from Ti/Si/TiC powders" *Metallurgical and Materials Transactions A* 33, **2002b,** 3321.

Zhang, Z. F.; Sun, Z. M.; Hashimoto, H. "Low temperature synthesis of Ti_3SiC_2 from Ti/SiC/C powders" *Materials science and technology* 20, **2004,** 1252.

Zhang, Z. F.; Sun, Z. M.; Hashimoto, H.; Abe, T. "A new synthesis reaction of Ti_3SiC_2 through pulse discharge sintering Ti/SiC/TiC powder" *Scripta Materialia* 45, **2001,** 1461.

Zhang, Z. F.; Sun, Z. M.; Hashimoto, H.; Abe, T. "Application of pulse discharge sintering (PDS) technique to rapid synthesis of Ti$_3$SiC$_2$ from Ti/Si/C powders" *Journal of the European Ceramic Society* 22, **2002c,** 2957.

Zhang, Z. F.; Sun, Z. M.; Hashimoto, H.; Abe, T. "Application of pulse discharge sintering (PDS) technique to rapid synthesis of Ti$_3$SiC$_2$ from Ti/Si/C powders" *Journal of the European Ceramic Society* 22, **2002a,** 2957.

Zhi, C.; Bando, Y.; Tang, C.; Kuwahara, H.; Golberg, D. "Large-scale fabrication of boron nitride nanosheets and their utilization in polymeric composites with improved thermal and mechanical properties" *Advanced Materials* 21, **2009,** 2889.

Zhi, C. Y.; Xu, Y. B.; Bando, Y.; Golberg, D. "Highly thermo-conductive fluid with boron nitride nanofillers" *ACS nano* 5, **2011,** 6571.

Zhou, A.; Wang, C.-A.; Hunag, Y. "Synthesis and mechanical properties of Ti$_3$AlC$_2$ by spark plasma sintering" *Journal of materials Science* 38, **2003,** 3111.

Zhou, Y.; Chen, B.; Wang, X.; Yan, C. "Mechanical properties of Ti$_3$SiC$_2$ particulate reinforced copper prepared by hot pressing of copper coated Ti$_3$SiC$_2$ and copper powder" *Materials science and technology* 20, **2004,** 661.

Zhou, Y.; Sun, Z. "Microstructure and mechanism of damage tolerance for Ti$_3$SiC$_2$ bulk ceramics" *Material Research Innovations* 2, **1999,** 360.

Zhou, Y.; Sun, Z. "Crystallographic relations between Ti$_3$SiC$_2$ and TiC" *Material Research Innovations* 3, **2000,** 286.

Zhou, Y.; Sun, Z. "Micro-scale plastic deformation of polycrystalline Ti$_3$SiC$_2$ under room-temperature compression" *Journal of the European Ceramic Society* 21, **2001,** 1007.

Zhou, Y.; Sun, Z.; Chen, S.; Zhang, Y. "In-situ hot pressing/solid-liquid reaction synthesis of dense titanium silicon carbide bulk ceramics" *Material Research Innovations* 2, **1998,** 142.

Zhu, J.; Mei, B. "Fabrication of high-purity Ti$_3$SiC$_2$ by spark plasma sintering (SPS) of elemental powders" *Journal of materials science letters* 22, **2003,** 889.

Zhu, J.; Mei, B.; Xu, X.; Liu, J. "Synthesis of single-phase polycrystalline Ti$_3$SiC$_2$ and Ti$_3$AlC$_2$ by hot pressing with the assistance of metallic Al or Si" *Materials Letters* 58, **2004,** 588.

Zou, Y.; Sun, Z.; Hashimoto, H.; Tada, S. "Synthesis of high-purity polycrystalline Ti_3AlC_2 through pulse discharge sintering Ti/Al/TiC powders" *Journal of Alloys and Compounds* 456, **2008a,** 456.

Zou, Y.; Sun, Z.; Tada, S.; Hashimoto, H. "Effect of Al addition on low-temperature synthesis of Ti_3SiC_2 powder" *Journal of Alloys and Compounds* 461, **2008b,** 579.